Ph.D. Thesis

Development of Patient-Specific CT-FE Modelling of Bone Through Validation Using Porcine Femora

Nicholas John Emerson

September 2012

Department of Mechanical Engineering
THE UNIVERSITY OF SHEFFIELD

Abstract

A&E statistics in the UK demonstrate that as high as 60% of bone fractures occur as a result of trips and falls. Subsequently, many studies have been undertaken to simulate the occurrence of hip fractures. Little simulation has been considered outside of the older population. In 2010, 6,870 UK children were on the child protection register under the category of physical abuse (Non-Accidental Injury). The diagnosis of NAI is complex, and mis-diagnosis can have severe consequences.

Development of simulation techniques has allowed high resolution three-dimensional models of bone to be created from patient-specific medical imaging. To ensure accuracy in simulation, extensive physical validation must be undertaken. The 'gold standard' for human simulation is to use human bone samples. However, the inaccessibility of human samples often leads to small sample sizes, typically considering only a few injury types.

In this thesis, patient-specific simulation was used to investigate the torsional (spiral fractures can be an indicator NAI) and compressive fracture of long bones. Extensive physical validation was undertaken. Fundamentally, the applicability of animal substitution in testing and simulation was considered. This allows testing of samples that are more available than the human counterpart, offering the opportunity to test more samples, and to obtain developing bones.

Testing and simulation performed favourably; accurate results demonstrated the viability of the techniques used in simulation. The applicability of the simulation was confirmed through accurate prediction of the failure load of porcine samples.

Using validated, high accuracy simulation on a patient-specific basis is the future of healthcare. Combining the accuracy observed within this thesis, with developing bone samples from animals may be the next step in developing the simulation procedure for clinical application in NAI. This is a goal that has far reaching social implications and could help in the protection of the most vulnerable of patients.

Glossary and Nomenclature

Common engineering and simulation terms used within the thesis;

Boundary Condition	The manner in which a model is constrained at the start of simulation, and/or the manner in which forces are applied.
Couple	Equal and opposite forces applied at a distance from a central point, used to provide rotational force (Torque).
Discretization	The splitting of a mask or model into an array of smaller parts
Element	The smaller parts that are characterized by discretization and are solved in the Finite Element process.
FE	Finite Element
Greyscale	The relative brightness of pixels or voxels within a source image
Input Parameter	A modelling input such as the application of a force, or the assignment of a material parameter.
In Silico	'In Simulation' the process of testing using computational analysis
Mask	The area and/or volume of pixels/voxels within an image or stack of images that are selected for meshing and simulation.
Mesh	The collective noun for an array of elements.
Partial Volume (Effect)	The effect of averaging a result (for greyscale or material property) as a result of splitting an image into individual voxels. (Considered in detail within the thesis)
Pixel / Voxel	The pixels (2D) and voxels (3D) are the individual elements that make up a digitised image. Their size is defined by the resolution of the image capture, and the digitization process.
Segmentation	The process of selecting which voxels or pixels will be selected (masked) to form a model.

Common medical terms used within the study;

BMD	Bone mineral density
Comminuted (Fracture)	A fracture in which a piece of the bone is displaced (or splintered)
CT	X-Ray Computed Tomography – A clinical imaging method
DXA/DEXA	Dual-energy X-ray absorptiometry - A clinical measuring method used to calculate bone mineral density (BMD).

Epicondyle/Condyle	'Knuckle' prominence at the end of a bone. This is the region that forms the joint. 'Epi' refers to being upon the surface of the knuckle.
Lateral	The side of an object or part of the body that is furthest from the center line.
Medial	The side of an object or part of the body that is closest to the center line.
MRI	Magnetic Resonance Imaging – A clinical imaging method
NAI	Non Accidental Injury
Proximal/Distal	Nearest to/furthest from a defined reference point, or point of attachment.

Abbreviation	Value	Units
F	Force	N
E	Young's modulus, Modulus of Elasticity	Pa or N/m²
GS	Greyscale	N/A
I	Moment of Inertia	kgm²
J	Polar Second Moment of Area	m^4
L	Length	m
N	Poisson's Ratio	N/A
T	Torque	Nm
ε	Strain	N/A
σ	Stress	Pa

General Arrangement

Throughout the thesis the general axes are defined as follows: (Figure 1.1)

z direction: The vertical axis, aligned with the centroid of the mid-shaft where possible.
x direction: The lateral axis, spanning from the inner centre line to the outside of the subject.
y direction: The anterior/posterior axis, spanning from frontal to rearmost position.

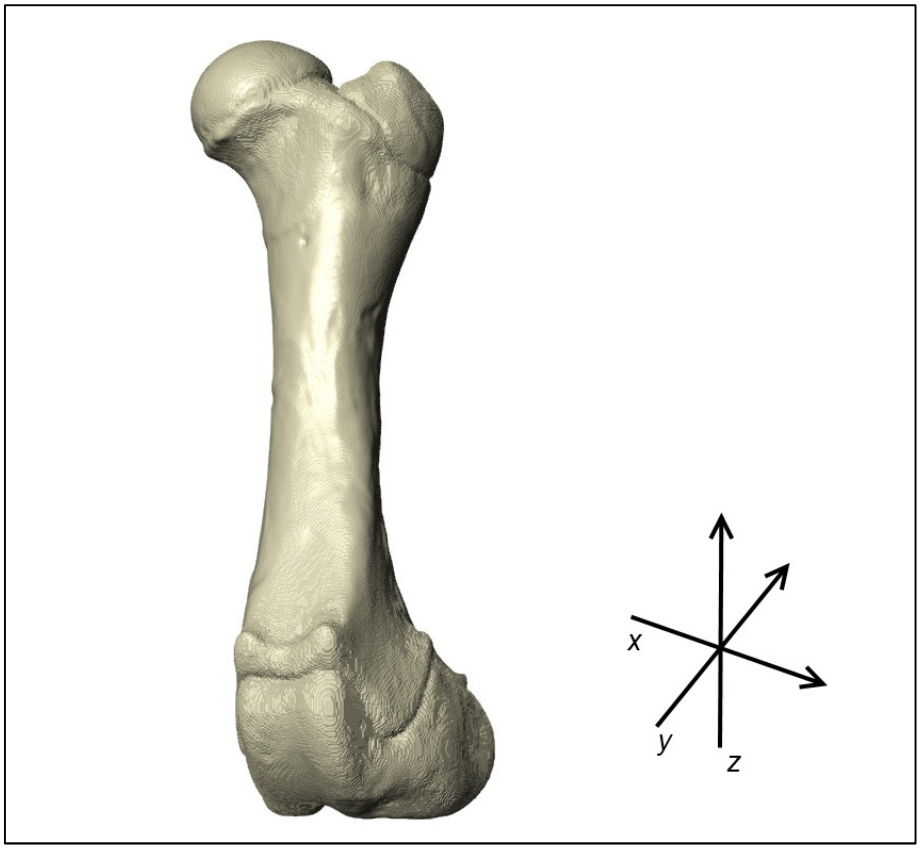

Figure 1.1 The general axes arrangement considered throughout the thesis.

Contents

Acknowledgements

I would like to thank a number of people for their contributions and help during the course of my PhD. Dr Matt Carré and Dr Gwen Reilly of the University of Sheffield for their continued support and guidance. I would like to thank Professor Marco Viceconti, with whom I have had only two or three hours of contact, but who's guidance in such a short period was greatly received.

Dr James Clarke and Dr Robert Barthorpe for their personal experiences and peer support. Richard Kay and Jamie Booth of the University of Sheffield for their valuable help in the preparation of the physical tests. John Middlemiss and Dr Brad Wynne of the IMMPETUS team for continued access to the IMMPETUS test rig, and their support in physical testing.

From Sheffield Children's Hospital I must thank Dr Amaka Offiah and Ms Yvonne Vickers; without whom there would be no data to create the models.

The EPSRC for their funding assistance, and Simpleware for their technical and financial assistance.

I'd also like to thank Lisa-Marie, whose experience and support over the past three years has been immeasurable. Finally a quick thanks to Palmer, who has ensured I get the most out of each day, with a prompt 5.30am wakeup call - every single day.

1 Introduction

The development of simulation techniques has allowed high resolution three-dimensional models of bone and other biological tissues to be created directly from patient-specific medical imaging such as Computed Tomography (CT). In addition to accurate geometry, the density information within CT images can provide patient-specific material parameters in bone simulation, producing highly accurate results. This type of simulation has been used to assess numerous parameters, such as the mechanical properties of bone, surgical fixation techniques, and the behaviour of different formations of bone microarchitecture in the ageing population. Crucially, the simulation has focussed almost exclusively on the older population. High fracture risk in this age group may be a contributor to this interest, as may the increased access to samples; however, the ability to assess fracture risk on a case by case basis has the potential to be expanded into a much wider range of clinical applications.

In this thesis, patient-specific Finite Element simulation based upon computed tomography scan data was used to simulate the torsional and compressive fracture of long bones. Extensive laboratory-based physical validation was undertaken to investigate if the all-important geometry and material property mapping functioned correctly within the simulation. Fundamentally, the applicability of animal substitution in physical testing and simulation was considered. This allows for testing of samples that are more readily available than the human counterpart, and to move away from simulation of the older population, validating the simulation procedure for bones of differing ages and development. It is proposed that substituting animal bone (allowing larger numbers of test samples) will offer the opportunity to test the simulation techniques in a wider variety of fracture cases, increasing the rate at which the procedure as whole can be validated and thus applied in a clinical context.

The spiral fractures of long bones, as assessed in this thesis, are listed as an indicator of potential abuse (particularly in non-ambulatory children). Combining the accuracy observed in torsional and compressive simulation within this thesis, with bone samples from younger animals may be the next step in developing this aspect of the CT-FE simulation procedure for clinical application. The ultimate goal of which is to aid in the determination of non-accidental injury.

Non-Accidental Injury in Children

From 2009 to 2010, 6,870 children in the UK alone were on the child protection register under the category of physical abuse (also known as Non-Accidental Injury (NAI)). A number of indicators of abuse exist, including pre-existing injuries, excessive bruising, and the presence of indicative injuries such as the spiral fractures of long bones in non-ambulatory children. The mis-diagnosis of NAI has the severe social implications on both the child and the carer. Clinicians from Sheffield Children's Hospital expressed interest in the bone modelling techniques as they are regularly called upon to

provide expert witness evidence in court cases considering suspected non-accidental injury. The diagnosis of non-accidental injury is a complex process, and dependent upon a number of key factors including:

- The location and intensity of the observed injuries
- Identification of further injuries and bruising
- Time taken and/or delay before presentation of the child to hospital
- A lack of plausible history or plausible explanation from the carer, combined with difficultly in communication with young children.
- Assessment of pre-existing conditions, nutrition and general health of the patient
- A general assessment of the forces involved to create the observed injuries.

Whilst the clinicians in these cases have significant knowledge on the subject of non-accidental injury, the evidence they provide is often anecdotal, and based upon their personal professional experiences. This is particularly prevalent in 'the assessment of forces involved stage' at which point the clinicians may refer to generally accepted guidelines regarding the drop height or pushing force required to produce a given injury in a child within a certain age range. This does not allow for patient-specific propensity to bone fracture, which may be incurred through the irregular bone geometry of a given child, the specific material properties of a patient's bones, through pre-existing health or injury conditions, or through a combination of all of these. Evidence is regularly based upon traditional two-dimensional assessments of injury provided through radiography.

Recent high profile cases in the media have shown that court decisions in which clinicians have given evidence regarding non-accidental injury have been overturned as a result of patient-specific information. This is generally observed following appeal, and frequently hinges upon a lack of confidence displayed by the clinician when categorically stating whether a pre-existing condition may or may not have affected the fracture risk.

Whilst some fractures (such as compressive fractures of the ribcage) are directly indicative of abuse, others, such as long bone fractures, can be instigated through both abuse and accidental injury. Long bone fracture is increasingly prevalent through child development and increased mobility, often occurring as a result of a trip or fall. Long bone fractures are also commonly observed following rough handling by a carer, as a result of a pulling, or a combined pulling and twisting motion. As such, spiral fractures may occur as a result of compressive, torsional, tensile forces, or as a combination of each of these.

Whilst valid, assessing each of these causes through physical testing would require a significant number of human samples, and be time intensive. Physical testing would also only provide averaged values for fracture and input load, removing the patient-specific aspect of testing. As such, the assessment of these forces lends itself to simulation, where a smaller number of samples can be simulated, with physical testing providing validation. Following appropriate validation the technique could then extrapolated to a larger range of samples, providing accurate assessment on a case-by-case basis.

An extensive literature review into the development and application of bone simulation demonstrated that, whilst using CT data for Finite Element studies (CT-FE) shows a good level of development, aspects of the process require further consideration and validation.

With this in mind, the majority of the studies in this thesis focus upon the creation, simulation and validation of the models with the aim of creating a solid foundation of the simulation process, appropriate for expansion and application in the future.

As a result of the proposed applications of the simulation technique, the following was considered:

- A reliable data source was required from which to obtain accurate geometry and material properties. CT should ideally be used as this includes density data for material mapping.
- The process should consider long bone and torsional fracture, to align with the interests of the clinicians and consider fields that had yet to be extensively investigated in literature.
- Animal substitution could be considered to allow for larger sample fracture testing and to provide a sample source that could be scanned without incurring exposure issues in CT.
- Extensive validation and accuracy checks would be required for each study in the thesis.
- No attempt at CT-FE simulation had been considered by the research group prior to this thesis. It was therefore considered prudent that testing should include a replication of studies detailed in the literature (such as compressive testing). This would provide a reference to compare the accuracy achieved during simulation in this thesis, with the accuracy in previous literature.
- Consideration of fracture risk and the predicted fracture load of a given sample should be simulated to ensure that the process could ultimately be applied in a predictive mode, such as NAI and injury prediction.

The aims of the thesis were:

i. **Computationally Simulate Animal Bone: Investigate the capability and accuracy of the general Computed Tomography Finite Element process in the substitution and simulation of animal bone.**

ii. **Physically Test Whole Bone Samples: Consider the behaviour of samples in alternative loading regimens (such as torsion) and identify the manner in which the samples fail physically.**

iii. **Validate the Simulation Procedure: Demonstrate the accuracy achieved during the animal CT-FE modelling process through appropriate laboratory validation.**

iv. **Test the Simulation Sensitivity: Consider the effect of various input parameters, and the sensitivity of the modeled solution to small changes in the modelling procedure.**

v. **Apply the Validated Simulation Procedure: Consider the ultimate applicability of the animal CT-FE process through the prediction of the fracture load of a given sample.**

Overall Research Question:

The combination of the individual aims provides the overall research question which is:

Can the CT-FE methodology derived for human samples and predominantly used for the assessment of uniaxial compression be extrapolated to consider alternative species and fracture modes? In addition can the technique accurately and robustly predict the fracture load of a given bone sample from CT data alone?

1.1 Thesis Outline

The thesis is comprised of ten chapters and two appendices. These are as follows:

Ch.	Title	Description
1	**Introduction**	Summary, glossary, nomenclature, contents and the project introduction, background and aims.
2	**Literature Review**	A review of the techniques involved and the literature published that uses the CT-FE procedure, followed by the thesis aims and objectives.
3	**Finite Element Model Creation**	Considers the segmentation, meshing and assignment of material properties to the Finite Element model.
4	**Physical Testing Methodology**	Details the physical testing methodology used within the study for both sub-maximal and fracture testing, as well as the constraining protocol and the implementation of strain gauged testing. Also the analytical calculation procedure used to compare the physical results.
5	**Physical Testing Results**	Results of the analytical calculation and fracture testing processes. Includes discussion of the testing process and any limitations incurred
6	**Comparison of Lab Results with FE Simulation**	Implements the theories proposed in literature to compare the stress results determined through strain gauged testing with those proposed through Finite Element analysis. Strain correlation is also detailed, determining the accuracy of the modelling process as a whole.
7	**Sensitivity Assessment**	A variety of changes to the input parameters were assessed to determine the effect on the observed results and accuracy.
8	**Optimisation and Application**	Following sensitivity assessment the modelling process was optimised, used to consider the material relationship for porcine bone and finally successfully used to predict the fracture load of a number of porcine samples.
9	**Discussion**	The discussion chapter considers the achievement of the project aims and the future work.
10	**Conclusion**	Thesis Conclusions
A1	**Appendix A1**	Assorted supporting data including detailed graphs of the physical and simulation test results

2 Computed Tomography Based Finite Element Simulation: A Literature Review

Accurately simulating the response of bone under load poses a significant challenge, and has been the subject of many investigations. The development of biomechanical simulation has been continuous, from physically determining the material characteristics of small samples of bone tissue, to simulating the whole-bone fracture risk of a patient-specific sample.

The majority of bone assessments ultimately aim to determine fracture risk. This has been proposed through a number of techniques, including simplified beam-based mechanical models, assessment of generalised and averaged bone geometry and more recently, through computational simulation.

Clinically, assessments of fracture risk are commonly undertaken in response to pre-existing risk factors and medical conditions, such as osteoporosis. Following the identification of a risk factor, assessment is considered on the basis of general bone quantity without examination of the general bone geometry. Assessment techniques such as dual-energy X-ray absorptometry (DXA) and Peripheral Quantitative Computed Tomography (pQCT) are commonly used. Physical testing has been used to demonstrate that fracture load correlates directly with Bone Mineral Density (BMD) as measured using DXA [1]. However, as would be expected of any structural system, it is a combination of both the material parameters and the geometry that determine ultimate strength, with research suggesting that accurate geometry provides the greatest contribution [2, 3]. As such, estimation via DXA, pQCT and other isolated-geometry methods are considered to give only 60 to 70% of the information required to determine true bone 'strength' [4]. This limitation may explain the variation and error observed in attempts to determine overall bone strength through non-invasive methodologies [5]. DXA uses two X-ray beams with varying energy levels to test the absorption of the bone to each, with the resulting response used to determine the BMD of the patient. It is generally an accessible and low cost methodology, and is commonly used to determine BMD. It has also been used in the determination of material density in soft tissues [6, 7]. The system is limited to individual point measurements, and additionally the isolation of geometry, and the potential contribution of soft tissues in DXA assessments (it has been proposed that despite the use of dual X-ray energies, there remain limitations in the DXA process, namely that a proportion of softer tissues *may* be included in assessment, which may reduce the measured value) has led to proposals that DXA alone should not be considered appropriate for Bone Mineral Density (BMD) and fracture risk calculations [8]. Consequently, techniques that include an estimation of the geometry of the bone, in addition to density measurements have been developed to better assess patient-specific fracture risk [9].

Using medically scanned data as the basis for bone geometry has been proposed as a means to increase the accuracy in biomechanical simulation. This has led to the development of geometrically accurate, whole bone simulation [10]. Additionally, using CT data specifically, Young's modulus can be assigned with respect to the density information carried in the source images. Obtaining density

data directly from the source images allows for the rapid production of models that are both geometrically accurate and provide a good estimation of the material characteristics throughout the whole of the model.

The development of the Computed Tomography based Finite Element (CT-FE) process has improved the understanding and accuracy of simulation techniques. The applicability of the process has been demonstrated in a number of fields, including the determination of fracture risk, notably for subjects with pre-existing risk factors such as medical conditions, surgical fixations or as the result of a geometrical propensity to bone fracture.

The current review considers CT-FE simulation, including the techniques implemented and the research published during the development of the process. An estimation of the accuracy shown through physical validation is considered, as are the applications for which the CT-FE process has been deployed. The review finally summarises the gaps in published research, in which future testing could be employed.

2.1 Introduction to Computed Tomography

Originally proposed in the 1960's and 70's, X-ray Computed Tomography (CT) is an imaging technique that was developed to examine the structure of the soft tissues of the brain. The CT image was able to 'look around' artefacts that would otherwise interfere with the penetration of an X-ray scanner [11]. As an X-ray based methodology, CT benefits from clear definition of calcified bone tissue, but ultimately has some limitations due to radiation exposure. One of the key outputs in the development of CT scanning was the investigation of the proportion of the original X-ray that was absorbed by the scanned material. Comparing this to known quantities within the image, (such as the absorption noted when scanning water or air) allowed for the relative density of the scanned object to be derived [11].

At approximately the same period Magnetic Resonance Imaging (MRI) was developed [12]. MRI uses magnetic forces to image the internal structure of an object through the excitation of the water molecules within the scanned tissues [13]. MRI is particularly useful in areas in which there is little change in the density of adjacent materials, such as within the brain and soft bodily tissues (Figure 2.1(a)) [14]. MRI is also comparatively non-invasive, with no lasting effects of exposure reported to date, as found within CT.

Both MRI and CT have been demonstrated to be accurate data sources for the geometry in biomechanical simulation [15, 16]. However, the attenuation response provided by calcified tissues (Figure 2.1(b)), and the ability to accurately assess the density of an object has led to CT being the predominant geometry source in Finite Element studies of bone tissue [17-19]. Radiation exposure concerns have been generally mitigated through the use of cadaveric and *ex vivo* sample testing and validation [20-22]. As MRI uses imaging in which water molecules are defined, it is often employed

to as a biomechanical simulation tool as a source for geometry in soft tissue studies, wherein CT scanning has limited capabilities in differentiating soft tissue types [23-26].

(a) 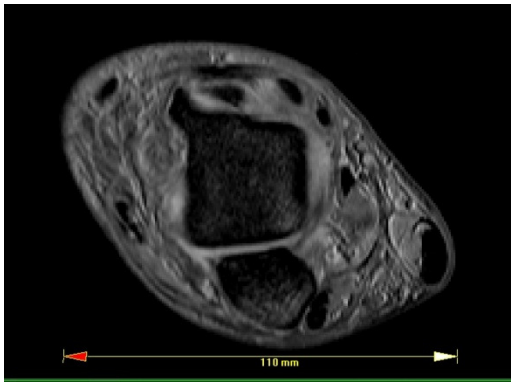

(b) 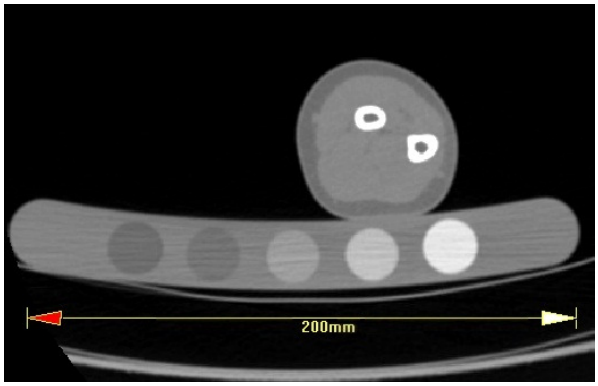

Figure 2.1. MRI and CT images showing firstly an MRI capture of the ankle (adult) (a), and secondly a CT image of the radius and ulna (child) (b).

Development of the CT based Finite Element process has been consistent, with early examples of geometry creation from basic CT to Finite Element conversions [9] to more recent complex examples, which provide an accurate assumption of the correct bone geometry [27]. Recent developments in modelling software and technology have included the development of software that allows for the semi-automated conversion of medical imagery (both MRI and CT) into Finite Element models [23, 24].

The development of medically linked simulation techniques and software is, in part, due to the development of the scanning equipment used for data gathering, which has shown a significant increase in accuracy. The image resolution, pixel count, total scan time and the development of contiguous helical scanning processes have all helped to increase the accuracy of three-dimensional shape that can be recreated. In the clinical field, this has enabled operators to view smaller fractures in more detail, providing greater clarity in the diagnostic process and allowing them to observe fractures that previously may have passed undiagnosed. The increased capability of modern medical scanning has shown that CT can almost match the performance of a full physical autopsy for the determination of pre-existing bone fractures and can even exceed the capabilities of an autopsy in the identification of fractures in cranial scanning [28].

2.2 Introduction to Long Bone Anatomy

Long bones, such as those tested within most CT-FE studies, constitute a number of distinct sections with varying construction. Firstly, the diaphyseal region, which is located along the mid-shaft of the

bone and accommodates the majority of the length of the sample. This region is comprised of more dense, compact bone and displays the most regular structure of the bone as a whole, with distinct semi-regular structures repeated through its depth. This section provides support to the bone and determines the extent of the medullary (or marrow) cavity, which encompasses the bone marrow. The marrow provides no structural assistance or support to the structure as a whole. As it provides no physical resistance, marrow is omitted from all simulation in this thesis, and the medullary cavity is simulated as empty. The diaphyseal region is primarily constructed of cortical bone. Cortical bone is responsible for the majority of the support of the human body, providing protection for the internal organs and applying force and movement from the muscles and tissue [29]. It is significantly more dense than the cancellous bone found within the epiphyses; however, cortical bone remains at least partially a non-linear material, with varying material properties between the longitudinal and circumferential axis.

At the proximal and distal ends of the diaphyseal region lie the metaphyses. These sections are located at the points at which the mid-shaft starts to widen and, in developing long bones, incorporate the epiphyseal plate, which is the region at which bone matrix is formed in developing bone and thus essentially responsible for the longitudinal growth of developing bone. The diaphysis determines the boundary of the final sections, the epiphyses, which are the larger rounded sections at the extremities of a given bone (Figure 2.2). The size and shape of the epiphyses are determined by the position and the role of the bone within the body; however, the shape is also defined by the interaction between neighbouring bones, as these are the regions at which the joints are located. The construction of bone within the epiphysis is significantly different to that of the diaphysis, with a thinner cortical ‘wall’ and a significantly less dense interior structure known as trabecular bone. This is significantly less dense than compact bone, and is typically softer and less stiff. This bone type is filled with trabeculae, which comprises of a multitude of small beam-like systems, created to provide resistance to load in an otherwise less structured material. The construction of the various regions within the epiphyses are determined by the role of the region and its location within the joints, with distinguishable ‘pressure’ regions transmitting and supporting load from the main joints (e.g. shoulder and hip) whilst ‘traction’ regions provide ligament connectivity and are utilised in providing controlled mobility to the bone. Due to the interactions with the other bones in the body, the epiphyses are covered with articular cartilage within the joint regions. This reduces the friction between the two mating surfaces, allowing relative movement without inducing wear in the bone tissue.

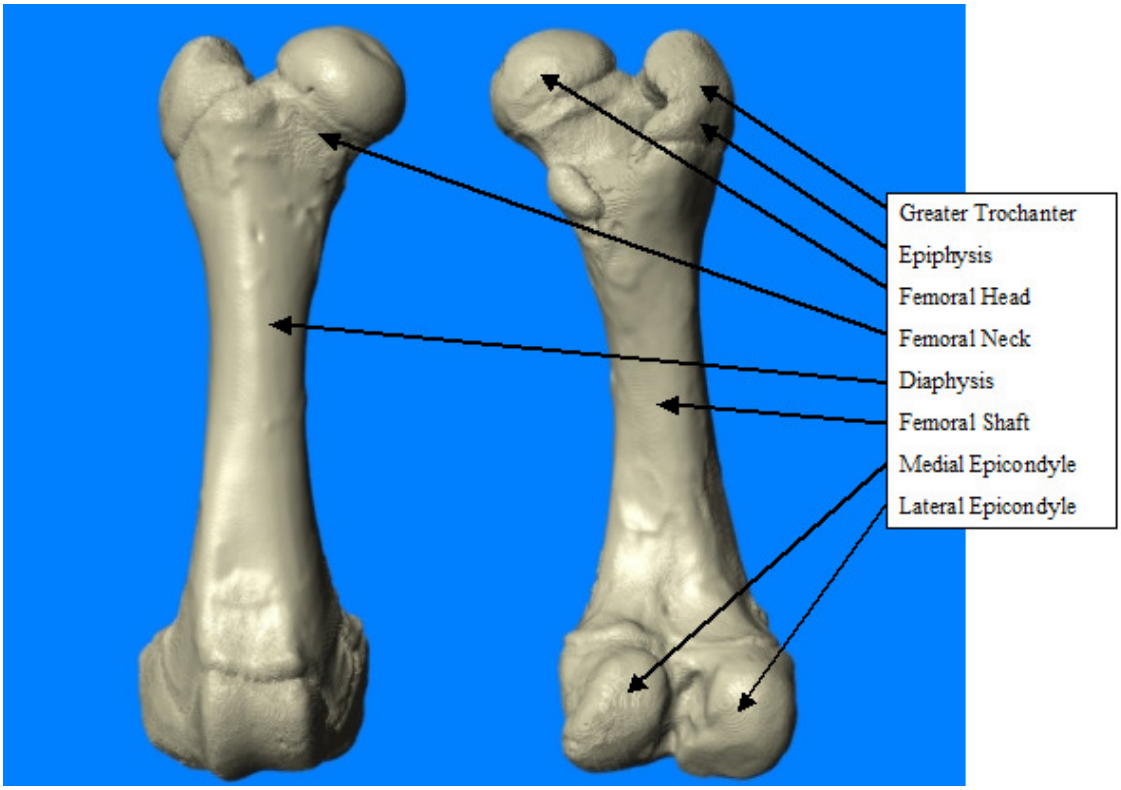

Figure 2.2. Images detailing some notable aspects of the geometry of the porcine femur.

2.3 CT Data as a Basis for Geometry in Simulation

The first studies that automatically recreated the geometry of bone from CT images showed a significant breakthrough when compared to the two-dimensional and simplified assumptions that had been undertaken up to that point [30-32]. The use of automated mapping in terms of both the geometry of the bone and the assigned Young's modulus was essentially developed from that point, until the refined and highly accurate models that are currently used. The methodology used in the original papers reflects the technology available at the time, basing the production of the simulation geometry on 24 independent CT slices, each with a width of 3 mm (Figure 2.2). This is a consistent limitation of early CT-FE studies, and affects the resolution of the data and the consequent minimum element size (The models typically used cubic elements to define the geometry, with an edge length of around 4 - 5 mm). In Finite Element simulation, a system is broken up into smaller parts (elements), which as a whole are collectively described as the 'mesh'. The refinement and resolution of this mesh is a key function of the Finite Element process and thus the general element size is indicative of the modelling complexity and theoretically the accuracy of the solution. In addition to the large elements used, early, slower imaging techniques had a propensity for motion artefacts (blurring and distortion as a result of the subject moving during the scan).

In addition to increased resolution, recent developments have provided continuous helical acquisition systems, in which there are no segmented gaps between the image data, and the imaging rate is vastly increased. Modern helical acquisition scanners can scan the length of the human body in less than 30 seconds, significantly reducing the chance of motion artefacts .

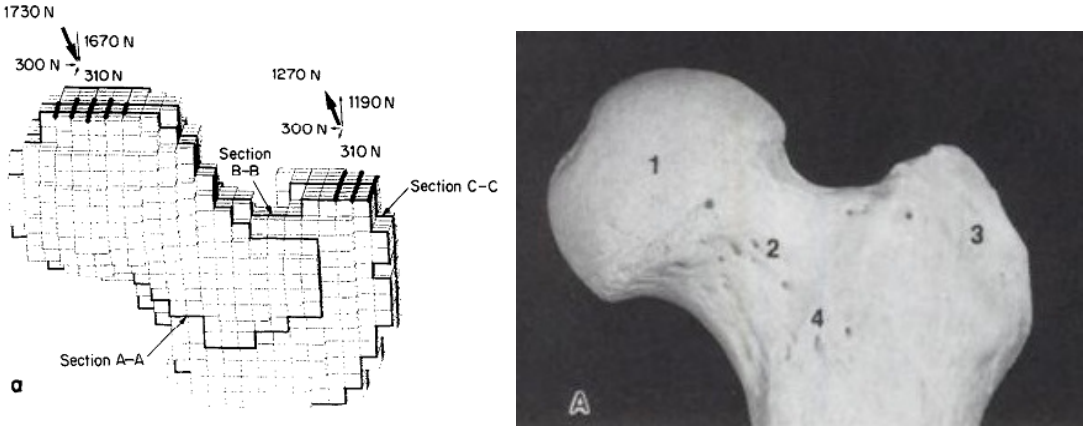

Figure 2.3 Image taken from Keyak et al. showing how, historically the geometry was described with a series of large cubic elements (modelled in 1990). The second image shows the ventral view of the human femur for comparison, and labels the head, neck, greater trochanter and inter-trochanteric line respectively [33].

At the time of the early CT-FE studies, the cubic methodology used was thought to give an 'adequate representation of bone' [9] but lacks refinement by modern modelling standards. The aggressive step changes in the curved surface of the femoral head and greater trochanter fail to match the non-uniform and tri-axial curvature of the true form of the bone surface (Figure 2.2). Step changes in Finite Element modelling as a whole are generally ill-advised, giving rise to stress concentrations and singularities. This effect was detailed by Marks et al., who undertook further investigation into the initial study provided by Keyak et al., observing the effects of smoothing on the original meshes [34]. Development of the early modelling protocol was proposed via voxel-based model meshing which used meshes based upon directly exported CT data [35].

Despite the inaccuracy of the meshing protocol used in comparison to more recent studies, voxel-based meshing techniques were able to describe the principal stresses observed for a number of loading patterns with reasonable accuracy.

Significant increases in accuracy have been observed as a result of the improved imaging techniques in CT and MRI [36-38]. Improved geometrical accuracy is vital in the pursuit of accurate simulation, as the varying arrangement of trabecular bone from sample to sample can have significant effects on the ultimate strength and fracture risk [39].

Following the manual masking and meshing methodologies in early CT-FE studies [9, 40], developments were made to increase the automation of the CT-FE process, leading to new modelling software such as that developed by Simpleware and Materialise [41, 42]. These packages offer greater automation of the modelling process, combining the various procedures for geometry production, meshing and material mapping. The packages are able to accommodate a number of data sources, including both CT and MRI and have been shown as viable for accurate geometrical and material mapping across a variety of anatomical sites [24]. The use of this technology additionally allows for the recreation of geometry from microCT, which is a prevalent imaging technique in dental studies [43]. MicroCT provides higher spatial resolution of data, leading to higher refinement of meshing and more complex solutions. The literature shows that material mapping is often excluded from the studies in favour of homogenous material types [43].

2.3.1 Meshing

The majority of recent studies utilise geometry produced and meshed through automated mapping and meshing algorithms. The accuracy of a number of these automated meshing techniques has been investigated, comparing the results observed with manual meshing procedures [44]. Each of the meshing techniques was compared with physically derived results from a 'standardised femur' in controlled laboratory testing; this methodology was subsequently used in a number of further CT-FE papers [45-47]. Comparison with physically derived results demonstrates that both manual and automated meshing is viable, whilst tetrahedral and hexahedral meshing, which are the most commonly used CT-FE meshing methods, are shown to provide the most accurate results for simulation.

The determination of convergence and the mesh refinement process is atypical in biomechanical simulation and consequently the selection of convergence criteria can be complex. Convergence determination in homogenous mechanical systems often uses global estimations of error [48, 49]. However in CT-FE studies, a number of the common techniques are rendered invalid due to the manner in which the rapidly changing Young's modulus is defined on an element-by element basis. The assessment of convergence at a local level is generally approached through the comparison of a simulated result to a 'real' result, derived through physical validation or analytical calculation. The procedure involves the re-meshing of a model with increasing refinement, adjusting the element count in regions of interest until a constant result is achieved [50-52]. Within automated CT-FE studies this process may not be suitable, as the element size and material value assigned to the element are often not mutually exclusive factors. Methodologies to mitigate this effect have been proposed, through the comparison to further simulated results using homogenous materials [53].

Despite the increasing use of automated CT-FE protocols and demonstration that volume based meshing is appropriate [54], there is no consistent agreement demonstrated in the literature with

regards to the most accurate meshing protocol. An investigation into the accuracy of meshing techniques has proposed grid-based hexahedral meshing [44]; however, well referenced and generally-accepted subsequent studies have been undertaken with the use of tetrahedral meshing [45]. Additional research details the use of both techniques in a single study [51]. The two methodologies offer comparative accuracy. The level of development in both is sufficient for studies to provide accurate reconstruction (in terms of numerical robustness in mesh generation and comparative sample weight) for almost any developed bone type found in the human skeleton [46].

2.4 Defining Young's modulus

The material behaviour of organic tissue is inherently complex to simulate. Finite Element simulation techniques were originally derived for the assessment of regular, heterogeneous structures and the structure of bone displays few of these characteristics. Bone is a mineralized organic tissue, predominantly comprised of collagen type one and carbonated hydroxyapatite, which forms the 'mineral' aspect of bone structure. Despite appearing heterogeneous with the naked eye, the microscopic structure of compact bone is complex, with nerve and blood vessel filled canals spanning the length of the structure, surrounded by dense layers of mineralised bone matrix. The construction and strength of bone varies between subjects, and as a highly anisotropic material is dependent upon position within a given bone sample [29, 55-57]. In addition, the mechanical properties of bone *in vivo* are naturally manipulated by the body to provide the optimum support in response to loading and consequently the bone structure can become role-specific [58, 59]. This means that contralateral samples taken from the same subject (i.e. both left and right femur) can exhibit significant variation in behaviour despite geometrical similarities.

The variation in mechanical properties exhibited through load-based remodelling extends to the internal construction of individual bone samples, and provides issues when selecting partial (rather than whole bone) samples of bone for physical testing. Comparison of samples that are aligned with the primary axis of loading and samples that are non-aligned can result in material property changes of as high as 40% [60]. This mis-alignment is observed within paired samples taken with only 15 degrees difference in alignment, and is furthermore observed despite comparable physical material parameters (hardness and ash density), which are commonly used as indicators of bone strength.

The integration of error when defining material behaviour is generally confirmed as a key issue in the determination of the material and structural behaviour of whole bone samples [61]. To overcome this, the selection of discrete material samples is often observed, and described as 'one level below that of whole bone'. This is a means to describe the behaviour of bone material at a more refined level, and then utilise this information to describe the behaviour of whole bone samples, under the assumption that the level of varying anisotropy is not too high [62]. Bone testing in this manner is prevalent, with small samples (physical sample size varies significantly depending on bone and testing type, Evans et

al. for example test specimens under a tensile regimen with samples of approximately 76 mm x 3.81 mm x 3.81 mm [57]) taken from cortical and trabecular bone tested in varying orientations. The results offer data for most human bone types and locations, offering averaged and area-specific benchmarks that can be adopted or compared to modelling results during *in silico* testing [9, 63, 64]. As with all organic tissue testing, the importance of correct sample preparation requires consideration. The general procedure with respect to bone is to maintain consistency in hydration, with samples actively hydrated throughout obtainment, storage, preparation and testing [62].

2.4.1 Bone properties for Computational Modelling: E-BMD

The relationship between Young's modulus and apparent bone mineral density, as reported by both Keller et al. and Ciarelli et al., is key in the determination of physical properties for *in silico* studies [65, 66]. Despite initial studies reporting a lack of correlation in findings for some bone types [67, 68], the Young's modulus/Bone Mineral Density (E-BMD) relationship has ultimately been subjected to detailed investigation. Following further development, the accuracy of mapping samples using CT has been shown to have sufficient resolution to provide an assessment of regional density changes under specific medical conditions such as metastatic lesions [69].

The E-BMD relationships proposed in literature (and consequently the outputted materials properties for a given density) vary significantly. This variation highlights the importance of correctly defining the initial densities upon which the E-BMD relationship is based [37] and correctly determining the E-BMD relationship [70]. E-BMD relationships have been proposed that consider the variation in bone composition and from differing anatomical sites [71-73]. For example, samples taken from across the human body, notably vertebral, tibial and femoral samples, require specific E-BMD relationships for each location [72]. This large array of relationship data was compiled and compared in a literature review in 2007, based upon over 60 papers that had undertaken an elastic property/bone density relationship [74]. Whilst this is a large number of relationships, literature has demonstrated a preference for certain relationships, suggesting that for CT-FE at least, some may be more accurate than others [70].

Fully validated CT-FE studies have favoured a select number of the E-BMD relationships from the literature, notably those derived by Morgan et al., Keller et al. and Carter & Hayes [72, 75, 76]. Of these, Morgan et al.'s relationship has been repeatedly demonstrated as providing the best agreement for predicted vs observed stress results through physical validation of human femoral samples and consequently this has had the most prevalent use in CT-FE studies [45, 46, 70].

2.4.2 Material Mapping

The material mapping process in CT-FE studies requires the identification of the voxel brightness within the CT image. This brightness is provided in response to the level of calcification of bone

tissue, and therefore provides a measure of the bone mineral density at a specific point. Early, large scale investigations of BMD measurements from CT data were undertaken with meaningful accuracy as early as 1993 [9]. Using a greyscale to density and a density-elasticity (E-BMD) relationship, the data within the CT scan can be used to calculate the bone mineral density and the Young's modulus for each individual voxel.

Automated algorithms such as *Bonemat* use these calculations with significantly improved accuracy over homogenous assumptions [77, 78]. The use of automated algorithms allows for the rapid mapping of Young's modulus to scanned tissues, and can also be implemented in isolation of meshing protocol. This is of key consideration when determining material characteristics in combination with automated meshing procedures. It should be noted that the materials outputted during the density-elasticity mapping process are linear-elastic in nature. The elasticity of samples under load has been considered extensively in compression, and does not significantly limit the accuracy observed in whole bone studies [22, 45, 79].

The CT-FE material mapping protocol generally assesses the material parameters on a voxel-by-voxel (as above) or on an element-by-element basis. Attempts to increase the accuracy through material mapping procedures that allow for variation within each element have failed to consistently improve upon the accuracy observed [70, 80].

2.4.3 Bone properties for Computational Modelling: Other Methods

Techniques other than E-BMD mapping have been considered to define the Young's modulus of bone [81]. Homogenous material models have been used to define a single material value for an entire bone, providing a very rapid testing methodology at the expense of reduced accuracy [82]. This technique may be applicable for large scale testing in which elementary assessment of bone as a rigid member is required; however, the inaccuracies incurred are likely to induce difficulties when attempting to validate the models on a local level. Despite the authors concluding that the process had been successful, little tangible validation was demonstrated, with the exception of cursory image correlation [81].

Other techniques such as modal analysis (which uses enforced vibration of a sample to calculate the resonant frequency of a sample and thus its apparent stiffness) have also been proposed to determine Young's modulus for bone [83]. Despite positive results for averaged material mapping, it is unlikely that these are capable of accurately describing the material property gradient and the behaviour of bone at a local level. Consequently, such techniques are considered to be less accurate than BMD-based inhomogeneous mapping.

2.4.4 Limitations of Material Property Mapping

The complexity of bone cannot be overestimated, and whilst general strength parameters are determined by the bone mineral density, geometry and the structure of the bone, research has shown that additional factors on a smaller scale can have a significant effect on the ultimate strength of a system [29]. The effect of crystallisation, the porosity of bone samples and the appearance of micro-cracks with respect to ultimate strength all suggest that, for ultimate accuracy, Finite Element assessment on the small scale is required for fracture prediction. The level of simulated detail is a consideration for all Finite Element studies, and care must be taken to ensure that an appropriate allowance for error is made when undertaking general characterisations of bone material. The importance of geometrical accuracy has been proposed via examination of the internal structure of bone in fatigue tests, which show the position of the constituent fibres, may be fundamental in the determination of true fracture risk [84]. Observation of the constituent structures highlights the complexity of bone as a whole. Fundamentally it must be considered that Finite Element simulation is an approximation, and furthermore than CT-FE simulation with spatial resolution in the order of 0.5 mm is a significant simplification of the true material. The various structures and sub-structures within bone are schematically defined by Rho et al. (Figure 2.4) [61].

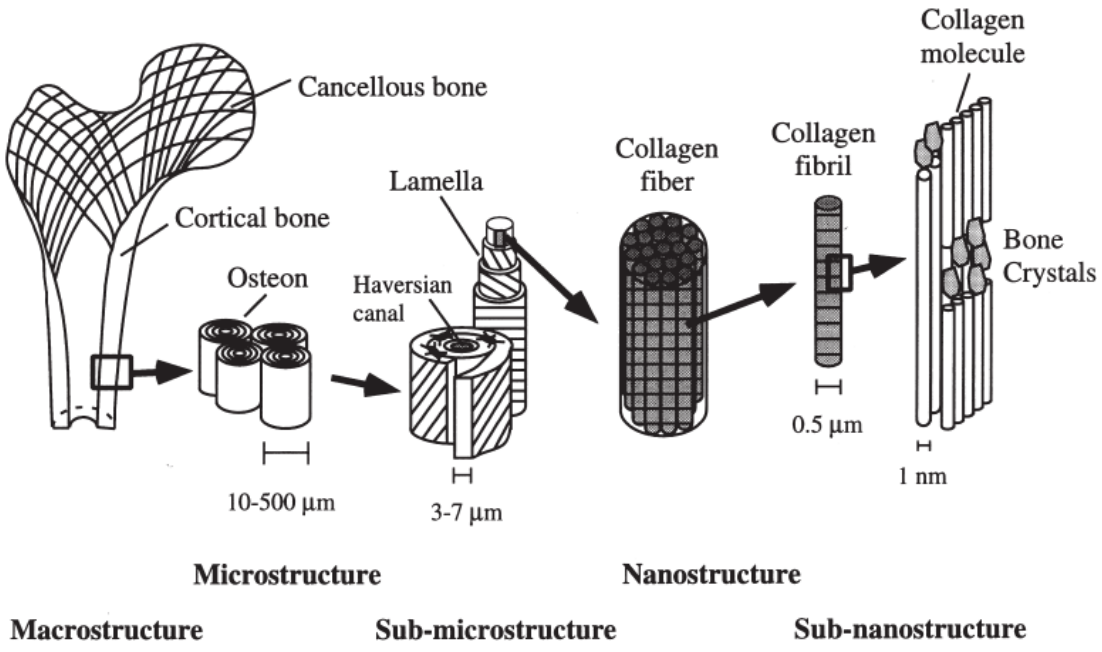

Figure 2.4. Images taken from Rho et al. show the hierarchical structure of bone.

2.5 Loading Regimens in Bone Simulation

The large majority of research pertaining to the simulation of bones using CT-FE has focused upon hip and femur fracture. Failure of this region as a response to trauma is predominantly achieved

during a direct impact to the femoral head, typically as a consequence of a trip or fall [85]. This precise failure mode is representative of a direct blow and rapid impact and consequently the fracture condition does not lend itself to the pseudo-static loading conditions generally selected for Finite Element simulation.

Consideration of the forces observed during typical (non-impact) compressive loading such as that experienced in walking have been undertaken to determine the orientation and movements that provide the highest fracture risk in the human femur [20, 36]. Research including the influence of muscular connectivity and some soft tissue support confirms that loading provided during general standing and vertical ambulation is via compression rather than bending, despite the application of force on the femoral head at a lateral distance from the centre of the main shaft [86].

2.5.1 Failure Criteria

Information regarding the yield criteria must be obtained to accurately predict fracture in CT-FE studies. Kopperdahl et al. undertook physical testing to determine the yield criteria of trabecular bone taken from human vertebral samples [87]. Disparity was found between the tensile and compressive failure conditions, which has been used to successfully predict the fracture loads and initiation location in laboratory-tested and simulated femoral necks in whole-bone testing [36, 45, 88].

Failure criteria must be correctly assigned not only for loading orientation and failure mode, but also for bone type. As a consequence of varying structural geometry and mechanical properties, it has been demonstrated that the physical strength of cortical bone is around 25% higher than trabecular bone [45]. This effect has been confirmed in studies relating to high detail Finite Element assessment of trabecular bone, using small-scale cubic elements based upon micro CT images to accurately represent the internal structure of trabecular bone in the assessment of failure [89]. Asymmetry of the failure load required under tension and compression has been observed through the use of automatically adaptive strain failure criterion, ultimately replicating laboratory tests on small scale samples with a high level of accuracy [45, 90].

As has been demonstrated through the testing of samples from differing anatomical sites, the appropriate failure criteria is also dependent upon location, [72]. Research has shown that the femoral head had the greatest resistance to compressive strain, whilst samples taken from the vertebrae had the highest resistance to tensile forces. Whilst differing from site to site, the results were repeatable within each location [72]. This result allows for the mapping of a failure criterion to a whole anatomical region, for example mapping the entire femoral neck using the same strain-based failure criteria across its volume [45].

Despite high occurrence in the literature, the majority of fracture studies consider the relative behaviour of different failure criteria rather than absolute predictive results of failure load. High-speed video analysis of the fracture of the femoral neck has demonstrated the applicability of various failure

criteria [45]. The ultimate strain criterion is proposed as the most accurate at predicting both fracture load and location within simulation of laboratory validated samples. The preference for strain rather than stress-based criteria has been subsequently confirmed in more recent studies [36, 45].

Strain-based criteria offer relative simplicity in implementation and correspond well with the elastic and brittle nature of bone failure. Furthermore, the determination of stress within a Finite Element solution is dependent on both the strain and material matrices, and consequently has limitations at the bone surface due to the manner in which Young's modulus is mapped. The effect is compounded due to the selection of the stress failure criteria itself, which has been proposed in literature (based on physical testing) to link compressive yield stress with material density, consequently displaying further limitations due to the loss of density registration close to the bone surface [9, 75].

The determination of both *yield load* and *fracture load* have been considered [36, 91]. The former, utilising selection based upon a 5 % yield strain criterion considers the onset of yielding to indicate the instability and failure of the bone material, and retains accuracy in the proposal of linear-elastic material modelling. This yield criteria is less elegant than other proposed techniques (including the consideration of surface microdamage through digital image correlation [92]) but has been demonstrated to be robust and offers rapid application for multi-sample testing.

Very few papers have considered the behavior of samples after the point of yield. Attempts have been made to replicate the complete failure through the use of 'element kill' modelling procedures ('killing'/removing elements exceeding a proposed limiting stress value) [91]. Despite accurate results and development in modelling capability (study undertaken in 2010), the increased complication of these techniques leads to the assessment of the bone geometry on a two-dimensional basis, which is a significant limitation in patient-specific simulation.

2.5.2 Fatigue-Based Failure

Failure of bone samples through a fatigue-based pattern of cyclical loading has also been considered. This is a process in which bone has been shown to have a relatively poor resistance to failure, with fully reversed cyclical loading producing failure in 1000 cycles at just 50% of the ultimate strain value [93]. Cyclic failure depends on the range of the cyclic loading rather than the absolute mean. Attempts to calculate the number of cycles to failure of bone through repeated loading have been proposed, with some success [94], which may aid in the accurate modelling of cyclical loading and practical application of bone modelling *in silico*.

In contrast to osteoporotic and ageing bone conditions, in which instantaneous fracture is observed, fatigue and stress fractures most commonly occur in high mobility and athletic environments.

The high intensity of exercise during the training of military recruits, for instance, can lead to an increase in the rate of observed stress fractures, with incident rates as high as 31% for a given military sample [95]. These fractures have been shown to most commonly occur in the tibia and femur as a

result of repeated loading [96]. High incidence rate in military environments reduces the viability of extensive patient-specific analysis on a case by case basis, and consequently research has considered the analysis of more simplistic risk factors. Giladi et al. considered the width of the tibia in a large sample of Israeli recruits, demonstrating that width alone correlated with the occurrence rate of stress fractures [96]. The results demonstrated that those recruits with stress fractures had significantly narrower (in the medio-lateral plane) tibias than those without. The consideration that geometry alone can provide a measure of pre-disposition to injury supported work regarding the varying risk of fracture between sexes, and further validated the use of patient-specific modelling to analyse injury risk [97].

2.6 Observed Accuracy and Validation Techniques

In some respects, the determination of the accuracy of bone modelling is inherently difficult. The confirmation of a proposed fracture load cannot be undertaken without fracturing the simulated sample. Consequently, confirming predictions is limited to the sample size available, and ultimately unlikely in *in vivo* studies. Additionally, determining accuracy through exclusion or estimation of bone geometry is fundamentally flawed [98]. Isolated studies have considered physical trials to confirm the predicted fracture risk following extensive corrective surgery [99]. This is a valid technique, predicting (correctly) that the post-surgery recovery was sufficient to allow walking exercises without the risk of further fracture. However, confirmation of the accuracy of the study is limited to a single patient and a single result and consequently other methods are generally used to ensure accuracy is retained in simulation.

Laboratory-based validation has been proposed as a method to confirm the applicability and accuracy of simulation [52, 100, 101]. Whilst more feasible than *in vivo* validation, the complexity of the human skeleton and the soft tissue interactions at the bone surfaces often reduce validation to a discrete section of an entire structure or simplify the boundary conditions used in physical testing and simulation [70, 79, 102]. Validation of any kind should be included as a matter of course, however an assessment of the limitations of each validation study is required to ensure that errors are not incurred concurrently in both simulation and in the validation process.

Strain gauging has been proposed as the most accurate methodology for the validation of simulation in both traditional engineering and biomechanical systems. Despite the inherent complexity of gauging organic tissues, gauging of soft tissue biological systems has been investigated [103]. Strain gauges have also been used for the measurement of strain response in *in vivo* testing of both animal and human bone samples [22, 51, 104]. Gauges placed on supporting bones such as the tibial surface have been used to describe the local strain and deformation of live samples during prescribed movements. Despite showing the viability of *in vivo* testing and the movement types that incur peak stresses, the lack of accurate imaging in these studies is a limitation. Three-dimensional imaging

techniques (such as CT) would provide better correlation with respect to the location of the gauges and potentially provide information regarding the material parameters at the gauge location. This limitation, added to the specific, single point nature of the strain information means that this type of data cannot retrospectively be applied to validate CT-FE studies with sufficient accuracy.

Ex vivo sample testing allows for image capture and testing of the same sample, providing precise correlation of the modeled geometry and Young's modulus, ensuring that validation remains patient-specific. This has been proposed as the most accurate method to validate simulation, provided suitably accurate methods are undertaken to determine the location of the gauges on the bone surface [46]. Principal *strain* correlation between predicted and observed results has been demonstrated effectively at the bone surface using this testing arrangement [36, 105]. Alternative validation methods such as speckle pattern correlation interferometry (in which a pattern is sprayed onto the surface, and the relative movement of the speckles are used to measure local displacement and thus strain) have been proposed to determine strain on the bone surface [106]. The technique has been used extensively for mechanical systems [107-109], and has been implemented effectively in geometrically-isolated bone sample testing [110]. Ultimately the technique may incur issues in whole-bone testing due to the inhomogeneous volumetric material definition and continuous surface curvature [106, 111].

In addition to accurately describing strain at a specific point, *stress* correlation can be performed following determination of the Young's modulus. This material quality can be defined from the original CT data, allowing the calculation of the stress state in the region of interest for both the *in silico* and physical tests. Determining local stress in this way has been shown to be an appropriate technique in determining correlation and accuracy on a *predicted vs observed* basis [46, 70]. Partial volume effects, spatial inaccuracies and products of rotating imaging such as beam hardening (in which the central portion of a subject is images more regularly due to the rotation of the scanner) as a result of CT scanning provide complications in the geometrical and material mapping at the bone surface. Consequently, validation on a principal *stress* basis is generally determined at a sub-surface level [45, 82].

2.7 The Application of CT-FE Simulation

The focus of the majority of published research has been upon validatory studies [52, 100, 112] and the drive to increase the accuracy of the CT-FE process [37, 47, 89]. Proportionally fewer studies have considered the ultimate application of the techniques; however, the following have been considered.

2.7.1 Ageing Bones and Implant Technology

The behaviour of the human femur and in particular the proximal femur and femoral head is the subject of the majority of CT-FE research [27, 39, 59]. Ultimate application varies; however, studies predominantly consider the effects of ageing, bone degradation and the mitigation of fracture risks [28, 113-115]. Further research into human femora has included reviewing the various types of hip replacement therapies and the behaviour of the replacements within the femoral cavity during bone remodelling [116, 117]. The use of CT-FE has been extrapolated to simulate the behaviour of implant technology within the human body, allowing vastly reduced test periods when compared to fatigue-based physical testing and providing accurate portrayal of the behaviour of the implant and bone surface at the joint-implant interface [118].

2.7.2 Bone Remodelling

The processes involved within the adaptation of the human femur to implanted prostheses are generally focused around the natural remodelling process of human bone, commonly described as 'Wolff's law' [59, 116, 119, 120]. Wolff observed that trabecular bone in the proximal femur was aligned to provide the most efficient supportive structure (in terms of structural strength to weight) when subjected to loading [121]. Despite the common use of 'Wolff's law' as a descriptive phrase for remodelling, the manner in which the bone is remodeled is perhaps best theorized by Wilhelm Roux, although this is a subject of much discussion [122, 123]. The various aspects of these remodelling processes have been investigated at both a cellular and whole-bone level, and even investigated *in vivo* in live animal subjects [58, 124-127].

Despite interest with regards to the outcome of adaptation to loading, the actual processes involved in bone remodelling are outside of the scope of the majority of CT-FE studies, particularly when modelling *ex vivo* samples and general fracture risk.

Age related fracture risk as a result of remodelling has been considered through a quantitative assessment of the 'amount of bone'(weight of bone per unit volume of structure), apparent BMD and geometry of the femoral neck [128]. The remodelling process leaves the unloaded superlateral femoral neck at risk from a reduction in material deposition as a result of reduced mobilization with increasing age. Studies show an observed and predictable thinning of the cortex on the upper femoral neck as a result of the remodelling process, which may represent an increased fracture risk in the region during lateral trauma as the result of a trip or fall. Provided the scanning resolution is suitably high, the general CT-FE modelling process should accommodate this thinning and demineralisation, altering simulation results accordingly when compared to 'normal' cases.

The distribution of mineralisation within trabecular bone has been assessed using high resolution CT-FE to consider the non-regularity observed within bone samples from older patients [129]. The calculated apparent stiffness recorded during CT-FE assessment shows significant variation amongst

the sample population. This variation demonstrates the limitations of geometrically isolated BMD-only assessment processes undertaken by clinicians such as DXA. This further demonstrates how accurate portrayal of the geometry and material distribution within the trabecular regions of bone should be considered for all fracture risk assessments.

2.7.3 Soft Tissue and Musculoskeletal Modelling

No common methodology is observed in the previous literature for the assessment of muscular forces and soft tissue influence in skeletal testing and simulation. Combined musculoskeletal modelling remains a significant challenge. Physical tests have been undertaken using varying methodologies, including the application of force through nylon straps [20], which confirmed the increased accuracy available in strain gauge comparisons through the inclusion of muscular interaction.

Application of the CT-FE procedure has been undertaken in ligament modelling, notably within the knee [130] and foot [26]. Within the former, the technique was used to determine the contact mechanism between the anterior cruciate ligament (ACL) and the neighbouring intercondylar notch. The varying angles that induce contact are described, and some effort at validation is undertaken through the use of physical cadaveric studies. Validation of such complex systems is inherently complex, as shown through the lack of meaningful validation in Wu et al.'s study. The model shows a high level of complexity, modelling each of the bones within the foot, the distribution of soft tissues, and elements of ligament connectivity for force transfer. Whilst CT is used as an accurate basis for the model geometry, the lack of validation in these complex musculoskeletal studies means that the results are considered on a comparative basis only, with no validation of the absolute observed values. The combination of femoral and soft tissue modelling, including estimation of the influence of muscular forces has been examined [131], but the absence of physical validation reduces the reliability of the proposed data.

Large-scale projects are currently in progress to create fully-validated musculoskeletal models of the entire human body [102]. This represents a significant challenge, with multiple considerations and limitations for each constitutive aspect of the overall process. A recent review of the overall development of the Living Human Project [132] highlighted the current limitations in research, which included a lack of data and accuracy in modelling muscular force interaction, and suggested expansion into alternative failure regimens and bone types [46, 102].

2.8 Recommendations and Gaps in Research

Despite increasing investigation into the methodology and accuracy afforded through high resolution CT-FE analysis, there remain areas of investigation which have been given little consideration. In addition, the *application* of CT-FE has been generally limited. As such there remain gaps in the research that should be considered by future studies.

2.8.1 Torsional Testing, Shear and Multi-Axis Loading Regimens

Compression and bending of bones has been considered in detail [65, 86, 99, 133]; however, other failure mechanisms such as torsion have undergone less investigation in CT-FE studies [134, 135]. Torsion has been proposed as an optimum means by which to evaluate whole bone strength in physical testing due to the manner in which the force is transferred to the entire sample rather than in a specific plane, as may be expected in compression or bending [136, 137]. In comparison bending, and induced bending forces through off centre compression can lead to complexities in loading assessment and alignment of the samples, which has been shown to induce error in simulation [60].

Torsion has been considered from a purely mechanical perspective [136, 138], with stress-based failure assessed. [86, 139]. These tests were undertaken upon various animal samples, and showed that torsional fracture of bone from a cyclical loading perspective occurs after significantly fewer cycles than comparative cyclical loading in alternative orientations.

Further tests have demonstrated that this propensity to fracture was highlighted by a fracture risk increase of greater than two in torsion when compared to other loading regimens [140]. This highlights the importance of the consideration of torsional loading in failure studies [134]. Despite published results from physical investigations, the inherent complication of applying torsional to a bone sample has also been noted in studies considering (and subsequently omitting due to complications during testing) spiral fractures [1].

2.8.2 Animal Sample Substitution

The use of animal substitution is prevalent in physical bone testing, having been used for surgical technique experimentation, dietary and cellular studies, and implant development as well as many other environments [9, 133, 141, 142]. Testing using animal bone has inherent advantages such as ease of sample obtainment. Such benefits allow for greater sample sizes [143, 144], which can correspondingly allow for increased fracture testing due to the ease of sample replacement. The use of substituted animal tissue may also mitigate some of the other disadvantages found in alternative substitutes such as composite replica bones, which studies have shown exhibit incorrect behaviour depending on loading regimen [100].

Some development of equine studies in CT-FE has been undertaken, whilst porcine bones, by comparison, have undergone very little investigation. This is despite regular substitution of porcine bone for human samples in physical testing methodologies due to the compositional similarity of the two bone types [145-148]. Some data exists with regards to the material response of various dietary changes and supplements in porcine samples [133, 149] and the reverse of this process, in which the strength of a given sample was used to determine mineralisation and estimate the nutritional condition of porcine bone [142]. Recent physical testing has demonstrated that the effect of strain remodelling in humans continues into porcine samples, with varying Young's modulus relating to the location from which the sample is obtained [147]. This data was provided in the form of mechanical material testing only, with neither medical scanning, nor Finite Element consideration.

2.8.3 Young and Developing Bones

Despite significant interest in pediatric studies, and the physical determination of the behaviour of bone samples from all ages in literature, young and developing bones have shown very little investigation in the CT-FE modelling process [57, 150, 151]. Additional research is required to determine if the reduced mineralisation observed in developing bone, is mappable using traditional E-BMD relationships in CT-FE, and consequently if the mapping procedure accounts for the increased elasticity and energy absorption exhibited by developing bone.

The need to limit exposure of children to harmful scanning such as CT may provide an explanation for the majority of assessments of BMD using DXA techniques [7, 150]. DXA has limitations as described previously, but may provide values to compare CT-FE material applications, and has been used as a marker with which to correlate fracture load in physical testing [1].

Despite the preference for DXA studies, investigations using CT for the imaging of bone development and movement have been undertaken, notably to characterise overall bone size, mass and geometry [115, 152], to quantitatively assess individual aspects of the skeleton [153] and to assess the relative motion of skeletal components [154]. Combining CT data with investigation of developing geometry, bone strength, cortical thickness and muscle growth within the proximal radius and forearm has been considered [115, 155-158]. However, meaningful geometrical assessment has been ultimately limited by the use peripheral quantitative computed tomography (pQCT) and other two-dimensional assessments techniques.

Accidental fractures in children are common, occurring from a variety of situations, which can correspondingly provide differing fracture patterns. Studies have been undertaken to describe the varying long bone fractures, in order to provide a better assessment of *accidental* versus *inflicted* injuries and aid in the diagnosis of the causes of injury [159]. Certain fracture types, such as spiral fractures are only observed following a correspondingly specific application of load (in this case torsion). Whilst it is possible for these to be incurred through an accidental process (such as trips and

falls) spiral fractures are less commonly observed than other fracture types and are used as an indicator of possible abuse, due to the twisting mechanism required for fracture initiation.

The determination of fracture risk using non-invasive techniques has been considered in literature with varying success [2, 5, 98, 101]. This research has included the use of infant animal samples in physical testing in an attempt to correlate predicted risk with testing. This showed consistent results with respect to bending stiffness and fracture through bending, but failed to correlate the indicative-of-abuse torsional fractures successfully. Whilst wholly predictive models providing consideration of non-accidental injury are in development, the general procedure is that of simplistic biomechanical models from drop test data combined with detailed clinical history [160, 161]. Additional work is required to test the expansion of CT-FE modelling to aid in the determination of non-accidental injuries in children. The reduction in bone strength as a result of medical conditions such as Ricketts and Osteogensis imperfecta as reported in physical testing [162, 163] should be investigated to assess the robustness of the modelling and material mapping procedures.

2.8.4 Investigation of the Limitations and Resolution of CT-FE

Despite offering an effective tool for the determination of stresses within a complex body, Finite Element modelling should be approached with caution without assessment of the inaccuracies involved in the modelling procedure. Identification of the sources of error in a simulated system should be approached sequentially, detailing each individual aspect of the modelling process. This parameter identification highlights the importance of each aspect of simulation, and has shown little investigation in the CT-FE process [82, 164].

Another key consideration in assessing patient specific modelling is the resolution of the simulation procedure. In effect, this questions the change in predicted fracture load, for small changes in the original geometry. The simulation procedure used in CT-FE means that small changes in the geometry may result in significant changes to the predicted fracture load. However, physical testing has shown that significant defects in a sample can be accommodated with no detrimental effect on the observed failure load [165]. Clinical advice during operative procedures suggests that 50% of the bone diameter is the maximum permissible size for an induced defect. Physical studies have shown this advice should be reduced, with a 20% defect causing significant reduction in strength, and further research extends this further, suggesting that defects as small as 10% of the diameter of the cortex can have detrimental effects upon the maximum permissible torque [145]. Physical and computational studies regarding defects and post-operative conditions often use the opposing limb as a control, [99, 166, 167]. This assumes that geometry, structure and overall strength are consistent between opposing limbs, which is not necessarily the case [97]. Validated CT-FE offers an opportunity to test this theory, and in addition to test the resolution of the CT-FE process with regards to simulating small changes in geometry and construction defects.

2.9 Thesis Aims

The literature review highlighted a number of key areas in which there had been a limited amount of investigation.

- Parameter identification and modelling limitations
- Resolution in simulation
- Animal sample substitution
- Young and developing bone samples
- Investigation of alternative failure modes

These five areas are not necessarily mutually exclusive. Of the five, it was considered that the investigation of alternative failure modes offered the greatest development for the CT-FE process as a whole. Torsion was considered, as this overcomes theoretical complications found in buckling and bending, and is representative of common *in vivo* fractures of the mid shaft. Torsional testing is also of interest, considering spiral fractures that are commonly observed in both non-accidental injury and accidental events in children. In order to fully understand the manner in which samples fail in torsion, animal substitution was proposed. This allows for fracture testing of an increased number of samples, providing the description of the entire load path to failure. As animal substitution has not been previously investigated in depth, examination of the general procedure for substitution, and the accuracy observed when using techniques derived for human samples would also be required.

Consequently the aims of the thesis are as follows:

i. **Computationally Simulate Animal Bone: Investigate the capability and accuracy of the general Computed Tomography Finite Element process in the substitution and simulation of animal bone.**

Should this investigation prove successful, it will serve to demonstrate the applicability of animal substitution in CT-FE studies. The use of animal substitution provides the potential for increased sample size fracture studies and demonstrates the general ability of the CT-FE process in expansion towards alternative bone types.

ii. **Physically Test Whole Bone Samples: Consider the behaviour of samples in alternative loading regimens (such as torsion) and identify the manner in which the samples fail physically.**

The investigation of failure modes other than simple compression has shown limited investigation in literature. The detailed investigation of torsion is important, being a common failure mode for long bone fracture.

iii. **Validate the Simulation Procedure: Demonstrate the accuracy achieved during the animal CT-FE modelling process through appropriate laboratory validation.**

The ultimate capability of Finite Element modelling can only be demonstrated through appropriate validation. Extensive validation will be undertaken to demonstrate the capabilities of the modelling procedure at both a whole-bone and local level.

iv. **Test the Simulation Sensitivity: Consider the effect of various input parameters, and the sensitivity of the modeled solution to small changes in the modelling procedure.**

There is a large array of input parameters in complex CT-FE simulation. Modification of a single parameter can have a significant effect on the observed results. It is therefore important to assess the sensitivity of the modelling process to changes in the input and validation procedure. In addition the modelling procedure itself will be examined to determine the appropriate simulation conditions required (mesh refinement etc.)

v. **Apply the Validated Procedure: Consider the ultimate applicability of the animal CT-FE process through the prediction of the fracture load of a given sample.**

The main focus of the thesis is the validation and observed accuracy when applying the CT-FE process in new directions (animal substitution and torsional fracture). However, the ultimate application of the process is in the prediction of fracture risk and the fracture load for a given subject. The final aim of the project is to demonstrate that the process is capable of predicting the fracture load of a given sample with a reasonable level of accuracy.

3 Creation and Verification of the Finite Element Model

Finite Element simulation was selected to examine the behaviour of whole bone porcine samples under load. A semi-automated process, using proprietary software (ScanIP, Simpleware inc.) was used to create the model. There are a large number of developers providing software for the segmentation of CT images, however a fewer number integrate this segmentation with automated meshing algorithms. The software used combines various aspects of CT-FE model production into a single package. Despite the increased automation offered by such software, they merely facilitate a process, and changes in the input variables can have a significant effect upon the observed results and the accuracy observed during simulation. Throughout simulation, the effect of manipulating the input variables was assessed to ensure that accuracy was retained.

The creation of the Finite Element model falls into two distinct processes: firstly pertaining to the creation of the model geometry and defining the element mesh, and secondly determining and assigning the Young's modulus. Tests confirming the accuracy of the various processes were undertaken; following which the standard modelling methodology was determined.

3.1 Geometry Production

The first stage in Finite Element simulation, and the key to accurate representation of a given system, is the creation of the model geometry. This is a common source of error within simulation of complex systems, and in particular in the modelling of biological geometry. Simulation of biological material is complex, with a requirement to model complex shapes, rapid shape changes, and general forms that would not be commonly utilised in engineering structures. The simulation of biological tissues has become more prevalent with the development of modelling software, and increased geometrically accuracy as techniques have improved.

The studies in this thesis use technology based upon the principle of converting medical data into three-dimensional Finite Element geometry. The software used is Simpleware's ScanIP; a commercially available system that allows for the segmentation, meshing and mapping of Young's modulus onto a mask created from medically sourced images. The software is able to mesh geometry from any type of image source (medical or non-medical), but was initially derived to create models from medical data such as MRI and CT [168]. Research using the ScanIP software package has been published in a diverse range of fields, from the modelling and description of dinosaur bones to completely inorganic objects such as examining reinforced engineering composites [169, 170].

3.1.1 Selected Data Type

As discussed in Chapter 2, there are inherent limitations in both CT and MRI scanning, which were considered when selecting the appropriate data source from which to create the model geometry. CT produces relatively high levels of X-ray exposure, but provides increased resolution of well-calcified bone structure, whilst MRI has no exposure issues, and performs better in the definition of soft tissues. Due to the magnetic nature of the MRI system, metallic artefacts are not permitted within the scanning equipment.

CT was selected for data acquisition for this study. It was considered that the increased resolution of bone material was vital to the accurate simulation of bone geometry and that the effect of exposure had no influence on the material characteristics measured during the physical tests, and thus could be ignored. The ability of CT to image metallic artefacts was also of consideration, allowing the scanning of the proposed constraints and strain gauges as required.

Each of the bone samples that were simulated in the thesis were scanned using a Lightspeed VCT CT scanner from General Electric Healthcare [171] (Figure 3.1). The 'lower extremity bone' setting was used throughout data acquisition. This is pre-configured for the scanning of legs, and uses thin-slice helical acquisition at 100 kV/50 mA, which represents a relatively low X-ray dosage. A calibration Phantom from Mindways (also a subsidiary of GE Healthcare) [171] was placed beneath each sample in order to allow comparative analysis of the attenuation (brightness) observed in each scan (Figure 3.1).

Each bone was scanned in isolation, with the exception of saline soaked cloth and the calibration phantom. Previous CT-FE studies have scanned samples immersed within liquid; however, recent research has demonstrated that this has little benefit on the accuracy of the scanned geometry, and consequently this technique was not used [105].

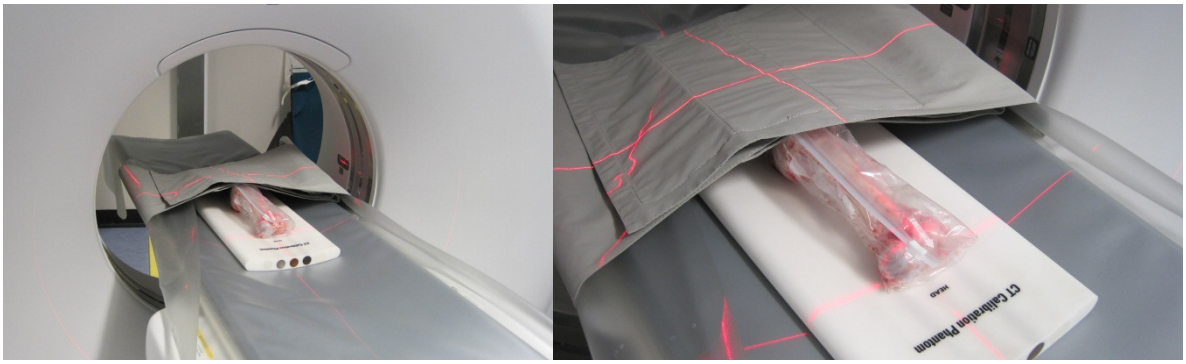

Figure 3.1. Images showing the CT scanning process within the Lightspeed VCT scanner.

3.2 Masking the CT Images

3.2.1 Axial Slice Masking

The CT images used for geometry production are commonly reviewed by clinicians on a two dimensional basis. This permits viewing on a traditional display screen, and allows the clinician to quickly consider a subject throughout its depth by moving from one image to the next. To create this two-dimensional image, the data is split into a stack of images on any given plane, allowing the review of each of the 'slices' in discrete intervals. The resolution and accuracy of the CT image s defined by a number of factors, including the size of the source (known as spot size due the manner in which the electron beam is focussed into a spot shape), the distances between the scanned object and the receiver, and in film based imaging, the grain size in the type of film used. When the CT images are digitised they are converted to 3D voxels, and at this point some resolution may be lost, and from this point the voxel size in the images ultimately defines the image resolution.

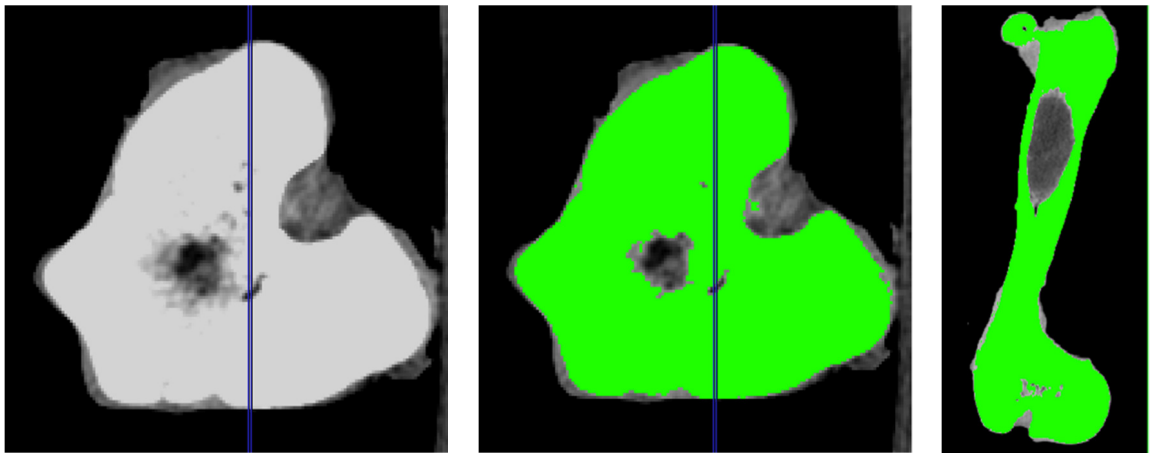

(a) (b) (c)

Figure 3.2. (a-c) The masking process of a single section of a porcine femur. In (a&b), the mask has been painted onto the CT image to map the denser and more mineralised bone. Image (c) shows a slice through the coronal aspect, in which the stacked mask slices can clearly be seen.

The general process for geometry mapping (sometimes referred to as 'segmentation') is to determine the areas within a source image that are of interest (in this case mineralised bone material) and apply a 'mask' to that region. On a slide-by-slide basis, the depth of the applied mask will be determined by the voxel size of the original CT scan, and typically this technique requires the operator to 'paint' the mask onto regions of interest (effectively by hand). Creating a three-dimensional image in this way can map both the internal and external surfaces of the bone, and allows for greater control of the process, as each slice can be reviewed visually to confirm conformity to the required mask region. A

disadvantage of this approach is that it may induce step changes and inaccuracies in the boundary between the discrete sections. The boundaries between slices that have been masked in this way generally require attention in a process known as post-smoothing. Figure 3.2. shows each step of the axial masking process.

3.2.2 Threshold Masking

The segmentation described in the section above provides visual inspection of the masking process on a slide-by-slide basis, however the validity of the mask is dependent upon the modeller applying the mask accurately throughout the depth of the scan. For a single plane this can be as high as 500 slices, and consequently this technique is prone to human error. An alternative method for geometry creation, *thresholding,* is a technique in which pixels with a greyscale value within a predetermined range are masked automatically. The process is regularly used in the clinical environment whilst reviewing patient data, where images can be automatically trimmed to display only sections pertaining to soft tissue, fat, fully calcified bone etc. as pre-determined by standard settings in the viewing software.

In its basic form, automated thresholding 'looks' at an image and selects any voxels or pixels inside a prescribed range, and deselects all of the other voxels. More complex algorithms are available, such as hysteresis thresholding, which considers voxels that are locally connected to those selected within the standard threshold method, and also selects these. The effect of this more complex algorithm is a reduction in the selection of isolated voxels. However, the method may incur increases in the general mass of an object in the CT-FE application, selecting additional and unrequired voxels at the boundary.

Thresholding is not without limitations; in particular, issues may arise when looking to mask areas of bone that are less dense and therefore harder to differentiate from the surrounding soft tissue. This is of lesser importance when assessing adult porcine samples (as used within this thesis), as the epiphyses are fully formed and distinct in the CT images. However, issues may arise when considering developing bone from younger sources. The differential between fully calcified bone, and growing bone material is less distinct, therefore complications may occur when defining the boundary between the two. Figure 3.3 shows the thresholding process upon a young (<3 years of age) human tibia and fibula, highlighting the loss of refinement that occurs when attempting to define the correct thresholding settings. The issue is increased when masking bone *in vivo*, where the external boundary between bone and the surrounding soft tissue is less distinct.

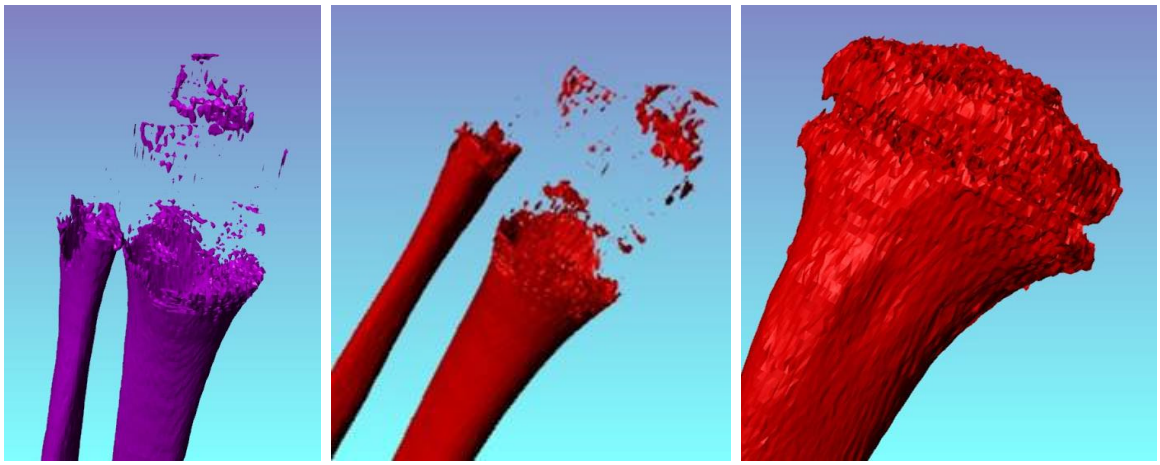

(a) (b) (c)

Figure 3.3 (a-c). Images showing the thresholding process on a non-adult tibia and fibula. The mask loses refinement as the thresholding levels vary (a-b). Image (c) details a mask prior to the smoothing process.

Despite the difficulties when defining the levels for thresholding developing bone, this methodology typically increases the rate at which the mask can be applied. Consequently the time required to process the CT data into a full three-dimensional mask is significantly reduced. The boundary issue between slices is also removed, reducing geometrical error.

Automated (not hysteresis) thresholding was undertaken throughout simulation in this thesis. The greyscale boundaries selected for defining the geometry of each sample were initially selected by reviewing the greyscale histogram in the masking software. This shows the occurrence rate of each greyscale, and can be used to determine wherein the required geometry lies. The thresholding levels were set to ensure that the simulated bone sample had the same external dimension as the physically-measured sample. This was checked via physical measurement with Vernier calipers (measured to nearest 0.1mm) and cross referenced with the source CT image at key locations to ensure that the physical size of the sample was accurately maintained. Measurements (Table 3.1) were taken from each finite element model and each physical sample, as shown in Figure 3.4.

Mask statistics could be examined following thresholding, showing the miniumum greyscale value for all samples (mean 204.4 +/- 18.7), maximum greyscale value in the masks (mean 2215 +/- 94.0) and the mean greyscale value in each of the masks (mean 559 +/- 56.7).

Measurement	Dimension (mm)	
	x	*y*
Width 50mm from proximal extremity	32.4 +/-0.80	33.1 +/-0.78
Width at midpoint	24.1 +/-0.44	21.4 +/-0.90
width 50mm from distal extremity	37.1 +/-0.96	31.4 +/-0.98
Height	181.3 +/-5.2 mm	

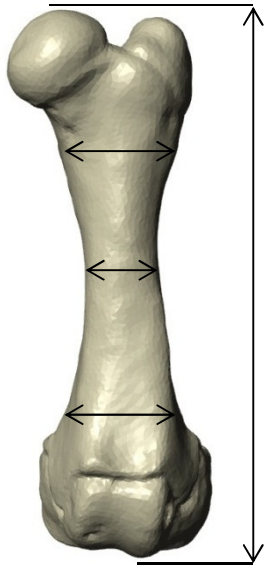

Table 3.1, Figure 3.4 Measurements taken from the physical samples used to ensure thresholding had prescribed the correct geometry. Image shows the measurement points on a sample (measurements taken in both *x* and *y* directions).

3.3 Smoothing the Mask

Following masking, the model must be assessed to ensure geometrical validity. One of the key processes here is 'smoothing', which is essentially the removal of unwanted voxels from the exported mask. The process is commonly used to ensure that the surfaces (internal and external) are accurate, smooth and regular, as aggressive geometrical changes due to inaccurate masking can provide point of stress concentration during simulation. This was undertaken using a Gaussian-based smoothing algorithm, which considers the relative geometry of adjoining voxels within a defined region (typically the region is twice the voxel dimension).

An additional source of error that requires attention is 'noise' within the source image. During the automated thresholding process this 'noise' (which shows as brighter voxels) will often be included within the mask. This is because the standard automated process refers only to the greyscale values of each voxel and not the logical position within the source image or the bounding voxels either side of those selected. Any noise encountered must be removed, as these brighter voxels will be masked, defined as bone material and then exported into the final model. These detached voxels can lead to fatal errors during solving due to their unconstrained nature and must be removed. An additional automated algorithm completed this process, removing any section of mask that had a number of voxels below that of a prescribed limit. Typically this was set at 1000 voxels, ensuring that only the larger geometry of the main structure of the masked bone would be exported. Care is required during

the general smoothing and island removal processes, as aggressive smoothing and noise reduction can impact on the simulated geometry, reducing the definition of key geometrical features that should be retained to ensure accurate modelling.

3.4 Meshing the Mask

The backbone of all Finite Element simulation is the determination and nature of the mesh of elements that are used to define the geometry and material parameters of a system. The elements can be of varying form, and are bound by nodes, which determine their outer points and the inter-element connectivity. As all Finite Element calculation is an estimate of a 'true' solution, it is often the mesh of elements that determines the accuracy of the modelling. It is the structure of the mesh that is investigated when examining the *convergence* of the solution. Convergence relates to the manner in which refining the mesh increases or decreases the accuracy of a solution (as well as increasing/decreasing the complexity and therefore the solve time). It is considered that for a solution to converge, repeated results obtained during iterations of increasingly refined meshing will be heading towards a constant solution. As can be seen from the results below, there may be instances of local maxima and minima, towards which the result may be appearing to converge. There are a significant amount of publications regarding the most appropriate convergence assessment criteria for Finite Element studies [49, 172-174]. Despite this, convergence assessment is a 'grey area' within simulation, with no ultimate and well defined criteria for all models to adhere to. An extensive meshing and convergence assessment was undertaken for each model in this study, as detailed within section 3.5.

Meshing can be implemented using a number of techniques, typically involving a third-party meshing application such as Hypermesh (developed by Altair Hyperworks). Using medical data to define the Young's modulus and geometry in simulation adds complication to the meshing process. The varying values for Young's Modulus, for example, are applied to the completed mesh on an element-by-element basis. For this reason, the software used for this study incorporates integrated meshing algorithms, allowing the conversion of the three-dimensional mask into a fully meshed model with Young's modulus assigned to each individual element as appropriate. Two meshing algorithms are available within the ScanIP software, both of which are automated (Figure 3.5).

(a) 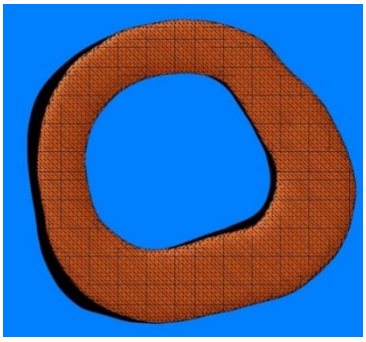 (b) 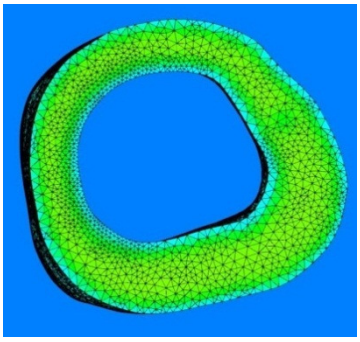 (c) 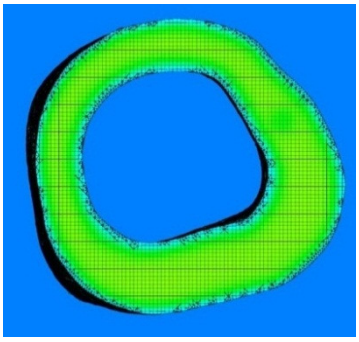

Figure 3.5. (a-c) (a) The voxel arrangement of a single sample; (b) a mesh created using FE Free, showing tetrahedral element arrangement; (c) the FE Grid meshing protocol, which utilises a rigid grid structure.

The first (image (b) in Figure 3.5), 'Grid Meshing', produces meshes based upon the voxel resolution of the source image. It combines tetrahedral elements, which are used to define the bone surface, and more regular hexahedral elements, which are used to create the interior volume. The second protocol, 'Free Meshing' was introduced more recently (2011), and uses the tetrahedral surface mesh created using FE Grid, but then re-meshes the volume of the mask with further tetrahedral elements, optimised to reduce the total number of elements required. The optimisation is based upon a number of additional parameters, such as the ability to detail local features, and the rate of curvature of the surface and voids within the mask. In general terms, the FE Grid system produces a more regular grid-based mesh such those implemented in a manual meshing procedure. This is considered more acceptable in engineering structures, where regular mesh structures are used to map the relatively simple geometry of regular and often homogenous systems. The FE Free system provides the type of meshing that is more prevalent in biomechanical simulation (fully tetrahedral). This mesh allows for finer depiction of the subject's features and can also provide more generalised, coarse meshing of regions of lesser interest to decrease the solve time of the model as a whole. FE Free uses more memory during the meshing process, but ultimately provides a more 'optimised' mesh, using topographical features to define more refined regions, whilst increasing decimation in areas of lesser interest. Both meshing systems allow for control of the mesh refinement (via element edge length control in the structured FE Grid mesh and through a general mesh coarseness value in FE Free) and in addition can have regions of interest retrospectively applied, within which further mesh refinement can be undertaken.

3.5 Convergence Assessment

The basis of a Finite Element model is the splitting of a system into a number of discrete intervals, known as elements. Convergence assessments are generally undertaken to understand the error induced when splitting a model into these discrete sections (discretization error). Discretization error

is essentially the occurrence of errors as a result of unwanted stress or strain gradients across the width or depth of an element. Generally reducing the size of the elements reduces the area over which a result is recorded removing the 'averaged' nature of the results as a whole and thus reducing the discretization error. The reduction in element size is shown graphically in Figure 3.6.

It is generally considered that convergence should be observed graphically as opposed to numerically, to take count of any local maxima or minima occurring in the mesh refinement process. Convergence is generally determined through the observation of the behaviour of an absolute Finite Element result (such as maximum principal stress in a region). If an ideal result is known, convergence may be determined through comparison of the difference between the simulated and ideal results noted for increasing mesh refinement. Level of mesh refinement is generally calculated through the number of degrees of freedom (DOF) of the model. The DOF Figure is similar to a total element count, however it takes into account the selected element type, the number of nodes in the elements, and the manner in which these nodes are able to translate and record results. The meshing protocols used in this study exported a tetrahedral elements when paired with Ansys as an Finite Element solver. ScanIP offers the exportation mid-order nodes, which are included at the mid-point of each side of the tetrahedral elements. This increases the validity of the solution, allowing the element to handle the irregular shapes produced in biomechanical simulation.

The other effect of this additional node is that the element can predict the gradient of behaviour across each element more accurately, reducing discretization error. Each ten-noded tetrahedral element has three degrees of freedom per node, allowing translation in each of the global axes. The element type selected is able to account for a number of additional parameters that are not assessed within this study, such as plasticity and creep, however they are also capable of large-scale deflection and large levels of local strain, which may be incurred during simulation.

(a) 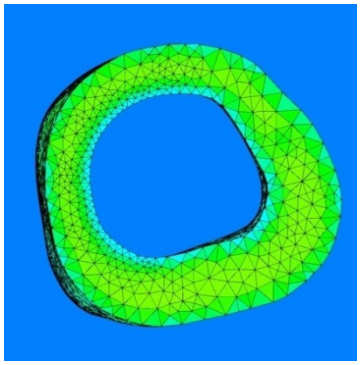 (b) 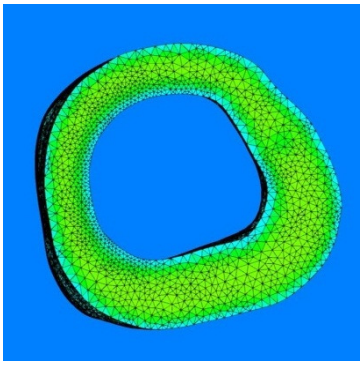 (c) 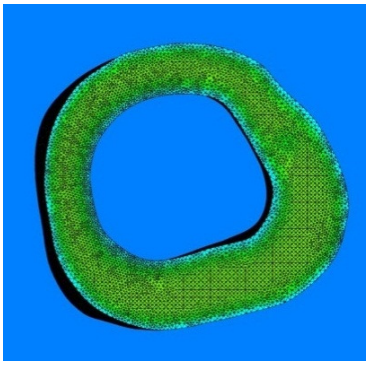

Figure 3.6. (a-c) Varying levels of mesh refinement. The section shown here, which had a total sample length of approximately 5% of a complete porcine femur showed an increase from 11,600 elements in the first iteration (a) to 260,900 in the final image (c).

Changes to the mesh properties for a single sample under simple loading conditions were investigated. The meshing protocol is independent of a number of the other key parameters in simulation, such as the general boundary conditions and the geometry of the sample, allowing these meshing changes to be reviewed in isolation. Meshing in biomechanical simulation differs from standard engineering applications due to the determination of material characteristics in inhomogeneous material models. Despite the use of linear material models, the method by which the materials are applied is on an element-by-element basis. Consequently, changing the meshing protocols alters the mapped material characteristic to a given region of elements. As the convergence criteria relates to a finite result that is dependent on both mesh size and material property it should be noted that these two parameters are not mutually exclusive in an inhomogeneous model and should be considered independently of one another. The meshing and convergence assessment was consequently reviewed in two parts, firstly with the inclusion of inhomogeneous material mapping, and secondly using a homogenous and continuous material assumption, to isolate the effects of material mapping.

Keyak et al. first investigated the effects of element size on the results of Finite Element bone modelling [50]. Despite significantly larger meshes in that study (all element dimensions larger than 3.1 mm), the investigation highlighted the importance of convergence assessment in isolation of material mapping. The ultimate refinement of the paper is limited as a result of the technology available at that time. Despite this, the paper highlights the key result of how, despite achieving 'conventional' convergence in terms of strain energy, further refinement of element size and the mapped material mesh had a continued effect on observed results, generally reducing the absolute results of the simulation.

Viceconti et al. investigated various automatic meshing algorithms, in which tetrahedral meshing (as used in the ScanIP FE Free protocol) was described as 'mature… widely available… probably the best method when a solid model of the target object is available' [44]. The authors suggested that hexahedral meshing (as provided internally via FE Grid) provided the most accurate results but was resource intensive. The paper presented laboratory-derived results as the ideal with which to compare error and convergence of each of the meshing algorithms. In order to use this methodology, the limitations of laboratory testing methods must be fully investigated to ensure that potentially detrimental physical errors are not incorporated into the convergence assessment. The limitations of the paper highlight the development of Finite Element modelling hardware and procedures, with 100,000 DOF being the uppermost limit at which the modelling procedure was curtailed.

3.5.1 Inhomogeneous Material Convergence Assessment

To investigate the convergence of the meshing and material mapping protocol in inhomogeneous material mapping, a single femur sample was masked, cropped and constrained to mimic a simple laboratory test. The distal extremity was constrained at the level of the medial and lateral epicondyles,

and the epiphysis was fully exposed at the proximal extremity. Including the entire lower density proximal epiphysis ensured that the behaviour of the meshing process could be considered when the material mapping protocol had been implemented across a wide range of density values. (Figure 3.7)

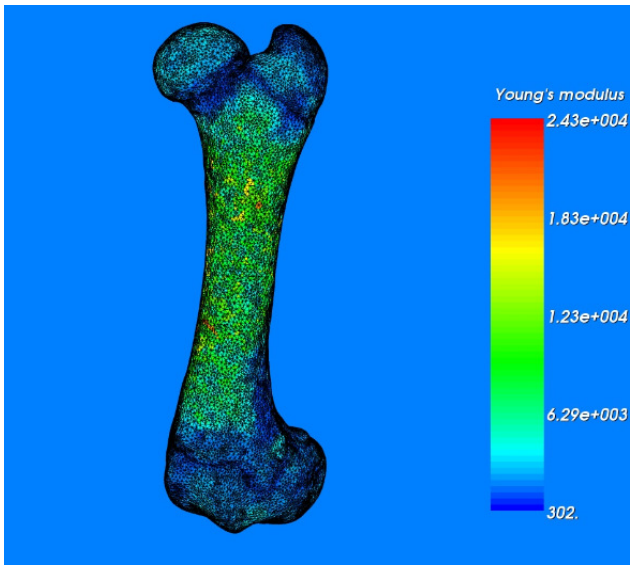

Figure 3.7. The inhomogeneous mask used for convergence. Prior to simulation the distal extremity was cropped at a depth of 50mm. The image details the applied Young's modulus in MPa.

50 Nm of torque was applied by means of opposing couples, and results were recorded for 1st principal stress, and for the x component of stress (Figure 3.8). The ideal outcome of convergence as defined by Burnett [175] is that as the size of each element tends to zero, the stress across each independent element approaches a single value. The test used FE Free to mesh the model mask, which has the ability for general adaptation of the mesh parameters via a single control, with an overall descriptive figure ranging from –50 to +50. Changing this figure adapts a number of parameters concurrently, primarily adapting the target minimum edge length of the meshed elements, and the permitted maximum edge length for the element as a whole. This controls the size of the meshed elements directly. As an example, an allotted value of –25 gives a target minimum edge length of 0.705 mm whilst a figure of –5 would provide a target minimum edge length of 0.265 mm.

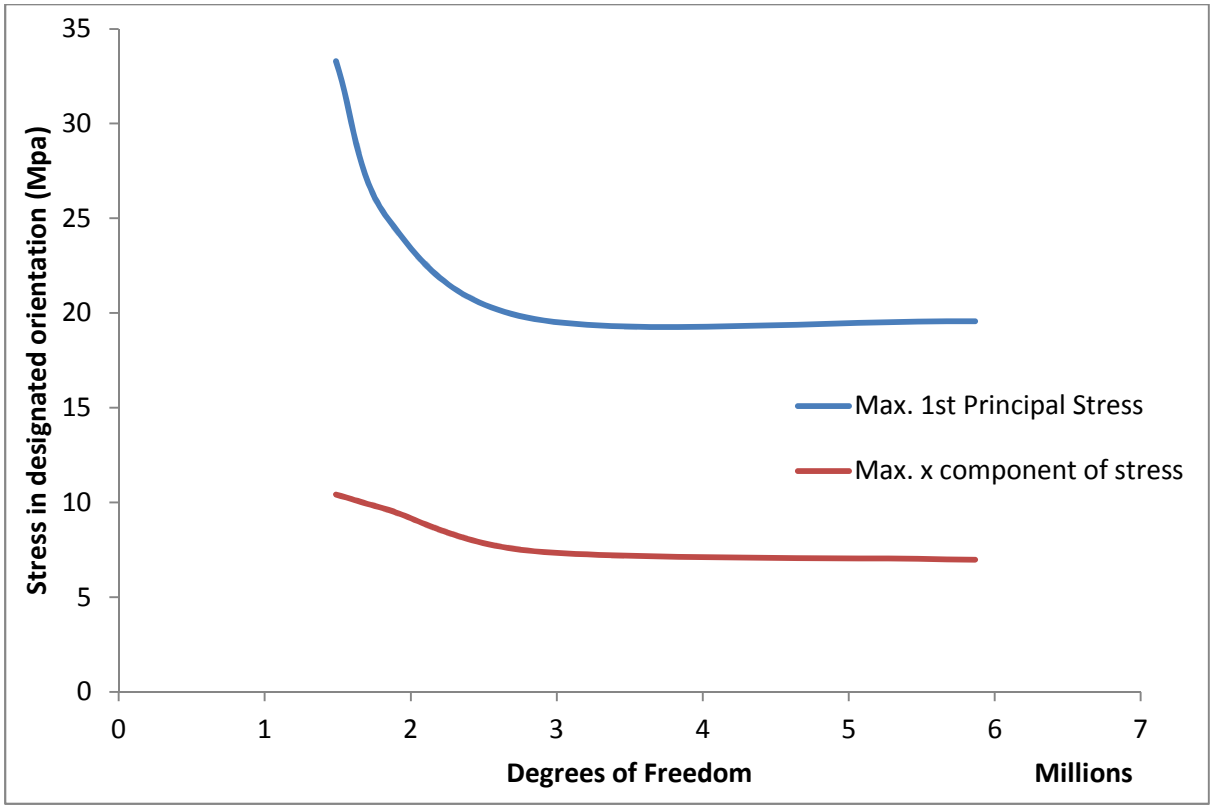

Figure 3.8 The response of the inhomogeneous model in terms of maximum 1st principal stress and maximum *x* component of stress as the total number of degrees of freedom is increased. The result for each component tends towards a single value at approximately 2.5 million degrees of freedom.

The test results shown in Figure 3.8 relate to settings of between –45 and –7, with the value determined for convergence (2.5 million DOF) occurring at around –20 to –15. This relates to a target minimum edge length for samples of approximately 0.5 mm. Controlling the edge length in this manner results in the thickness of the cortex being meshed by more than 10 elements in any given plane, for the majority of the length of the cortex. Increasing the number of elements through the thickness of the cortex wall improves the accuracy of the changing geometrical and material characteristics of the sample. Additionally, this level of refinement provides an accurate estimation of the geometry of the surfaces, both internal and external. Ten elements across the wall is a significant increase in the number of elements used in key literature, where similar comparisons in human femoral samples show approximately four to five elements. Total element count is also increased in this thesis, from approximately 76,000 elements for a (notably larger by volume) human femur as opposed to approximately 330,000 elements for each femur simulated in this thesis [70].

3.5.2 Homogenous Material Mapping Convergence

Homogenous material mapping was applied in a second convergence study to confirm the validity of the inhomogeneous assessment and to test additional, general convergence criteria. This reduces the compounding of error issues, isolating the material-mapping algorithm from the exported mesh. The base, static value for material property (Young's modulus) was selected as 17.4 GPa, a figure selected from literature for porcine cortical bone [147]. This property is applied to all of the elements within the mask, and is likely to result in an excessively stiff structure (the material property will also be applied to the less mineralised regions, which should be less stiff). As a consequence, the absolute results should be reviewed in isolation, being provided purely as a means to assess convergence rather than an absolute value to compare the results from simulation with those measured in the laboratory. Due to the homogenous assumption, the mask was cropped to mimic a region within which the Young's modulus remain relatively constant, namely the diaphysis. Cropping in this way produces a sample that is approximately cylindrical in shape (Figure 3.9). Force was applied to the proximal surface of the cropped piece, whilst the distal surface was fully constrained in all directions.

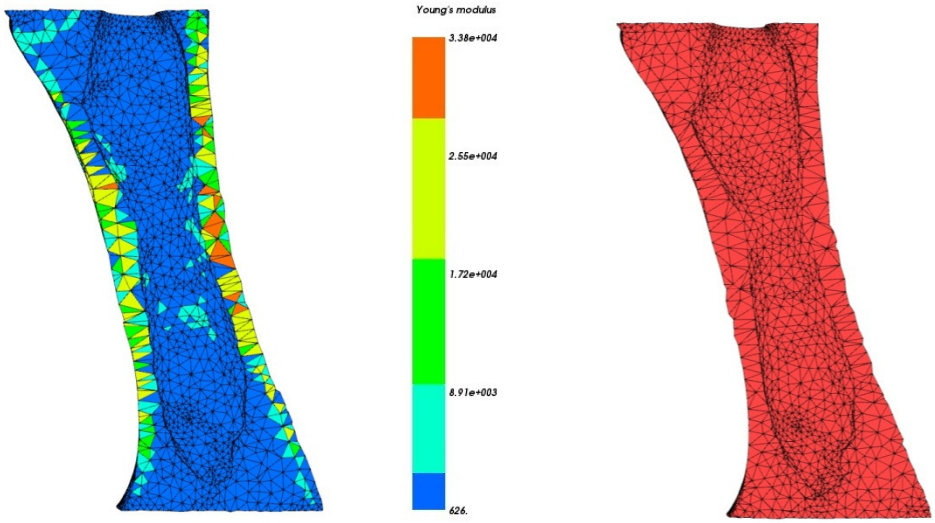

Figure 3.9. Screen captures show the heterogeneous and homogenous material mapped samples as cropped and tested in the general assessment of error case. The homogeneous model is assigned a static Young's modulus value of 17.4 Mesh refinement is coarse in the images (-25 setting in FE Free)

3.5.3 General Assessment of Error

Using a single homogenous material removes the material gradient between elements that are observed in inhomogeneous material mapping. This then allows the assessment of percentage energy errors of the model using the error calculation algorithms within the Ansys package. These errors are produced through discrepancies between the calculated stress in the elements of the model and the global continuous displacements in the model derived at the nodes. This is known as the 'percentage

error in structural energy norm' (SEPC) and is a result of the manner in which elemental stresses are averaged to provide continuity from element to element. The percentage error will ultimately converge to zero should the mesh be continually refined. The assessment methodology used in this thesis to assess SEPC error uses the Finite Element accuracy criteria detailed by Shah et al. [48]. This criteria firstly assesses the global SEPC error of the whole model, and then uses 'waves' of assessments to determine the error at a selected location of high stress, and then on a widening basis, increasing the region of interest in discrete iterations (Table 3.2). The SEPC error function used in Ansys to determine the discrepancies between the continuous displacements at the nodes and discontinuous stresses in neighbouring elements is based upon the work of Zienkiewicz and Zhu as follows [176]:

Firstly, the element nodal stresses are averaged, providing the stress at each node:

$$\{\Delta\sigma_n^i\} = \{\sigma_n^a\} - \{\sigma_n^i\}$$

where:

$\{\Delta\sigma_n^i\}$ is the stress error vector at node n of element i

$\{\sigma_n^a\}$ is the average stress vector at node $n = \frac{\sum_{i-1}^{N_e^n}\{\sigma_n^i\}}{N_e^n}$

N_e^n is the number of elements connecting to node n

$\{\sigma_n^i\}$ is the stress vector of node n of element i

Then, for each element

$$e_i = \frac{1}{2}\int_{vol} \{\Delta\sigma\}^T [D]^{-1}\{\Delta\sigma\} d(vol)$$

where:

e_i is the energy error for element i

vol is the volume of the element

$[D]$ is the stress-strain matrix evaluated at reference temperature

$\{\Delta\sigma\}$ is the stress error vector at points as needed

The energy error over the model is:

$$e = \sum_{i=1}^{N_r} e_i$$

where:

e is the energy error over the entire model

N_r is the number of elements in model or part of model

The energy error can then be normalized against the strain energy.

$$E = 100\left(\frac{e}{u+e}\right)^{\frac{1}{2}}$$

where:

E is the percentage error in energy norm

u is the = strain energy over the entire model

Table 3.2 Data from the converging mesh schedule and results for convergence assessment under Shah's criterion. The results are curtailed at -10 due to hardware limitations.

Mesh Level	Element No.	Target Min Edge (mm)	1st principle stress (MPa)	Error to Previous Run	SEPC Global	SEPC w1	SEPC w2
-45	106939	1.141	17.512	-	3.1015	1.2515	1.3571
-35	143825	0.922	18.418	5.2% (+)	2.1892	1.5383	1.8325
-25	215759	0.703	17.786	3.4% (-)	1.7704	1.5694	1.5932
-15	519795	0.484	17.611	0.98% (-)	0.9619	0.8	0.85513
-10	961707	0.375	17.54	0.4% (-)	0.8333	0.7134	0.795

The first criterion is that the SEPC error within the entire system (excluding regions of enforced boundary conditions such as loading and constraining) should be lower than 15%. The second criterion relates to local error as the node within the region of highest stress in the model is selected. All elements connected to this node are selected and the error of this region is determined. This is the first wave. At this point all of the nodes within these elements are selected, and the elements bordering and connected to those nodes are then selected, determining a second, larger region of interest. This is the second wave. Shah et al. states that the energy error result of both the first and second wave local areas should be lower than 10%.

Figure 3.10. shows the results of Shah's criteria. At all levels of mesh refinement, the stress error criteria are met, and progressively improving results are noted through the refining iterations.

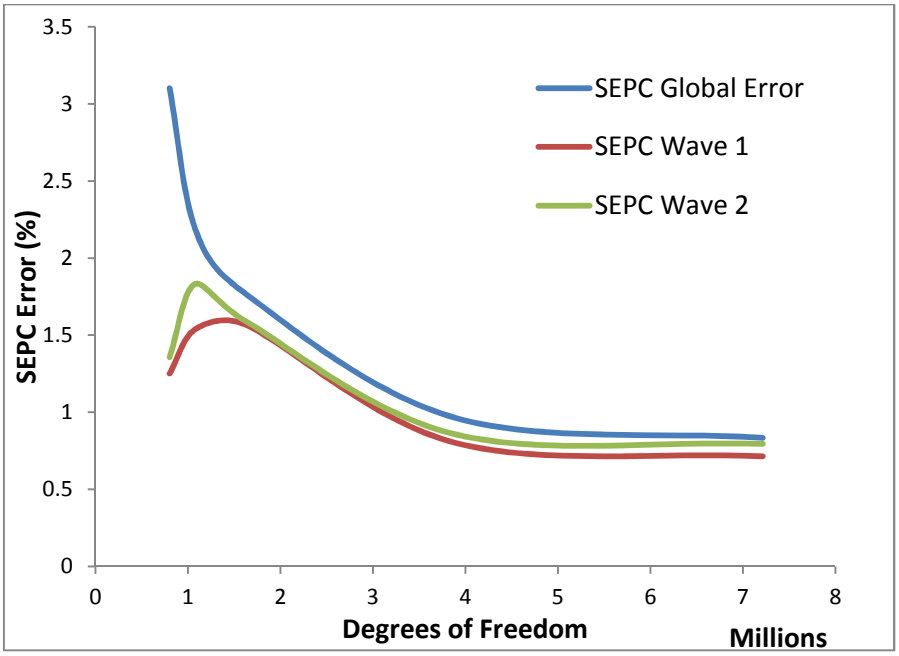

Figure 3.10. The SEPC error behaviour as the mesh is refined. The rate of error reduction slows considerably as the model exceeds 4.5 million degrees of freedom, at which point SEPC error for all regions falls below 1 %.

Shah et al. related the percentages they defined to the 'current hardware and software tools', suggesting that a global target of 15% should be easily met at that time (2002). With this consideration, and ten years of Finite Element modelling development, it is perhaps acceptable to consider a value of beneath 5% rather than 15% for global error to be reasonable. The criteria set by Shah et al. were in use unadulterated as late as 2004 [177].

The absolute results obtained for principal stress are similar to those detailed by Keyak et al., continually reducing as mesh refinement is increased. This is shown graphically in Figure 3.11. in which the percentage error from one iteration to the next and the rate of result change is plotted. As can be seen, the rate of change reduced to a limit of 0.4% at the limitation of processing capability; however, small levels of reduction were continuing at this point. The reduced rate of change is significant enough to determine that the model is converging, although the ultimate minima cannot be reached as a result of hardware limitations.

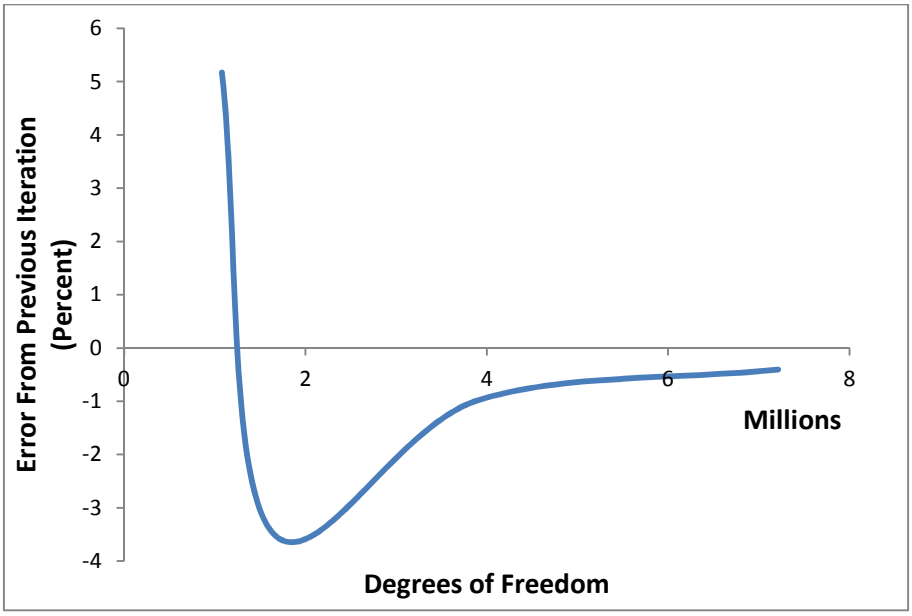

Figure 3.11. The convergence response of the homogeneous model of sample six with respect to the percentage change in an absolute result (first principal stress) from the previous iteration.

Marks et al. investigated some of the initial results published by Keyak et al., suggesting that the ultimate convergence of Keyak et al.'s initial assessment may never truly converge as a result of singularities in the geometry [34]. These are induced through the step changes in geometry when meshing with cubic elements, but the occurrence of singularities is still relevant with more modern tetrahedral meshes, particularly when meshing tight curvature and detailed geometry in biomechanical simulation.

Singularities generally produce divergence within results, where increasing refinement reduces the size of the element at the crack or radius tip, reducing the averaged nature of the result at this point, and increasing the absolute result. This is observed by Burnett et al., who used the removal of singularities as a qualifying requirement in the methodology of convergence studies [175]. Marks et al. suggested the use of post-smoothing following the meshing procedure to reduce this effect. Post-smoothing was used as a matter of course throughout the computational testing within this study, however its effect was not independently assessed.

3.6 Meshing Technique

Following the results of the convergence studies, meshing was undertaken using ten-noded tetrahedral elements and the FE Free method, with an arbitrary coarseness setting of between –15 and –10, depending on application, ultimate volume of the exported model, and the total exported element count. This provided approximately 3.9 to 7.2 million degrees of freedom for a given sample of

cropped cortex. Convergence at this level of meshing is detailed in Figure 3.8. Despite the negative polarity of the arbitrary value assigned for meshing settings, the level of mesh refinement is high for hard tissue modelling at this scale, and provides target elemental edge lengths of between 0.484 mm and 0.375 mm (and thereby meshing approximately 10 elements across the thickness of the cortical wall at its thinnest section), significantly more refined than meshes used in previous studies. Schileo et al., for example, undertook compressive modelling of human femurs, using elemental edge lengths of 3 mm within the diaphyses and 2 mm in the metaphyses [70]. Further mesh refinement in the ScanIP software which uses the positive values in the arbitrary coarseness settings is limited to smaller scale modelling, such as those considering the behaviour of tissue at a material level [168, 178].

Increasing mesh refinement has an effect on the time taken to mesh, export, import into the Finite Element solver and finally to solve the complete model. Typically inputting the geometry and solving with Ansys took from approximately 10 minutes for a 100,000 elements to around 18 hours for 2,000,000 elements. Data processing and meshing was undertaken using a single workstation with a Dual core 3.2 GHz processor and 16GB of RAM.

The ultimate limitation of all convergence studies is determined by the hardware used for analysis, and in this instance meshing refinement was halted at the assigned value of '-7'. Here, the production of approximately 2.3 million elements leads to Ansys creating working files of approaching 30 GB. Despite continued upgrades to the solver hardware used in testing; this working file size resulted in complete system instability due to the virtual memory requirements and page file used by the FE solver. The convergence studies were consequently curtailed at '-10', despite the potential for further reductions in error beyond this point.

It is considered that the meshing levels used within the studies in this thesis provided a good balance of a suitably converged model and manageable solve time, with a significant improvement on the level of meshing refinement shown in previous literature. An example meshed model is shown in Figure 3.12.

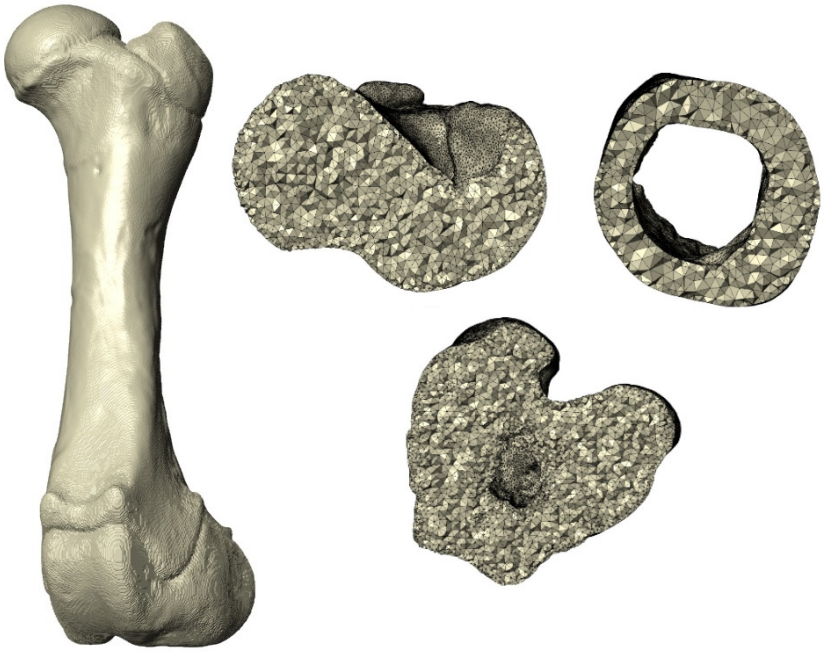

Figure 3.12. An example mask ready to be cropped for exportation and analysis. Cutaways in the axial plane detail the meshing arrangement at the extremities and within the mid-shaft.

3.7 Defining Material Behaviour

In order to accurately predict the behaviour of a simulated system, knowledge of the material properties must be obtained. With biological material this is inherently complex; the material is likely to be inhomogeneous and of irregular structure, with varying response to loading as a result of this irregularity. Analysis of the properties of a material on a small scale is generally undertaken by physical testing, be this simple bending, torsion, compressive tests or more detailed methodologies such as nanoindentation. It should be considered that bone does not represent a single substance, but rather a compound incorporating numerous different materials each with their own material characteristics. In addition, the boundary between these different materials is fine to the extent of being almost imperceptible.

Published research regarding CT-FE analysis is dominated by studies considering adult human femoral samples [9, 27, 59]. Consequently the mapping of Young's modulus in human samples has had a significant level of investigation. Within these studies, the inhomogeneous nature of bone is accommodated using various material mapping techniques, with an increasing level of accuracy as the process has developed [31, 46].

Little research has been undertaken to determine if the mapping process functions appropriately outside of the remit of adult human samples (with the exception of a number of equine studies [77, 143]). Therefore a significant aspect of this thesis determines if the substitution of porcine bone

within CT-FE testing was valid. The validation and laboratory testing were undertaken using porcine bone samples. Selecting porcine bone offers increased repeatability due to the consistent supply through a local abattoir. Porcine bone was selected as a substitute as it is generally considered to be very similar in construction to human bone, having had significant investigation for use as a substitute in physical testing [146, 148]. This is despite obvious limitations regarding the geometry, the load supporting capabilities and the fact that pigs are quadrupedal. Despite its regular use as a substitute for human bone in testing, at the time of this study there was limited published research defining the precise Young's modulus of porcine bone.

The definition of Young's modulus of porcine bone fall into two distinct sections within this thesis; the determination of the physical properties of the samples, and the determination of the relationships required to assign these moduli within simulation. This section considers both the physical material properties of porcine bone and the material property mapping process.

3.7.2 Physical Testing of Whole-Bone Samples

Whole bone testing in torsion was initially selected as a testing methodology in this study due to its comparative lack of investigation in CT-FE, and its links to significant bone injury (NAI and sporting injuries). The manner in which a bone sample is constrained and manipulated when subjected to torsional testing can provide complication in physical testing, generally requiring potting of the bone. Consequently large sections of the sample are regularly isolated from torsional testing [166].

Compressive testing (as commonly observed in whole-bone CT-FE studies) is not normally favoured for the derivation of material behaviour due to the complex manner in which compressive failure occurs. In compression, the failure mode and even the derived material properties in sub-maximal testing are a consequence of both the material properties and the geometry of the tested sample [179]. The exhibition of buckling rather than compressive failure can lead to incorrect assumptions regarding the material properties of a sample. As a result, engineering material tests are more commonly undertaken in tension, and in torsion [137, 180], both of which display more linear load and failure characteristics for typical homogeneous materials.

Pin-jointed tension of homogeneous materials allows for the free orientation of the sample within test apparatus, reducing the chance of off-axis loading during testing. However, as a biomechanical test regimen, tension has seen the least investigation, with the exception of smaller material-based testing [72, 88]. Tension *in vivo* is more likely to provide ligament and soft tissue damage before the onset of bone damage, which may be a contributor to the rarity of this fracture type [103]. In addition the fracture is particularly hard to replicate ex-vivo which may be an additional factor for the scarcity of whole bone testing in tension.

3.7.3 Material Testing of Porcine Bone Samples

During the course of this thesis, new research into porcine bone material was produced [147]. This investigated the material properties of the cortex depending upon the location from which the sample was taken, and helped to determine the testing protocol used to measure the physical material properties of porcine bone in this study. The samples in this thesis were supplied from a single source, and consequently the values determined by Bonney et al. were used as a check to confirm that the values measured in this thesis represented the porcine population as a whole, and were not the product of a specific rearing or feeding pattern.

In addition to the inhomogeneity of bone material as a whole, the distribution of calcification and the structure of the material itself is also non-uniform. The highest level of irregularity in a given sample is observed within the trabecular bone of the epiphyses, where both the structure and the calcification of the material vary depending on location and role. When physically testing the samples in torsion in the laboratory, these regions were gripped, effectively isolating a large portion of the epiphyses. Correspondingly, to simplify material testing, and allow comparison with similar tests observed in previous literature, material tests were performed on mid-shaft cortical bone only.

As with trabecular bone, cortical bone is able to undertake *bone remodelling,* a process in which bone tissue is reabsorbed and new tissue is formed in its stead. This may occur as a result of fractures in the bone tissue, but is also shown to respond to mechanical stimuli through repeated loading *in vivo* and the onset of microdamage. In effect this means that identical bone samples from the same source can have varying material properties, not only from bone to bone, but also from differing sites upon the same bone [56]. This makes the prediction of the behavior of a single bone sample difficult without investigation of the calcification of the sample, and/or investigation of the material's behaviour during physical testing. One way to overcome this is to apply averaged figures from completed quantitative studies [84]. However, this is a significant simplification, and there is limited research regarding animal bone samples taken from the specific orientations considered during physical testing [147]. Additionally, testing using averaged values may not consider important physical differences between bone samples from different cohorts and backgrounds – particularly in animals, where the age of slaughter, feed, the weight of the animal and the manner in which the animal is reared can all have a significant impact on the bone and material characteristics. The anatomical position and role of the bone is also of importance, providing varying properties from region to region. An extreme example of this change in properties is given in the literature, where the increased bending strength of a cow's femur is compared to a fin whale's tympanic bulla (a bone located in the inner ear) [181].

Typically bone material can be demonstrated to exhibit linear elastic behavior before a distinct yield point. Consequently, the behavior of a whole bone under certain loading conditions can be shown to be linear (or close to), depending on the boundary conditions and loading regimens used for testing. As a result of this, and to aid simplicity in simulation, previous CT-FE studies almost exclusively use

linear material models for material mapping [37, 53]. Despite this prevalence, it was considered prudent to demonstrate, using appropriate laboratory testing, that porcine test samples could act in a linear manner before embarking on the use of linear material models in simulation. This important part of the validation processes, demonstrates that the simulated material behaviour matches that displayed physically.

To test the material properties and linearity of isolated bone material, physical material testing was undertaken through 3-point non-destructive bending tests of cortical sections of a selected number of femoral samples. This type of testing is defined by the application of force to the centre of a sample, whilst the extremes of the sample are supported by 'knife edges'. The knife-edges allow for the support of the sample piece, whilst permitting relative rotation with respect to the constraints. The test sample length was determined by the maximum length that could be extracted from the surface of diaphysis without excessive curvature (the curvature of the sample location can be seen in Figure 3.12). Inclusion of curvature adds unwanted complexity to the calculations used within the 3-point bend test and consequently the test sample length was specific to each individual bone sample used. Average sample length was approximately 84 mm, allowing a knife-edge supported exposed test section of approximately 80 mm. Force was applied by means of a knife edged cradle onto which calibrated weights were hung. Force was applied at the medial aspect of the upper face of the sample, at the midpoint of the distance between the two knife edges. Deflection was measured at the same point. Sections of cortex were removed from five femoral samples for the 3-point bend tests. Samples were cut from each femur sample using a high-speed, thin-bladed (< 0.5 mm) disc cutter, previously used for slicing and examining photoelastic samples. Water-cooling was employed throughout the cutting process to ensure that the temperature of the sample was not allowed to increase to a level that may have affected the Young's modulus. Despite this, the temperature during this process was not recorded, and it remains a potential limitation of sample cutting that the process of cutting may alter the mechanical properties of the sample piece. The width of the samples was determined by the geometry of the specific femur used (Figure 3.13). To simplify the test procedure, it was considered that the flattest section in all dimensions would be used and correspondingly slimmer bone samples provided narrower samples, whilst samples with a larger diaphysis diameter offered a reduced amount of circumferential curvature, and thus wider samples could be taken. Average sample width was in the region of 5-7 mm. Depth of the sample is determined by the thickness of the cortex, and consequently varies both from sample to sample, and also along the length of each individual sample. Each sample was cut at the point at which the mid-shaft bone joined the metaphyses, as this is the region in which the cortex thins considerably. The result of this sample selection was that thickness along the length of the specimen generally ranged between 2 and 4.5 mm. The samples were sanded on the interior surface to reduce the thinning effect, and to remove any less dense material from that may have contributed to the measured width but provided little additional material strength. All samples were cut from the anterior surface, as this displayed the least curvature along its length, allowing increased

sample lengths to be tested. Figure 3.13 shows a single sample and the results of physically testing two samples in bending.

(a)

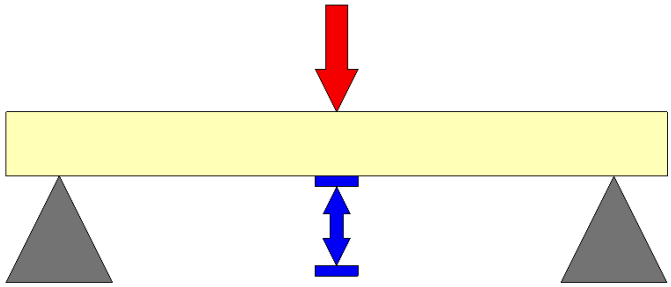

(b)

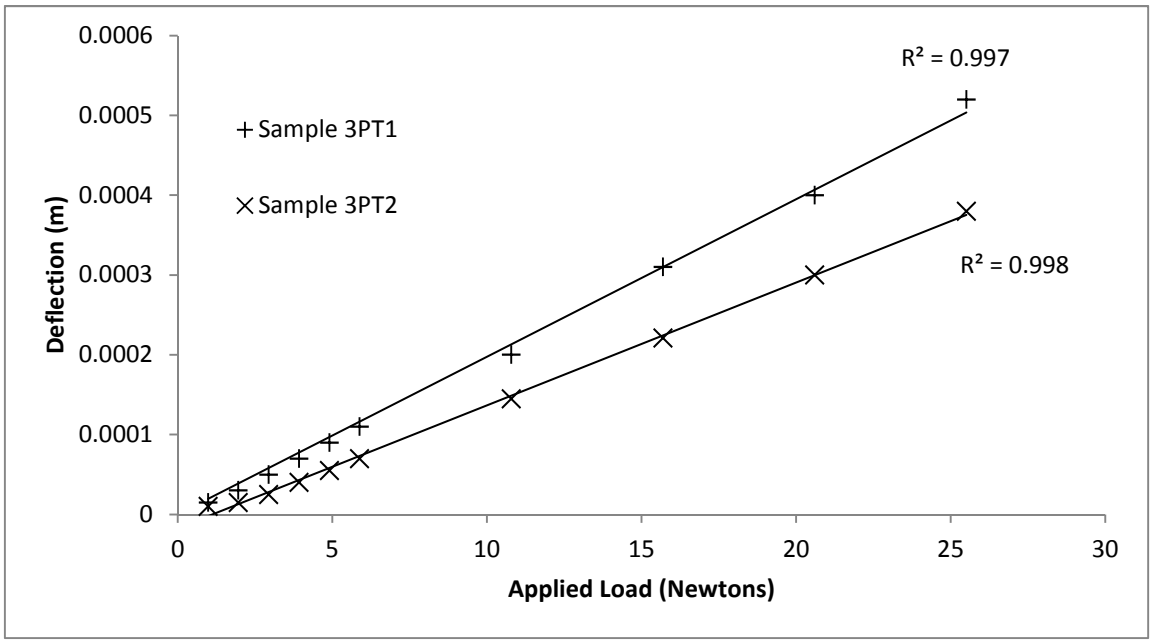

(c)

Fig. 3.13 (a,b&c). Photograph of a donor mid-shaft section of femur (a). Sketch (b) shows the general testing arrangement. The corresponding graph (c) details the results of the material testing performed on two of the samples and the linear regression performed to provide the slope for the constitutive material calculation.

Linear regression exercises performed upon the results obtained for the load-deflection curves obtained during testing showed strong linearity and fit ($R^2 > 0.99$) for all samples tested. Determination of Young's Modulus for bending using the load/deflection relationship is then possible, using the equation shown in *Eq. 3.1*. The relationship is determined for a simply supported beam (i.e

allowed to rotate at the supported ends), with length *L*, second moment of area *I*, and *S* (the maximum deflection) being recorded at the centre of the beam.

$$E = \frac{FL^3}{\mathrm{S48I}} \qquad 3.1$$

The average Young's Modulus for bending observed within testing was 17.9 +/- 1.9 GPa. Five samples in total were tested. Bonney found that for porcine samples as a whole, the average bending modulus was 17.4 +/- 1.1 GPa [147]. The results shown there exhibited higher bending modulus on the anterior face, but split the samples into two parts, one accommodating the proximal region, and one pertaining to the distal region. The proximal anterior sample in particular provided increased bending modulus results, returning a modulus in excess of 20 GPa. Splitting of the sample into proximal and distal sections was not investigated in the course of this study.

Results for the deflection in 3-point bend testing are plotted in Figure 3.13. It should be noted that a proportion of the variation in material properties may be due to error in the measurement of the dimensions of each of the tested samples. Whilst the length and width of the samples could be controlled with reasonable accuracy, the depth of the sample is dependent on cortical thickness, varying along the sample's length, and consequently proving difficult to measure accurately at all points. Additionally, despite attempts to mitigate the effect, the samples contain an element of curvature along their length, which will have an effect on the loading regime. Explanation of these factors is omitted from Bonney's results, which may partly explain the variance in their obtained results, and the differences between the testing they produced, and the results recorded here.

3.8 Simulated Young's modulus

With effectively linear results in the initial material-only testing, the use of continuum elements and a linear simulation was considered appropriate for investigation in porcine simulation. Breaking down a test sample into an array of linear material models is a technique commonly used in CT-FE studies, and provides an excellent methodology in mapping properties to larger samples [18, 20, 27, 74]. The mapping procedure has been considered recently by both Simpleware (the manufacturers of the masking and meshing software used in this study) and Materialise, whose 'Mimics' software provides a similar service. Both of these software developers include a mapping algorithm within their modelling software [53, 82, 182]. The use of multi-part linear material models allows the structure to be constructed so that the model is effectively inhomogeneous, with varying Young's modulus depending upon location and observed calcification/density, but with the model ultimately displaying a linear response to loading.

The general relationship that forms the basis of the material mapping algorithms is based upon the correlation between the levels of attenuation (greyscale value) within the source CT image, and the minerilisation, apparent density and thus Young's modulus of the item being imaged. The greyscale values used for the calculation are obtained from the source images, and allow for the automated adjustment of Young's modulus mapped onto the model. The relationship between greyscale value and Young's Modulus has been under some investigation since the first use of the technique, with subject-specific studies providing widely ranging material relationships depending on location, bone type etc. [53, 74].

3.8.1 Determining Young's modulus from Greyscale Values

The determination of Young's modulus from CT images, and specifically the assignment of Young's modulus, is based upon two relationships. The first of which converts the greyscale value (commonly referred to as CT number, and synonymous with Hounsfield Units) into an apparent bone mineral density (BMD). Hounsfield Units (HU) are units used to standardise the attenuation response of a scan, aligning the data to a scale in which water is assigned a value of 0 HU and air (such as that surrounding the sample in these CT images) is assigned a value of –1000 HU. The second relationship (commonly known as a density-elasticity relationship) converts this apparent density into a value for Young's modulus.

3.8.2 Greyscale to Apparent Density and Phantom Calibration

The greyscale/density relationship has been shown to be linear [9, 77, 143], and is commonly used by clinicians to determine the density of a bone sample under review, and consequently provide an estimation of a sample's material quality. Bone mineral density in general can be clinically assessed in a number of different ways including the use of CT. On samples where exposure is of reduced concern (such as the animal samples used in this study) CT provides an excellent medium for BMD analysis, offering true geometrical reflection of the sample, ensuring that the values obtained can be determined from a precise region of the bone sample. The capability of this is further enhanced through the ability of the CT scan to map the density through the volume of the scan, allowing accurate BMD portrayal throughout the entire depth of the bone structure.

The greyscale/density relationship can be calculated using generic values for the apparent density of bone, water or air, but in order to be examined accurately, a known quantity should be included within the scanner during acquisition of the CT images. In this thesis this is provided in the form of a calibration phantom, which is a device containing a selection of materials, each of which have a known density or provide a known greyscale response in the images produced from the scan. The phantom is scanned along with the item of interest so that the user can determine the level of attenuation produced across the phantom materials, and compare it to the subject item being scanned.

Calibration phantoms are included as a matter of course in the majority of CT scans, and provide a means for a radiologist to rapidly compare a level of attenuation to a known value, such that they can quickly gauge the density of a scanned item. The phantom used in the study was provided by Mindways [171] and included five solidified materials in a slightly curved pattern. These five materials were pre-selected by the manufacturer to provide the attenuation response of bodily materials of various compositions such as bone, fat, etc.

This phantom differs from others used in some CT-FE studies as all five reference mediums are of solid rather than liquid composition, incorporating the use of varying solutions of Dipotassium Hydrogen Phosphate (K_2HPO_4) (Figure 3.14). The use of such solidified solutions requires an additional calculation procedure to determine the apparent density of an object, but has no bearing on the ultimate response or accuracy of the phantom.

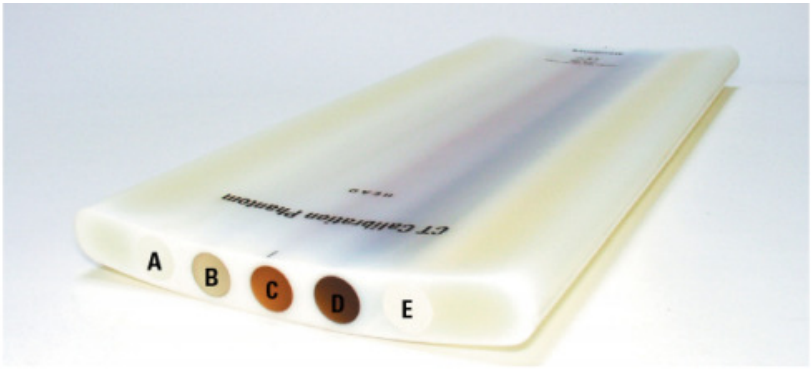

Typical Composition of Various Solid Reference Materials		
Reference Rod	Eq. H_20 density (mg/cc)	Eq. K_2HPO_4 density (mg/cc)
A	1012.2 +/- 2.3	-51.8 +/- 0.1
B	1057.0 +/- 1.9	-53.4 +/- 0.1
C	1103.6 +/- 1.7	58.9 +/- 0.1
D	1119.5 +/- 1.8	157.0 +/- 0.3
E	923.2 +/- 2.1	375.8 +/- 0.9

Figure 3.14 The calibration phantom used during scanning and the composition of the reference materials.

The calibration process is recalculated following each independent scan, and follows the following principles (Table 3.3):

- The average greyscale value is recorded from the CT data for each chamber within the calibration phantom.
- This figure is converted to a ‘pixel’ value by adding 1000.
- The equivalent water density of each chamber is subtracted from the recorded pixel value.

- *Eq.* K_2HPO_4 density is then plotted against the Pixel Value - *Eq.* H_2O density value, producing a straight line relationship (Figure 3.15).
- The equation of the line is recorded, and correction factors provided by the pgantom manufacturer are used to account for the amount of liquid displaced by the K_2HPO_4 in the water, and to normalize with respect to the density of water at room temperature (Eq. 3.2- 3.4)
- The new values are then used to calculate the equivalent BMD K_2HPO_4 (mg/cm) using Eq. 3.5
- Table 3.3, can then be recalculated proving a new set of values (Table 3.4)
- Relationships from literature can then be employed to convert the equivalent BMD K_2HPO_4 value to an apparent BMD value for bone (Eq. 3.6, Table 3.2 column 3) which can then be re-plotted against the original greyscale value for each phantom chamber, and therefore extrapolated across the mask to map density values across a model.(Figure 3.16) [143].

Table 3.3 The first process in the calibration procedure (arbitrary values are shown for greyscale to demonstrate the process)

Chamber Number	**Image Greyscale Vale**	**Eq. K_2HPO_4 density (mg/cc)**	**Pixel Values (GS + 1000)**	**Eq. H_2O density (mg/cc)**	**Pixel Value - Eq. H_2O density (mg/cc)**
A	**-125**	-51.8	875	1012.2	-137.2
B	**-75**	-53.4	925	1057	-132
C	**180**	58.9	1180	1103.6	76.4
D	**375**	157	1375	1119.5	255.5
E	**600**	375.8	1600	923.2	676.8

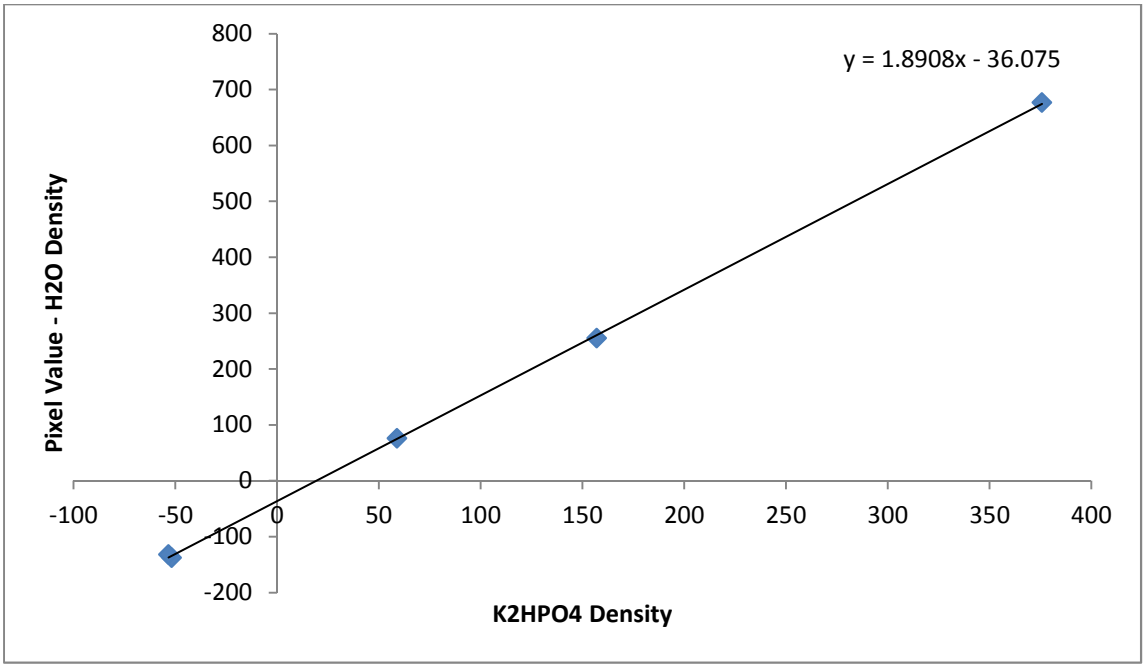

Figure 3.15 Eq. K_2HPO_4 density plotted against the Pixel Value - $Eq.\ H_2O$ density value, producing a straight line relationship for calibration.

$$y = mx + c \text{ (measured from graph)} \quad 3.2$$

$$n = m - 0.2174 \text{ (correction to account for } K_2HPO_4 \text{ proportion)} \quad 3.3$$

$$d = c + 999.6 \text{ (normalized with respect to } H_2O \text{ density} \quad 3.4$$

$$\rho_{BMDequivk2} = \frac{(Px-d)}{n} \quad 3.5$$

$$\rho_{BMD} = 0.0011\rho_{K_2HPO_4} + 0.039 \quad 3.6$$

Table 3.4 The second process in the calibration procedure, wherein the BMD equivalent K_2HPO_4 is listed with respect to greyscale, and additional relationships are employed to convert this to apparent BMD of bone.

Letter	GS	*BMD Eq.* K_2HPO_4 density	Apparent BMD (Bone)
A	-125	-52.9013	-0.0192
B	-75	-23.0220	0.0137
C	180	129.3624	0.1813
D	375	245.8916	0.3095
E	600	380.3484	0.4574

The relationship between greyscale value and apparent density has been under investigation for some time, with a number of relationships pertaining to specific simulation applications and different bone types [77, 183]. Relationships that link apparent BMD directly with CT number have also been derived in previous literature [67, 166]. Rho et al. provided relationships for the apparent density of a number of human bone sites, including the proximal and distal femur [67]. The relationships plotted in Figure 3.16 were originally devolved for equine samples [143] for human samples [68], and through direct mapping without the use of calibration phantom [67]. The greyscale value of each of the five reference materials is converted into an apparent density in g/cm³. In the plot, the linear relationship connecting the phantom data points is extrapolated to a value of GS = 1900, which represents an estimate of the expected greyscale value for cortical bone. The plot demonstrates that the variation between the three relationships calculated from porcine phantom scanning and Rho's direct mapping of greyscale values extends to as much as 8.2% at the uppermost greyscale value in a given source image.

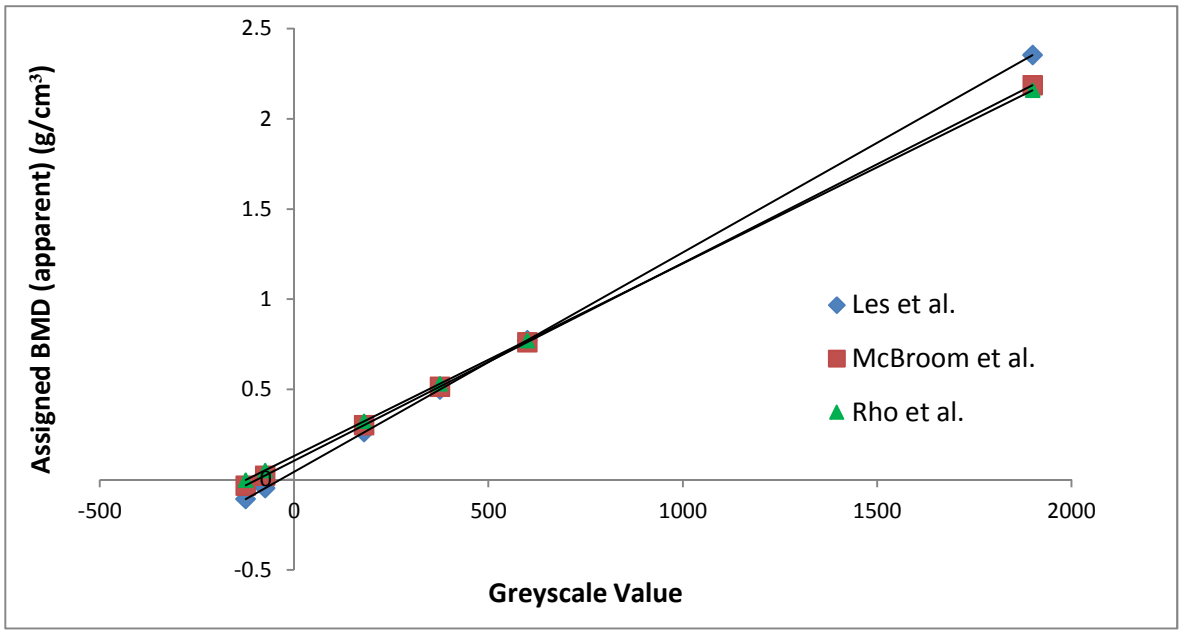

Figure 3.16. Shows the Greyscale/BMD relationship for the five reference materials contained within the calibration phantom (GS values < 1000) and one predicted value using a linear relationship (GS = 1900).

Examining scan data from a single sample demonstrates greyscale values of approximately 1800 +/- 200 for cortical porcine bone and 500 +/- 250 within the trabecular regions. Consequently, using a sample relationship, such as that determined by McBroom et al. provides equivalent BMDs of between 1.85 to 2.3 and 0.38 to 0.93 g/cm³ respectively [68].

The importance of accurately assigning density to a model should not be underestimated, as this value is used to determine the Young's modulus [37, 70, 184]. There are small changes in the manner in which each sample is scanned and the dosage and calibration of the CT scanner, which may affect the outputted apparent BMD between scans. Consequently, within this thesis, for each geometrical model created, the relationship between greyscale value and material property was recalculated.

An example of pre and post calibration is shown in Figure 3.17. Here, two samples groups (approximately 15 samples in each group) are calibrated, and the distribution of the mean greyscale value within each masked model is shown. As can be seen, the median of each group is more closely aligned, as is the interquartile range. The extremities of the whisker plots (representing the most and least dense samples in each group) remain similar to their pre-calibration values.

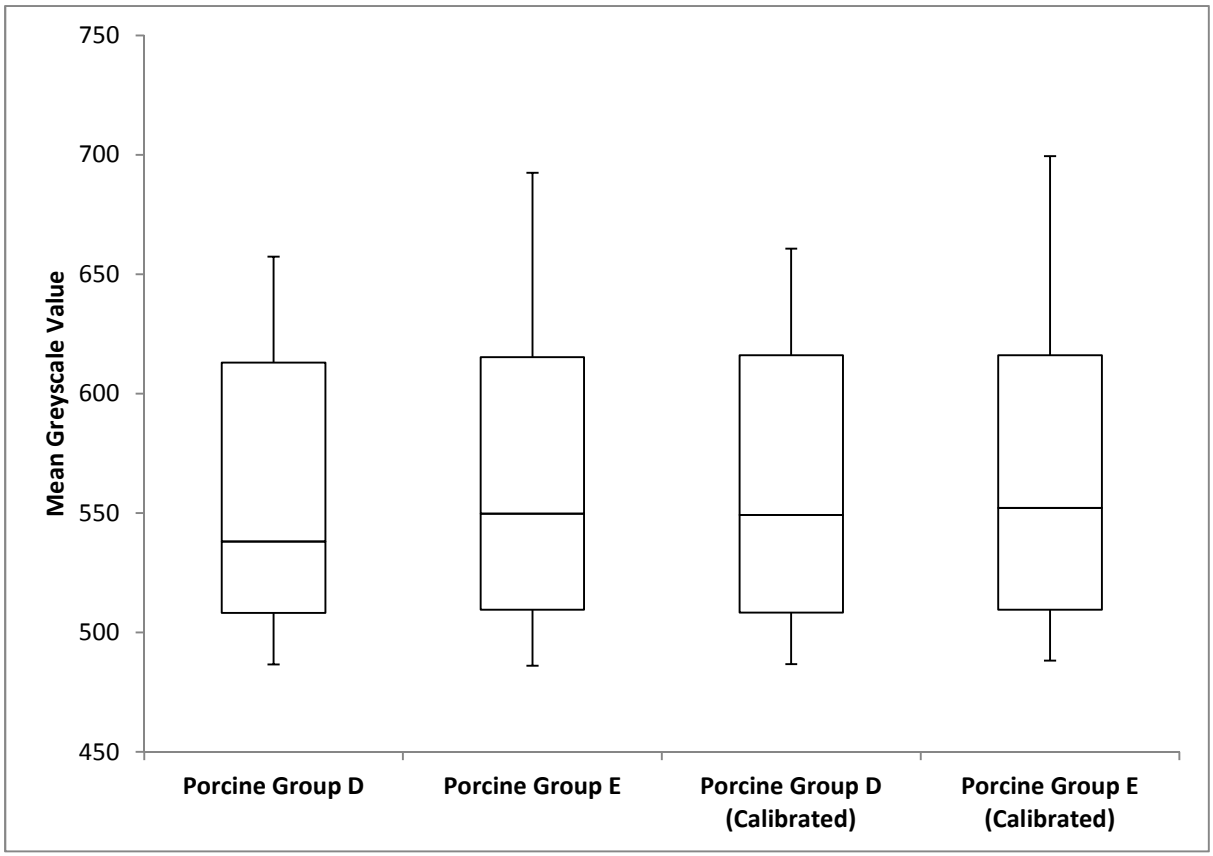

Figure 3.17 Shows the effect of CT calibration on the median and interquartile range of two batches of scanned samples (approximately 15 samples per group.

An important consideration when mapping bone mineral density is the specific type of density being measured. There are four main types of density measurement listed within the literature; these are apparent density (ρ_{app}), ash density (ρ_{ash}), dry density (ρ_{dry}) and CT density (ρ_{CT}). The determination technique for each differs slightly, but generally is provided through a calculation of the physical weight of the sample divided by its volume. Ash density is determined by reducing the sample to its ash constituents through incineration; dry density similarly involves the removal of moisture through

heating; and finally apparent density refers to the bones wet weight as would be expected *in vivo*, divided by the bulk volume. CT density refers to the density mapped to the bone volume in a methodology as shown in Figure 3.16. The majority of elasticity-density relationships use apparent density as the reference density. Schileo et al showed that the ρ_{ash} to ρ_{app} ratio is constant at a figure of 0.6, and also demonstrated that ρ_{CT} and ρ_{ash} are essentially interchangeable if the correct ρ_{CT} determination is utilised [37, 45]. In this thesis, care was taken throughout testing to ensure that the appropriate density consideration was taken when investigating the elasticity-density relationships.

3.8.3 Apparent Density to Young's Modulus

Following the determination of the apparent bone mineral density, a second relationship can be employed to determine the Young's modulus as attributed to each density value. This density-elasticity relationship has been extensively investigated, culminating in a review paper in 2008 [19], in which density-elasticity relationships from 23 different studies were analysed (it should be noted that many are represented from the same author). The relationships and studies varied in output, including linear models for cortical bone, non-linear relationships for cortical bone, trabecular bone, and relationships capable of mapping entire bone structures (both bone types). The relationships were generally derived via physical measurement of the deflection of a given sample under load, which are then referred to the apparent density of the same sample, as measured during the CT scan.

Although relationships have been determined that define the segregation between cortex and trabecular bone samples, very few results have been published pertaining to the behaviour of developing bone samples, or those of animal samples. Consequently the selection of an appropriate relationship for this study was determined as part of this thesis via a sub-study of a number of relationships that were initially deemed as appropriate for mapping porcine bone. Figure 3.18 shows the distribution of greyscale values across two sections of the bone mask.

As can be seen in the images, the cortical bone segment demonstrates independent distributions of high greyscale values at the cortices, whilst the trabecular section demonstrates a continuous mass of lower greyscale value voxels. In addition to recording values for bone material density, Figure 3.18 demonstrates regions in which a negative value is achieved for the greyscale value of a pixel region. This is normal and acceptable, and relates to the manner in which the greyscale values relate to Hounsfield Units.

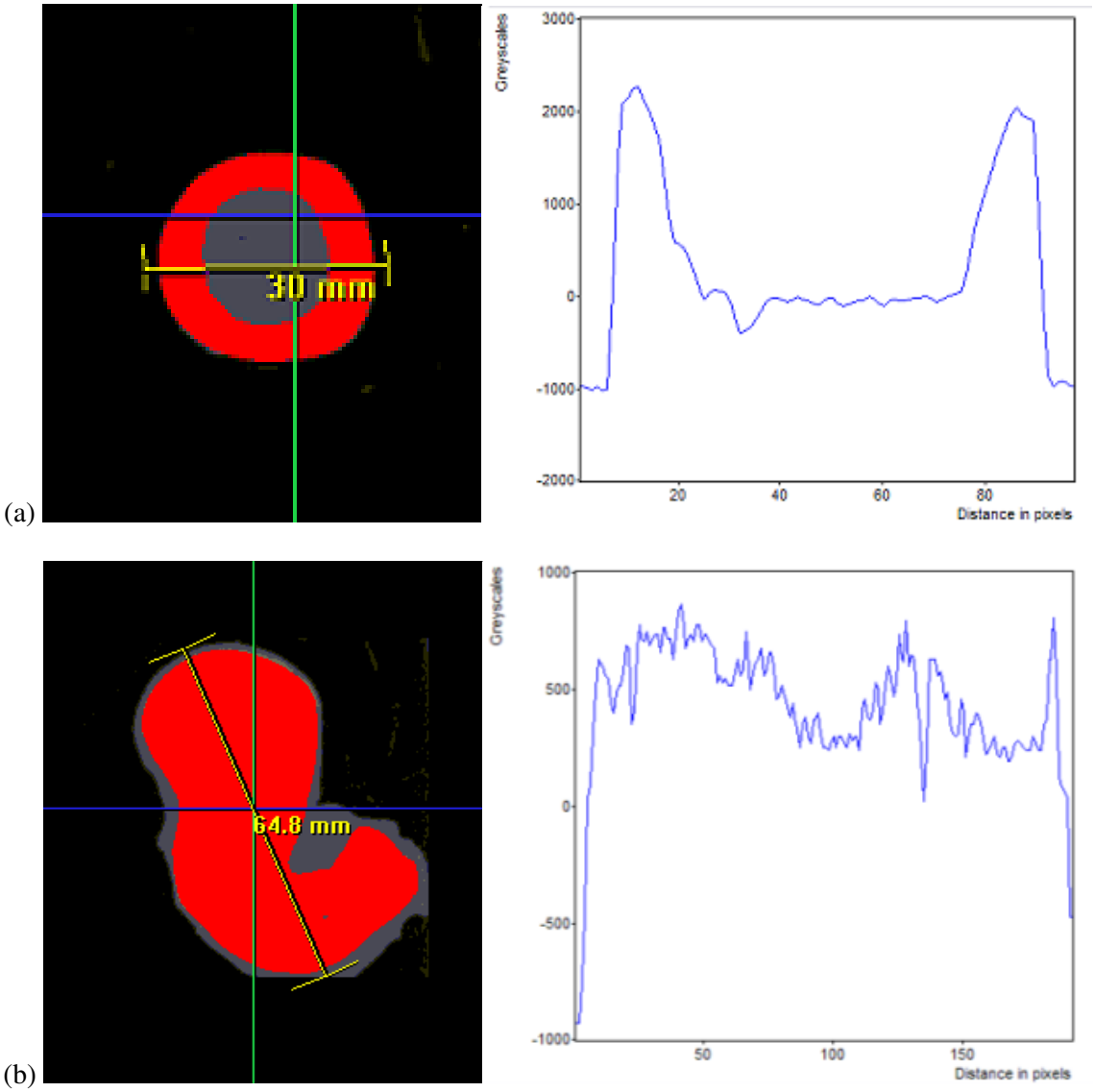

Figure 3.18. Screen captures from the masking software demonstrate the distribution of greyscale values across slices of bone mask in the mid-shaft cortical (a), and proximal trabecular (b) regions.

3.9 Mapping Simulated Porcine Bone Properties

In order to select a suitable density-elasticity relationship for the simulation of *porcine* bone from previous literature, a review of the physical material data on porcine bone was undertaken. The figures obtained (as shown in section 3.4.2) were then correlated with the figures obtained for apparent BMD for cortical porcine samples (as shown in Figure 3.19, 1.75 g/cm³ to 2.3 g/cm³). This provides a 'window' of ideal results, allowing for a systematic review of each of the 23 density-elasticity relationships for *human* samples as described in the review paper produced by Helgason et al. [74] to determine if any were appropriate for porcine mapping on a density-elasticity basis.

The review provided four relationships that were capable of mapping suitable results within the range expected for porcine cortical bone. These are tabulated in table 3.4, and were provided by Keller et al., [75], Morgan et al. [72] Lotz et al. [71], Carter and Hayes [185] and Snyder et al. [73].

Table 3.5. The four relationships selected for further investigation in material mapping following the correct assignment of Young's modulus at the appropriate apparent bone mineral density.

Paper / Author	Relationship
Mechanical Properties of Trabecular Bone from the Proximal Femur: A Quantitative CT Study, Lotz et al [71]	$E = -13.43 + 14.261\rho_{app}$
Trabecular bone modulus–density relationships depend on anatomic site, Morgan et al. [72]	$E = 6.850\rho_{app}^{1.49}$
Estimation of mechanical properties of cortical bone by computed tomography, Snyder et al [73]	$E = 3.891\rho_{app}^{2.39}$
Predicting the compressive mechanical behaviour of bone, Keller et al [75]	$E = 10.5\rho_{ash}^{2.57}$
The Compressive Behaviour of Bone as a Two Phase Porous Structure, Carter and Hayes [185]	$E = 3.79\dot{\varepsilon}^{0.06}\rho_{app}^{3}$

The manner in which Young's modulus is mapped to the final Finite Element model is a direct response to the relationship used, with higher power equations providing an increased rising rate at higher apparent greyscale/BMD values. The relationships are thus more easily viewed graphically, as shown in Figure 3.18.

The linear relationship shown in this Figure was provided by Lotz et al. and was derived specifically for use within cortical samples [71]. Unfortunately, mapping of isolated cortex sections in porcine modelling demonstrated significant occurrence of lower greyscale values within the mask. These greyscale regions predict apparent BMD values that are too low for Lotz's relationship, culminating in the prediction of negative values for Young's modulus, and consequently rendering the relationship unable to predict the material response of these cropped samples.

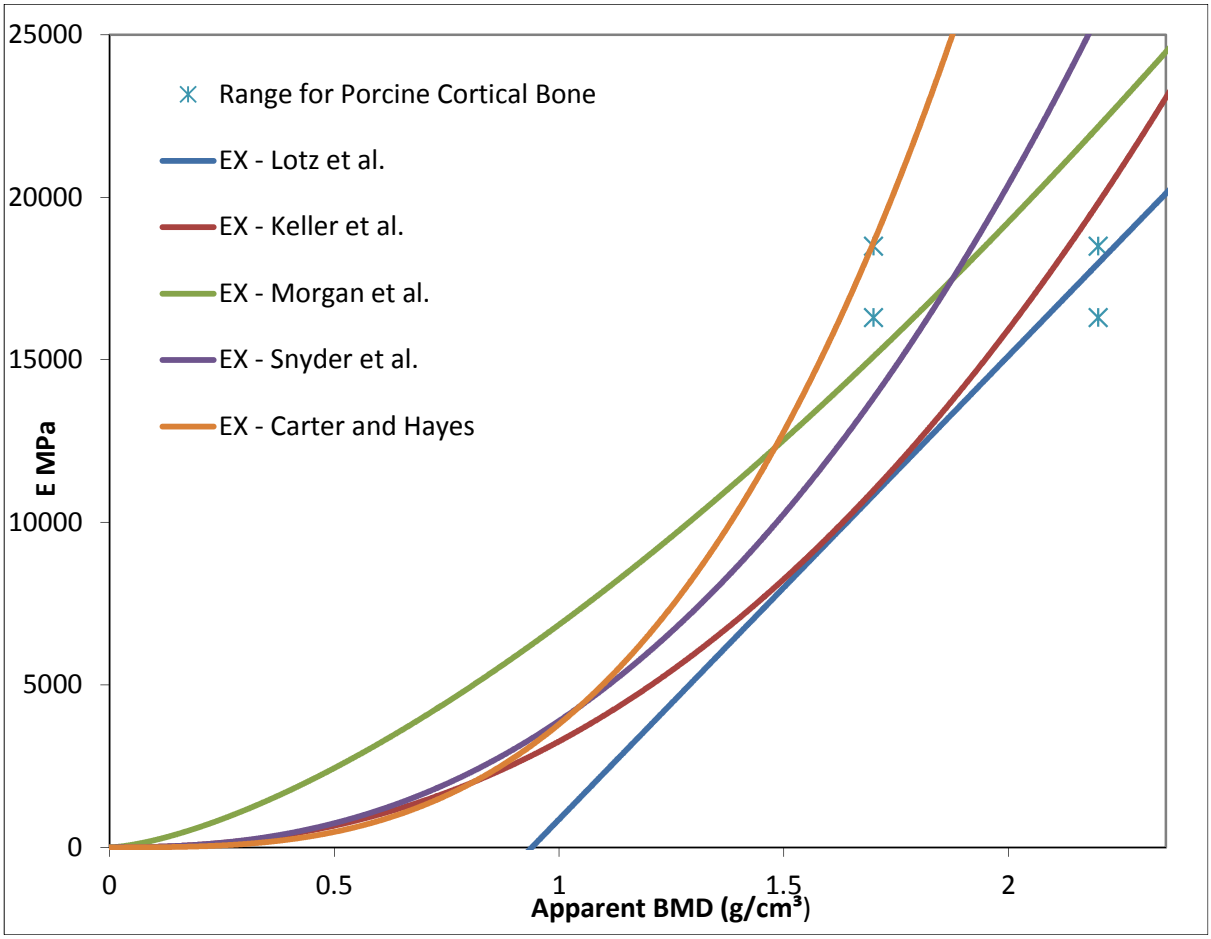

Figure 3.19. The relationship between apparent bone mineral density and elastic modulus for the four relationships that meet the criteria for mapping porcine cortical bone. The boxed region demonstrates the range of values expected for both apparent BMD (as calculated through review of greyscale values) and elastic modulus of cortical porcine bone (as published by Bonney et al. [147]).

To obtain further information regarding the material property mapping, each relationship was mapped to a bone sample, which was cropped to simulate the diaphysis only, coarsely meshed and exported into the Finite Element solver. Selecting each relationship and exporting into the solver identifies each of the material property markers that are exported for use within the Finite Element model. These individual markers denote the intervals at which Young's modulus is applied to the model, and contain data referring to the density, Poisson's ratio and Young's modulus that are attributed to each of the individual elements. Figure 3.19. plots this relationship for the cropped section of bone sample, showing the same rising rate material definition as defined in Figure 3.19, but plotted with reference to the marker number that is exported within the assigned mask. This provides a comparison of the occurrence of each of the material markers in terms of a percentage of the elements included within the entire model.

The model exported for this example utilises a relatively coarse mesh, limited to approximately 300,000 elements. Additionally, for the purpose of this demonstration, a relatively small number of material markers were exported; in this case 146 markers. For the general simulation procedure, this was increased to 300 individual markers, reducing the material property gradient between neighbouring elements as a result of the reduced change in each interval.

As can be seen within the Figure 3.20, the presence of markers 0 to 40 is significantly higher than the other material markers. This marker group pertains to an average BMD achieved within trabecular bone, consequently demonstrating that the occurrence of elements in this region is significantly higher than in pure cortical bone. The effect demonstrated is in keeping with the masking process where, despite cropping the diaphysis more elements, by volume, are assigned to the trabecular regions of the bone samples at the extremities of the cropped sample.

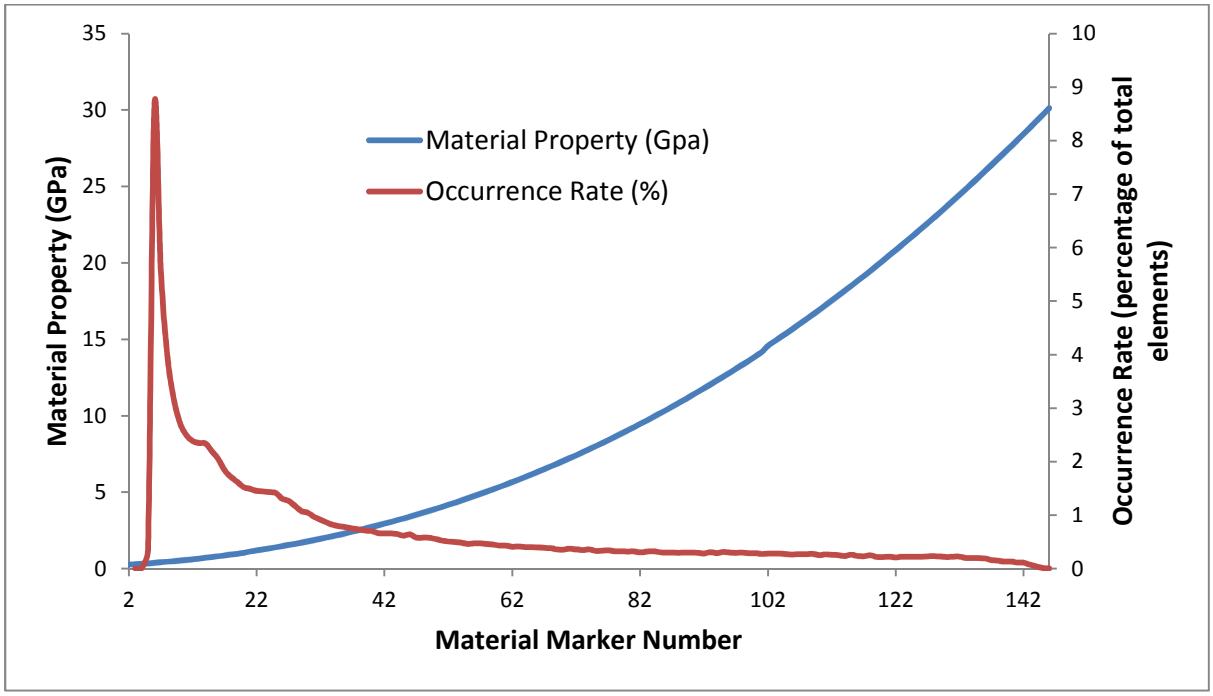

Figure 3.20. The exported material property (primary vertical axis) of each exported material marker, and the occurrence rate (secondary vertical axis).

3.9.1 Anisotropy

A single Poisson's Ratio was assigned throughout the completed mask. The anisotropy of bone is therefore effectively ignored which, similar to the selection of linear material models, may ultimately provide a limitation in testing. A significant number of studies have demonstrated changes in Poisson's Ratio depending on the tested axis and sample location [186]; however, a key consideration is that no relationship has been determined that links the change of Poisson's Ratio with the apparent

BMD. Consequently, the single figure approach is commonly undertaken in CT-FE studies, with the figure of 0.3 chosen most regularly (as used within this study) [20, 70]. It is accepted that this is ultimately a limitation of the modelling procedure, and may be a contributor to the measured inaccuracy of the modelling procedure as a whole; however, its common use in CT-FE studies that observe accurate results suggests that its effect on the simulation results may ultimately be small.

3.10 Testing the Material Mapping Relationship

The high occurrence of low-density elements within the bone mask for an apparently isolated cortex shown in Figure 3.20 demonstrated that more elements (by number) occurred within the material marker numbers that had a Young's Modulus that was consistent with that expected for trabecular bone. To confirm if this was appropriate, and that the sample would perform correctly in simulation, an *in-silico* test was devised to determine if the material mapping process could obtain loading response similar to that observed during physical testing. To match the physical testing, an 8.3 x 2.9 x 56.1 mm sample from the anterior cortical section of a sample was isolated.

The isolated section was masked and had Young's modulus applied using the relationship determined by McBroom et al. for greyscale-density conversions. Following this, the relationships in Figure 3.17 were used to determine the elasticity mapping. Smoothing of the model was not undertaken, to preserve the sharp edges created during the cutting of the physical samples, and to ensure that the model retained the dimensions required. The model was exported using fine meshing, creating approximately 20,000 elements for the 56 mm sample (Figure 3.21).

During the course of this thesis, the software developers continually introduced revisions, which were subsequently released to academic and professional researchers. Changes included further visualization options, allowing the automated mapping of Young's modulus to be demonstrated visually, providing a means to rapidly check the material distribution across a sample. The visualization of Young's modulus can be seen in Figure 3.20, which shows significant variation of the attributed Young's modulus, despite this being a selected sample of isolated and (theoretically) all-cortical bone.

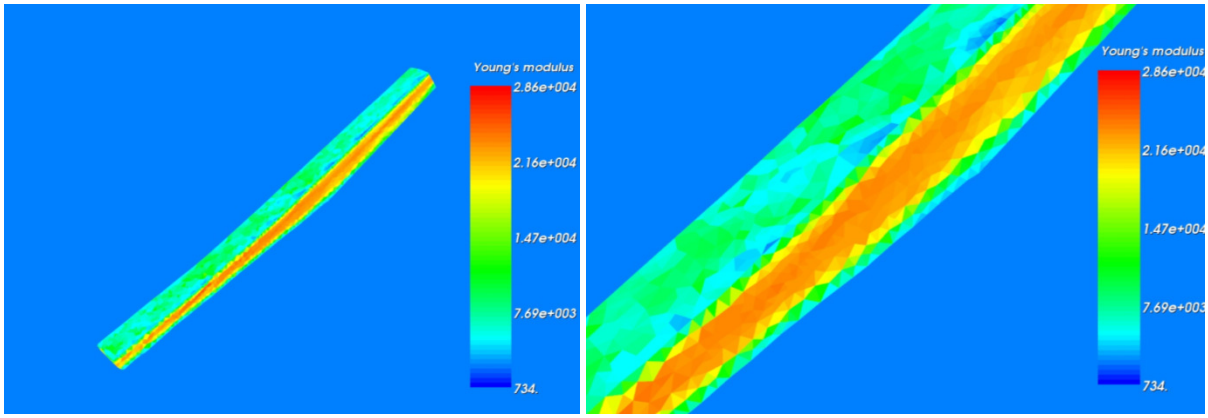

Figure 3.21. Screen captures from the masking software demonstrate the distribution of Young's modulus across the volume of the cortical sample piece.

The maximum attributed value for a single element using the relationship proposed by Morgan et al. is 27.1 GPa (the values in the screen capture are in MPa), however the majority of the interior cortex section is defined to be in the region of 20 – 26 GPa. This is over and above the values from previous literature; however, it should be noted that those values are derived from testing the entire length of a sample and, in the case of non-uniform materials, must be summed to provide an averaged Young's modulus for the sample as a whole. Taking the volume-weighted average value with respect to all of the elements in the sample mask gives an average assigned value of 15.71 GPa, which is close to (although ultimately *lower)* than the value determined in physical testing.

Re-mapping the Young's modulus using the linear relationship provided by Lotz et al. demonstrates the manner in which this relationship is unable to appropriately map low-density elements. Despite the sample pertaining to isolated cortex only, values below 0 are demonstrated for assigned Young's modulus below material marker 42 as shown in Figure 3.22. This relationship was therefore excluded from further comparison. The relationships detailed by Keller et al. and Snyder et al. provided volume-weighted material averages of 15.5 and 18.6 GPa respectively.

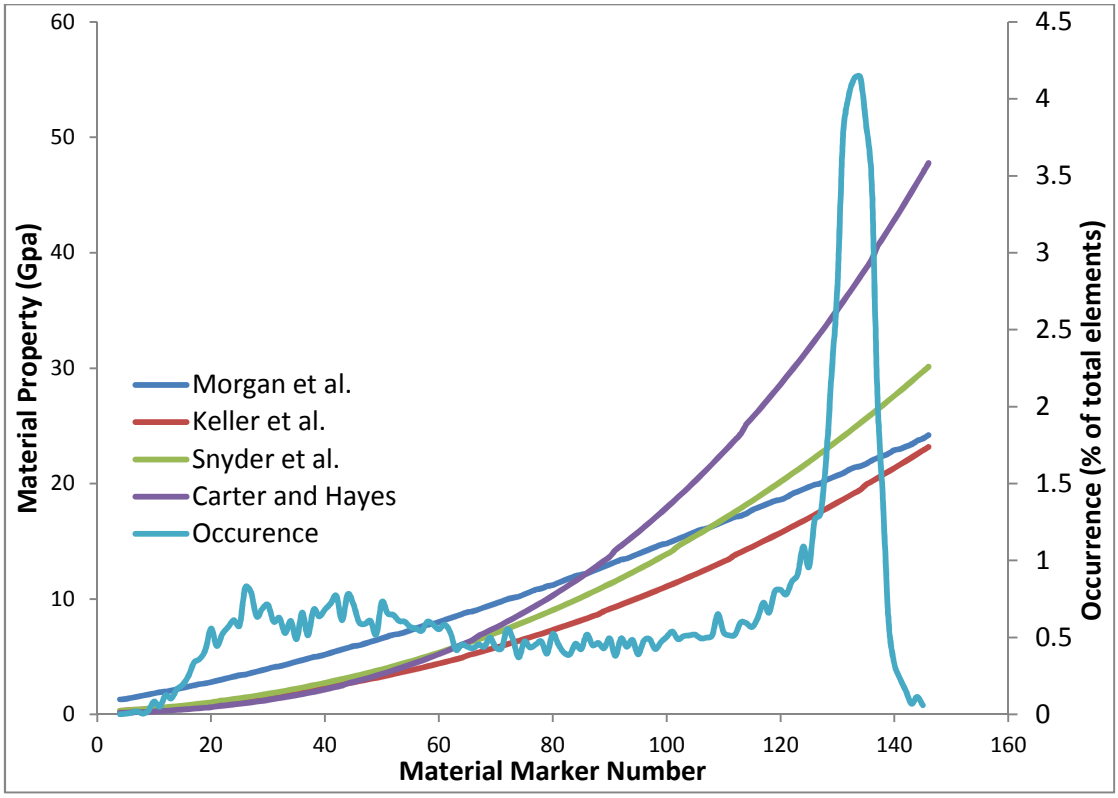

Figure 3.22. The chart above plots the material relationships that were considered in small sample testing. The relationships are overlaid over the occurrence rate of the material marker on the basis of percentage of all elements within the meshed sample of all-cortical bone.

The geometry of the bone sample, the meshing protocol and the distribution of greyscale values within the source image were all maintained throughout this test. The use of linear material models means that the accuracy of the results of matching the three-point bend tests responds directly to the average assigned Young's modulus in the Finite Element model. On this basis, the 'best' relationship in testing was provided by Snyder et al., which produced a stiffness response closest to the average found in physical testing. With the exception of the relationship provided by Lotz et al, all relationships were within 14% of the average Young's modulus and within 3% of the range derived in physical testing. The potential applicability of each of the relationships is a key result in the testing process, and is an early indicator that the material mapping relationships defined for human bone may be appropriate for mapping porcine samples [46, 70].

3.11 Limitations of Material Mapping

Despite high levels of investigation and prevalent use in computed tomography-based Finite Element studies, material mapping has a number of limitations that may affect the observed accuracy. These are inherent limitations of the general CT-FE process, and are discussed below.

3.11.1 Partial Volume Effect and Beam Hardening

Partial volumes provide a significant impact in all three-dimensional medical imagery. The partial volume issue is compounded when assigning Young's modulus due to the manner in which the mapping refers back to the source image to determine the apparent density from the greyscale values. The general effect is a consequence of the spatial resolution of the scanner hardware, and the image processing software. Essentially, all digital images are broken down into a grid of pixels in two dimensions, or an array of voxels in three dimensions, each of which has a finite edge length. If the reference item being scanned inhibits curvature, or has an angled boundary, then a single voxel may be required to cross this boundary. The greyscale from one side of the boundary to the other is likely to have a changing value and thus that voxel returns an average greyscale across the two sides of the boundary. The effect can be described neatly via a two dimensional histogram, (Figure 3.23) in which segregated averaged bars produce stepped averaged intervals, whilst the 'true' result in this case show a curved surface. The accuracy in terms of matching the curved result is a factor of the spatial resolution, which in this analogy is the width of the selected bars, and in CT-FE is the voxel resolution.

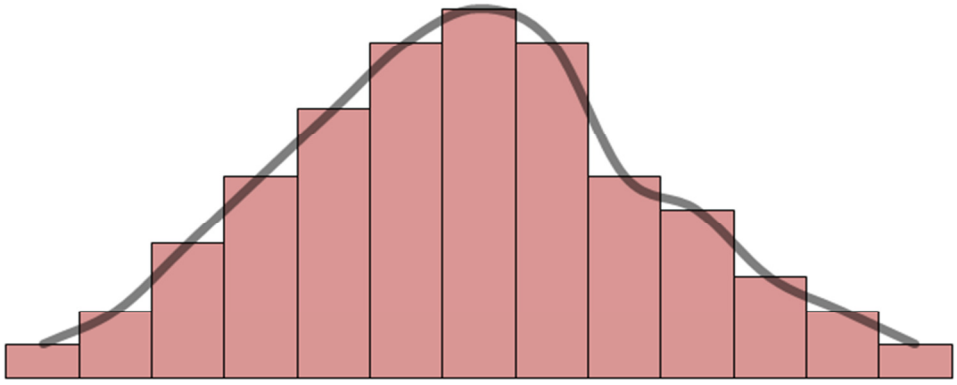

Figure 3.23. The sketched histogram demonstrates the effect of a given spatial arrangement (shown by the smoothed line) and the assigned averaged assessment of this geometry attributed via discrete intervals.

The partial volume effect is intensified further due to the meshing protocol. The issues with resolution are compounded by re-meshing the mask into discrete elements, which are not limited to size of the original voxel and are often large enough to cross numerous voxel boundaries. As the material mapping protocol requires a single material value for each element, coarser meshes crossing a number of voxel boundaries, provide an averaged material property for the region, rather than a specific result for each individual voxel. Figure 3.20 depicted a lower Young's modulus assigned at the surface, as the CT numbers assigned to the external voxels are essentially averaged results from a combination of the high positive values at the bone edge and the high negative values of the air surrounding it.

The partial volume effect is further complicated as a result of beam hardening. As each object is scanned from all sides in the rotating scanner, the central aspect of the item is imaged more regularly than the external aspects, providing a greater attenuation response. This is generally mitigated through the use of circular filters. The effect of this is the production of images for cortex in which the brightest greyscale values are observed at the wall centre (Figure 3.24).

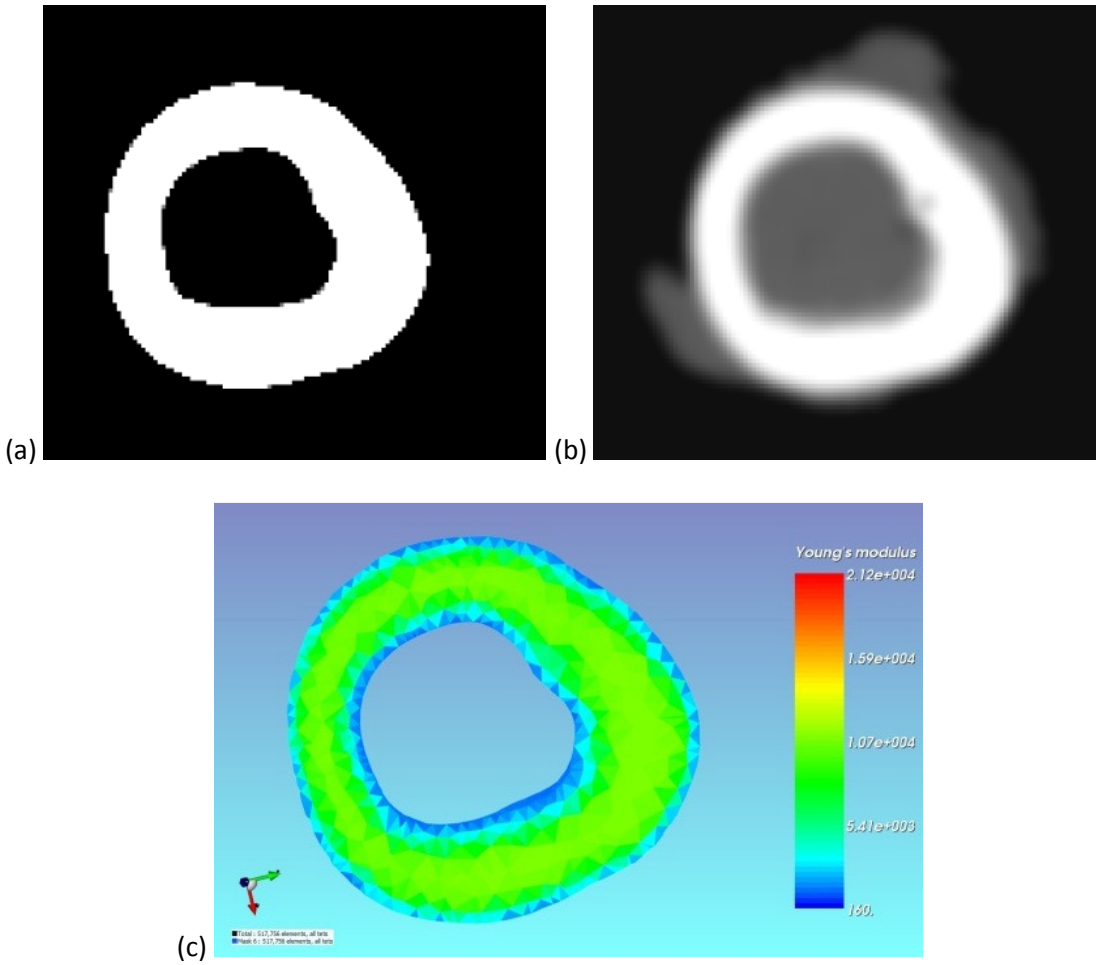

Figure 3.24 (a-c). The effect of changing the contrast to observe changing greyscale values across the bone sample interior (a&b), and the effect of partial volumes and X-ray penetration on the assigned Young's modulus (c).

Figure 3.24 shows the same section of cortex with varying contrast effects to highlight the pixel definition. In image (a) all bone material is contrasted to a high level, allowing the observation of the 'true' geometry of the bone. This is the region that will be thresholded to depict the three-dimensional mask. The image represents the correct geometry of the bone, such that the dimensions of this section are the same as the original sample. Image (b) shows the true greyscale values contained within the source image for this section. As can be seen there is an amount of soft tissue that will be de-selected through thresholding; however, there is also a variation in the intensity and greyscale results obtained

for the masked area shown in image (a). The gradient rises from external edge to the central wall, with the pixels becoming progressively brighter. Image (c) shows the manner in which the mapping protocol accommodates this effect. The outer edges are assigned a lower value due to the effects of partial volumes and X-ray penetration. The material within the cortical wall shows a gradient of increasing assigned Young's modulus towards the centre, at which point the apparent density is higher.

3.11.2 Material Gradient

The 'material gradient' observed within the Finite Element model is a product of the material mapping protocol, partial volume and X-ray penetration effects described above. The gradient itself refers to the changing values of the Young's modulus mapped to neighbouring elements, and can lead to errors in results analysis. In a similar way to an unrefined mesh losing resolution as it takes an average result over too large an area, a smaller number of material numbers will provide larger intervals between material changes, reducing the effectiveness of the mapping protocol. As such, material mapping should be defined to allow as many material markers as possible, such that each individual element is provided with a material number that suits its apparent density.

The effect can be minimised by increasing the number of material markers and accurate thresholding, providing that geometrical accuracy is retained. Figure 3.25 shows the manner in which the material mapping is altered through re-thresholding, with the model in image (b) excluding the low material property elements as defined via dark blue contours in image (a). The effects of X-ray penetration remain visible, and the mask's wall thickness is now reduced (particularly noticeable in the upper right portion of the image). The effect of this wall thickness reduction and any general geometry changes must be carefully observed to ensure that geometrical accuracy is retained in testing.

(a) 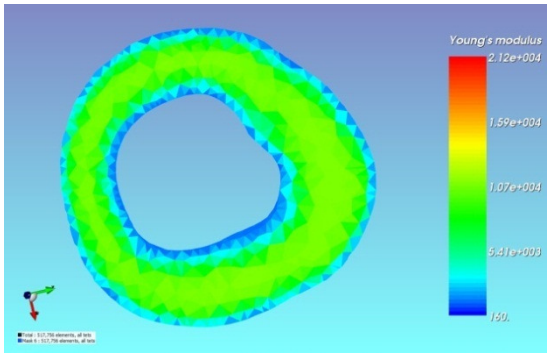

(b) 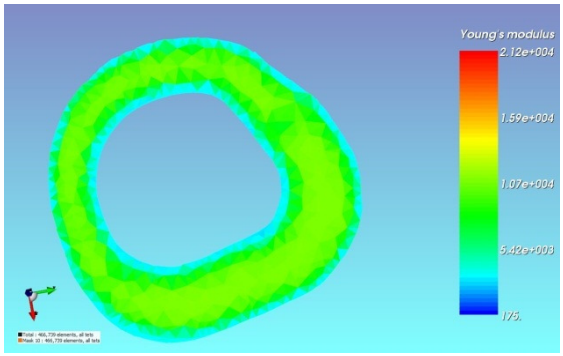

Figure 3.25 Images detailing the changes observed through re-thresholding the same model to mimimise the partial volume effect at the bone surface.

The re-thresholding process is of particular importance for surface-mounted strain gauge studies, in which the local effect of reduced Young's modulus at the surface can have a detrimental effect in local stress and strain comparisons at the site of the gauge. Of equal importance is the correct determination of geometry, such that the location of the gauge can be appropriately mapped to the Finite Element model, and thus care must be taken to ensure an appropriate balance is maintained.

3.11.3 Linear Material Models

The material mapping algorithm lends itself to the exportation of high number of material markers into the Finite Element solver package. Ultimately, this provides a non-uniform distribution of Young's modulus across the volume of the bone material; however, the individual material markers assigned to the meshed model are *linear* in nature. This reduces the complexity of the model, allowing the non-linearity of material distribution to be assessed, and providing a subject-specific response to material distribution and subsequent behaviour.

As a consequence of linear material mapping, the observed Finite Element results are proportionally linear, such that a linear response will be noted for a given increase in loading condition. The key limitation of this methodology is in the determination of fracture conditions after yielding. The methodology allows for the determination of high stress regions and thus the predicted yield load and location; however, no plastic deformation will be incurred after this point, and the *in silico* model will simply continue to exhibit continuing linear behaviour. This is not a limitation regarding the behaviour up to the point of fracture, but it determines the methodology used to determine the failure conditions, requiring the selection of a limiting value, after which it is assumed that failure occurs.

3.12 Exporting the Model for Analysis

Following segmentation of the model geometry, and the selection of the required material relationships, the final steps of the process are to complete the model for exportation into the Finite Element solver package. The models are checked visually to ensure that no 'floating' elements (elements that do not connect to the bone material as a whole) were contained within the mask. A detailed visual check of the smoothing process was undertaken to ensure that the appropriate level of refinement had been taken and that no apparent singularities were observed upon the surfaces. Additionally, before exportation the model is 'shrink-wrapped' – a process in which all data outside of a certain distance (normally within two pixels of the maximum dimension in each axis) from the object of interest was omitted. This process aids in the reduction of the overall file size of the exported model and consequently reduces solve time.

Prior to exportation, each model was aligned with respect to the global axes such that the samples' orientation matched those used within the laboratory testing. This positioning was determined via a secondary, post-testing CT scan, which included the cemented constraints used during testing.

(a) 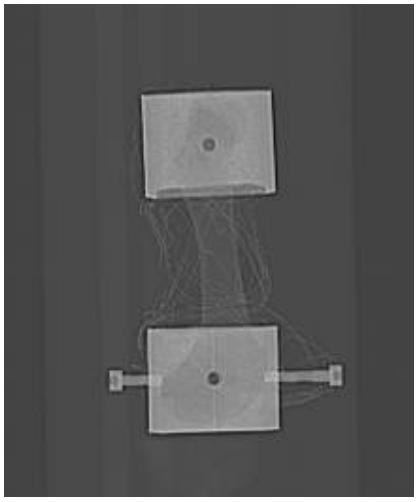 (b) 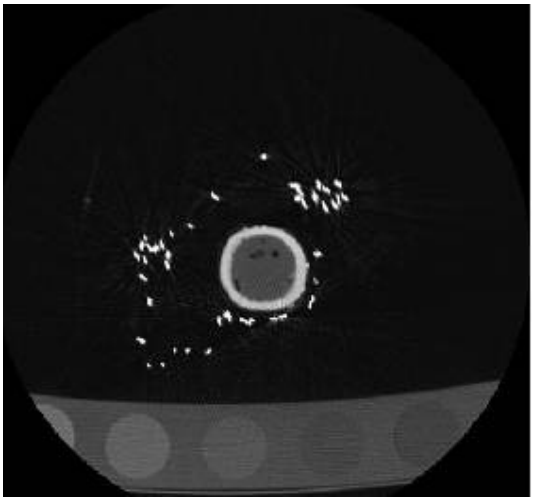

(c) 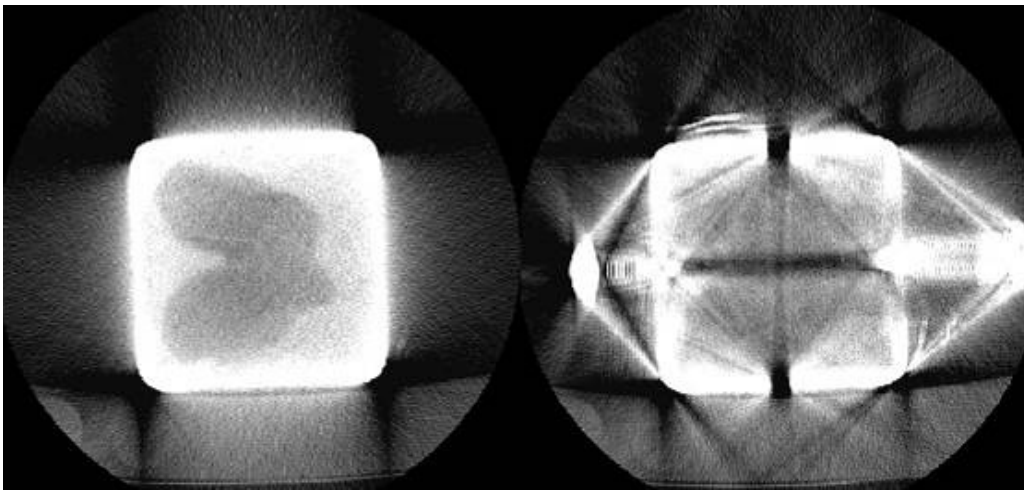

Figure 3.26 (a-c). Images of artefact streaking within a CT scan. The locating static X-ray shows the location of the metallic constraints and the bone sample (a). The smaller lines wrapped around the sample are strain gauge wires. Image (b) demonstrates that away from the site of the artefact location, meaningful data can be extracted from the CT scan. The images in (c) show the effects of artefact streaking at the site of the artefact.

As the constraints were constructed from extruded box section steel, the process introduced a significant amount of 'artefact streaking' – a situation in which non-permeable metallic artefacts are introduced into a CT scan (Figure 3.26). The lack of penetration results in 'shadows' within the image, which cause streaking due to the rotation of the scanner around the subject. This is a common occurrence in medical scanning in general, affecting patients with replacement joints, pacemakers etc. Despite high levels of artefact streaking within the post-testing scans, the images contained data that

could be used to align the sample. At a distance from the constraints, the cortex of the sample is clearly defined, as are the constraint edges. The relative position of the constraint edges and cortex edges could then be used to determine the appropriate angle for the sample. The post-testing cortex was re-created in isolation from the constraints, and overlaid onto the 'clean' model for simulation, such that the relative rotation of the two could be determined. This section was also used to determine the position of the constraints, so that isolation could be mimicked through the cropping of the cortex, prior to exportation.

3.12.1 Import into Finite Element Solver

A number of solver packages were assessed during the study, including Ansys, Abaqus and LS Dyna. Ansys was finally selected for use in solving the models. The ScanIP software integrates neatly with this solver, allowing the automated creation of .ans input files, which carry meshing and material mapping information directly into the Finite Element model, without the need for reassignment within the solver. This significantly reduces the preparation time prior to the solving process.

Once imported into the solver, the model was constrained in the manner determined by the testing procedure, and loads were applied to match the required test case. Figure 3.27 shows a final meshed and material mapped sample ready for exportation, and a subsequent results plot within the Ansys solver package, displaying contours for principle strain, which were used in this load case for the determination of the *in silico* fracture point of the sample.

(a)

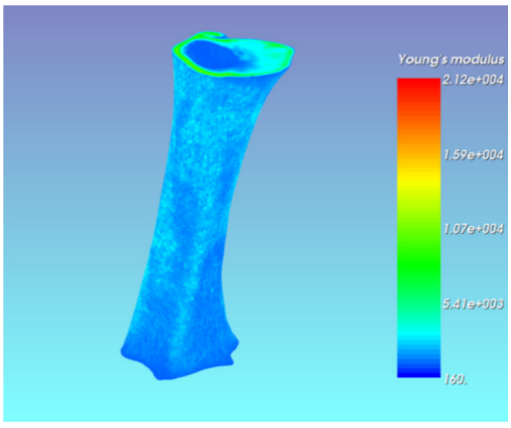

(b)

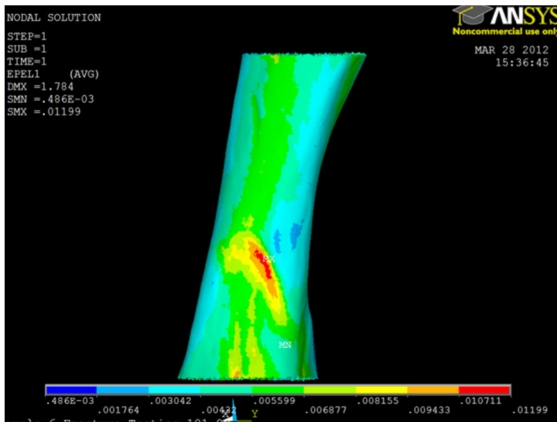

Figure 3.27 (a&b). A single cropped sample at the exportation stage post-meshing within the Scan IP software (a), the sample following fracture load testing in the Ansys solver package (b).

For the strain gauged testing used later in the validation process, markers that indicated the gauge location were placed around the surface of the exported model. These markers were provided through

the inclusion of additional sections of mask, which were assigned arbitrary Young's modulus and fully constrained during testing. The markers had no interaction with the model or the solving process, and were included for referencing the gauge location only.

3.13 Chapter Summary

The accurate representation of the test geometry, the meshing protocol and the assigned Young's modulus are the key components of accurate Finite Element modelling. This chapter has considered the complications of modelling biomechanical systems, and tested a number of the key input parameters as follows.

- CT data was used as a source for modelling as this accurately captures the geometry required for bone simulation. Threshold segmentation offered a semi-automated and rapid modelling method.
- Production of the Young's Modulus was undertaken through greyscale to density and density to elasticity calculations on an element-by-element basis.
- Using CT for segmentation and material definition provides complication when using traditional determination methods for convergence. This has been addressed, and convergence was demonstrated upon homogenous models, and also through the assessment of material-mapped methods.
- Linear-elastic material markers were used for simulation. Despite limitations in the modelling of plasticity, these markers have been shown in previous literature to provide accurate simulation results for biomechanical simulation.
- Alignment and spatial registration was accommodated through CT scanning. The effect of further changes to the geometry production and sample alignment were investigated during testing to ensure accuracy is retained within subject-specific modelling.
- Despite determining an accurate general methodology for material application, the relationships tested were those determined for *human* samples and the relationship that best suits *porcine* modelling had yet to be determined, this was to be further examined during testing.

4 Physical Testing Methodology

Finite Element computation offers an excellent opportunity to rapidly simulate varying test conditions, provided that an appropriate level of validation and error identification is undertaken. Validation in simple engineering structures is regularly demonstrated using analytical/mathematical calculation and physical testing. In biomechanical, tissue-based simulation, physical validation is often limited as a result of the inaccessibility of large numbers of bone or soft tissue samples [112, 187]. The use of animal substitution, (such as the porcine samples used in this study), provides an opportunity for greater understanding and validation of the fracture process by testing larger sample groups.

Fully validated CT-based modelling allows for the simulation of highly detailed effects that are commonly ignored in quantitative studies, such as geometrical and material variances between samples, providing true subject-specific modelling.

One of the key outputs of the literature review was that CT-FE simulation had focused primarily in the application of axial load to the proximal femoral head, and upon the bending of smaller samples, which were isolated from the true bone geometry. Additional whole-bone loading regimens such as torsion have been considered in significantly fewer studies and yet torsional fractures are observed regularly in the clinic. To date, the focus of the majority of CT-FE studies has been the ageing population. Mapping fracture risk in torsion has potential for application in a number of areas, including the younger population

To develop the understanding of alternative fracture modes, to contribute to the field of CT-FE research, and to align with potential applications in NAI and long bone injury, this thesis considers torsional fracture. The following chapter details the common physical testing methods and the procedures used during testing. This physical testing was undertaken to validate the computational simulation of porcine bone.

4.1 Sample Procurement, Storage and Preparation

The obtainment, preparation and storage of the bone samples was common throughout the entire laboratory testing procedure. Each of these was undertaken according to the best practice techniques described in the literature [188]. This is an important consideration in the testing of organic tissue, as the loss of moisture and incorrect storage of samples can have a detrimental effect on the observed Young's modulus, and consequently upon the loading response.

4.1.1 Obtainment

The samples were obtained from a local abattoir, following slaughter at approximately 22 weeks of age (slaughter age is dependent on development of the porcine litter a whole). In the United Kingdom, pigs are bred for one of two markets; fresh meat or bacon. Pigs bred for the bacon market are generally grown for longer to increase the fat content of the finished product. The samples used in testing were taken from pigs reared for the fresh meat market, which slaughters once the pigs reach a total carcass weight of approximately 60 kg.

Porcine samples were selected due to their construction and regular substitution in laboratory-based bone studies [145, 146, 148]. The animal is also of a large enough size to provide samples that have scope for fracture testing at a significant load. This allows for submaximal testing of the samples to an appreciable level of loading, reducing any possible loss of accuracy in the recording of low-level loading and strain readings. The larger size of porcine bones in comparison to smaller alternatives such as rodent samples also provides a surface area that is large enough to allow strain gauging in almost any location, which has not previously been undertaken in torsional testing for CT-FE studies [140].

Whole bone femoral samples (proximal bone in the hind leg) were selected to replicate the most commonly assessed bone in human CT-FE studies and allow for the comparison of the results in this study to the similar load cases tested in literature. The porcine femoral samples offer a comparable shape and structure to human bone, with fully developed cortical and trabecular regions, as well as a total sample length of approximately 200 mm. The femur was selected as it provides a single supporting structure to the skeleton *in vivo*. Having no significant interaction with other bones along its length and being constrained only at the extremities, the bone is naturally required to resist loading in a variety of regimens within the body, including isolated torsion. As such the behaviour of the bone under loading can be justifiably assessed *ex vivo* and in isolation, subject to considerations regarding the constraining of the extremities of the bone samples.

4.1.2 Preparation

The samples were delivered after the removal of the bone from the animal carcass at the abbatoir. The amount of soft tissue attached to the bone varied from sample to sample. All soft tissues were removed from the samples by way of cutting and scraping with a scalpel, with care taken to avoid indentation, scratching or damage at the bone surface. Removing the soft tissue reduced the risk of excess moisture being secreted during testing and minimised slip between surfaces within the constraints and gauging instrumentation. Removal of soft tissue included the removal of the periosteum from the mid-shaft of the bones such that the surface could be more easily marked for visual identification of deflection and in later tests, be appropriately prepared for strain gauging. The removal of all soft tissues also allowed for the accurate physical measurement of the samples and

aided in the accurate geometry defining stage of the computational mapping process. In both cases the creation of a solid reference point at the surface provided a clearly defined boundary between hard tissue and the surrounding air.

4.1.3 Storage

In accordance with recommended practice, the bone samples were kept moist using cloths soaked in saline solution, throughout the storage and testing procedure. The drying of bone can have significant effects on the Young's modulus, with research showing that soaking in saline solution is the most appropriate means to preserve the original properties of the bone [188]. Each sample was wrapped in saline soaked cloth from the preparation stage, throughout storage and to the time at which they were tested. Any periods where the bone was uncovered (such as for the marking of the surface or the mounting of strain gauges) were kept to a minimum.

For long-term storage samples that were frozen at –20 degrees Celsius (or below) in a standard domestic freezer. The samples were kept segregated from the main freezer compartment in a sealed, airtight container to ensure that the local temperature remained consistent. This ensured that thermal effects on the stored bones were minimized, and no partial thaw/refreezing processes were observed. 24 hours before the bones were to be used for testing, the frozen samples were placed into a domestic refrigerator in order that they could thaw as steadily as possible to a temperature of +5º C. During the thawing process the samples were retained in an additional sealed container to reduce the thaw rate and maintain the consistency of temperature change. A few hours prior to testing, the samples were allowed to approach a consistently retained 'room' temperature of approximately 18 +/- 3 degrees centigrade. The process ensured that the samples were fully defrosted before testing, reducing the chance of excessive stiffening of the marrow, or of liquid leaching during the cementing phase and affecting the potting of each sample. The testing temperature was recorded and maintained throughout the testing procedure, until the samples were discarded or retained for post-fracture analysis, at which point they were re-frozen.

4.2 Analytical Calculation

Whilst accurate Finite Element modelling can provide exceptional capability in the determination of stresses in complex structures, it is considered prudent to undertake analytical calculation to verify that the received results are logical. In the case of complex structures, analytical calculation requires the geometry and material characteristics to be simplified.

Published research regarding the determination of stresses within bone samples have shown a number of geometrical assumptions to simplify the loading cases for analytical calculation [189, 190]. These range in complexity from simple beam theory of constant diameter cylinders [191] to more involved

assumptions, more accurately mapping the geometry of a small number of slices by assigning a Fourier series to match the external and internal geometries [189]. The geometrical and calculation accuracy of such techniques is significantly lower than that achieved by more advanced CT-FE methodologies. However, as a means to rapidly test the general behaviour of a Finite Element model, such methods are acceptable and consequently this type of hand verification was proposed in this thesis. The analytical calculation process was undertaken concurrently with the torsional laboratory testing. This allowed for provisional results comparisons between the two testing methodologies, allowing a further logic check over and above comparing the analytical calculation directly with Finite Element simulation.

4.2.1 Testing Procedure

One of the key benefits of using a high resolution CT data for the basis of geometry is that a refined level of geometrical data can be provided. This means that the accuracy of the boundary of the bone can be determined with a high level of precision, particularly within clearly defined bone regions such as the diaphysis. For example, a given crop in the Z-axis of a sample (isolating the diaphysis), provides approximately 150 discrete images in the transverse plane.

Assuming no operator error, each of these slices can describe the geometry of the bone to within an accuracy of approximately the width of a single voxel (generally less than 0.5 mm). Using basic mechanical theory combined with applied yet simplified geometry from CT as per the method defined by Arangio, it was considered that a suitably accurate result could be obtained [189]. A thin-walled composite ellipse solution was used to provide an estimation of the overall geometry of the diaphysis. The solution used discrete elliptical shapes matching the maximum number of transverse slices from the CT data set. These discrete sections were combined to provide one complete, stepped elliptical cylinder. Figure 4.1 demonstrates a sketched example of the hybrid structure, where elliptical ‘rings’ were created as described by the interior and exterior aspect of the CT data set.

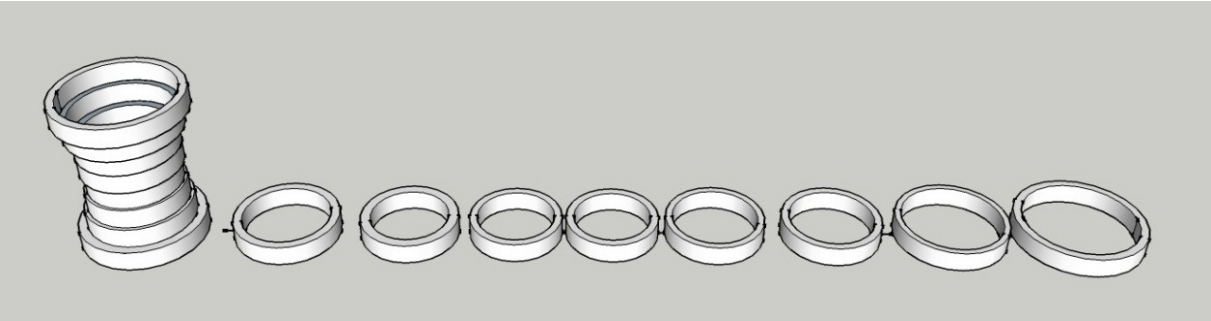

Figure 4.1. Sketch shows a simplified demonstration of the composite solution. The sketch differs from the ultimate solution, showing eight discrete ellipses, whereas the geometry used in calculation used 147 ellipses.

4.2.2 Geometry

To preserve the simplicity of the analytical calculation assumption, it was considered that testing should be provided for cortical regions of bone only. This not only simplifies the geometrical assumption, but also reduces the variation in mechanical properties, and better matches the constraints that were used within the torsional laboratory testing. Figure 4.2 shows a screen capture of the geometry noted within this region, and a sketch of the assumed ellipse that accommodates this geometry.

(a) 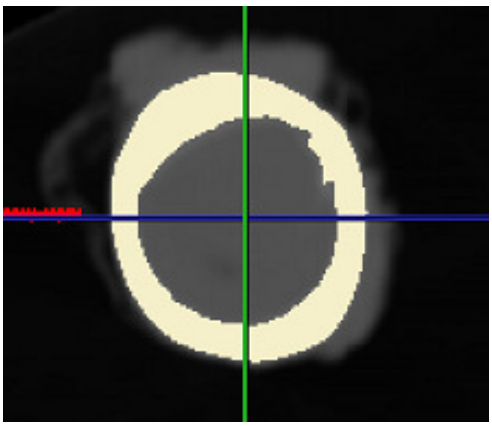 (b) 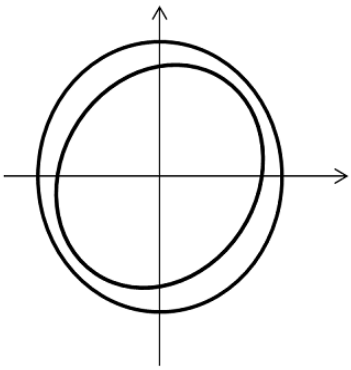

Figure 4.2(a&b). Screen capture (a) from CT dataset used to provide the geometry for the internal and external position of the diaphysis. (b) a sketch of the assumed geometry for this sample slice.

To define the geometry of each elliptical slice the following process was used: firstly, the CT data was attributed a mask to the regions of interest using the geometry production process described in Chapter 3. This was undertaken through thresholding, enabling the rapid segmentation of the material of interest, isolating any soft tissue interaction within the original source image. The centroid of each individual transverse CT slice and mask was then found. Following this, the anterior-posterior and medial-lateral axes were defined through the centroid. The location of the internal and external wall of the diaphysis for each axis was then determined, and these positions were used to describe two elliptical rings around the reference centroid. The polar second moment of area was calculated for each ellipse using equation 4.1, measured at two opposing points across each slice.

$$I = \int \frac{\pi}{4}\left(a_o {b_o}^3 - a_i {b_i}^3\right) \qquad 4.1$$

Where:

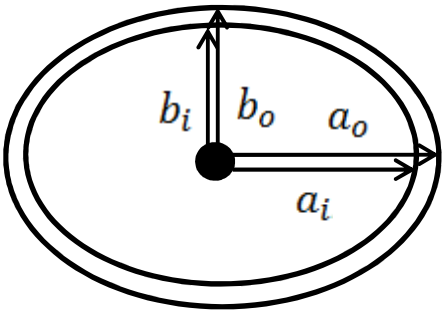

I is the polar second moment of area
a_o is the outer radius along the longer dimension
a_i is the inner radius along the longer dimension
b_o is the outer radius along the shorter dimension
b_i is the inner radius along the shorter dimension
All measurements are made from the centroid of the slice.

The calculated force was then applied concurrently and individually to each slice, with the results integrated to provide a solution for the test piece as a whole. The final gauge length of the isolated diaphysis composite test sample measured approximately 110 mm.

4.2.3 Loading

Simplified geometry allowed for rapid changes in the applied boundary conditions in the analytical calculation model. This allowed for a cursory examination of parameter identification so that the key input factors affecting the outputted results could be quickly identified at a basic level.
The general equation used for torsion in analytical calculation is shown in (*Eq*. 4.2). The equation requires the input of applied torque *(T),* segment length *(L),* second moment of area *(J)* and an assigned shear modulus *(G)* and is then integrated to provide the summed result for the structure as a whole. Each of these inputs was assessed in turn during the analytical calculation process. Shear modulus is of particular interest, as this material constant had little consideration in the literature compared to other constants such as Young's modulus [53, 82]. Consequently this was the first parameter that was assessed in analytical calculation.
The algorithms used in the ScanIP process and the general Density-Elasticity relationships used for material definition in CT-FE studies export Young's modulus rather than Shear modulus. In isotropic models (such as those used during modelling) the two moduli are converted with the equation shown in (*Eq*. 4.3).

$$\theta = \int \frac{TL}{\mathrm{GJ}} \qquad 4.2$$

$$E = 2G(1 + \nu) \qquad 4.3$$

A range of boundary conditions was examined, providing a range of results that were then confirmed via testing in the laboratory and in Finite Element simulation. The test parameters investigated in analytical calculation included the assigned shear modulus, the sample gauge length and the applied load. The one parameter that remained unchanged throughout testing was the second moment of area attributed to each slice, as this was determined from the scanned CT images. One such observation was the relative geometry of each of the slices, which was plotted with respect to a result for a given set of input parameters (Figure 4.3).

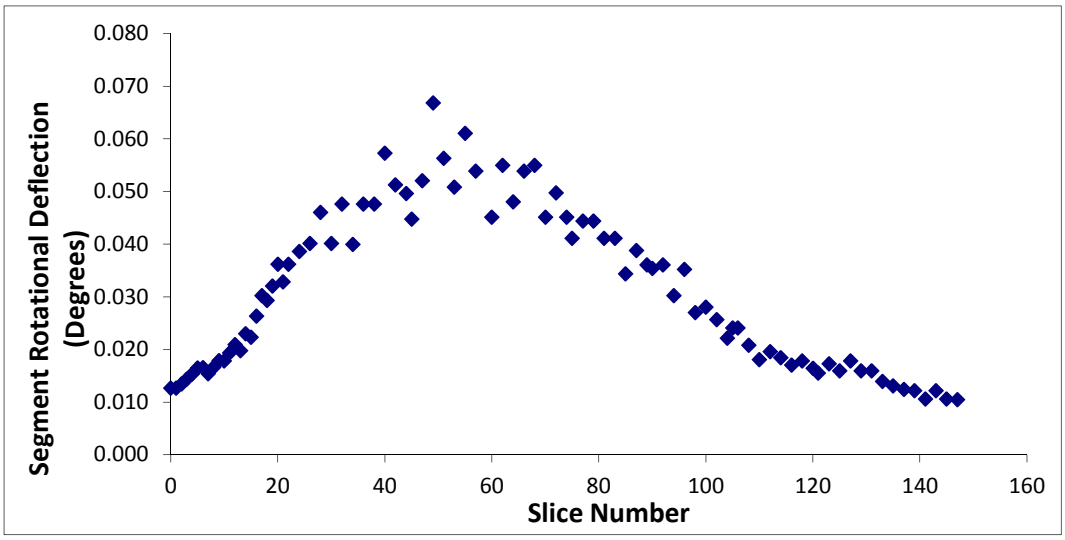

Figure 4.3. Plot shows the results of angular deflection for a given set of input parameters across the length of the composite sample for each independent slice. As can be seen the decreased diameter, wall thickness and consequent reduced second moment of area in the central section increases the deflection noted.

This plot demonstrates the effect of the changing polar second moment of area, and consequently the responsibility of each slice in the resistance of torsional force (assuming consistent Young's modulus). As can be seen the central sections (in which the diameter of the sample and the wall thickness are reduced) are responsible for a larger proportion of the deflection of the sample as a whole. This process verifies the importance of the composite rather than plain cylindrical solution, showing the change in deflection along the length of the sample as a result of the continually changing shape.

The general equation used for compression in analytical calculation is shown in (*Eq*. 4.4). To simplify the analytical calculation assessment, the vertical deflection of the sample was considered to follow Hooke's Law of proportionality, and therefore not exhibit buckling, bending or barreling. This is a limiting assumption, but for small deflections may be considered appropriate. The equation requires the input of applied force *(F),* sample or section length *(L),* area *(A)* and Young's modulus *(E).* Each

of these inputs was assessed in turn during the analytical calculation process, with the exception of A, which was dependent upon the specific geometry of each slice.

$$\frac{\partial L}{L} = \frac{F}{A} \tag{4.4}$$

4.3 Laboratory Test Equipment

The literature shows that physical validation of CT-FE studies has been typically undertaken in a single axis only. This has been demonstrated in the form of compressive tests [46] in which the application of load general follows a linear path. Some physical investigation outside of CT-FE has been undertaken in torsion, which provides a more complex loading scenario and has resulted in the development of rigs that convert linear actuation to rotational displacement [140]. The general concept for the test equipment utilized in literature is that a single load cell records live results as a response to a single actuator acting in a single strain path. To confirm the actuation in this single strain path, expansion and rotation in the non-measured axes is generally mitigated through the use of free rail systems, such that no additional or off-axis forces are applied during testing. As these forces are proposed as fully isolated any load in this region is generally disregarded, without being recorded.
In 2002, the Institute for Microstructural and Mechanical Process Engineering at The University of Sheffield (IMMPETUS) developed test equipment to measure the complex strain path created by metals in 'hot deformation processing conditions' such as rolling and forming, during which time the metal is subjected to cooling and recrystallization processes whilst under continuous load [192, 193]. The test rig was dubbed Arbitrary Strain Path 2 (hereby known as ASP) (Figure 4.4).

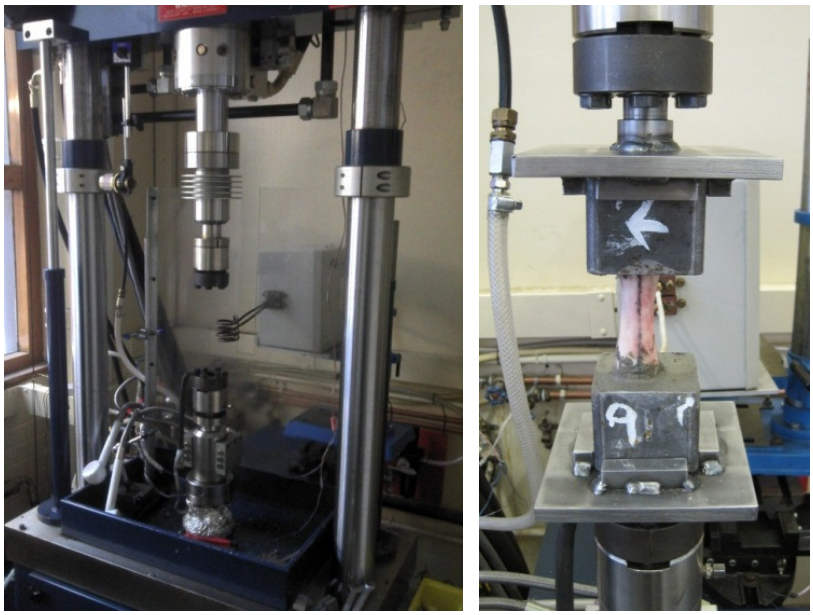

Figure 4.4. Photographs showing the ASP test rig within the IMMPETUS laboratory. The second photograph shows a femur sample located within the two opposing crossheads, potted in the standard constraints.

The behaviour of this equipment differs from those characterised by standard linear actuators in that the rig can be controlled in multiple axes at the same time, using servo-controlled hydraulic actuators. The use of hydraulics allows for full and continuous rotation (unlimited degrees of rotation in either direction), tension and compression, and for a combination of tension/compression with simultaneous rotation. Servo control also provides a large range of strain rates, and rapid switchover between load paths, allowing fast cyclical loading to be undertaken.

The ASP equipment was used for physical testing in this study as a result of the capabilities highlighted above, which provide the opportunity to test at varying load levels including values above and beyond the fracture limit of the porcine bone samples. In addition to the loading capabilities, the ASP rig was selected because of the data acquisition options that it offers. Data can be sampled for all operational load and displacement parameters concurrently, at sample rates ranging from approximately 1 to 1000 Hz, which allows for accurate description of bone behaviour, including rapid, elastic failure.

4.3.1 Constraint Design

The ASP equipment is capable of testing a limited range of sample sizes using a sliding jaw at either crosshead. These crossheads provide the relative motion of the tested samples during testing, with the lower of the two continually static, and the upper crosshead providing the application of force. The jaws within the crossheads operate in a vice-like manner, and allow the fixation of samples of approximately 20 to 40 mm in diameter. The metallic samples commonly tested within the IMMPETUS laboratory are machined such that the clamped regions have flat sections, which fit directly into the jaws and mitigate the risk of the sample twisting relative to the crosshead during torsional loading.

For bone testing, custom constraints were designed and manufactured (Figure 4.5) to allow multi-axis alignment and to accommodate a sample width greater than the 40 mm allowed by the standard jaw. The constraints were produced in two parts, the first of which was bolted into the ASP rig, and remained aligned within the jaws throughout testing. The first section of the constraints was manufactured from steel plate, incorporating a 30 mm diameter steel bar section, which was machined flat on opposing edges to match the crosshead jaws.

This machined section was then bolted and welded centrally to the main 10 mm thick steel base plate. Four further sections of 10 mm plate were welded to the base plate; these described a 70 x 70 x 10 mm ‘box’ shape on the surface of the plate, with an open upper side to allow the second part of the constraint to be located within.

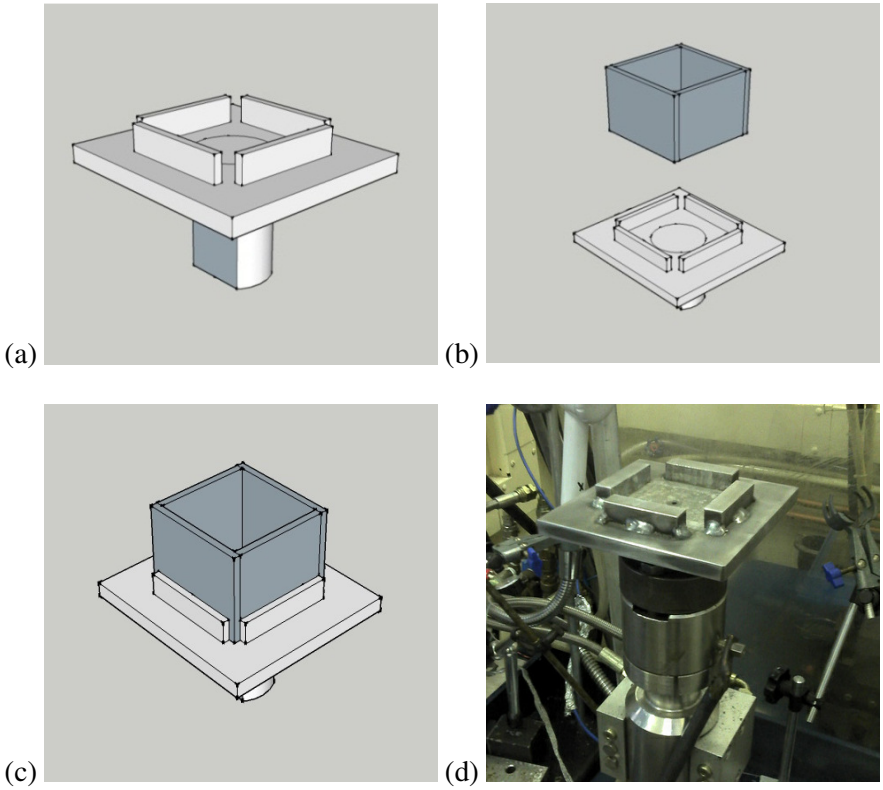

Figure 4.5 (a-d). The two-part constraints used for bone testing. (a) shows the outer part of the constraint, which remains in place within the crossheads throughout testing. The second section (b&c) aligns within the outer part. The photograph (d) shows the outer constraint bolted into the lower crosshead arrangement.

The second constraint component was steel 70 x 70 x 60 mm box section, with a wall thickness of approximately 3 mm. This section was designed to house the bone ends, allowing for free positioning of the bone sample in all axes. The tested bone samples were potted within this steel box section to provide alignment of the sample. Potting bones in this manner is common in physical testing [70, 82, 194], and provides a logical means to transfer force to the bone sample in any orientation. Each sample had two of the extruded sections (one mounted at either extremity), which were retained with the specific sample throughout the life of the test piece. The two separate parts of the constraints were not physically bonded, but held together due to the designed tolerance of the respective parts, and the loading regimen. As a result, the design of this constraint could be pulled apart vertically, and therefore would not be suitable for testing the samples in tension.

Mounting the bones in two-part constraints also allowed for the samples to be quickly and easily changed during testing, with the two base plates being the only parts that needed aligning, at the start of testing. The alignment of the base plate was continually checked throughout testing, to ensure that the original and correct positioning remained consistent. It was considered that this two-part

constraint methodology was an improvement when compared to previous studies relating to torsional fracture of porcine femurs, [166] offering a faster, more cost effective testing process.

4.4 Sample Fixation

Typically, medical grade rigid setting polymers are used in the bone potting application as they provide a clinical substance for testing within clean laboratories. These tests generally involve a lower sample number than was proposed in this study; Taddei et al. for example, tested a single bone, potted at one end only [46] leading to a much smaller volume of potting medium than was used in this study. Availability and expense were considered when selecting a potting cement and consequently a rapid-dry aggregate-based construction cement was selected to fixate the bone samples (Cementone waterproof rapid setting cement). This offers a combination of low cost, high volume and high availability. Additionally the cement had a rapid and low temperature cure when compared to resins and adhesives of similar strength. This helped to minimise unwanted thermal effects on the tested organic material.

To provide an estimation of the rigidity and integrity of the cement when tested at load, a potting sample was tested within the laboratory. A single 50 x 20 x 20 mm piece of mild steel section was cut, following which a hole was drilled part way through the material piece and then blind tapped such that an M12 steel bolt could be located within the hole. The test piece was then located within an outer constraint, and set in place. Once the cement set, the test piece was constrained and torque was applied to the bolt. The point at which the integrity of the cement was compromised was to be noted visually via cracking and increasing deflection. Images from the testing are shown in Figure 4.6, in which the relative components and the outcome of the test are observed.

(a) 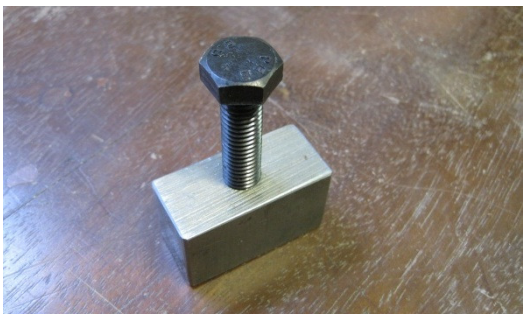 (b) 

Figure 4.6. Images of the section of mid steel into which an M12 bolt is set (a). The result of the simple torque test, showing the sheared bolt (b).

The bolt was subjected to increasing loading at stepped 20 Nm intervals, and showed no visible signs of deflection or loss of integrity until a load value of approximately 170 Nm, at which point the bolt sheared. The cement was carefully inspected at this point, and showed no signs or indicators of

damage. It was considered that whilst the test represented only an approximation of the likely loading in testing, the cement was likely to be capable of supporting a suitable load (maximum failure load under torsion for a porcine femoral sample is in the region of 100 Nm.

4.4.1 Fixation Methods

The manner in which the samples were potted within the constraints determined the application of forces in each load case and ultimately, the boundary conditions for Finite Element simulation. Applying torsional force to a test subject increases complexity over simple single axis loading, as the force is no longer applicable at a single point and the sample must be effectively 'gripped' within jaws or by a suitable potting material. The fixation and potting methods used within testing are detailed below.

4.4.2 Fixation for Torsional Testing

Torsional testing was undertaken via the complete cementing of the epiphyses within deep section steel constraints (Figure 4.7). This is a testing method that is demonstrated in literature in compression with a single constrained end [46] or complete potted torsion [166]. In the latter, the methodology is unclear as to whether the geometry of the bone itself is manipulated, as the constraints seem to have been constructed with a smaller diameter than that that would be expected for the epiphyses of the bone samples used. Throughout testing in this study, the integrity of the bone was to be maintained, and as such the bone samples were not manipulated. This allowed for the retention of geometrical accuracy between scanning, modelling and physical testing, and consequently ensured that the boundary conditions were accurately depicted *in silico*.

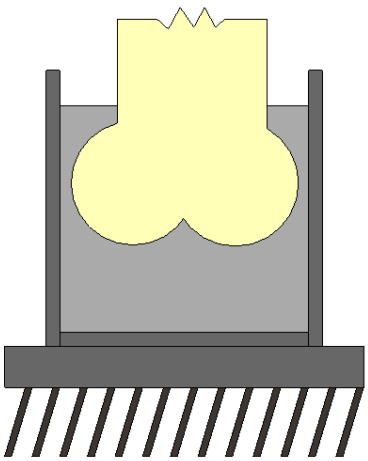

Figure 4.7. Sketch shows the 'fully potted' torsional constraint arrangement.

In torsional testing the constraint provided complete potting of the bone and total isolation of the bone cortex. This was provided via potting of the epiphyses of the bone samples up to the level of the metaphyses. The samples were cemented to a depth of approximately 50-55 mm within the 60 mm steel constraints. The samples were potted in such a manner that the mid-shaft was aligned as close as possible to the *z* axis. A clamp and guide arrangement was used, with one extremity (the lowermost) potted in turn, whilst the sample was held rigidly. Curing was claimed to be 20 minutes by Cementone, however each extremity was allowed one hour to ensure that a full cure had been achieved. It would be impossible to cement to such a degree of accuracy to negate the need for post-test scanning, and as such this scanning process was ultimately used to determine the correct alignment.

4.4.3 Fixation for Compressive Fracture Testing

Compressive testing and the failure of full-length test samples through buckling provides complications at the point of failure. The failure mode noted when a sample is loaded past the point of yield is likely to be a combination of both compressive yield and buckling. The propensity to buckle is generally determined by Euler buckling theory as shown in (*Eq. 4.1*).

$$F = \frac{\pi^2 EI}{(KL)^2} \tag{4.1}$$

In this equation the value for *K* is taken as an 'effective length factor' and consequently depends on the end conditions of the column, reducing (which increases the critical buckling load) for built in ends, and increasing (reducing the critical load) for pinned subjects. *I* is the moment of inertia, a measure used to describe the cross sectional geometry of a subject at a given point, or summed along its length. Expanding the effective length factor component shows that for slender columns with pinned ends ($K = 1$), the critical buckling load is ultimately defined by the slenderness ratio of the object. The slenderness ratio is a comparison of the effective length of a subject to its thinnest section. This thin section is defined by the least 'radius of gyration' - a measure of the average distance of material within a subject from the centroid of the cross section. This is denoted by the letter *r*, as shown in (*Eq*. 4.2).

$$r = \left(\frac{I}{A}\right)^{0.5} \tag{4.2}$$

Consequently this yields the equation shown in (*Eq*. 4.3) which defines the slenderness ratio of a sample.

$$\lambda = \left(\frac{l}{r}\right) \tag{4.3}$$

Substituting the formulae shown in (*Eq*. 4.2) and (*Eq*. 4.3) into the initial Euler theory for critical load, as shown in (*Eq*. 4.1) yields the following equation for maximum permissible stress within the column.

$$\sigma = \left(\frac{F}{A}\right) = \frac{\pi^2 E}{\lambda^2} \tag{4.4}$$

Ultimately, this derivation shows that tall, slender objects are more likely to exhibit buckling rather than true compressive failure, however in actuality the failure mode is a combination of both. The ratio of the amount of each failure type is defined by the effect length and width of the sample. The inherent geometrical differences between human and porcine bone suggests that a porcine femur is more likely to exhibit signs of compressive failure rather than pure buckling, with a sample length of approximately half that of a human sample, and similar cortex width and thickness.

The extremity to extremity length of the adult human femur is in the order of 413.29 +/- 28.4 mm [15] Whilst the porcine femoral samples in this thesis displayed average maximum sample length of 192.0 +/- 5.9 mm. Additionally the geometry of the unloaded the human femur displays an increased medio-lateral bend and angle, which increases the propensity to bending and thus buckling failure. Figure 4.8 shows the geometrical differences between human and porcine femurs. Despite the similarities in construction, obvious geometric and spatial differences are apparent, including initial curvature of the mid shaft, and the alignment of the distal joint with respect to the angle of the mid shaft. The alignment of the femoral head (measurement defined as the *proximal breadth* in literature) also shows significant variation. This is narrower, and therefore provides a femoral head that is much more closely aligned with the cortex in the porcine samples, whilst at a more significant lateral distance in human samples.

(a) 

(b) 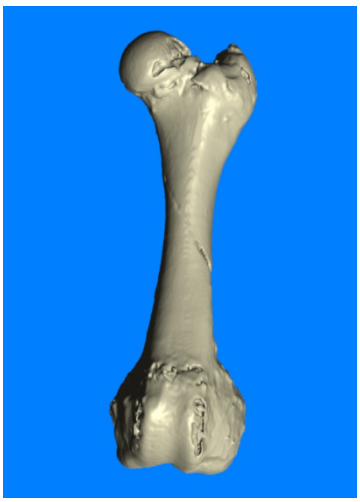

Figure 4.8 (a&b) The geometrical differences between human and porcine femurs. (Figure 4.7(a) is provided by SciencePhotoLibrary [195]).

The application of force may also have an effect upon the manner in which the subject fails. Applying compressive force away from the centroid of the main shaft (i.e. upon the femoral head) will induce initial bending moments during testing, increasing the propensity to buckle and putting the femoral neck at greater risk of fracture. The initial bending moment is dependent upon the distance of the load from the centroid, further suggesting that full-length human femoral samples are more likely to fail by buckling, than porcine equivalents.

In testing of the porcine femoral samples, the bones were constrained to mimic the boundary conditions found *in vivo* and permit some rotation and angular displacement. Constraining in compression was undertaken using a 'semi-potted' solution (Figure 4.9). Firstly, the standard constraint from torsion was part-filled with cementing compound. At this point the sample ends were covered with a thin plastic wrap, and used to make an indentation into the partly cured cement, creating a subject-specific mould. Sufficient time was allowed such that cement could be cured, to reduce the chance of the cement expanding into the mould during the cure and affecting the manner in which the bone was constrained.

Creating a 'custom' mould for each bone within a specific constraint mimicked the bone as it would be constrained *in vivo*, for example allowing anterior and posterior lateral movement, but restricting rotation at the knee joint. This provides an excellent solution for loading, allowing the bone to be restrained, but the joint surfaces to be appropriately supported. This prevents crushing against an otherwise flat surface, or local deformation as is likely incurred under point loading applied directly to the epiphysis.

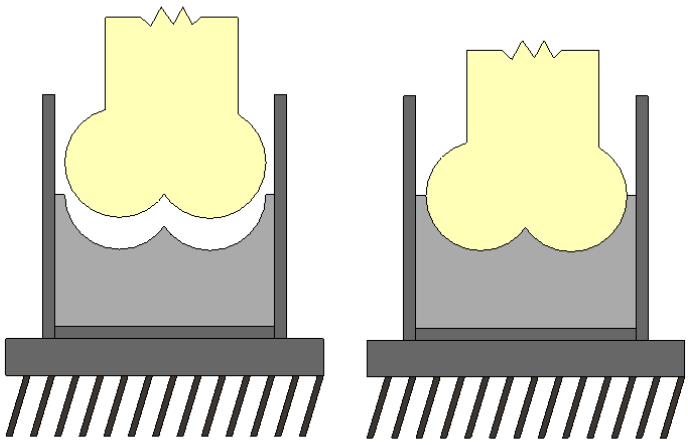

Figure 4.9. Sketch of the 'moulded' constraint solution, showing the indentation and fitting of the bone sample within the constraint cup

This compressive constraint methodology used in this study is a significant departure from the techniques used in literature for the assessment of the proximal femur, which commonly pot a significantly higher proportion of the distal region [37, 45, 82]. The failure of those samples is generally noted within the femoral neck, but due to the manner in which they are constrained, it is unclear whether this is a result of increased fracture risk in this region, or the 'built-in' nature of the tested sample. Fracture risk is commonly simulated in the femoral neck due to the occurrence rate of these fractures in the older population. However, other risk factors such as osteoporosis and remodelling as a result of inactivity may contribute to the high occurrence rate of fractures in this region.

4.5 Fracture Testing Regimen

The orientation of each porcine sample was noted so that the samples were continually tested in torsion in the same direction, in this case from medial to lateral direction at the distal end. This replicates fracture with the femoral head constrained within the acetabulum (cup portion of the pelvis) and the knee twisted towards the outside of the body.

The samples were constrained in a manner that theoretically isolates the diaphysis for torsional testing of the midshaft, as was cropped within the Finite Element simulation. Initially, mid to low-level loading (in the order of 20 Nm) was employed to take up the slack within the various constraint sections, and ensure that the sample was correctly aligned. With the low level loading removed, a natural start point was found for the point at which zero torsion was indicated on the load cells, and this allowed results values to be calculated from this point onwards.

To maintain a pseudo-static loading approximation (as used within the Finite Element modelling), the loading rate was set using the strain rate control of the test rig at a strain rate of 0.1 deg/s for all samples. The material response of bone has been shown to be strain rate dependent with bone providing a stiffer response for faster loading rates [196, 197]. The rate selected lies approximately at the midpoint of the rates shown in strain rate studies, thus representing a rate that is intentionally neither fast or slow. All samples remained unconstrained in the Z-axis, allowing the sample to expand in this direction whilst under torsional load. Data was sampled at a rate of 10.24 Hz, and values for rotational position, torsional load, Z-direction position and Z-direction load were recorded. This psuedo-static torsional testing procedure is not strictly pure torsion, but rather a 'twist' test. The difference being that one end of the sample is rotated whilst the other remains fixed, as described by Saunders [140], whereas a 'pure' torsion test has equal and opposing torque applied at each end simultaneously.

Data was recorded from the point of the activation of loading until the point of fracture. For sub-maximal testing, data was sampled for both the loading and the unloading phases, such that any effect

of hysteresis could be analysed. Data capture was also undertaken for the preliminary loading and unloading case used to align the sample and remove slack. This data could then be reviewed to ensure that the sample had been cemented effectively, and was not subject to excessive yielding under initial load application.

In compressive testing, moulded constraints were used. Following alignment, low-level loading (0.5 kN) was employed to settle the sample completely within the test arrangement. At this point a 'zero' level was found from which to observe the results of the tests. Compressive load was applied at the rate of 0.01 mm/s to mimic the effect of a steadily increasing load during standing, and to ensure that the static loading undertaken in Finite Element analysis remained was appropriately matched whilst some relative rotation was permitted through the production of cupped constraints, resistance was provided via the moulded aspects of the potting medium. Data was sampled at the same rate as the torsional tests. The sample was fully constrained at the lower crosshead, whilst the upper was forced in the Z-direction, and allowed to rotate in the x and y axes, to reduce the effects of off axis loading.

4.6 Strain Gauge (Sub Maximal) Testing

Computational simulation can be used to map the stress and strain patterns under different loading conditions across the entirety of a given structure. These plots can be used to identify fracture location and risk, and yet without suitable physical validation, they are often error-filled and can be misleading. The ASP rig that was used for physical validation in this study offered high-resolution data in terms of overall load/deflection of the tested samples, but whilst this is accurate and valid for fracture load testing, it cannot be used to validate the behaviour at the sample surface, as outputted in the simulation plots. Sampling only load and deflection integrates any errors in the small-scale behaviour within the entre sample, providing a single result for load/deflection for a given loading interval. Consequently strain gauging was proposed, which allows for assessment of the local and small-scale behaviour of the bone, providing true correlation of the fracture risk plots created using simulation.

Strain gauged investigations have been extensively used in mechanical testing for a large variety of structures to provide information regarding strain at a point on a subject's surface [103, 104]. The key limitation of using strain gauges for the purpose of Finite Element validation is that the data obtained is provided at discrete locations only, rather than mapping the structure's entire surface. However, the use of physical strain gauges benefits from a higher level of accuracy in comparison to techniques that provide continuous strain fields and surface mapping techniques such as speckle interferometry and digital image correlation [198].

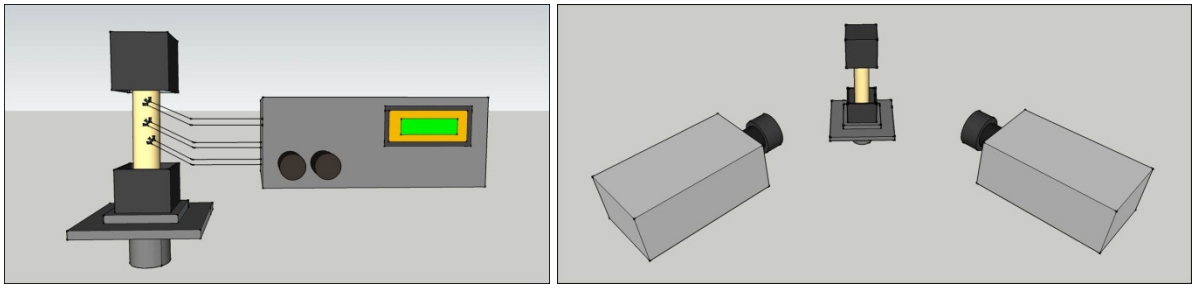

Figure 4.9. Sketches show the general strain gauging and image correlation processes.

Digital image correlation is a developing technology and historically has had greater accuracy in regular mechanical structures than in biological tissue. Recent studies have considered these techniques for CT-FE simulation but as yet there is no agreed methodology or general protocol. By contrast, strain gauging in physical bone testing and validation has been undertaken by a number of investigators [45, 70, 100, 199]. It is generally accepted as the most accurate methodology for stress and strain correlation in biomechanical investigation. The development of the biomechanical gauging technique is exhibited extensively in literature [36, 70, 82]. The gauging protocol used here was developed from these studies to allow direct comparison with data in literature. Following published protocol allows for the direct comparison of the results and accuracy observed in this thesis, with those published in literature.

4.6.1 Methodology

Metallic, foil backed circular strain gauge rosettes were selected for the testing procedure (Tokyo Sokki Kenkyuojo co., Ltd. – FRA-1-11-1L). This gauge type consists of three individual gauges, pre-aligned in 45-degree intervals. Due to the constant curvature and varying geometry of the surface of the bone samples, gauges with the smallest possible gauge length (1 mm) were selected. This selection reduced the effect of strain averaging over the applied surface area, offering an improved solution for measuring the behaviour of the sample at a specific point. The accuracy of strain gauging is generally determined by the gauge length, with smaller sensing areas providing more accurate results. This is of increased importance in biomechanical testing as the higher resolution offered by the smaller gauge size accounts for the rapidly changing strain gradient observed in simulation. Historically, larger gauge lengths have been used for biomechanical Finite Element validation, which may have contributed to the reduced accuracy noted in some studies [40].

The gauges were placed at regions of interest, as determined by cursory modelling and initial fracture testing. Strain gauges were bonded to the proximal anterior surface, the proximal medial surface in line with the greater trochanter and towards the distal end of each sample between the posterial and lateral surfaces, as shown in Figure 4.8. Three strain gauge rosettes were utilised for each bone sample, totaling nine individual strain gauges for each test. Figure 4.8. utilises a sample mask created from post fracture scanning, highlighting the proximity of each rosette location to the fracture line

observed under torsional fracture testing. As can be seen gauge one is located in an area of plane surface, away from the fracture line in this (and other torsional fracture) cases. Gauge two is positioned along the predicted fracture line, beneath the hip joint and greater trochanter. Gauge three is positioned to the rear of the bone surface, close to a position of ligament connectivity and at an indentation in the general geometry of porcine femora. This region showed high stress gradients in the initial Finite Element modelling, and regularly demonstrated the displacement of sections of cortex following elastic fracture.

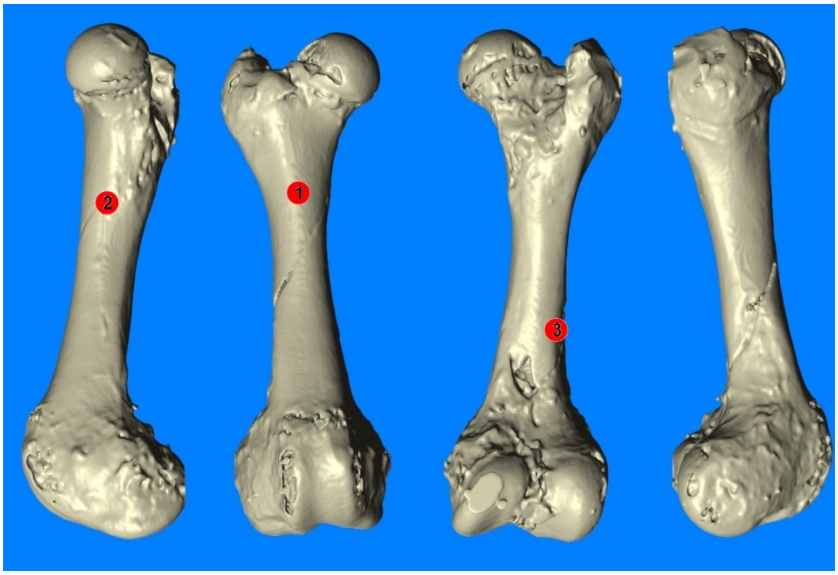

Figure 4.8. Images showing a mask created from post fracture scanning, detailing each aspect of the bone surface. The three red markers show the location of rosettes two, one and three respectively.

4.6.2 Surface Preparation

Bonding of the strain gauges to the bone surface is important for accurate readings of local strain. In traditional mechanical systems, this requires fixation through the liberal application of a strong bonding medium, however in biological tissues the excessive application of bonding agent can lead to localised strain hardening as the agent is stiffer than the local material property at the region of interest. To ensure that the gauges were suitably bonded, but that the bonding agent would not reduce the local strain values incurred, the agent was used as sparingly as possible.

The samples were prepared following the standard methodology. The proximal extremity was forced, whilst the distal was fully constrained in all direction. The bones were fully potted, using the original torsional methodology described previously (Figure 4.9). The surface identified for gauging was checked to ensure that the scalpel scraping undertaken to remove the epiphysis had not scratched or deformed the local surface and then sanded to minimize local surface roughness. The surface was then

cleaned with an alcoholic cleansing wipe material to remove any surface grease. A single component cyanoacrylate bonding agent was used, which offers a cold cure, and thus minimises unwanted thermal effects. A small amount of the agent was employed to fill the local pores and seal the surface of the bone to prepare for the gauge application. Alignment of the gauge was pre-determined through application with a removable tape, to ensure that the final position was correct. A further amount of agent was then added directly to the gauge surface, and the gauge applied to the sample. Sufficient time was allowed before testing to ensure that the bonding had cured. This is particularly important due to the small size of the bonded region, and the use of pre-wired gauges, which can apply significant force to the mounted gauging during movement of the sample. The surface preparation and gauge application methodology was undertaken in line with similar methodology as detailed by Taddei et al. [82].

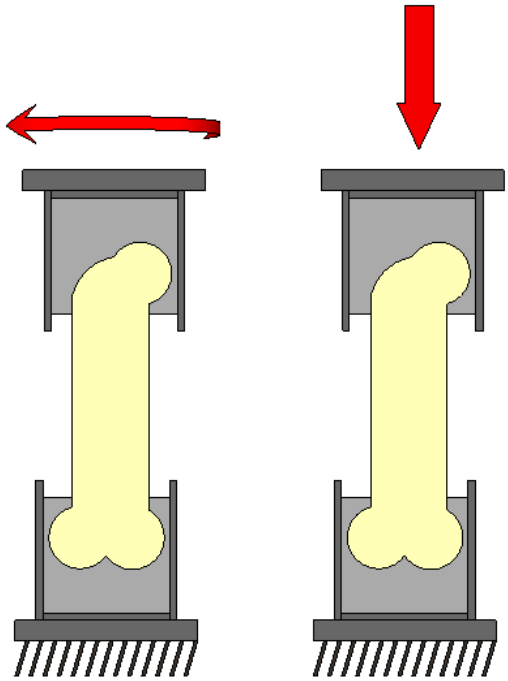

Figure 4.9 Sketch of the arrangement for sub-maximal (strain gauged) testing in both torsion and compression.

4.6.3 Testing Procedure

The sub-maximal testing follows the same procedure as detailed previously, however for strain gauged testing, loading is reduced to a sub-maximal level. Loading was significantly below the average fracture load at all times, as defined by the preliminary fracture tests. It should be noted that despite this load being sub-maximal, the maximum loading interval is significantly above the general working load experienced during *in vivo* loading (assuming an average slaughter weight of approximately 60 kg and reasonable level of mobilisation). Initially, load was applied to 50 % of the maximum testing load interval for each sample, and then released, such that any remaining slack

would be removed from the system. The strain gauges were reset at the start of testing and again when the samples were allowed to return to the pre-defined 'zero point' after each of the discrete loading intervals. The samples were allowed to 'recover' at the zero load point for approximately three minutes before reloading. Samples were loaded in 5 Nm intervals, and then after reaching 10 Nm, at 10 Nm intervals up to a maximum total torque value of 40 Nm.

Figure 4.9 shows a single sample gauged and prepared for the testing process, and secondly shows the gauge reading process itself. As can be seen, the reading of the stain gauge data was undertaken using a junction and switching box arrangement, and consequently gauge readings were not sampled concurrently for all nine gauges, however, on average, strain results were recorded approximately 30 seconds after the loading interval was reached. As the sample reached the loading interval, the load was held continuously, such that the strain gauge results for all nine gauges could be taken for a static and maintained load.

It should be noted that during the compressive test procedure in strain gauging, the mid-shaft of the bone remained isolated using the fully-potted constraints from the torsional test regimen. This differs from the general compressive fracture testing, in which the sample was constrained in a manner that allowed increased lateral deflection in bending (buckling). The constraining methodology used for strain gauged testing in compression matched the constraints used for torsional testing, and is demonstrated in the image in Figure 4.9. It was considered that the use of sub-maximal loading ensured that the incurred deflection was small and thus this constraint methodology was valid.

(a) 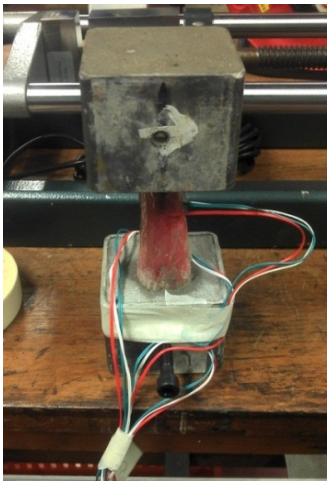 (b) 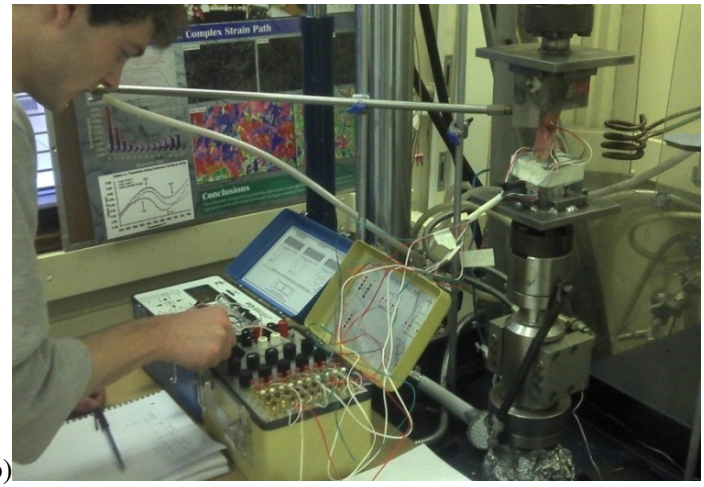

Figure 4.10(a&b). (a) A single sample following the gauging and wiring process. (The gauge wires are taped to the constraint edges to reduce the change of the gauge becoming dislodged during testing). And (b) a sample undergoing the 'zeroing' process prior to loading and strain reading.

4.7 Laboratory Testing Schedule

In total, 31 porcine samples were prepared for physical testing within the laboratory. The samples were tested in batches depending upon the testing regimen and access to test equipment. Table 4.1 and Figure 4.11 detail the test groups and constraint types tested throughout the laboratory validation and fracture testing procedures. Not all of the samples tested within the laboratory for fracture testing were scanned within the CT scanning process, and consequently these un-scanned samples were used for fracture testing only. Results provided from these samples were used as a means to test the capabilities of the laboratory validation process and for anecdotal information regarding fracture loads, rather than as a computational validation or simulation source.

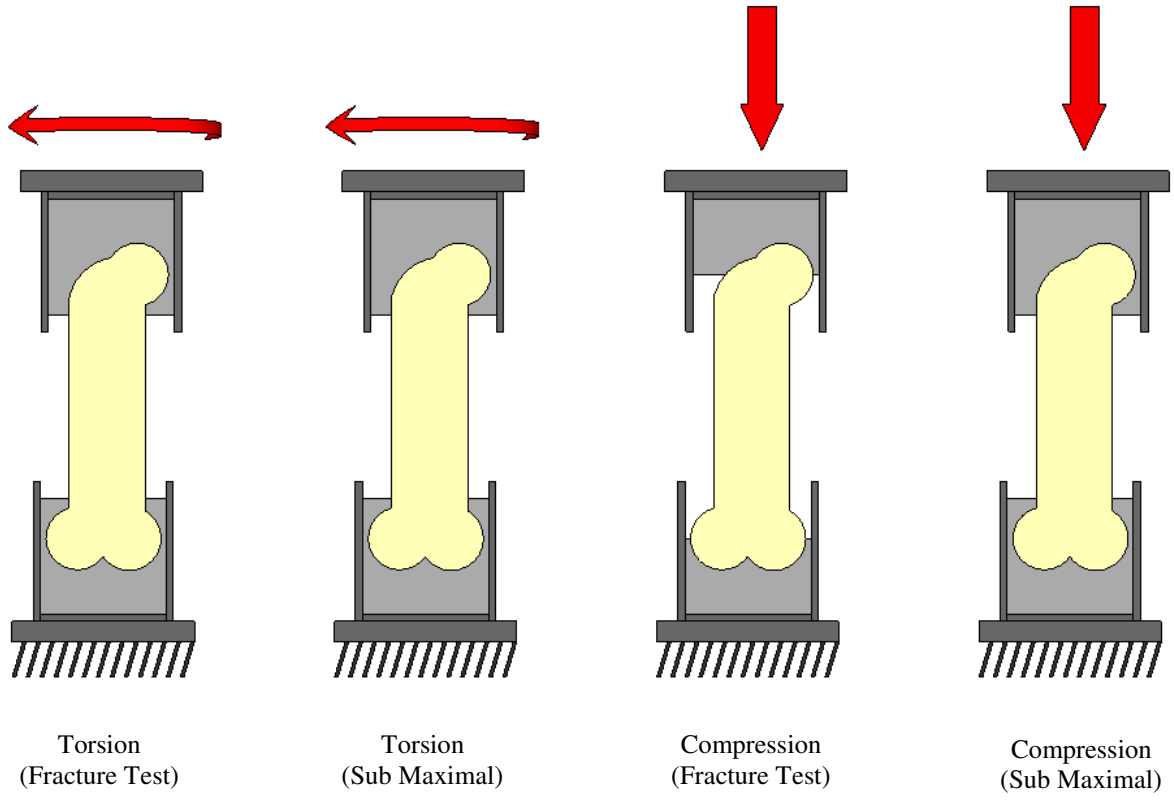

Figure 4.11 The potting techniques and boundary conditions of each test during physical testing.

Table. 4.1. Table detailing the 31 samples physically tested within the laboratory.

Test Batch No.	Number of Samples	Loading Regimen	Constraint Type	Maximal/Sub Maximal	Strain Gauged ?
1	4	Torsion	Fully Potted	Max	No
2	9	Torsion	Fully Potted/Bolted	Max	No
3	6	Torsion	Fully Potted	Max	No
4	6	Torsion/Compression	Fully Potted/Bolted/Moulded	Max	No
5	3	Torsion/Compression	Moulded	Max	No
6	1	Torsion/Compression	Fully Potted	Sub	Yes
7	2	Torsion/Compression	Fully Potted	Sub	Yes

4.8 Chapter Summary

Analytical calculation, fracture testing and strain gauged sub-maximal testing were proposed for validation of the Finite Element modelling process. The key factors considered in these procedures are as follows:

- The storage and preparation of the bone samples used for physical testing was informed by the generalised procedures demonstrated in literature
- A servo-controlled, hydraulically actuated test apparatus was used, allowing for the controlled compressive and torsional loading of the samples throughout testing.
- The methodology undertaken for physical testing and constraining of the bone samples was primarily derived in order to accommodate the torsional loading regimen. Potting of the samples was considered as a suitable fixation method, and a means in which to isolate the mid-shaft in torsional testing. Additionally semi-potting allowed for the replication of the natural support *in-vivo* for compressive fracture loading regimens.
- Custom constraints were designed and manufactured to offer an improvement upon the design solutions demonstrated in literature. These offered a more rapid testing procedure, and provided instant alignment of the sample within the test rig once the potting process was complete.
- Fracture testing was utilised in torsional and compressive regimens, whilst sub-maximal loading was employed in strain-gauged laboratory validation.

5 Laboratory Testing Results

This chapter contains the results of the analytical calculation and physical fracture testing processes, including the cursory parameter identification that was undertaken during analytical calculation. The results are addressed in the order that physical testing was undertaken, with torsional testing considered first, followed by compressive fracture testing and analytical calculation.

5.1 Torsional Testing

The main aim of this study was to consider the behaviour of samples under torsional load and therefore to investigate the spiral fracture of porcine femora. Correspondingly the majority of samples were tested in torsion. Prior to fracture testing, analytical calculation was undertaken. The results for both analytical and physical testing are considered below.

5.1.1 Analytical Calculation

Due to the inherent complications in biomechanical simulation, it is difficult to ascertain accurate values for input parameters such as the assigned Young's modulus of a given sample. Consequently, a range of values for the input parameters was used during analytical calculation. Rather than providing an absolute result, this provides a second range of values with which to correlate the results from simulation and physical testing.

During the course of this thesis, a paper was published that considered the effect of bone fixation devices in fractured and fixated porcine femoral samples [166]. In the study, porcine femurs were set in a metallic compound and increasing torque was applied until fracture was induced. The majority of the results within that paper were incomparable with the testing undertaken here due to the induced fractures, defects and fixation devices; however a control group (with no fixation devices) was also included in the paper. This group provided a mean maximum permissible torque of 83.67 Nm and a mean maximum rotational displacement of 17.95 degrees.

The result of the analytical calculation for rotational deflection was assessed while changing the inputted shear modulus, initially using shear moduli for human and bovine samples that had been derived physically in literature in combination with Eq.5.1 [62, 200]. In addition, values for shear modulus were used that were based on Young's modulus *(E)* derived in bend testing of porcine samples in literature [147], and as measured during the physical testing of porcine samples as discussed in Chapter 3. Finally, values were used that had been calculated from the average Young's modulus of material-mapped isolated diaphysis Finite Element models of porcine samples (process also shown in Chapter 3). These values were provided using the density-elasticity relationships from Morgan et al., Keller et al. and Snyder et al. [72, 73, 75].

A sample calculation is demonstrated below and the results of the comparison are shown in Figure 5.1. This shows that the result for deflection reduced as the applied shear modulus increases, as is to be expected with a stiffening structure. The results demonstrate a deflection of between 2.72 and 18.01 degrees for the tested section. The total length of the section tested in analytical calculation is approximately 55% of the full length of an average test sample (110 mm). No data was published for the tested gauge length within the study produced by Ho et al. [166]. Consequently, it is difficult to directly compare the results for deflection, however is would be reasonable to assume that the total gauge length ranged from the full length of a sample, to approximately 100 mm less than this value (to allow suitable space for the potted constraints). This assumption predicts shear moduli for the tested samples of between 1.39 GPa and 2.31 GPa. This initially seems low, however the calculation is based upon the geometry from a single CT scan in this study, which may be noticeably different from the geometry of samples tested by Ho et al. Additionally, the predicted result remains within the confines of the range plotted in Figure 5.1, falling approximately at the shear modulus from the material relationship defined by Snyder et al. [73].

Taking Bonney et al's Value for Young's Modulus:

$$E = 17.94\ GPa$$

Convert to Shear Modulus using Eq.4.3

$$E = 2G(1 + \nu)$$

Yields:

$$G = 7.592\ GPa$$

For a single slice of thickness (L) 1.25mm and Second Moment of Area $4.33x10^{-8}$
Applied Torque (T) 80Nm

$$\theta_s = \frac{TL}{\mathrm{GJ}}$$

Where $\theta_s$is the deflection of a single slice.
Yielding:

$$\theta_s = \frac{80\,\frac{1.25}{1000}}{7.592x10^{9} * 4.33x10^{-8}}$$

$$\theta_s = 0.0003\ radians = 0.017\ degrees$$

Integrate for each slice to yield total deflection for a shear modulus of 7.592 GPa:

$$\theta_T = 0.06551\ radians = 3.756\ degrees$$

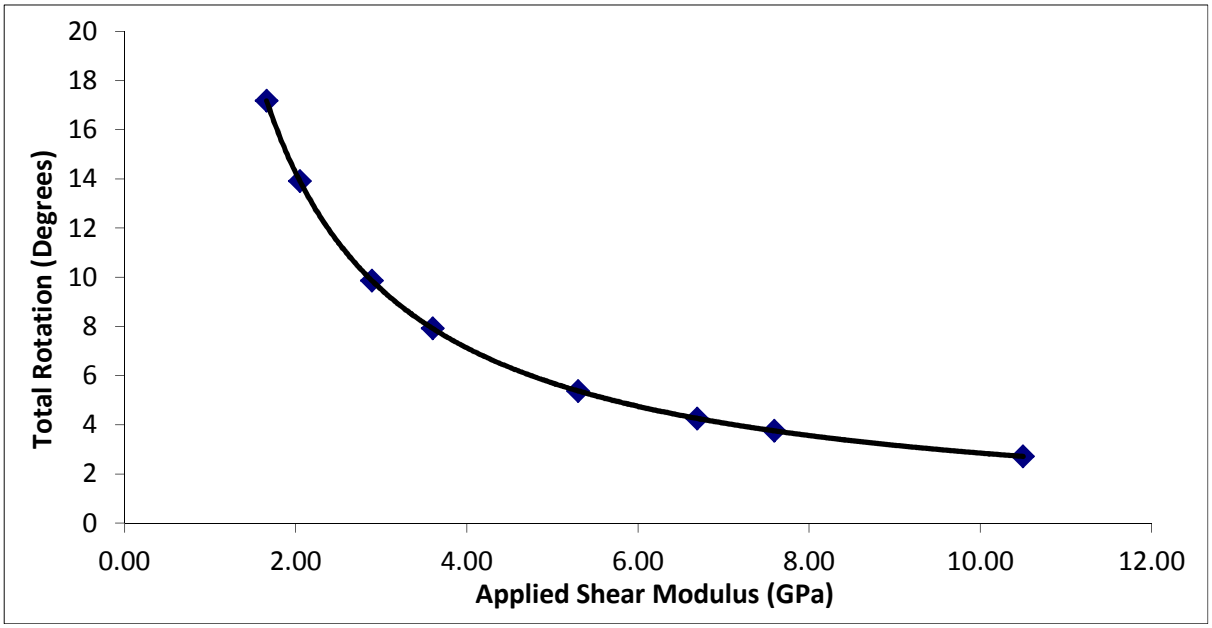

Figure 5.1. The results of material parameter changes for a given torque and geometry. The results show the general decreasing level of rotation as applied shear modulus increases.

Following the assessment of shear modulus, the changing maximum shear stress was calculated. This is defined by the equation in (*Eq*. 5.3) and relates to the applied force and second moment of area, as well as the radius at the external surface. Consequently in the composite ellipse solution it is possible to define the slices that experience the highest stress, and thus determine the regions of interest with respect to the assumed failure of the sample (on a maximum shear stress failure criterion).

$$\sigma = \left(\frac{T}{J}\right) r_{max} \qquad 5.3$$

Figure 5.2 shows the changing maximum shear stress noted within each of the transverse slices when tested to three differing torque values. The upper of these is the 83.67 Nm average failure load observed by Ho et al., whilst the lower values represent 50 and 20 Nm of applied torque respectively.

As can be seen the stress noted in each slice varies considerably, but is greater in the mid shaft of the sample. This is of importance, as it suggests that stress-based failure of the bone under torsional load would occur within the central mid-shaft region.

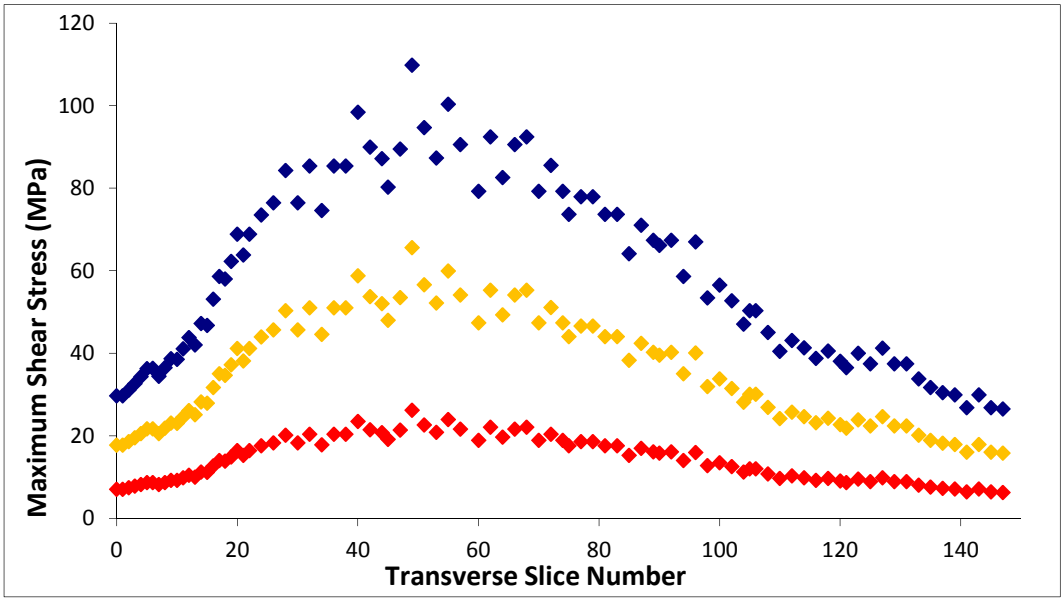

Figure 5.2. The maximum shear stress results noted for each transverse slice in the composite analytical calculation model for three different levels of applied torque.

The values change considerably from step to step, which highlights the inaccuracies of the geometry simplification process in analytical calculation.

The review of literature demonstrated very little information regarding the limiting shear values of bone, however Park et al. provide a tested value of 65-71 MPa for shear strength in human cortical bone taken from torsional testing of cylindrical samples of human femora [201]. The result observed in analytical calculation would suggest that the on the basis of individual slices this limit is too low, as the stress result is exceeded significantly in the 83.67 Nm iteration. Averaging the stress over the length of the samples provides an average of 58.9, 35.2 and 14.1 MPa respectively for each of the iterations, significantly *lower* than the failure stress. The high results for the individual slices demonstrate the need for a robust and well-defined failure criteria in addition to well-informed geometry. A 'failed area' may also be considered as has been demonstrated for prediction of the failure of the proximal femur and femoral neck under compression [45].

5.1.2 Discussion

Both the key limitation and key benefit of analytical calculation is the simplicity of the calculation. Whilst homogenous simplified models have been used in literature [189], the range of values provided here demonstrates the significant variation that is observed through changes to the material input

parameters. The solution provides a useful range of results for the purpose of comparison, but the simplified model has limitations in its capability for predicting ultimate and finite test results. Additional error may be incurred in the prediction of maximum surface stress as a result of the inability of the analytical calculation to adapt to rapid geometry changes. Despite the high stresses noted above, the analytical calculation technique is likely to under predict the maximum stresses expected within a Finite Element solution, within which the complex geometry and material mapping will define regions of stress concentration more accurately. This highlights the requirement for high resolution Finite Element simulation of complex biomechanical structures.

5.1.3 Fracture Testing

During analytical calculations, physical fracture testing was also undertaken in the laboratory. The samples were subjected to increasing torque until fracture occurred, allowing for the complete mapping of the load deflection curve across the entire load range; i.e. past the point of yield and through fracture. The data acquisition in the fracture testing process gave values for the torque at failure, and ultimate rotational deflection, which allowed comparison with similar tests undertaken in literature [67, 202]. Approximately 50% of the samples were CT scanned before testing to obtain the precise geometry for simulation and fracture prediction.

5.1.4 Results

In testing, torque at failure ranged from 59.7 to 94.1 Nm, with an average of 78.8 Nm (compared to average in literature of 83.67 Nm [166]). The corresponding range of deflections observed was from a minimum of 11.4 degrees to a maximum of 18.4 degrees. Average deflection for all samples was 14.1 degrees (literature average was 17.95 degrees).

(a)  (b) 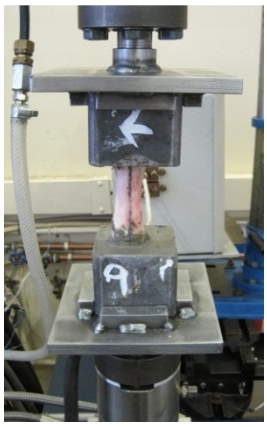

Figure 5.3. (a), A selection of potted samples for testing - clear differences in bone geometry can be noted. (b) A sample prior to testing with the direction of force application clearly indicated on the upper constraint.

This range in the values for torque and maximum deflection can be attributed to the varying geometry between samples. Clear differences were exhibited in diaphysis length, width and cortex thickness. It was initially considered that this effect would be minimised by obtaining the samples from a single source. However this was not the case and there was notable geometrical variation between samples, providing further justification for patient-specific modelling, even in very similar test groups. Figure 5.3 demonstrates the geometrical variation in a selection of the samples. The sample marked '1B' (far left) for example, has a notably wider distal cortex than the sample marked '2' (second from left) and the gauge length of the former is significantly reduced.

Figure 5.4 shows load deflection plots for five of the torsional fracture samples that demonstrated the typical behaviour observed within the laboratory. The plots have been curtailed at the point of fracture, which (due to the brittle nature of the fracture type) showed an instantaneous drop in force and corresponding increased strain response. Further plots of the additional fractured samples are provided in appendix A1.3, including a number of potentially anomalous results that will be discussed in later sections.

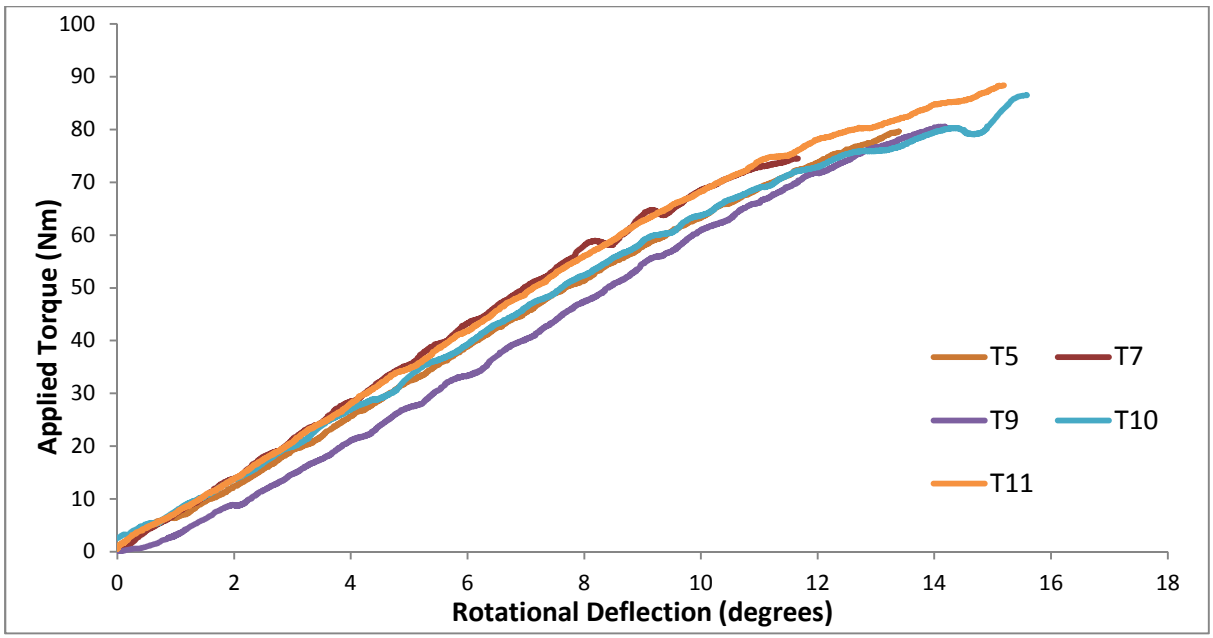

Figure 5.4. Load/deflection curves for five of the initial samples loaded to fracture under torsion. Data is cropped at the point of fracture for clarity.

As can be seen in Figure 5.4, the behaviour of the samples is linear for the majority of the load/deflection path, with some yielding/instability as the plot approaches the point of fracture. Samples T10 and T11 exhibit a slight departure from linearity towards the upper end of the deflection curve, however these samples are ultimately tougher, being able to withstand increased load and

deflection. Despite the decrease in apparent stiffness at higher load, these samples also demonstrate linearity for the majority of the load/deflection curve.

To examine the fracture mode in more detail, Figure 5.5 also plots the data points immediately following the point of brittle failure (T9). Two further data points are included, showing an almost instantaneous reduction in noted force and 'spring' in the calculated position of the crosshead. This 'spring' is a result of the sudden and complete failure of the sample. At this point the hydraulically forced crosshead attempted to maintain a consistent force, but with nothing to react against, demonstrated over rotation, before returning back to the appropriate position at the next data point. It should be noted that the results are sampled at 10.24 Hz, and consequently this failure, over shoot and return to correct position of the crosshead is undertaken in approximately 0.2 seconds.

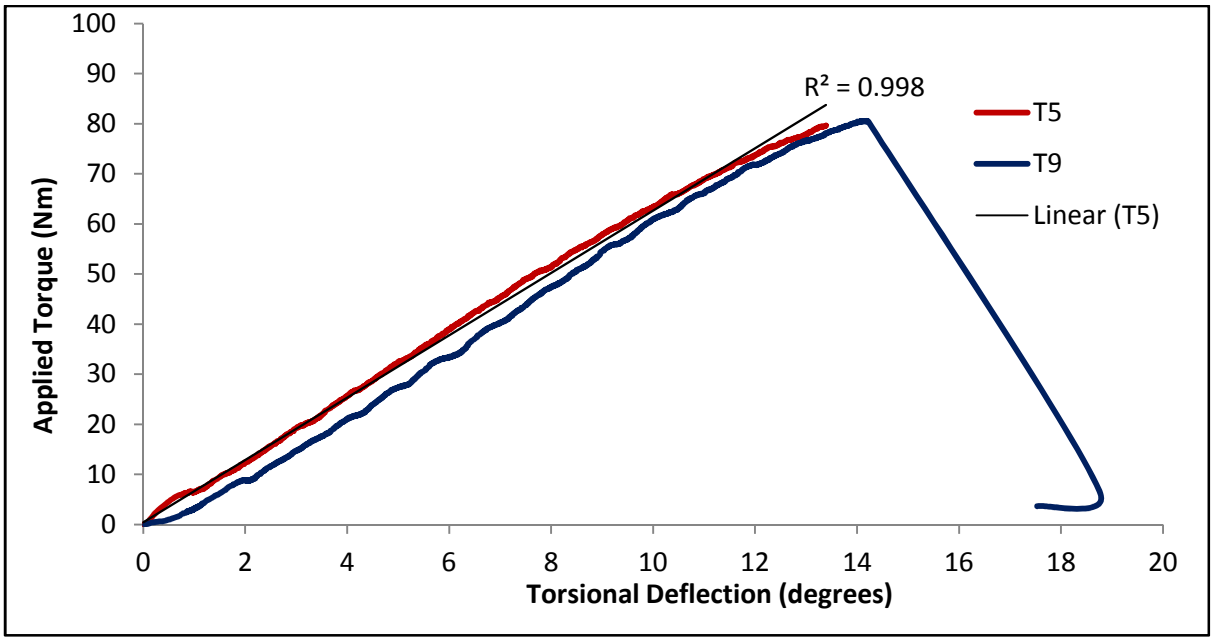

Figure 5.5. Load deflection curves for two samples. The plot of sample T9 has been continued to exhibit the immediate effects of brittle fracture. Linear regression performed upon the plot for sample T5 demonstrates the linearity under loading ($R^2 = 0.998$).

The second series in Figure 5.5 (labelled 'T5') addresses the linearity of the observed results in the sub-maximal region. R^2 and P value statistical tests were undertaken. The former is a measure (falling between 0 and 1) that demonstrates how well a regression line fits to a set of data. The latter measures the probability of obtaining a data set that is extreme as the observed result. Typically significance is determined by a P value that is less than 0.05 or 0.01 (depending on application). The strain response can be shown to be statistically linear ($R^2 = 0.998$, $P < 0.01$). Within the compiled sample group, the lowest R^2 value recorded was 0.961, with the average value for torsional tests of $R^2 = 0.988$ and the majority of samples returning $R^2 > 0.990$. The full results and statistical analyses are included in

Appendix A1.5. The consistent R^2 results demonstrate the linearity of the sub-maximal behaviour for torsion across the entire range of the data collected. P-values were also calculated for all samples, up to the point of yield and onset of non-linear behaviour, demonstrating $P < 0.01$ in all cases.

Of particular interest in figures 5.4 and 5.5 is that the strain response of each of the samples is largely similar. The test were undertaken to determine the point of fracture, rather than as strict material tests, and consequently the boundary conditions such as the potting depth changed from sample to sample. Consequently direct comparison of the behaviour is potentially flawed. However, despite differing toughness, fracture loads and yielding towards the fracture point, the gradient (demonstrating the arbitrary 'stiffness' of the sample) of each sample is shown to be similar. Analysis of the arbitrary stiffness ultimately demonstrated that the least stiff sample in testing demonstrated a deflection that was 47% higher than the stiffest sample in testing. Average arbitrary stiffness (arbitrary due to the exclusion of geometry in calculation) for all samples in test was approximately 6.7 Nm/mm.

Videos were recorded of a selected number of tests, but due to the fast-acting brittle fracture and (relatively) low frame rate of the recording equipment, little data could be taken from the images. High-speed video may improve this, and could be considered in future testing. Figure 5.6 shows stills from a sample video. The upper crosshead can be seen to rotate between frames, but the frame rate and resolution of the video meant that measurements could not be made regarding the fracture initiation or propagation.

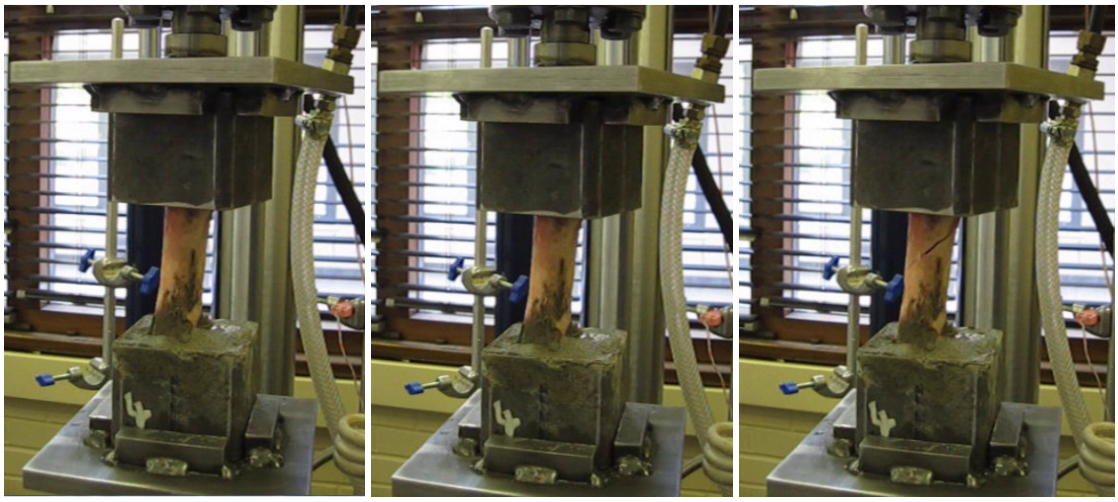

Figure 5.6. Three video stills taken from filming during torsional fracture testing.

5.1.5 Post fracture sample examination

Following fracture, the samples were removed from their constraints, and the fracture pattern was examined. General behaviour exhibited was that of a clean, helical fracture spanning the entire length of the diaphysis. A small percentage (approximately 20%) of samples displayed comminuted

fractures, with displaced sections of cortex. These pieces were retained. A selection of samples were reconstructed including any displaced fragments and re-scanned, allowing the remodelling of the fractured bone samples as shown in Figure 5.7. This recreation of geometry allowed for the examination of any signs of inelasticity and plasticity. Plastic behaviour would have been exhibited through stretching and tearing at the fracture edge. This plasticity was not observed for any of the fractured samples, confirming the linearity of the failure mode, and indicating that describing fracture using a strain-based failure criterion may be most appropriate.

The fracture line can be clearly seen in Figure 5.6. at the lower portion of the bone in the lateral view of the computational mask, rising through the anterior face and finally showing a change in direction as the fracture conforms on the medial face. The orientation of the fracture route was dependent upon the loading direction, as defined by the side of the animal from which the sample was taken.

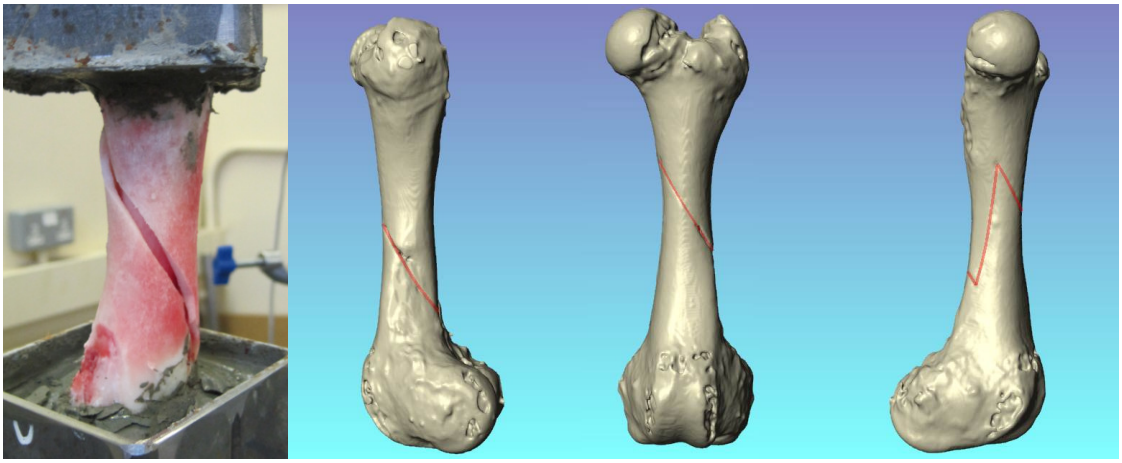

Figure 5.7. Photograph shows the spiral fracture in the sample mid-shaft. This was then computationally reconstructed to examine the brittle nature of the fracture.

5.1.6 Discussion

The initial laboratory testing of torsion tested to fracture performed favourably, with load/deflection results plots confirming that the fracture was occurring in a brittle fashion with linear-elastic sub maximal behaviour. The result demonstrates that whilst bone material can be shown to be anisotropic on a fine scale, the combined effect of the geometry and bone material is such that the structure as whole displays linear characteristics when tested in torsion. This is a key result in the testing process, as it dictates that it is valid to utilise linear-elastic material models. This reduces modelling complexity, vastly reducing the solve time of the computational process. Additionally the result confirms that the linearity of the proposed greyscale-density and density-elasticity relationships are appropriate for torsional simulation.

The results were comparable with those in Ho et al.'s control group (applied torque at 83.67 Nm, max rotational displacement 17.95 degrees) with this average falling within the range of values observed in testing (59.7 to 94.1 Nm, 11.4 to 18.4 degrees) [166]. The average fracture load was lower in this study (78.8 Nm, 14.1 degrees); however, as observed, the varying geometry of the samples within the test contributed to this variation, and with no accurate geometrical description provided by Ho et al, a direct comparison is ultimately difficult.

Comparing the results with those observed during analytical calculation demonstrates that a shear modulus of approximately 2.14 GPa would be most appropriate for the samples average. This (using linear conversion assumptions and an assumed Poisson's Ratio of 0.3) provides an estimation of 5.56 GPa for the average bending modulus of the porcine samples. This is within the range of values produced from the density-elasticity relationships from Snyder et al. and Morgan et al. [72, 73].

5.1.7 Potential Limitations

The laboratory testing confirmed the applicability of linear-elastic models, showing published relationships for human bone may be appropriate for simulation and demonstrating that the constraint design could be tested successfully; however there were a number of minor limitations found during the physical testing.

Misalignment of the bone sample

The first of these limitations was incurred due to the inherent geometry of the samples. Average epicondylar width of all tested samples was found to be 59.66 +/-1.01 mm. However, this dimension in some of the larger samples approached 64 mm, reducing the space in which to align the samples within the constraints. Additionally, due to the nature of the joint geometry, the centre of mass of the cortex is aligned towards the anterior (frontal) face. This has the potential to result in error with regards to the alignment of the sample within the test constraints.

This limitation is demonstrated visually in Figure 5.9. The images detail the displacement of the centre of the cortex from the centre of rotation at the distal end, resulting in the anterior/posterior angle as shown in the final image. As can be seen the centre of rotation is highlighted by the green circle, whilst the position of the cortex above the distal end is shown in the form of a dashed red ring. The second image shows how the narrowing geometry and alignment of the cortex, provides better alignment at the proximal region.

This misalignment has the potential to deviate the testing regimen from pure torsion. Whilst the alignment may not necessarily constitute a significant loss of accuracy, it should be accounted for when undertaking matched computational simulation.

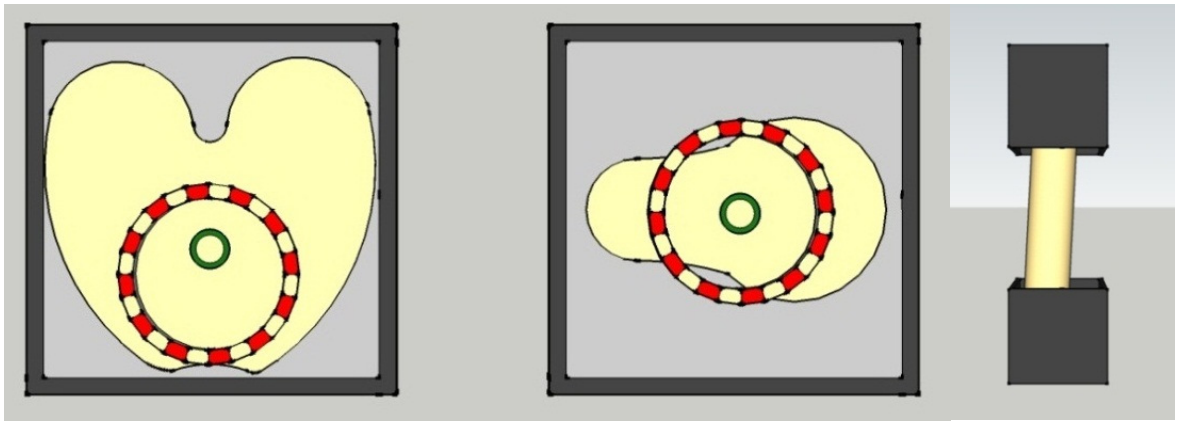

Figure 5.9. Sketched alignment of one of the larger samples within the constraints, firstly showing a transverse view of the distal joint; secondly the hip region set in the centre of the constraint; and finally the resulting misalignment observed from the lateral view during testing.

Isolation of the mid-shaft.

Another limitation of the testing procedure is the true gauge length and the point at which the sample should be 'cropped' to match the constraints. The full depth potting and the design of the testing constraints were intended to isolate the bone mid-shaft completely during testing. Despite this, force is applied at the keyway section of the outer constraint, and any movement in this region should be considered when comparing to computational results.

5.2 Compressive Testing

Compression and compressive failure were tested within the laboratory and through analytical calculation to investigate the capability of the modelling technique's assessment of alternative load paths. This provided a better understanding of the behaviour of the porcine samples, and a means to compare the accuracy achieved within this thesis with the accuracy detailed in literature.

5.2.1 Analytical Calculation

As with the torsional testing protocol, the first stage of calculation within compressive testing was analytical calculation. The geometry created was identical to that used for the torsional tests. Engineering theory for homogenous systems states that the failure of a beam with constant cross section under compression is either defined by true compressive failure, through buckling failure or through some combination of the two failure modes. To simplify the analytical calculation assessment, the vertical deflection of the sample was considered to follow Hooke's Law of proportionality, in which the deflection of the sample maintains a constant relationship with the

applied force. In actuality this is potentially flawed due to the manner in which bending moment and consequent buckling is induced, as described in Chapter 4; however, at small deflections the simplification is applicable.

5.2.2 Loading

Testing during the compressive study was performed under the assumption of a static loading case. Strain rate was controlled centrally using the ASP rig. Helgason et al.'s review normalised strain rates for linear compression to allow direct comparison of mapping relationships, selecting a strain rate of 0.01 s^{-1} [19]. Despite this, CT-FE studies have demonstrated strain rates ranging from as slow as 0.00001 s^{-1} to as fast as 10 s^{-1} with no significant differences reported as a result [179, 203]. The strain rate used in laboratory tests was determined through the movement of the upper crosshead and set a rate of 0.5 mm/s. This provides a strain rate of between 0.005 s^{-1} and 0.006 s^{-1} depending on exposed sample length. To match the manner in which force was applied in the laboratory, the analytical calculation was performed with the assumption of a distributed load at the upper surface of the composite ellipse, ignoring any local deformation effects on the top surface.

Homogenous Young's modulus were assigned throughout the analytical calculation in compressive tests. As with torsional testing this homogenous value was manipulated to observe the effects of changes to the structural stiffness.

5.2.3 Analytical Calculation Results

For each iteration, a single homogenous material value was applied to the composite solution. Changes to the assigned material property are detailed below (Figure 5.11). As can be seen the effect of material property with respect to observed deflection is a power-based relationship, as shown during torsional calculation.

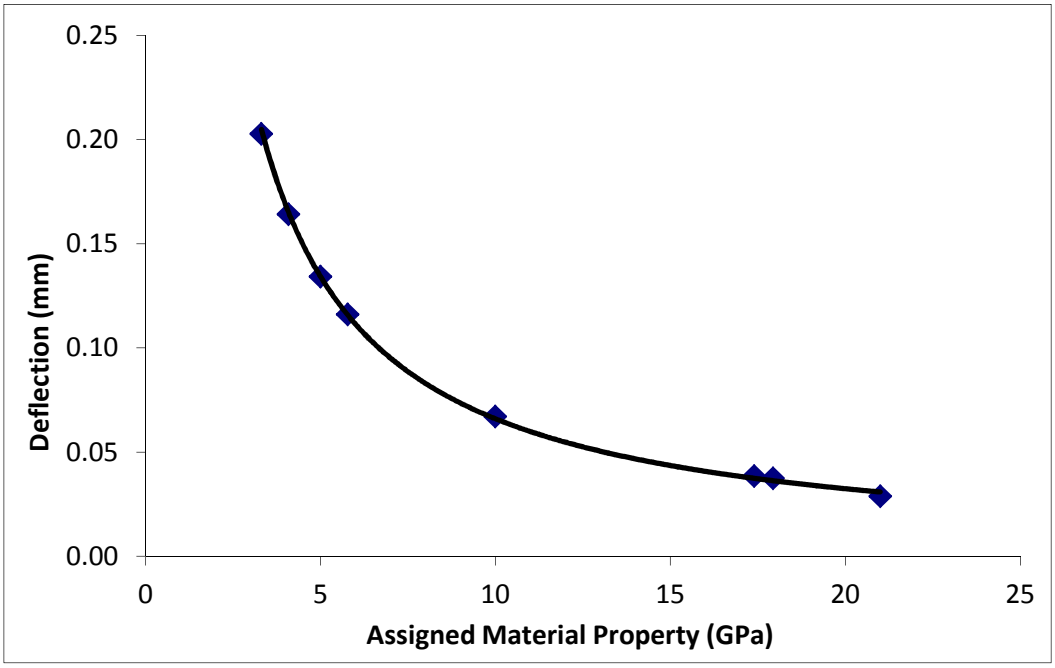

Figure 5.11. Vertical deflection of the composite ellipse solution with varying Young's modulus for an applied compressive load of 2 kN.

The plot shows deflection in mm, and notably produces a low level of absolute deflection throughout analytical calculation, with a maximum change in length of 0.18% for the least stiff material property. The low values of deflection demonstrates the importance of correctly defining the vertical behaviour of samples during physical bend testing, as inaccuracy in the measuring technique may affect the ability to assess such small changes. Changing the material property value to that defined via physical testing, and via the testing carried out by Bonney et al. provided a reduced deflection, in the order of 0.04 mm for a 2 kN load (0.035% of original) [147]. Failure criteria based upon maximum principal strain denotes a strain limit of 0.0104 for cortical bone material in compression [88].

Plotting the response on a slice-by-slice basis (as demonstrated in Figure 5.12) gives a comparison of the behaviour of the sample at a local level and consequently gives a better assessment of the likelihood of local failure. As noted previously the majority of the deflection is within the central section of the sample. The pattern differs from that shown within the torsional load application due to the manner in which the relationships are derived. Here the results are based upon the cross sectional area of each slice, which varies differently from the changing second moment of area that must be calculated for torsional loading.

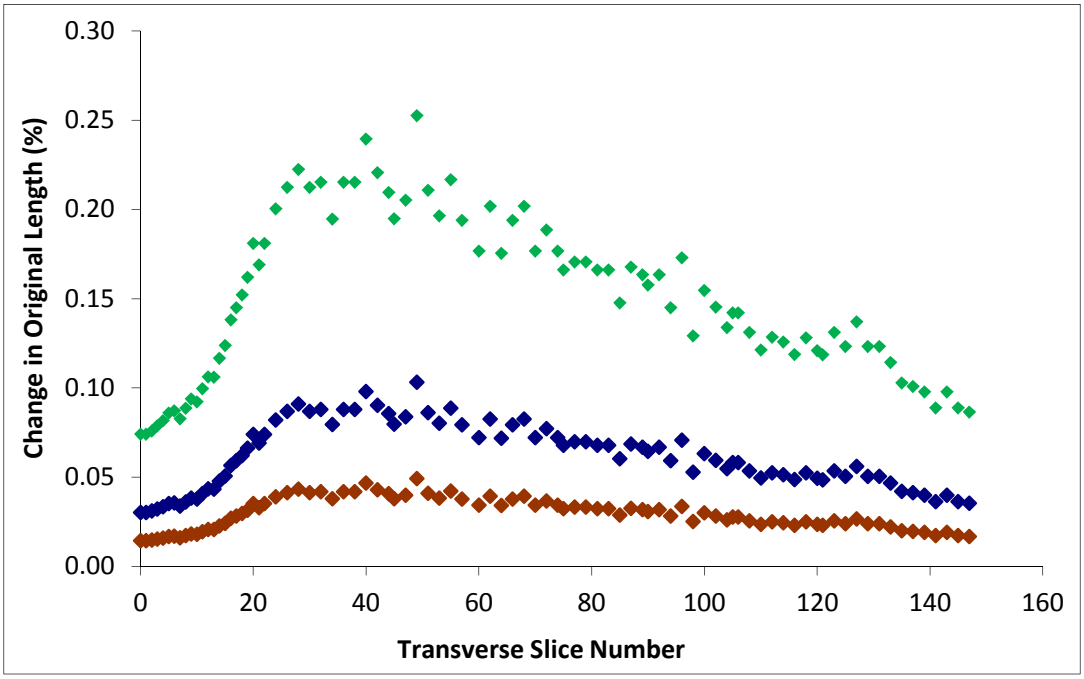

Figure 5.12 Vertical deflection for the composite solution on a slice-by-slice basis for each of the transverse slices at varying levels of assigned Young's modulus.

5.2.4 Discussion

The results for the ellipse solution demonstrate the limitations of testing a single value for axial deflection only, notably that the results calculated on the basis of cortical bone material only (as used for compressive deflection in analytical calculation) are small, and thus high resolution data capture would be required in the laboratory to ensure that measurement error is minimised. It should be considered that the inclusion of any soft tissue or constraint surface interaction is likely to dwarf the small percentage changes detailed in this homogenous material testing process, and thus care must be taken to accurately detail the compressive behaviour at the surface of the sample.

The simplified ellipse model ultimately has limitations in its capability for predicting the behaviour of the physical sample within the laboratory. As can be seen, the compiled results for vertical deflection demonstrate total strain within the sample that is greater than, or approaching the published strain limit of the material, at a relatively low axial load of 2 kN. Reviewing the strain data on a local slice-by-slice basis shows the strain in each transverse slice, providing a better estimation of the point of yield (assuming the sample fails via compressive rather than buckling failure). Very few results are published for the total physical deflection of femoral samples under compressive load, with a preference shown for strain gauging and measurement of the strain behaviour at local level [46, 70].

5.2.5 Physical Testing

Samples were tested to destruction in compression to allow the plotting of the complete load deflection curve and to analyse the linearity (or lack of) of the system as a whole. The tests also determined the resistance to compressive and buckling failure of the bone samples. The samples were prepared using the standard testing methodology detailed in Chapter 4, used moulded constraints to replicate the joints as found *in vivo.*

The samples were unconstrained rotationally, allowing free rotation throughout the physical loading process. The rotational load and position was recorded throughout to take account of this effect. In addition, the vertical displacement of the crosshead (and consequent displacement of the sample) and the axial load applied were sampled throughout the loading and unloading process.

Recording the unloading process aided in the observation of hysteresis and non-linear material characteristics in the test samples that were not tested to destruction. In the samples that were tested to destruction, data was recorded past the onset of failure, such that the load/deflection curve beyond failure could be retrospectively analysed.

5.2.6 Observed Results

Brittle failure was induced in all of the samples fractured within the laboratory. This fracture was indicated by a rapid and complete loss of supported load, increased strain response and distinctly audible failure. Visual inspection of the cortex was undertaken for all samples following the physical testing procedure.

Maximum permissible axial load ranged from 8.83 to 11.99 kN with an average of 10.32 kN. The corresponding range of maximum deflections incurred at the point of total failure was from a minimum of 7.78 mm to a maximum recorded value of 9.99 mm. Average deflection for all samples was 9.13 millimetres. The range in values for both maximum permissible load and maximum observed deflection can be attributed to the varying geometry between samples, notably the sample width and the total sample length.

It is prudent to note that as a result of this cursory examination, the risk of fracture of porcine femora through compression during the normal life of the animal is low. An average failure load of 10.3 kN is approximately equivalent to a static weight of 105 kg, significantly higher than the expected weight of the animal (approximately 60 kg at the age of slaughter). In addition, as a quadruped with relatively low mobility, it would be reasonable to assume the load would be shared across the animals' limbs.

5.2.7 Post fracture sample examination

Following fracture, each of the bone samples was removed from the constraints and the fracture pattern was examined. The behaviour exhibited was typically that of compressive failure of the medial

face, incorporating a general displacement of material rather than a clean, clear crack line. As discussed previously, this is not true compressive failure across the cortex, but rather compressive failure in an isolated location due to buckling. Buckling fracture is indicated by the compressive failure of the interior face (the region under greatest compressive strain, whilst the lateral face would be under significant tensile load (although no visible failure occurred in this region). None of the samples exhibited loss of material (comminuted fracture) as had been noted during the torsional testing regimen.

The failure along the medial face is clearly visible in Figure 5.13, appearing beneath the femoral head. This failure location was observed for all tested samples, confirming that the constraint had been designed appropriately, and provided the majority of force to the femoral head. Applying force in this location is a deviation from the manner in which vertical force is applied in the composite ellipse analytical calculation, but better replicates loading *in vivo*. The application of force at this point also provides a natural bending moment along the cortex, instigating a slight off-axis force due to the lateral distance from the centre of the cross section. This bending moment increases the propensity to buckling failure, as was observed in physical testing.

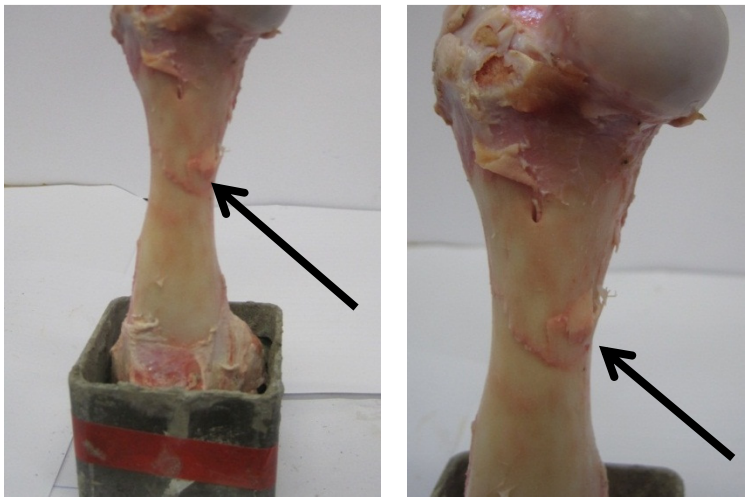

Figure 5.13. A single sample tested to destruction under compressive loading. As can be seen, fracture of the sample has occurred beneath the femoral head, along the medial face.

5.2.8 Numerical Test Results

Figure 5.14 shows an example of the load/displacement recordings that were taken during compressive testing. The test shown is sample C1, which exhibited a maximum axial deflection of 7.30 mm (in actuality this result is negative due to the compressive nature of the loading regimen) at a maximum recorded compressive axial load of 9.19 kN, before failure occurred. The plot also shows the behaviour of the sample immediately following fracture. Fracture is noted by the rapid step change in the supported load. Following the occurrence of fracture, the plot shows the response of the

bone to further loading, at which point the buckled structure continues to support a significantly reduced axial load. At this stage the strain response is increased dramatically, with a noticeable decrease in the apparent stiffness of the sample. The plot continues after this point to show the unloading cycle, in which the crosshead is raised back to the starting position, exhibiting slight negative load at the load cell, as the buckled sample is returned to its starting positions.

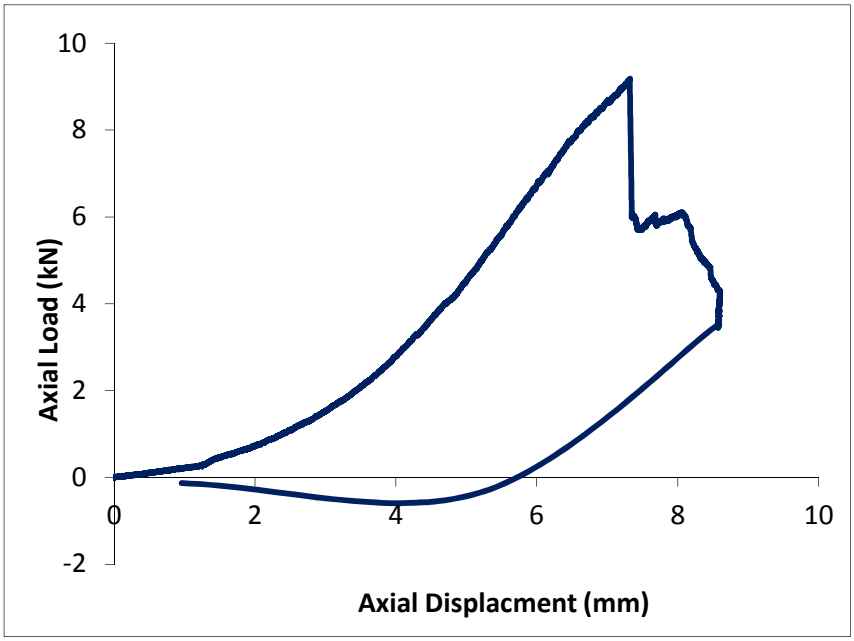

Figure 5.14. load deflection curves for the axial compressive loading and failure of sample C1. Data is recorded for both the immediate effect following failure, and the retraction cycle

Figure 5.15 shows a comparison of three samples that were loaded under compression to failure. The plots are curtailed at the point of fracture for clarity. An 'S' shape is observed during testing, which suggests some non-linearity of the material response. Further examination shows that all samples exhibited a 'take up' or 'toe in' period relating to approximately the first 4 mm of deflection, before the apparent stiffness rapidly increased, and a more linear response was observed. Towards the end of the loading regimen, the strain increases (shown by the curving of the plot as it approaches the final fracture point). Whilst there are notable differences in the values of fracture load and deflection, as with the torsional comparisons, the plot demonstrates that the gradient (and ergo apparent stiffness) of the central portion is comparable between all of the tested samples. Samples C1 and C3b are notably similar, whilst sample C2 shows a slight reduction in the observed gradient and consequently a reduced stiffness response.

A single result is shown in Figure 5.16. to examine the strain response of the sample in more detail and to consider the linearity of the central section of the result in isolation. The plot demonstrates an 'S' shaped load path. The early portion of non-linearity can be attributed to the construction of both

the sample and the constraint used. As detailed in the methodology sections, the cortex is prepared via the scraping of all soft tissue such that only hard, well-calcified bone is retained. However, upon the epiphysis this process is more difficult, and elements of cartilage and soft tissue remain upon the surface. Cartilage is more compressible than calcified bone, and the consistency of this 'take up' period observed from sample to sample in the results suggests that this layer (which retains a relatively constant thickness between samples) may be responsible for the initial phase of loading which exhibits lower stiffness, incurring deflection of approximately 1 mm.

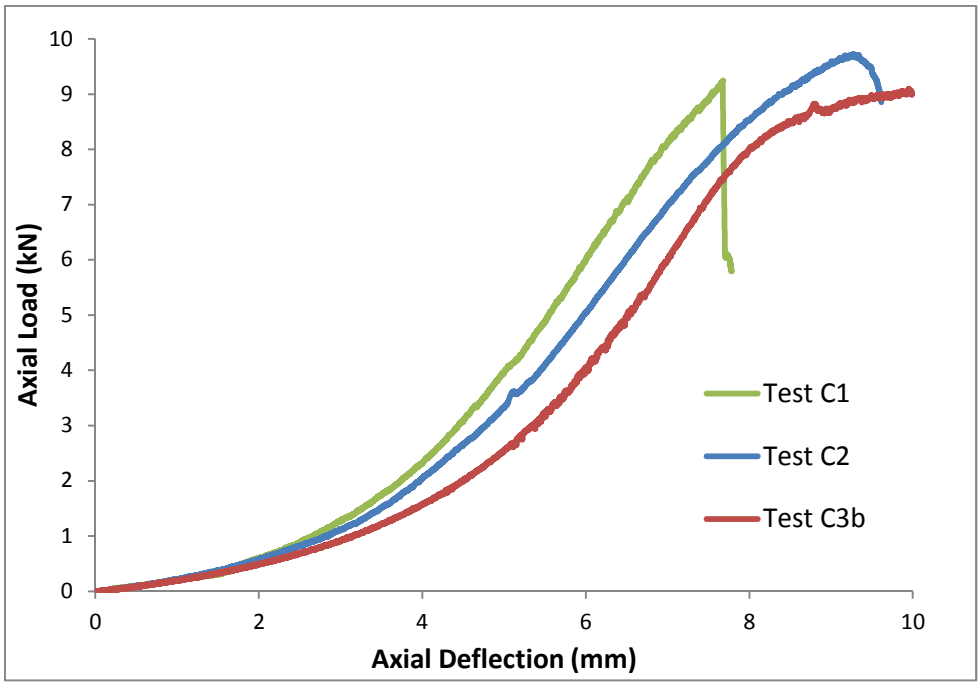

Figure 5.15. Load/deflection curves for the axial compressive loading of samples C1, C2 and C3b.

The hypothesis that this result is a response to soft tissue behaviour if corroborated by the results of compressive testing using the torsional test constraints (potted metaphyses). These tests (considered in detail in Chapter 6) considered the behaviour of the diaphysis only, and had a significantly reduced 'take up' period, demonstrating a significantly more linear response throughout the load/deflection path (Figure 6.4(a)). In those tests, the samples demonstrated linearity after approximately 0.3 to 0.4 mm of axial deflection.

The 'non-linearity' as the samples approach the total failure load a result of the propensity of the sample to exhibit buckling failure and the onset of yielding. At the start of testing, force is applied at the femoral head, which induces a small bending moment within the shaft as the head is aligned to the medial side of the centroid of the cortex. As the sample is compressed at higher loads, the onset of buckling yield further displaces the centroid. This lateral displacement has the effect of increasing the

bending moment applied to the bone, which increases the rate of buckling of the sample, and consequently may increases the observed yielding rate.

Despite the integrity retained in the sample as a whole, the observed increase in yield rate can plausibly be attributed to failure of the sample on the smaller scale and the production of 'microcracks'. Bone samples that have developed microcracks and show signs of microdamage have been demonstrated to display a reduction in energy absorption during fracture [204]. In particular, in compressional loading the observation of microdamage was shown to incur a reduction in energy absorption by as much as 40%. Closer investigation of the local effects of microdamage demonstrate that the small-scale geometry and internal features within more regular cortical bone are responsible for the propensity to crack, with the osteocyte lacunae (fluid filled cavities within the bone material that allow substances such as calcium to be transported through the bone matrix) providing stress risers within the structure [205].

Isolating the 'non-linearity' as discussed above, and observing the behaviour in the central portion of the results provides results that map more accurately to a linear assumption. This 'stiffness' taken from the linear portion describes the reaction of the bone structure to sub-maximal compressive forces, and assessment between samples can be undertaken by looking at this value in isolation.

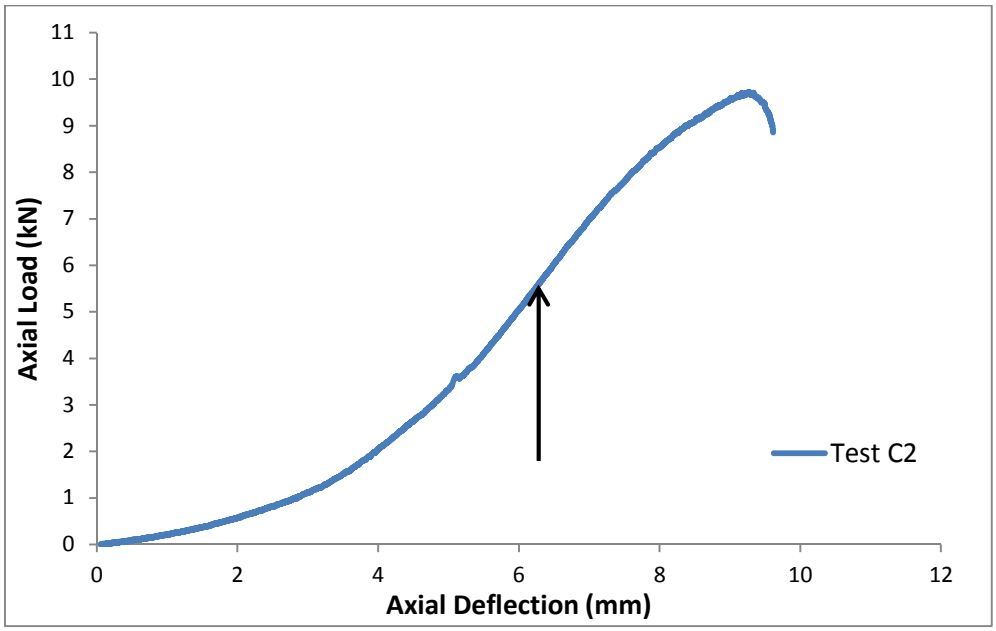

Figure 5.16. Load/deflection curves for the axial compressive loading of sample C2. The region at which linear behaviour is determined is highlighted.

The relative stiffness of each of the samples under testing was examined through comparative assessment of this linear portion from each of the load/deflection plots. Sample C2 provided the

stiffest result, with the least stiff sample showing a stiffness reduction of almost 15%. The samples typically exhibited linear behaviour over a total deflection of approximately 4 mm in the central portion of the load/deflection curve.

5.2.9 Validation of Test Constraints

It was considered that for completeness and to increase confidence when using the compressive test results, an investigation of the phenomenon of the 'take up' should be undertaken to ensure no additional phenomena aside from the compression of the outer layer of the epiphyses into the constraints were being accounted for in simulation.

To assess any 'slack' within the compressive system, a significantly stiffer sample was placed under compressive testing for comparison with the bone sample behaviour. A 200 mm long sample of 30 mm diameter mild steel bar was cemented into the constraints using the same protocol used for the compressive bone testing. The potted bar and constraints were then placed within the ASP rig, and compressive force was applied in stages, with deflection and load recorded at all times. The typical failure load for bone was around 5-6 kN and consequently the steel sample was loaded up to approximately three times this figure, up to a maximum of 15 kN.

The results, as shown in Figure 5.17 show a similar, but reduced amount of 'take up' as the steel sample settles into the constraints, in this case with a total deflection of around 1 mm, before linearity of testing is observed. It should be noted that the results plot the deflection of not only the sample, but also the entire system, incorporating the constraints and the additional length within the test rig. The gauge length of the test rig as a whole is significantly higher than the 200 mm sample length, and includes the two-part constraints as well as the additional length between the hydraulic actuator, load cell and the cross head. Consequently the behaviour of the sample is exhibiting elements of machine compliance, in which the true sample length tested exhibits increased deflection above and beyond that expected for the tested sample. One way to overcome this may be through the use of clipped gauges to assess the behavior of the sample is isolation; however, these were not included during testing. Steps that are not typically observed for compressive loading are shown in the plot. These are a result of the discrete loading intervals used, as the sample exhibits elastic relaxation as the loading is curtailed. Typical compressive results do not exhibit this behaviour due to the continuously increasing nature of the loading regimen used.

The deflection of the potted steel sample was significantly higher than the material-only value, as shown in Figure 5.17. This suggests that the testing apparatus exhibits elements of vertical deflection. It was considered that the results for deflection within the system should be used to offset the results obtained in compression throughout testing. Regression on the deflection results for the steel sample was undertaken. A polynomial relationship was fitted to the initial 3.5mm of deflection (Eq.5.4), following which a linear offset was applied which had been derived from the linear aspect of the steel

sample result (Eq.5.5). The ideal material-only response for the steel bar was subtracted from these offset values. This provided an offset that could be applied to each compressive test, ensuring that the test applies to the bone sample only, and therefore takes into account the potted end constraints and the deflection of the test equipment as a whole.

$$\text{For } x < 3.5mm \; y = y_1 - \left((-0.0707x^2 + 0.3425x - 0.011) + x\frac{\left(\frac{25}{1000}\right)^3}{200x10^9 I} \right) \quad 5.4$$

$$\text{For } x > 3.5mm \; y = y_1 - \left(0.1812x + x\frac{\left(\frac{25}{1000}\right)^3}{200x10^9 * I} \right) \quad 5.5$$

$$\text{Where } I = \frac{\pi}{4}\left(\frac{25}{1000}\right)^4 \quad 5.6$$

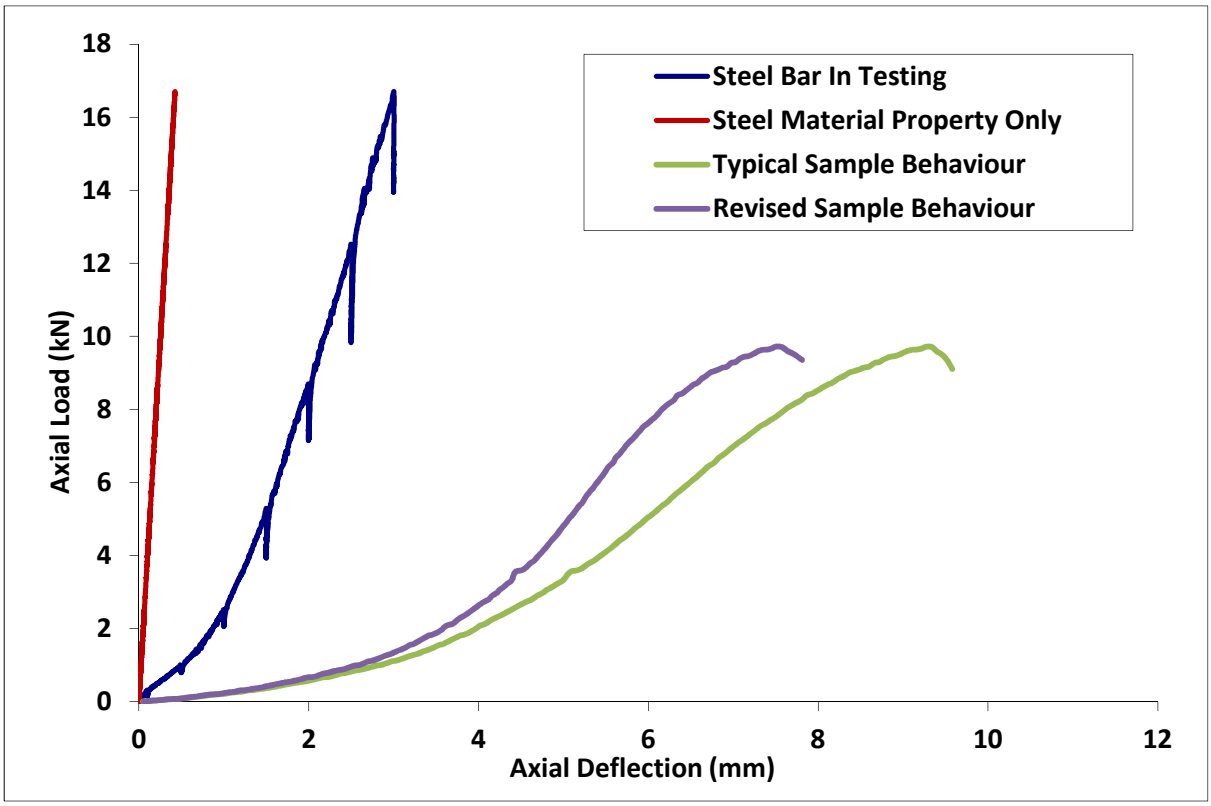

Figure 5.17. The response to loading of the steel bar using standard bone testing constraints compared to the theoretical response on a material-only basis, and a typical bone sample.

5.2.9 Discussion

The compressive failure of the porcine samples demonstrated a predominantly elastic response throughout testing, following some initial take up and before increased yielding nearing the point of failure. Linear regression exercises performed on the bulk portion of the results plots confirmed that the use of linear material models was appropriate for the bone behaviour as a whole, despite the occurrence of non-linear portions within the testing results. It was considered that the non-linearity of loading response at low level was a response to the inclusion of soft tissue at the epiphysis surface. This effect can be largely ignored in simulation, as the thresholding process used within the *in silico* modelling is selected to reduce the inclusion of soft tissue elements. This may represent a significant consideration in musculoskeletal modelling, where the inclusion of soft tissue is required. The results of testing a comparatively incompressible steel bar were determined to identify the components of this 'take up' region that were due to machine compliance. These results were used to correct the slope of the deflection results of the porcine samples, to ensure that accuracy in testing was retained. The mode of failure in compressive testing demonstrated the effects of bending and buckling through a noticeable lateral displacement of the mid-shaft (although this displacement was not measured in physical testing) in addition to compressive yield on the medial face, confirming the difficulties in the assessment of failure patterns through compressive loading at larger deflection, as defined in the Euler buckling theory.

The fundamental observation of the compressive loading process was that the porcine bones failed in the mid-shaft rather than in the femoral neck. This is a departure from the results commonly observed in human studies, in which the femoral neck is generally observed as the region of interest in fracture studies [20, 21, 27]. The change in failure mode is considered to be the result of one of two possibilities:

I. The inherent differences in the geometry of human and porcine bone mean that porcine bone has a greater propensity for failure of the mid shaft, and for human bone a propensity for fracture in the femoral neck. This is likely to be a result of the proximal breadth, which (being significantly wider in human samples) induces significant tensile strain in the proximal face of the femoral neck.

II. The manner in which the porcine bone was constrained did not apply load to the femoral head only, and distributed the load upon both the femoral neck and greater trochanter.

A final consideration is the manner in which samples are constrained during testing. Literature regarding fracture of the proximal femur regularly demonstrates constraining of as much as 60 % of the length of the proximal femur (Figure 5.18). This significantly reduces the slenderness ratio as

detailed in Chapter 4, increasing the buckling load of the sample as a whole. The observed difference in failure mode demonstrates the requirement for subject-specific modelling, which would detail the region of maximum fracture risk in each bone type.

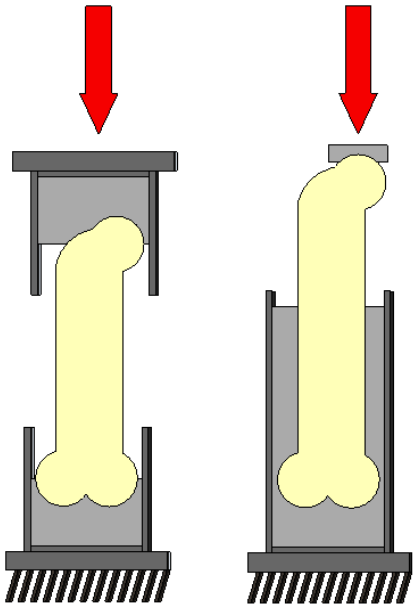

Figure 5.18. Sketches demonstrate the compressive testing method used in this thesis, and the method commonly used in literature. As can be seen the proportion of the mid-shaft that is constrained varies considerably between the two methodologies.

5.2.10 Limitations

Whilst four of the six test samples performed favourably and exhibited failure that was to be expected for this type of test, two of the samples (C3 and C4) exhibited behaviour that was not as expected. Figure 5.19 shows the load deflection plot for these one of these samples (C3), and typical plots for additional samples that behaved in the manner that was as expected (C1 and C2).

Post-testing investigation showed that an error was made during the constraints construction for these anomalous samples. The moulded ‘cups’ that had been created to mimic the proximal and distal surfaces had not cured appropriately before the removal of the bone sample, which resulted in an incorrectly moulded shape.

The product of this incorrect moulding was that the epiphyses of these two samples were forced into the narrower mould shape, causing significant deformation in these areas. The compression test results were therefore dictated by the compressive behaviour of forcing the epiphyses into the mould region, as opposed to the compressive behaviour of the sample as a whole. The results were retained for discussion, but omitted from any further comparison within the testing process.

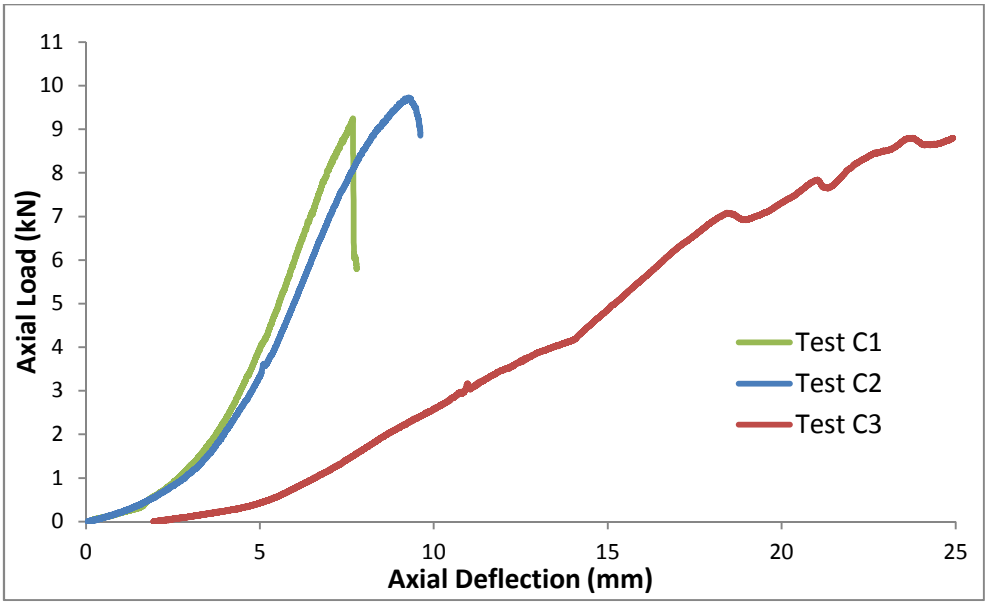

Figure 5.19. Load/deflection curves for the axial compressive loading of samples C1, C2 and C3. C3 demonstrates a significantly reduced resistance to loading, changing apparent stiffness, and an ultimate maximum deflection of more than 25 mm.

5.3 Chapter Summary

Physical testing of whole bone samples and analytical calculation of cropped samples were proposed as means with which to validate simulation. The fracture tests were completed successfully in all failure modes. The tests highlighted the importance of the resolution of data sampling, and the fine levels of control required to accurately record the strain response of the samples.

Analytical calculation provided a means with which to compare simplified results with those observed in literature. Additionally the methodology allowed for rapid investigation of the effects of changing input parameters such as the Young's modulus (although this was undertaken on a homogenous and simplified basis). The analytical calculation has limitations, including the isolation of the varying Young's modulus and construction of bone, and the simplified geometrical assumptions. The results consequently highlighted the requirement for more accurate behavioural depiction, as provided through Finite Element simulation.

Physical testing demonstrated the maximum permissible load and deflection in torsion and compression, as well the response to load throughout the load path. Torsional testing was undertaken successfully, with limitations regarding the constraints and alignment providing little effect on the linearity of the test results. Compressive loading differed, particularly in the manner in which the samples failed, notably bending and buckling, and displaying increased deflection over that calculated manually. The initial 'take-up' was considered to be the result of soft tissue at the bone surface, and linearity was observed in the results following this point. No attempt was made to quantify the

deflection of the potting material in isolation, and for completeness this may be advisable in future testing. The behaviour of the samples also differed from the behaviour demonstrated in literature, failing in the mid-shaft rather than within the femoral neck. This result could be considered further with simulation to determine the true cause of the result.

The results demonstrate the difficulty in using compressive loading to undertake material estimations, and demonstrated that torsional or tensional testing may be more appropriate for material parameter estimations and general depiction of whole bone behaviour. The physical testing results also highlighted the requirement for more accurate estimation of strain at a local level, to increase the accuracy of validation. No estimation was made for the strains at the surface during physical testing, which is ultimately a major consideration for validation purposes.

6 Comparison of Laboratory Testing and Simulation

Despite correlation with the results from analytical calculation and the clean elastic spiral fractures that were induced during fracture testing, the whole bone fracture tests alone are not sufficient for the validation of Finite Element simulation of bone. Further validation, in the form of stress and strain correlation is generally proposed in Finite Element studies, offering a means to determine the predictive accuracy of the simulation on a more refined basis. Studies within CT-FE literature have shown that strain gauging is the most accurate methodology to validate the simulation of bone [45, 70, 100, 199]. Consequently, strain gauged testing was proposed for this study to allow for the accurate portrayal of stress and strain behaviour at a local level. The strain gauging procedure also allows the results and accuracy achieved within this porcine study to be directly compared with the accuracy published in literature for human studies. Comparing with published figures demonstrates the appropriateness of simulating torsion and of utilising techniques such as the material mapping relationships, which were originally developed for simulating human samples on porcine bone.

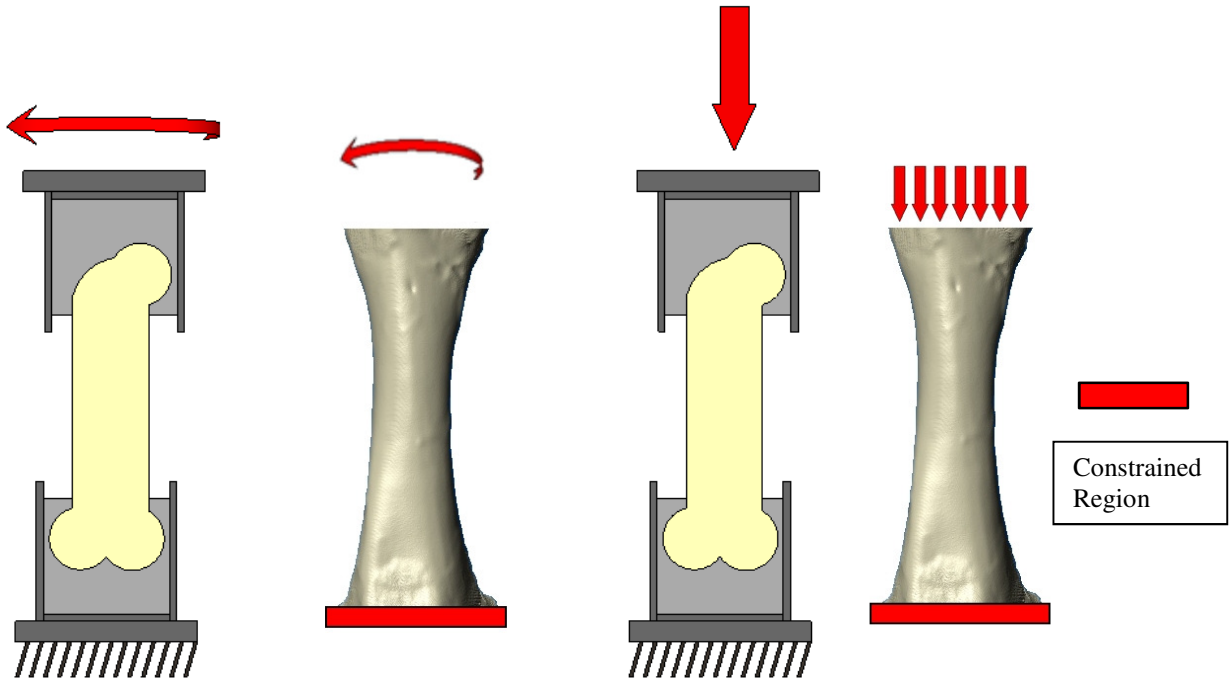

Figure 6.1 shows the arrangement for physical testing in torsion, simulation in torsion, physical testing in compression, and simulation in compression for the sub-maximal strain gauged process.

This chapter considers the strain gauge results, which were measured for sub maximal testing in both torsion and compression. Values for principal stress and principal strain were then determined from these strain results. The simulated stress and strain figures from the Finite Element simulation were correlated with those measured in the laboratory, allowing a comparison of the predicted figures (from simulation) with the observed figures (determined in the laboratory). It is this comparison of predicted

and observed results that determines the overall accuracy of the simulation procedure. Figure 6.1 shows the arrangement for simulation and physical testing for strain gauged correlation. All samples were fully potted throughout testing.

6.1 Strain Gauge Results

The methodology used to measure the strain response of the samples for each individual load step is detailed in the general methodology chapter (Chapter 4). The sub-maximal loading in both torsion and compression was pre-determined to fall within the linear-elastic portion of each sample's strain curve, and consequently the ideal observation in the laboratory would be complete linearity in the strain results. This would be indicated by consistent proportionality between the applied load and the measured deflection. The samples were loaded in discrete intervals, with loading removed following the strain reading and then reapplied to the next loading interval. This ensured that the strain measurement for a given load could be checked and repeated, confirming that the value was both accurate and repeatable, and therefore that the sample as a whole was consistently behaving in the ideal linear manner.

6.1.1 Torsional Testing

Strain results were recorded for each of the nine individual gauges on the three tested samples (gauge arrangement shown in Figure 4.8). Three samples were tested (hereby known as SM1 – SM3). Figure 6.2 shows the results recorded for a single sample (in this case sample SM1). Linear regression was undertaken for each of the gauges, displaying R^2 values of above 0.99 for the majority of gauges ($P < 0.01$).

The reduced linearity noted in gauge number nine is likely to be due to the effect of inaccuracy in taking the strain reading, either through a delay in taking the reading and consequent relaxation of the sample, or through the error incurred whilst physically taking the reading. The gauges results were noted in discrete intervals, with the switching box typically displayed swinging variation of +/- 9 microstrain whilst the readings were taken. Necessarily this represents a larger error by proportion in the gauges returning lower average strain readings.

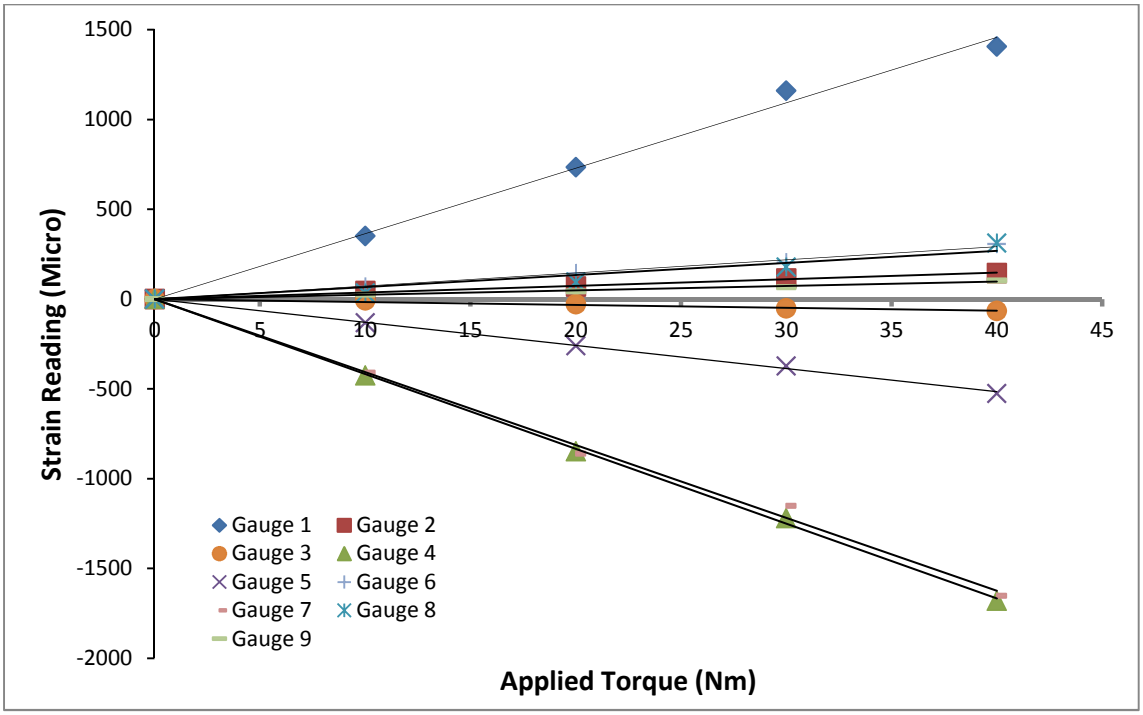

Figure 6.2. Measured strain readings for the nine individual gauges mounted to sample SM1 under stepped sub-maximal torsional loading.

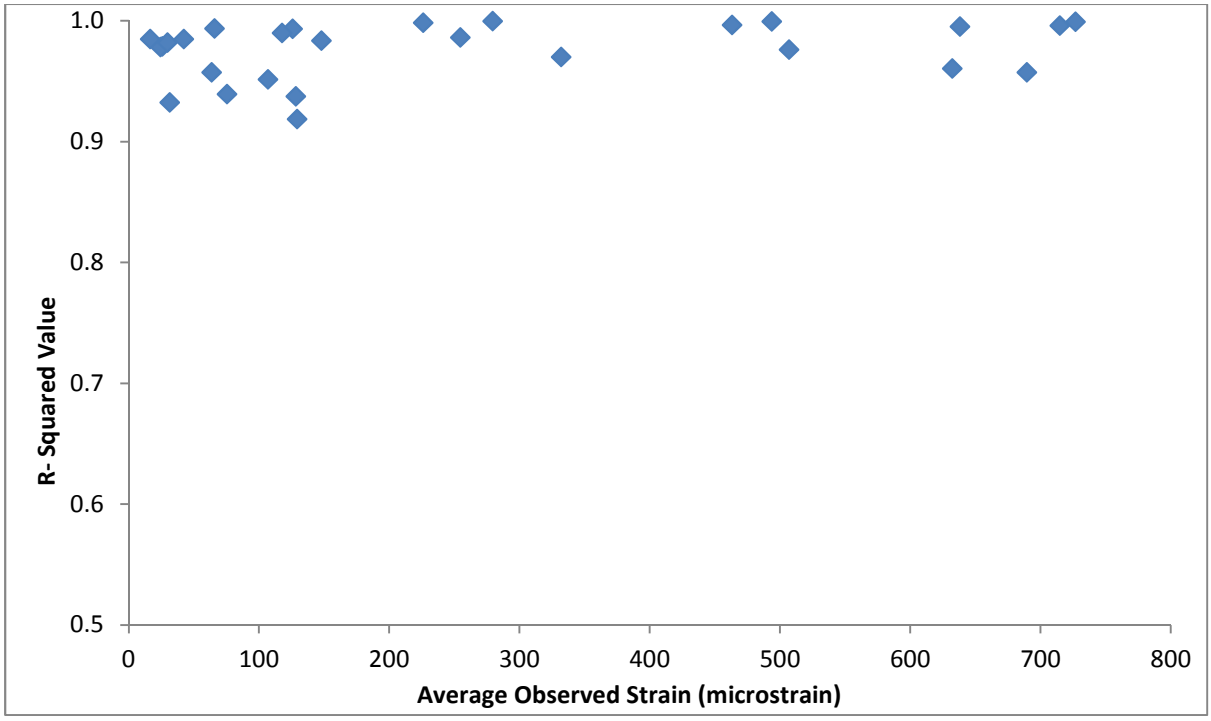

Figure 6.3. R^2 values obtained for each gauge used within the entire testing process (torsional loading only) with respect to the average absolute strain reading recorded (in microstrain) for each gauge.

The average gauge reading was calculated for each of the strain gauges in torsional loading. These averages were then compared to the R^2 results for each of the gauges (Figure 6.3). As can be seen, the results indicate linear, or close to linear behaviour (R^2 approaching or above 0.99) for the majority of results, and in particular those returning an average strain reading greater than 125 microstrain. R^2 fell significantly for two gauges. These gauges measured the lowest average results during testing (13.6 and 18.7 microstrain). The gauges that returned the highest absolute results were those in the 45-degree orientation, as would be expected in a torsional testing regimen. It should be noted that as a result of the higher absolute readings, the same gauges returned the 'best' R^2 values, with all 45-degree gauges returning values higher than 0.994.

6.1.2 Compressive Testing

As with the torsional testing protocol, the results for the strain gauged samples in compressive loading tests were taken in discrete intervals. Stepped compressive loading was undertaken to a sub-maximal level pre-determined (through initial fracture tests) to fall within the linear-elastic portion of the strain curve. Consequently (as with torsional loading) the ideal physical observation would be linearity of the measured strain results.

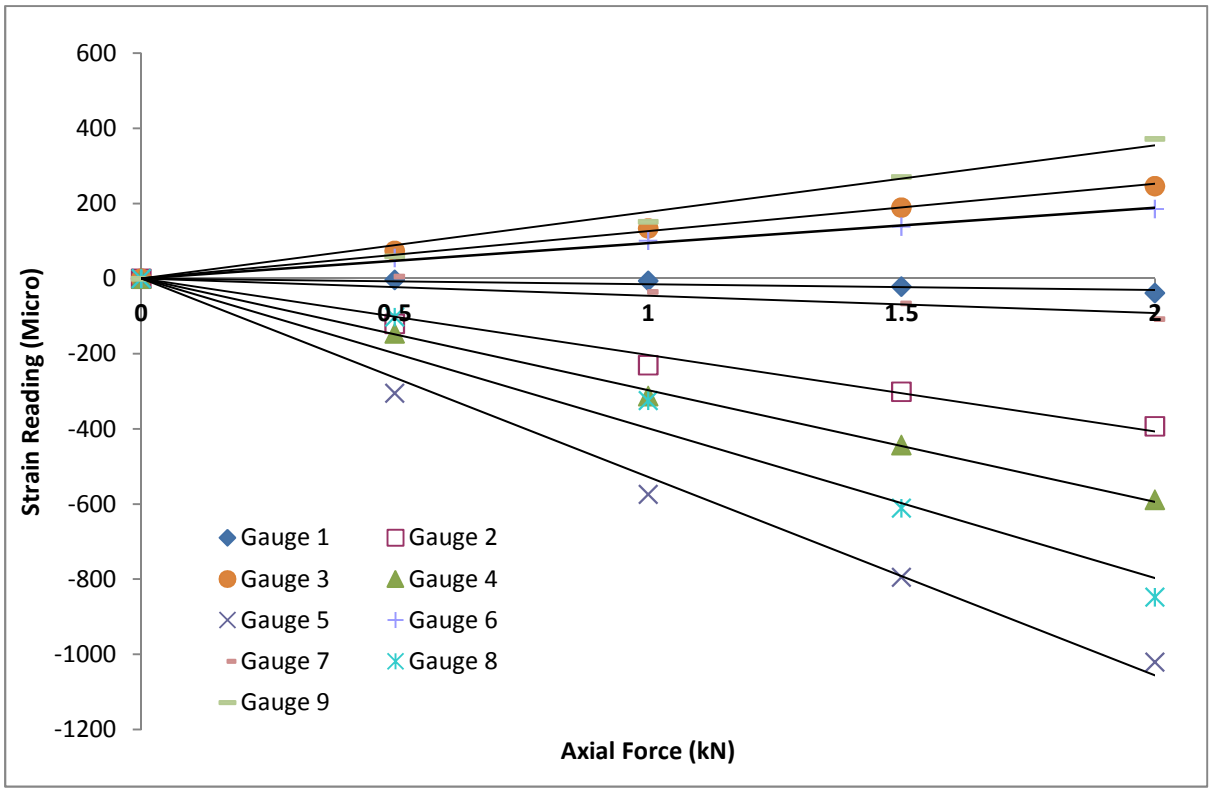

Figure 6.4. Measured strain readings for the nine individual gauges mounted to sample SM1 under stepped sub-maximal compressive loading.

The majority of the gauge results demonstrated negative strain due to the compressive nature of the loading regimen (Figure 6.4). The three gauges mounted vertically provide the highest absolute values, recording values as low as -1021 microstrain. The three gauges located horizontally and the three gauges located at a 45-degree angle show results closer to zero, varying from negative to positive in response to the alignment of the gauge and the local geometry of the sample. Linearity of the measured strain response in the compressive results was retained to a similarly high level to that shown in torsion, generally returning R^2 values above 0.98, again with the exception of those gauges returning consistently low strain results (Figure 6.5).

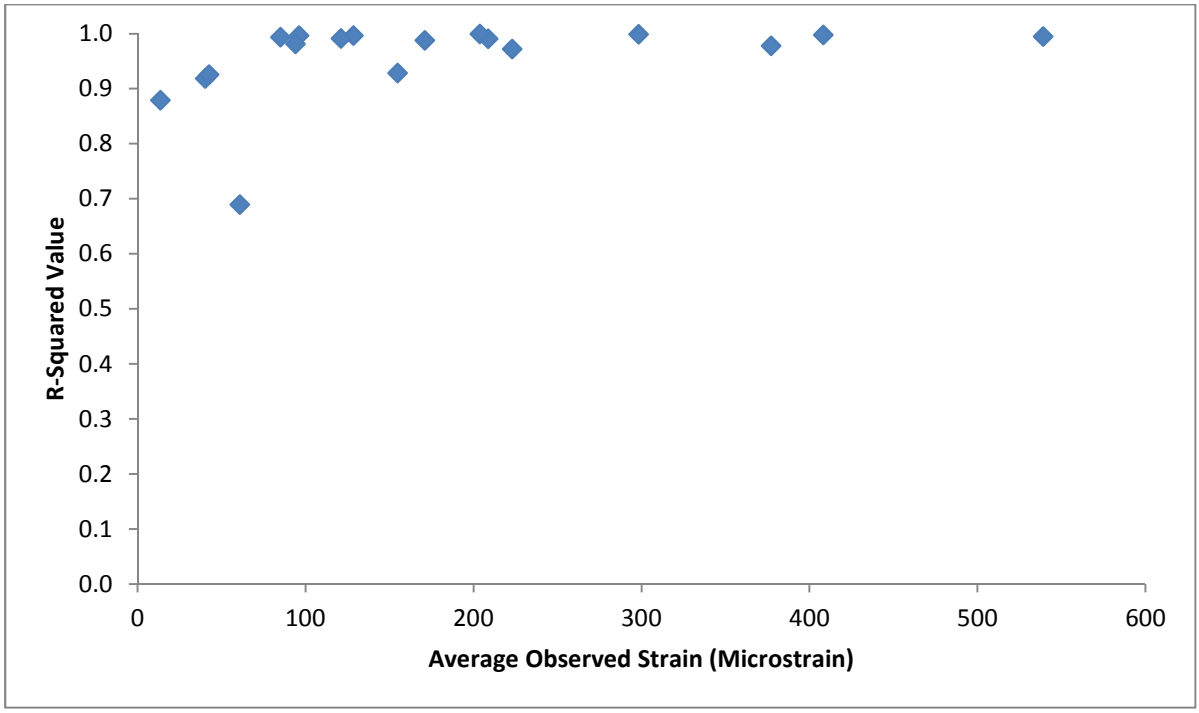

Figure 6.5. R^2 values obtained for each gauge used within the entire testing process (compressive loading only) with respect to the average absolute strain reading recorded (in microstrain) for each gauge.

6.2 Laboratory and Simulation Comparison – Principal Stress

6.2.1 Cross Sample Comparison

Results were obtained on a quasi-static basis (i.e. load applied and maintained during strain reading) throughout both the laboratory testing and computational simulation. The linearity of the measured strain results within the laboratory was retained throughout the range of applied loads during sub-maximal testing.

The load/deflection curve was examined independently of the measured strain gauge readings to increase the confidence in the assumption that the testing was undertaken within the elastic behaviour

region. This would confirm that the testing was capable of providing repeated strain results without incurring measurable damage within the samples. Figure 6.6. shows the load/deflection curve for a single sample under stepped sub-maximal loading. The 'take up' period noted in Chapter 5 is significantly reduced, with the sample demonstrating continued linear behaviour from approximately 0.3 mm until the incremental loading is curtailed. Applied force in Figure 6.6 ranges from an initial 1.5 kN to a second discrete step of 2 kN. The load was removed between intervals, and appropriate time was provided for the sample to completely return to the initial 'zero point' condition (3 minutes minimum for each test).

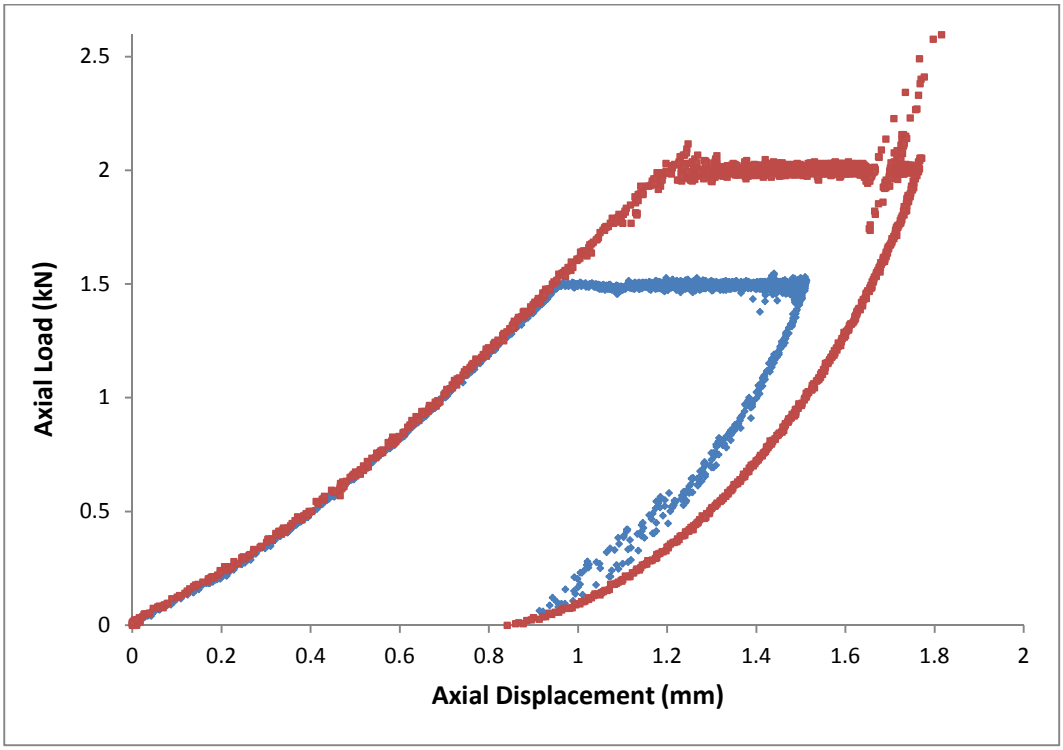

Figure 6.6. Graph depicting a comparison of two sequential compressive loads on the same porcine sample.

High resolution data sampling (10.24 Hz), results in a data response with a 'noisy' signal. This is exhibited by a scattering of a large number of data points, which when considered as a whole, plots to a smooth line, but when considering a single data point independently can be shown to vary either side of the 'true' (averaged) result. Consequently, it was impractical to compare a single measured result for axial deflection from one loading interval to the next. To overcome this, the complete data set for each loading interval was fitted with a line of best fit, and the equation produced for this line was then reproduced for each iteration and used to compare the data sets.

The loading portions of the plot were fitted with third order polynomial relationships. These relationships that were then replotted independently of the original data to a maximum of 0.9 mm

(after which the 1.5 kN test is curtailed). Third order relationships were selected as this offers a suitable balance of appropriate representation of the data curve without 'over fitting' to the noisy data, and incurring further error. The use of third order rather than linear relationships confirms that the strain response isn't linear at the early portion of the loading curve, as demonstrated in Chapter 5. This is likely to be a response to machine compliance; hence similar nonlinearity is repeated in independent loading intervals.

The R^2 values with the respect to the polynomial trend lines are 0.997 for the 2 kN load and 0.998 for the 1.5 kN load interval. This process demonstrates maximum difference between the two intervals (in terms of absolute reading) of 0.028 kN (28 N), occurring at the highest compared value (0.9 mm deflection). Maximum error in terms of percentage of the recorded result is (necessarily) found at the lowest compared value, representing approximately 10.1 %. Average error (as denoted by root mean squared error) is 11.17 N in terms of absolute values, which represents 0.79 % of the maximum-recorded value. The difference in vertical displacement for a repeated applied load of 1.2 kN from one iteration to another was 0.96 %, representing an absolute measured difference in of 0.0076 mm.

This comparison demonstrates that only a very small degree of difference is noted in consecutive testing of the same sample, and that the data sets are near identical. This investigation of the load deflection curves from testing showed no significant plastic deformation during the sub-maximal testing. The ability to compare the two data plots with minimal error demonstrates that the repeated testing used for strain gauging is applicable, and that there is no cumulative damage effect of testing to this loading level. As such, the repeated results can be treated as independent entities and therefore the compiled strain results measured during testing can be compared simultaneously on a single results plot.

6.2.2 Observed Principal Stress

After the linearity of the measured strain results had been confirmed, the readings were used to calculate values for maximum and minimum principal stress. This approach was undertaken to accommodate for the manner in which the material mapping procedure in simulation plots rapidly-changing Young's modulus to neighbouring regions of elements in the mesh. The comparison methodology was detailed by Taddei et al. [82], in which the assigned material property for the gauge location and stress calculation is taken from the Finite Element model rather than from material testing. This material property is then used to calculate the laboratory principal stress result from the strain gauge readings, essentially providing an accurate and non-invasive material property test at the precise location of the strain gauge. This ensures that the material aspect of the stress results is consistent between the laboratory and the Finite Element simulation.

The methodology was originally derived for bone testing in cancellous regions to accommodate for the differences observed in the mechanical properties and physical construction in the epiphyseal

regions (a harder layer of more calcified bone directly beneath the strain gauge location at the bone surface) with the simulated structure (a reduced material property value mapped at the bone surface and strain gauge location as a result of *partial volume* effects).

Principal stress results were exported from the Finite Element model at all sub-surface nodes directly beneath the sensing area of the strain gauge rosette, to a depth of approximately 2 mm, and then averaged. This mimics the manner in which the strain gauge averages the strain result over the length of the gauge and accounts for the changing Young's modulus observed away from the surface, through the thickness of the cortex. The material property of the elements beneath each gauge location was averaged, and this figure was used to create the principal stress results from the laboratory, using strain gauge transformation theory and the measured principal strains.

Three strain gauge rosettes were attached to each bone sample. These provided discrete values for principal stress for each of the loading intervals at specific locations upon the bone surface. Consequently a total of 30 data points were determined for each individual bone sample in torsion. Comparing the maximum and minimum principal stresses at each gauge location for all samples in both torsion and compression provided a total of 60 measurements that could then be used to validate the entire Finite Element simulation process. A third sample that would have increased this data pool to 90 results in torsion was omitted from simulation due to testing issue (considered in section 6.5.3).

The results for maximum and minimum principal stress illustrated in figures 6.7 - 6.11 are provided in the format of *predicted vs. observed* stress. The predicted result is provided as an output from the Finite Element simulation, whilst the observed is the measured result, as recorded within the laboratory. The ideal result from this comparison would be that the results describe a line of equation $x = y$ with the intercept at 0,0 and minimal deviation of the data points from this ideal line, as denoted by an R^2 value approaching unity.

The error between simulation and measured stress at each data point was assessed in terms of peak error, and for the data as a whole the averaged error (Root Mean Square Error - RMSE) was calculated to statistically observe the behaviour of the samples at each specific gauge location and in discrete loading intervals. RMSE was used as it offers a good analysis tool for this type of *predicted vs observed* data, assessment of error with respect to the sample size and also allows correlation with the results and average error detailed in literature. The ideal overall result would be an RMSE of 0, demonstrating that there is no difference between the predicted and observed values.

Plotting the data graphically (Figure 6.7) provides a simple means to visually assess the simulation of a single bone sample under torsion (in this case sample SM1). The details of the linear regression calculation are displayed within the plot, demonstrating the accuracy of the simulation of the sample with respect to the ideal linear result. As can be seen from the graph, the data points plot to a line that is approximately 3.8% removed from the ideal result of $x = y$ (which is shown in form of a dashed line) with a good level of fit as denoted by R^2 value ($R^2 = 0.961$).

Peak error was calculated for each observed result compared to each predicted result and was noted as a 49.9% over prediction. The maximum peak error of the results group in terms of absolute values was shown to be 9.77 MPa. Root mean squared error for the combined data pool from sample SM1 was 4.05 MPa, which represented 9.95% of the maximum value recorded during the physical testing.

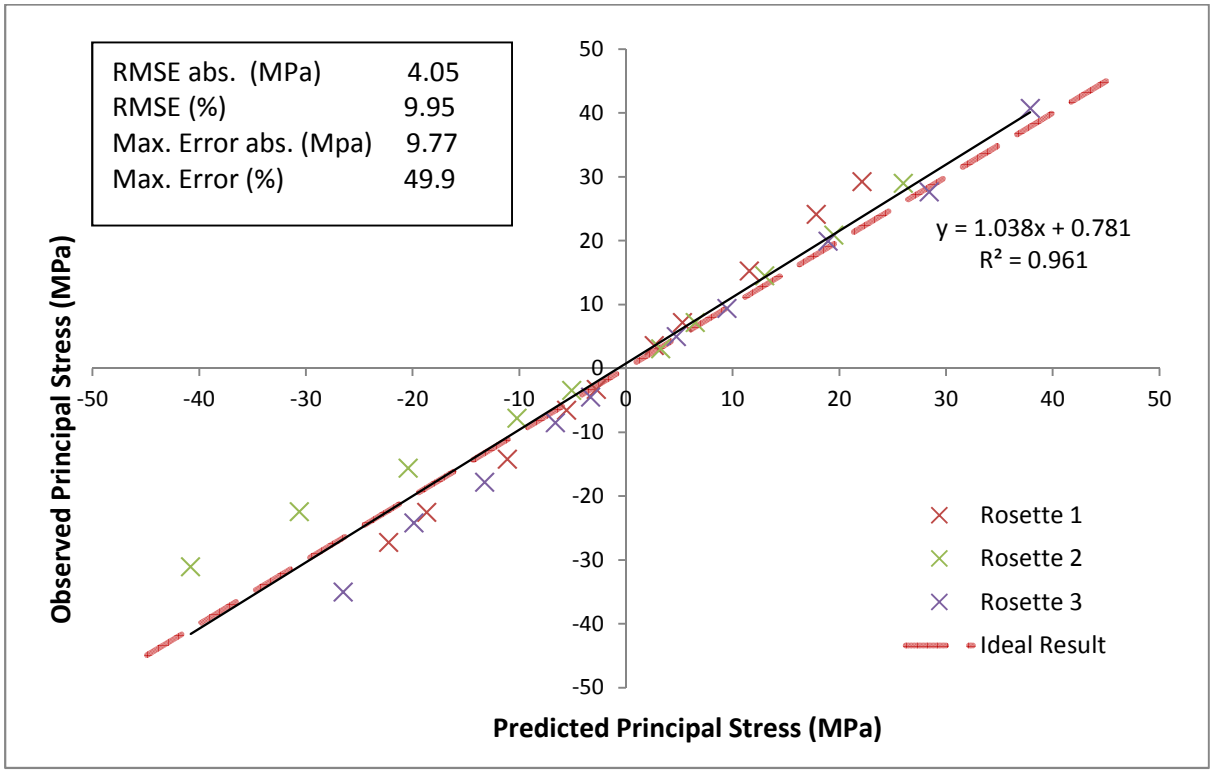

Figure 6.7. Comparison of the predicted (from Finite Element simulation) and observed (through physical measurement of the sample) principal stress results for all three gauge locations on bone sample SM1, tested under torsion from 0 to 40 Nm.

6.2.3 Compiled Principal Stress Results – Torsion

The accuracy of the torsional testing as a whole can be assessed by combining all of the stress results obtained through torsional testing for each of the tested samples. The combined accuracy is very similar to that obtained for sample SM1 only (Figure 6.7). A slight reduction in fit for the combined results was noted, to a line that is approximately 5 % removed from the ideal result. Peak absolute error of predicted to observed results for all comparisons during torsional testing was found during simulation of sample SM1, at 9.77 MPa (-40.8 MPa predicted, -31.0 MPa measured within laboratory). The maximum percentage error with respect to the predicted values was observed in sample SM2. Figure 6.8 plots the combined results of the torsional process as a whole, detailing the position of the results and the slight reduction in agreement with the best fit line than was noted for sample SM1 alone.

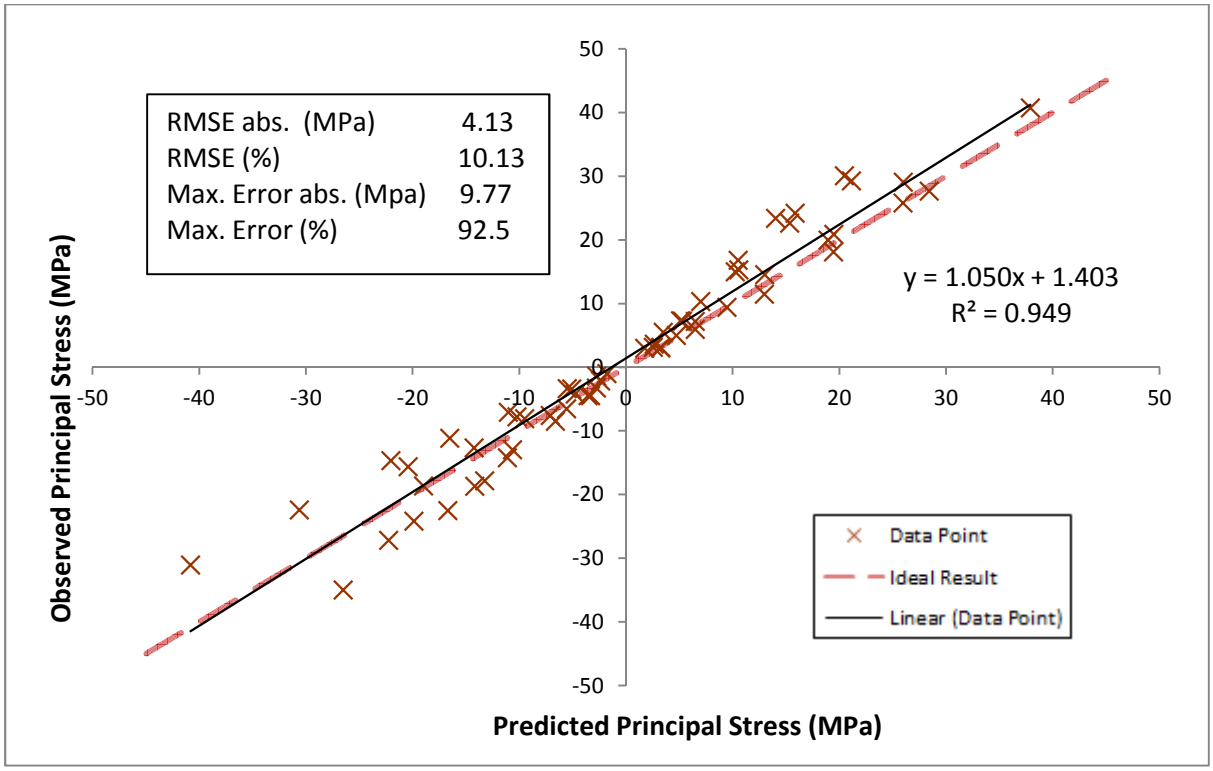

Figure 6.8. A comparison of the predicted and observed principal stress results for the compiled data pool (total of two samples) under torsional testing.

Sample SM2 demonstrated lower stress readings throughout testing, and thus lower *absolute* errors, yet higher *percentage* errors were observed. The maximum percentage error was thus observed during testing and simulation of sample SM2, and is noted as a 92.48 % over prediction. This was observed for a measured result of –1.43 MPa, which is the second lowest result measured throughout the entire torsional testing procedure, and thus potentially more susceptible to increased error, particularly on a percentage basis.

RMSE for the total data pool is similar to the result observed for sample SM1 alone, but shows a slight improvement due to the increased sample size, with an absolute value of 4.13 MPa, which represents 10.13 % of the maximum physically recorded value.

6.2.4 Observed Principal Stress – Compression

The compressive results were initially compared on the basis of comparing principal stress, using the same technique shown for torsional comparisons. With the strain gauges located in the same position as those used for torsion, the Young's modulus were retained for stress calculation. The predicted vs. observed plots for principal stress were then produced, firstly on the basis of a single sample (Figure 6.9 – sample SM1) and then for all samples tested in compression (samples SM1 and SM2 only due to the testing issues incurred within sample SM3) (Figure 6.10).

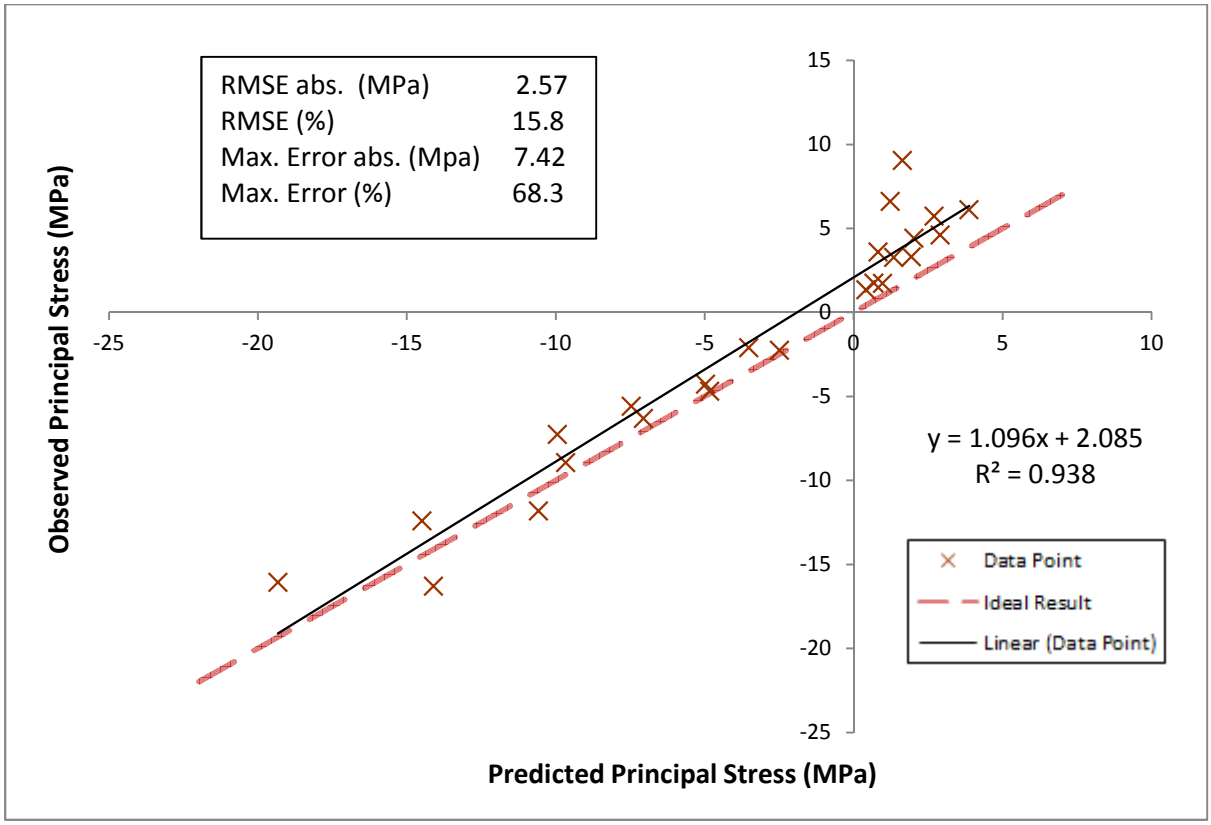

Figure 6.9. Comparison of the predicted (from Finite Element simulation) and observed (through physical measurement of the sample) principal stress results for bone sample SM1, tested in compression from 0 to 2 kN.

The details of the linear regression calculation are displayed within the plot, as are the error results recorded for the sample as a whole. R^2 is 0.938, the results plot to a line that is approximately 9.6 % removed from the ideal result of $x = y$. In the compressive test shown, the intercept is noted to deviate by more than 2 MPa from the origin. Peak error in terms of absolute value for a single gauge compared to a single predicted result was noted as a 68.3 % over prediction whilst the maximum absolute error was shown to be 7.42 MPa. RMSE for the combined results from sample SM1 was 2.57 MPa, which represented 15.8 % of the maximum value recorded during physical testing.

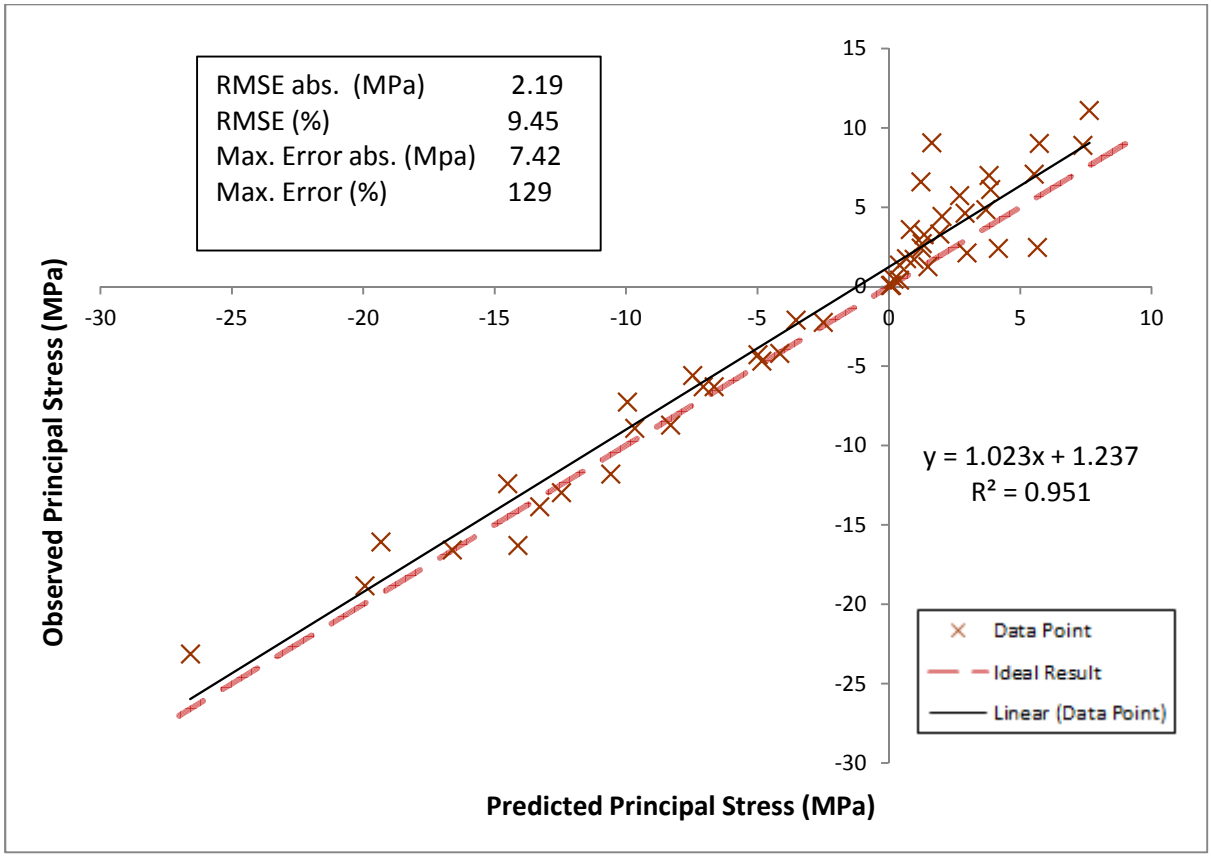

Figure 6.10. Comparison of the predicted and observed principal stress results for all samples in compression.

The sample shown in Figure 6.9 has good agreement to the linear trendline for the majority of data points; however, deviation (in the form of under prediction) is noted consistently for strain gauge rosette number three, which was located on the posterior surface of the bone. In particular this is shown in the positive aspect of the results, where the results from rosette three deviate significantly from the linear response of the main group. Isolating the results from rosette three, and comparing rosettes one and two only increases the linearity of the results as a whole. R^2 value consequently increases from 0.938 to 0.981. An additional effect is a reduction in the observed error for the experiment, with RMSE falling to 1.54 MPa, which is 25.3 % of the maximum-recorded value.

The effect of the erroneous positive results observed in Figure 6.9 continues when the data from the other samples tested within the laboratory is added to the plot (Figure 6.10). An additional departure in the positive orientation is noted which, in this case, is a result of the positive readings of gauge one on sample SM2. The results continue to plot to a linear line of fit; however, the effect of these two gauges is clearly identifiable in the positive axes and the R^2 value is reduced when compared to the values calculated for testing in torsion.

6.2.5 Combined Laboratory and Finite Element Results Comparison

The repeatability demonstrated in the sub-maximal loading (section 6.2.1) means that the strain results and the principal stresses derived from them can be viewed in isolation as independent entities, and consequently also compared directly from sample to sample. The techniques utilised for simulation were retained between samples and loading scenarios and consequently it is also applicable to compare the *predicted vs observed* results across differing loading regimens. Combining the results for torsion and compression allows for the comparison of the entire 108 individual stress results, providing an estimation of the simulation accuracy as a whole.

As can be seen in Figure 6.11, the accuracy obtained is demonstrated to be close to the theoretical ideal result, and displays an R^2 value of 0.950. Despite the high linearity of the agreement and the observed high R^2 value, the effect of the accuracy issues in the positive aspect of compression can be seen within the plot. The higher absolute values of strain observed for torsion dominate the results plot, and consequently linear regression partially conceals these errors observed at lower absolute values of stress.

Peak error in terms of absolute value for a single gauge compared to a single predicted result (9.77 MPa) was observed during the torsion of sample SM1, which had the highest absolute results overall. RMSE for the combined results from all samples in all loading regimens was 3.4 MPa, 8.36 % of the highest recorded value. Max error in percentage terms was observed in low-load compressive testing with a 129 % over prediction.

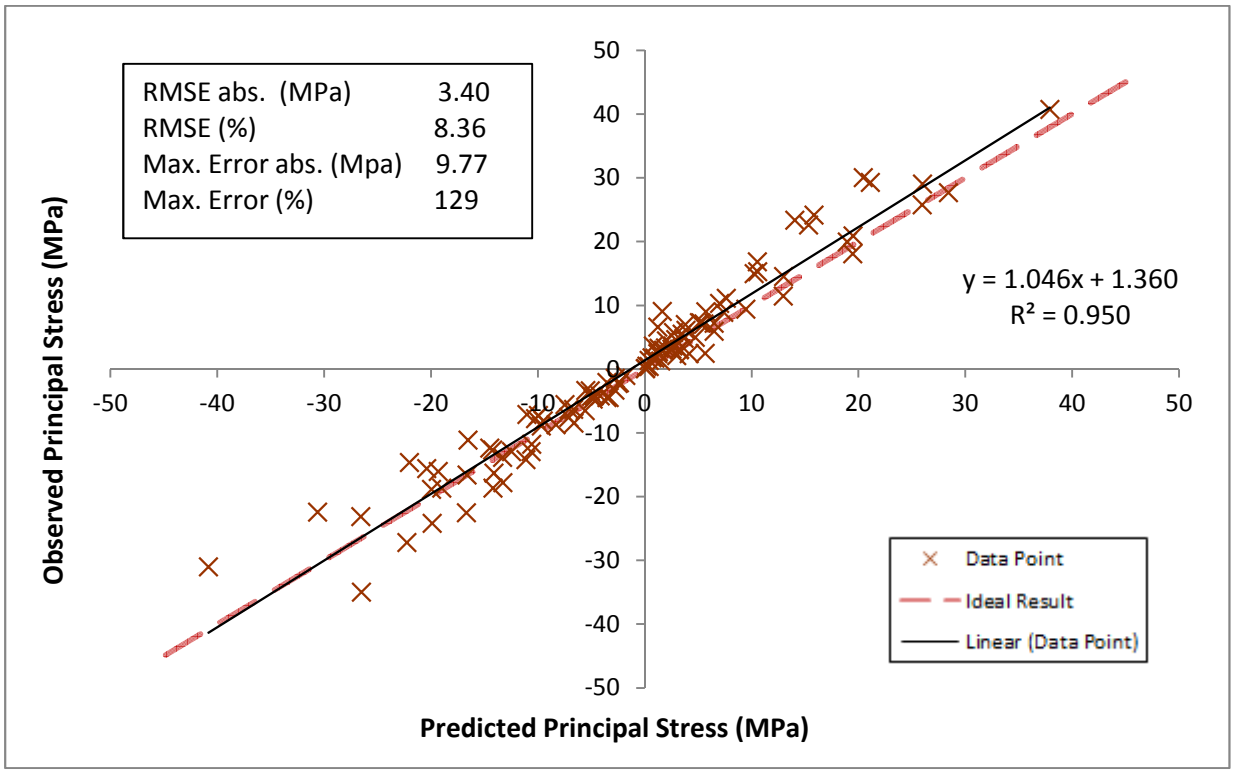

Figure 6.11. Comparison of the predicted and observed principal stress results for all samples, tested in compression from 0 to 2 kN and torsion from 0 to 40 Nm.

6.3 Limitations of Stress Comparison

Dalstra et al. previously considered the difficulties encountered when correlating measured strain gauge data with Finite Element predictions, highlighting that the continuously changing stress and strain field within the Finite Element model is inherently unlikely to predict the averaged response of the strain gauge at any specific location [112]. The small strain gauges, the fine mesh resolution and high-resolution spatial registration used in simulation in this thesis attempt to consider these issues.

The issues are best described graphically, and Figure 6.12 shows the local effects contributing to the complications. As can be seen, the manner in which the material values are mapped to the volume of the sample provides a natural stress gradient, increasing towards the centre of a given section of cortex. Taddei et al. discussed this phenomenon in the epiphyseal region, at which point a thinner cortical 'shell' surrounds less dense bone material. The commonly-used approach to mitigate this effect is to investigate the stress behaviour within a prescribed depth beneath the sensing area (the area directly beneath the strain gauge) rather than consider the stress or strain behaviour directly at the surface. This has be shown to be valid, and provides accurate results on an averaged basis; however, point results at individual nodes close to or beneath the sensing area can range significantly either side of the averaged value. Taddei et al. attempted to mesh their Finite Element models such that they included coincident nodes at the central point of the strain gauge rosette during meshing, thus correlating an individual node result from simulation with the measured strain data [46]. This technique was not subsequently adopted in any other study. With automated meshing and the use of irregular tetrahedral elements in this study, the inclusion of coincident nodes directly beneath the sensing location is notably more difficult. In fact, with the smaller elements used within the studies in this thesis, it was considered that the spatial accuracy was not sufficient to determine which of the nodes beneath the sensing area was the most central. Additionally with more than one node meshed beneath the strain gauge, no single node would provide the correct result for the sensed area (which averages over the entire gauge length). As a result, area averaging was employed for stress correlation.

The manner in which the averaged nodes are selected beneath the strain gauge introduces the possibility of inducing measurement error. The boundary of the sensing area from sample to sample is difficult to define as a result of the random orientation of elements from the automated meshing. With high gradient stress fields, the inclusion or exclusion of nodes close to the boundary of the sensing area may have an effect upon the indicated results, and thus alter the observed accuracy between consecutive tests on different samples. This effect is reduced when testing a single model with changing load, as the meshing protocol is retained between iterations when modelling a single bone. This allows the sensing area to be retained on the basis of the specific nodes and elements considered, ensuring that the same averaged area is considered in each of the simulation iterations. Therefore, the

comparisons between consecutive assessments remain accurate, and provide a true reflection of the changing boundary condition.

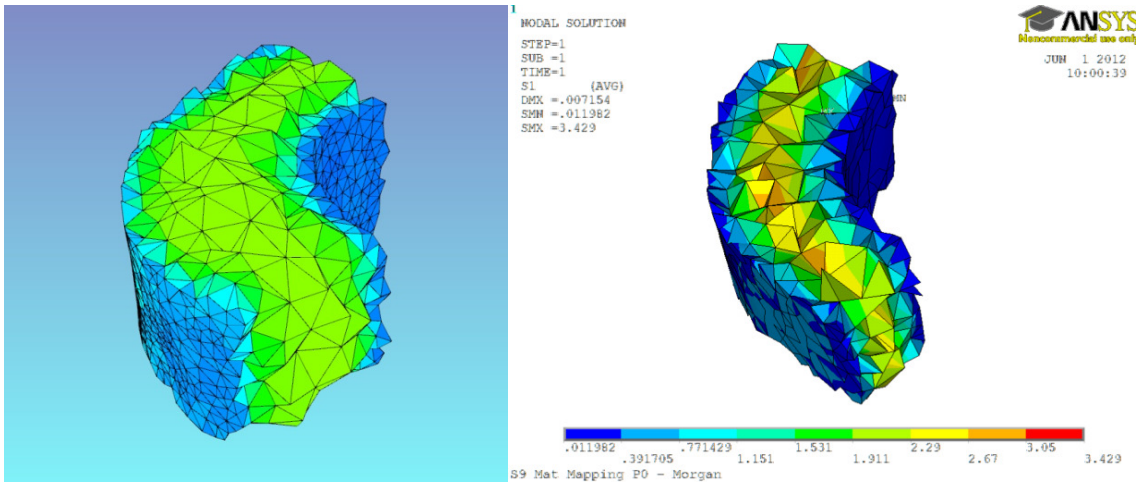

Figure 6.12. Screen captures from the ScanIP material mapping process (showing the material property gradient) and Finite Element solving process (showing the resulting stress gradient) demonstrate the source of the complications observed during stress and strain correlation.

Ultimately the principal stress correlation technique has been demonstrated to be valid, as can be seen by the accuracy achieved in this study and the prevalence of this technique in published literature. However, it remains a limitation of the CT-FE testing protocol that the principal stresses predicted at the surface and thus the location at which the strain gauge is mounted, will always be lower than those predicted towards the centre of the cortex. This stress gradient is a factor of the CT scan and partial volume effects, and as yet no capable systems have been developed that overcome this issue.

6.4 Laboratory and Simulation Comparison – Principal Strain

Following the extensive investigation of principal stress, the correlation of principal strain was considered for each gauge location. Whilst stress correlation is commonly undertaken in literature, the accurate determination of strain is vital when considering the fracture of bone and failure criterion in biomechanical simulation, which regularly uses a maximum strain limit as an indicator of failure. Correlation of strain has been undertaken in literature [36, 51], with accurate results demonstrated in the form of correlation to a line of best fit, but little in the way of assessment with respect to the statistical accuracy achieved during the simulation.

Both the key benefit and the key limitation of strain correlation is that the result is taken independently of the local material parameter. In practice, the benefit of this methodology is that it

allows for the correlation of the strain behaviour at the surface and therefore the precise gauge location, which theoretically increases spatial accuracy. This minimises the element-averaging process as shown in stress correlation. However, observing strain results in isolation excludes the local material definition and consequently has the potential to mask local errors induced within the modelling process.

6.4.1 Methodology

The methodology undertaken for strain correlation is notably different to that undertaken for the correlation of principal stress. The principal strain values at the each of the gauge locations are exported from the Finite Element model from the location identified through post-test scanning, and compared directly with the measured principal strains, as calculated using rosette theory.

The sensing area was determined as a section of the *surface* directly beneath the gauge location. This differs from the *sub surface* readings correlated for stress-based correlation. This demonstrates a limitation of the stress correlation procedure, namely that the material characteristics at the surface result in reduced stress values, and thus volume averaging is employed. Volume averaging was not employed in strain correlation, as the strain result is measured directly at the surface, and this can be replicated in the Finite Element model without the influence of the material gradient. In the selection process, an external layer of elements was chosen at the specific gauge location. Approximately 6 to 8 elements were selected at the surface, in a circular or square shape. Necessarily, due to the irregular nature of the tetrahedral elements, the shape of the selected region proved to be irregular at the majority of gauge locations. As described in Chapter 3, the level of mesh refinement produced a target maximum edge length of 0.5 mm, and consequently selecting 6 to 8 surface elements in a circular orientation leads to a sensing area of approximately 1 mm^2. This aligns with the sensing area of the physical strain gauge. Strain averaging was undertaken, combing the results of the 6 to 8 elements at the gauge location. The averaging process is not necessarily a limitation, and simply represents the manner in which the physical strain gauge measurement procedure provides an *averaged* strain result of the behaviour at the sensing surface.

6.4.2 Strain Correlation Results

The correlation of principal strain results is undertaken in a similar manner to the correlation undertaken for principal stress. For sample SM1, the peak error in terms of absolute value for a single gauge result compared to a single predicted result was noted as a 390.94 microstrain (Figure 6.13). This represents a 22.5% over prediction of the result measured in the laboratory, or an 18.9 % over prediction with respect to the maximum measured result in testing. Root mean squared error for sample SM1 was 190.1 microstrain, which is 9.2 % of the maximum value recorded during physical testing.

It is possible to combine the results for the independent loading regimens and samples with the same justification that was used for stress-based correlation. Firstly all samples in torsion were compared (Appendix A1), within which RMSE was calculated as 158.78 microstrain (7.67 % of the maximum measured value) and peak error increased to 456.48 microstrain (38.79 % over prediction). Secondly compression was considered (Appendix A1), RMSE = 65.2 microstrain (4.41% of the maximum recorded value), peak error = 188.8 microstrain (21.5% over prediction). Finally, the entire results pool was correlated, producing the plot shown in Figure 6.13. The higher absolute values recorded in torsional testing result in increased RMSE over compression-only results. (RMSE = 126.08 microstrain, 6.09%). Peak error is the value previously observed during combined torsional testing (456.48 microstrain, which is a 38.79% over prediction).

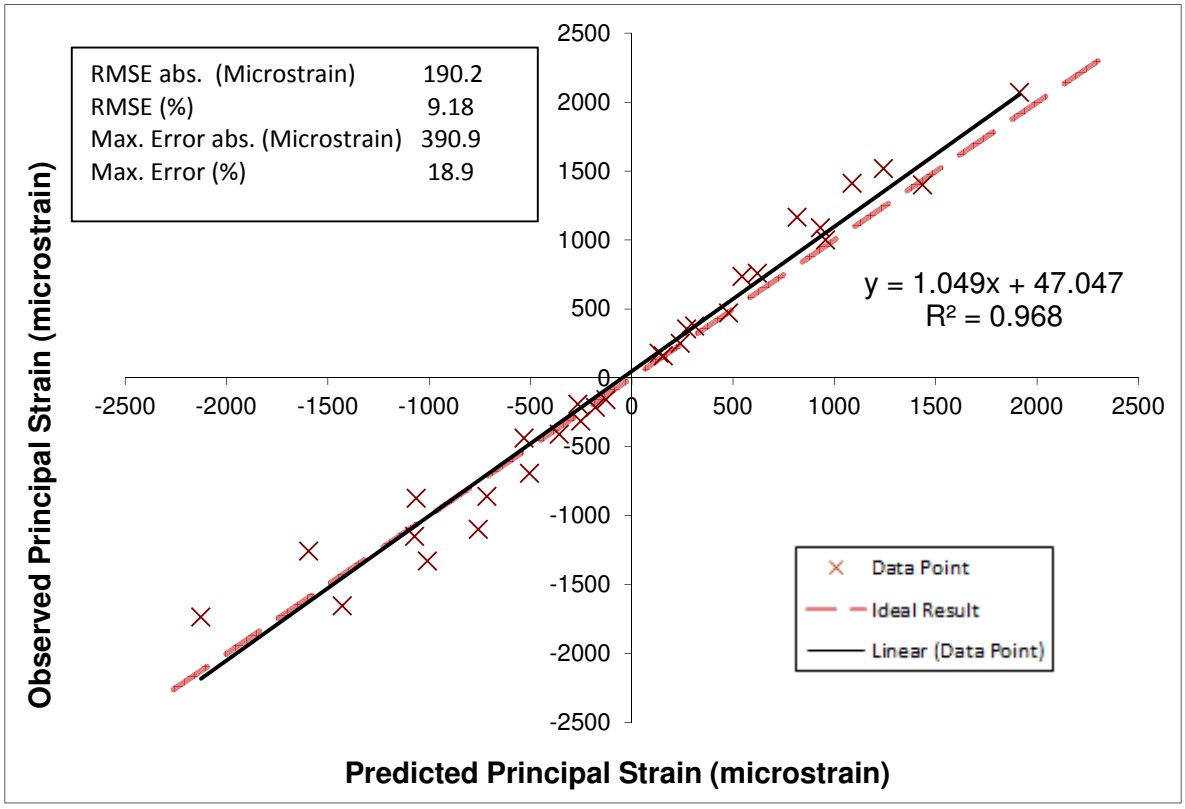

Figure 6.13. Comparison of the predicted and observed principal strain results for sample SM1, tested in torsion from 0 to 40 Nm.

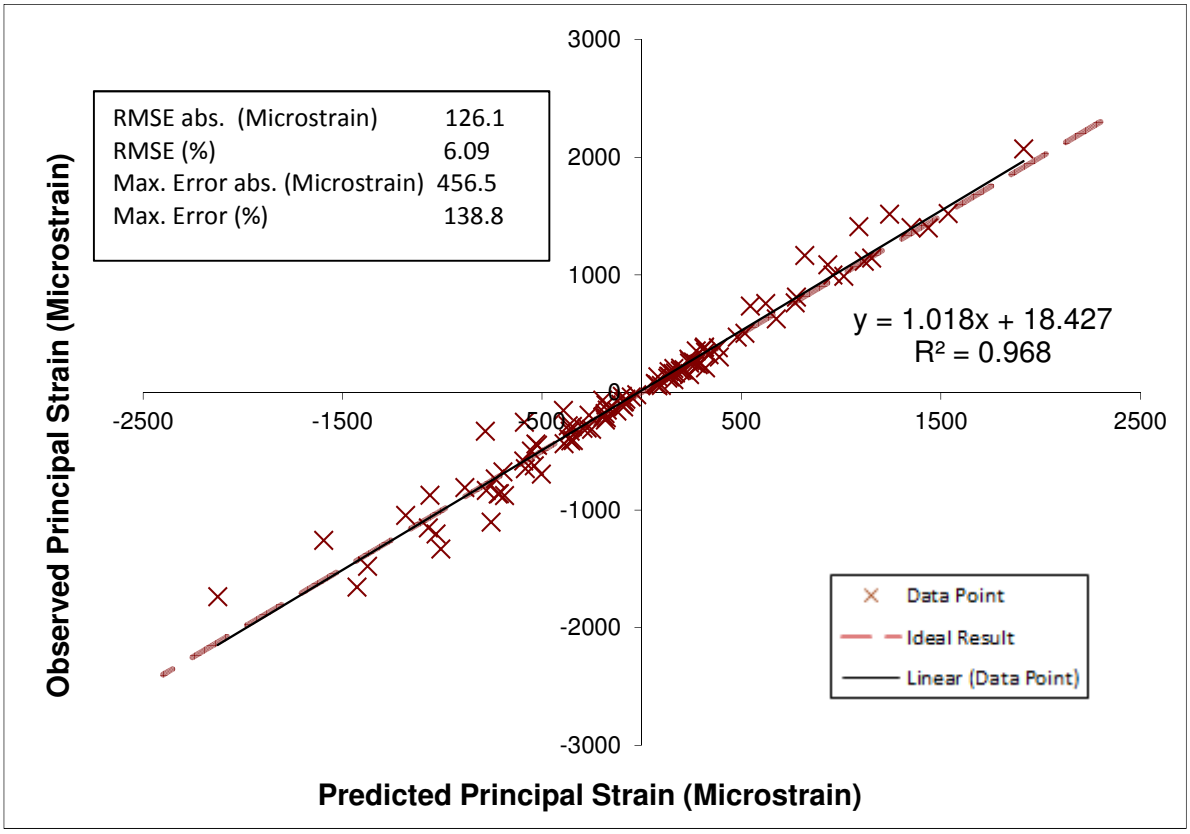

Figure 6.14. Comparison of the predicted and observed principal strain results for all samples, two tested in compression from 0 to 2 kN and two in torsion from 0 to 40 Nm.

6.5 Chapter Discussion

6.5.1 Principal Stress

The strain gauging verification in terms of principal stress that was undertaken in this study followed the methodology originally proposed by Lengsfeld et al., Dalstra et al. and Taddei et al. [40, 46, 112]. This ensured that the processes had been previously considered and were valid for the accurate testing of bone samples. Using confirmed techniques also allowed for the direct comparison of the overall accuracy obtained within this study with that detailed in CT-FE literature. Taddei et al. (whose study was the most recent) tested a single human femoral sample under compressive force, which was applied at varying angles to obtain stress results for different loading conditions. At the time of publication, that paper represented an improvement on previous techniques, with increased correlation (R^2 value) of 0.9099 vs. 0.66 [206], 0.59 [9] and 0.898 [79] in studies up to that point. The paper focussed primarily on the proximal aspect of the femur and the epiphyseal region, within which it is arguably more difficult to obtain accurate material results; however, only a single femur was utilised for the testing process, and single axis loading was employed, with the sample rotated to account for the various positions selected for loading.

Taddei et al.'s process was considered as the most appropriate for the comparison of stress-based accuracy in this thesis, as the paper was subsequently used as the basis for further investigation of additional aspects of the CT-FE process in human bone modelling, such as material mapping strategy and the selected density – elasticity relationship [45, 53]. It was considered that if the porcine studies in this thesis could obtain accuracy close to that achieved by Taddei et al., then the modelling process could be considered sufficiently accurate and thus validated for continuing investigation. Table 6.1 shows a comparison of the overall accuracy, agreement and error between the results observed for porcine testing in this study, and the results obtained by Taddei et al. for the simulation of the human femur.

Table. 6.1. Table details the comparison of agreement and error between the results observed for porcine testing in this study, and the results obtained by Taddei et al. in a human femur sample. Starred reading (*) denotes the difference between Taddei et al.'s methodology for calculating maximum error and the methodology used in this thesis.

	Accuracy Reported by Taddei et al.	Accuracy Observed in this Study
Agreement (R^2 Value)	0.91	0.95
RMSE (MPa)	2.6	3.4
RMSE (%)	8.6%	8.4%
Max. error (MPa)	8.3	9.77
Max. error (% of observed result)	27%*	129% / 24% *

Of particular note in the table is the starred item (*) for maximum error. Taddei et al. reported a maximum error of 27%, which, whilst not explicitly stated, seems to relate to the maximum absolute error, correlated to the maximum absolute stress result observed in the study as a whole. On which basis, the maximum error in this study would not represent the 129 % error reported here (5.66 MPa predicted compared with 2.47 MPa measured in the laboratory) but be significantly reduced to 23.98% (9.77 MPa maximum error in comparison vs. 40.7 MPa maximum measured result in the laboratory).

Further investigation into the patterns observed in the stress comparisons demonstrated the occurrence of a number of phenomena: firstly, at small positive values for the compressive tests, the Finite Element model was demonstrated to under or over predict the observed local stress at select locations. This was not maintained for all gauges on a given sample, and the other gauges demonstrated a more accurate and consistent agreement. The linking of this error to a single gauge indicates that the observed error could be a local consideration, such as the material parameters or loading regimen. The

same porcine samples were tested within both torsion and compression, with the gauge locations maintained. The same correlation error noted in compression was not observed in the torsional results, and thus these gauges couldn't be deemed faulty, and neither could this be a consequence of the local material derivation (also maintained between tests). Consequently, it is suggested that this error indicates that the boundary conditions in terms of applied loading or orientation are more likely to be the cause of the error.

Secondly, evidence of a dichotomy is noted in the negative results for torsional testing. The data shows two distinct split trends in the negative aspect of the predicted vs. observed stress plots. The effect of this is that the maximum error is increased, which highlights the importance of observing the error results. Observing the agreement to the trend line only would not exhibit this lack of agreement, instead averaging the difference between the two data trends.

These two observed effects indicated an issue with regards to the alignment of the model and the Finite Element model boundary conditions. This explains the inaccurate behaviour of a single gauge, despite continually linear strain readings observed during physical testing. Further testing is required in order to determine if this inaccuracy can be mitigated through alignment changes, or if there are additional factors affecting the ultimate accuracy of the simulation process. Similar deviation from the 'true' agreement of $x = y$ was noted by Schileo et al. during investigation of the effect of changes to the density-elasticity relationship in Finite Element simulation [37]. The changing material relationships used in that study ultimately reduced the observed effect with a significant increase in accuracy obtained through the use of Morgan's relationship (as used within this study) [72]. It is therefore considered that further testing into the material mapping process is required in addition to the alignment considerations, to isolate this as a source of error.

6.5.2 Principal Strain

Principal strain was considered as an additional verification procedure in this study due to the fact that this simulation output is regularly proposed for failure investigation [36, 45]. Consequently, the possibility of improving the observed accuracy the values published in literature is of particular interest for more accurate fracture prediction.

Significantly fewer papers in CT-FE literature have exhibited strain-based correlation than have published stress correlation, most likely due to the isolation of the mapped material parameters in the calculation of the results. Of those papers that demonstrate strain results, no information is provided regarding the error of either the data pool as a whole, or the statistical error of the individual results [36, 51, 105, 207]. Three example papers are considered in table 6.2. It should be noted that in addition to the lack of error data, the improved correlation results exhibited by Yosibash were based upon a total of only 5 correlated principal strain readings (compared to 108 readings in this study).

Table. 6.2. Table details the comparison of agreement and error between the results observed for porcine testing in this study, and the results obtained by Taddei in a human femur sample.

	Accuracy Reported by Trabelsi	Accuracy Reported by Yosibash	Accuracy Reported by Yosibash (Improved)	Accuracy Reported by Peleg	Accuracy Observed in this Study
R^2 Value	0.957	0.678	0.98	0.8095	0.968
Gradient	0.955	1.04	0.934	1.1035	1.0175
Intercept	-34	-289.8	-158	-50.949	18.42
RMSE (microstrain)	-	-	-	-	126
RMSE (%)	-	-	-	-	6 %
Max. error (microstrain)	-	-	-	-	456
Max. error (% of observed result)	-	-	-	-	139 / 22 %*

The results demonstrated in this study compare favourably with those published in literature, demonstrating the validity of the test procedure as a whole. The increased accuracy observed is likely to be a result of the increased resolution in physical data sampling and general improvements in the methods used in simulation. Mesh refinement in this study is considerably improved over both Yosibash et al. and Trabelsi et al., which is likely to significantly reduce the effects of localised strain averaging.

6.5.3 Sample SM3 Test Failure

It was initially proposed that three porcine femora would be used for the validation of the Finite Element simulation procedure in strain gauged testing. Two of which (samples SM1 and SM2, detailed above) would be fully constrained, (isolated diaphysis) whilst a third would be constrained using a reduced level of potting medium, similar to that used in the compressive fracture tests. It was proposed that the semi potted 'moulded' constraints may be suitable for torsional loading, provided that expansion in the *z* direction was controlled.

The sample was gauged using the standard procedure; however, it became immediately apparent in testing that torsion could not be applied without an element of slip at the contact surfaces. To mitigate this, axial load was applied. Whilst the ASP rig was capable of sampling the axial load and torque to a

high degree of accuracy, the testing demonstrated that the two were not mutually exclusive. Correspondingly increasing the applied torque had an effect on the applied axial load. This effect is shown graphically in Figure 6.15. Following the initial slip, the test was undertaken on the basis of strain control. This reduced the risk of the test equipment 'looking' for a load during testing, and consequently (theoretically) provides a smoother strain response. Also as a result of the slip at the surface, axial load was induced through the inclusion of an applied axial deflection of 1 mm. Following the application of rotational deflection, the increase in axial load can be observed, as can the non-linearity of the torque response that results.

The chart (which is plotted against an arbitrarily scaled time scale) demonstrates a static central portion during which the strain results are read from the strain gauges. Under load control, the torque or axial load applied to a sample is maintained during this period, helping to ensure that the strain results remain static whilst they are read. As can be seen in the plot, sample SM3 exhibited significant variation in both torque and axial load in this period. As such, strain values read at the start of this period were taken at higher load than strain readings taken towards the end of the period.

Unfortunately, despite significant investigation and simulation, the correlation of these strain results was not possible. The inability to determine the precise axial load and torque at the time of strain reading resulted in severe complications during simulation.

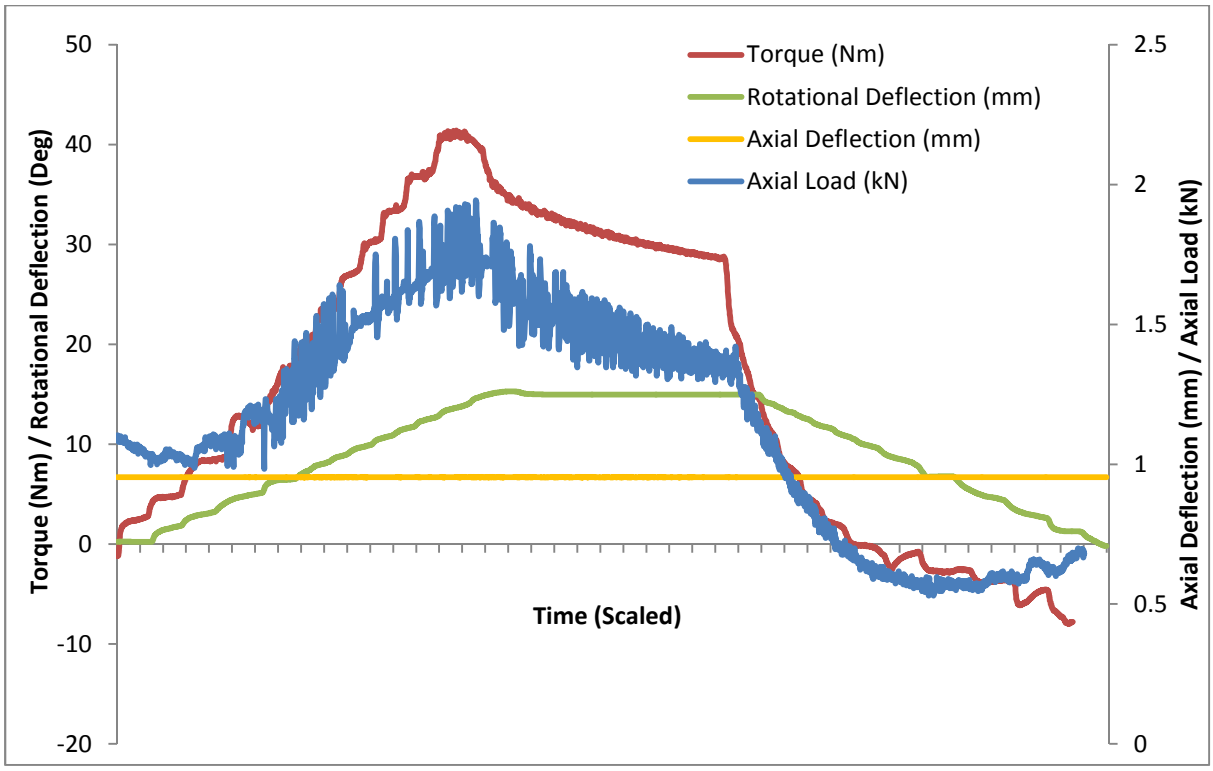

Figure 6.15. The load/deflection response of sample SM3 in both rotational and axial axes during a sustained 1mm deflection and an applied, held and released rotational deflection of 15 degrees.

The difficulties encountered with this sample highlight the importance of live/linked strain gauge data. It was felt during physical testing that the test was performing appropriately, and only in retrospect did the simulation problems occur. Live linking of the strain gauge data to the ASP test rig would mitigate the difficulties entirely providing an instantaneous reading with which to correlate the predicted and observed results.

6.6 Chapter Summary

The use of strain gauged testing was introduced to accurately define the 'true' behaviour of the bone samples during physical testing within the laboratory. Using strain gauges allowed for accurate assessment of the behaviour of the samples at a local level, and increased the accuracy of the validation methodology when compared to simple load/deflection analysis.

- The stress-based validation process was undertaken successfully with comparable accuracy to tests detailed in literature for human samples.
- Strain based correlation provided improved accuracy over the results observed in literature, most likely as a result of the increased data pool, and more refined meshing and simulation procedures. Accuracy in strain correlation demonstrated the potential accuracy achievable in fracture load testing.
- Complication in the testing of sample SM3 highlighted a requirement to improve strain reading techniques and potentially the requirement for live/linked strain data. This effect was mitigated during the testing of samples SM1 and SM2 due to the sustained strain reading periods used for these samples, as a result of load controlled loading.
- Patterns identified in cursory investigation of the strain gauge results correlation demonstrated potential error in the application of boundary conditions such as the Young's modulus and/or the orientation and alignment of the samples.
- Increasing simulation accuracy and observing the effects of changes to the boundary conditions should be considered. It is prudent to assess the effect of these changes within further simulation.

7 Assessment of Simulation Sensitivity

Comprehensive physical validation is a fundamental requirement when attempting to achieve high levels of accuracy in Finite Element simulation. 'Real' results obtained within a laboratory can be used to provide feedback into the modelling process for validation. This feedback can drive the manipulation of the input parameters for the Finite Element model, subsequently increasing the simulation accuracy. It is important to understand the sensitivity of the model to changes in the input parameters before these changes are made. This ensures that the input parameters are manipulated in an appropriate and logical manner.

Each of the input parameters and simulation changes listed below has the potential to provide variation in the simulated results and consequently each input is a potential source of error if amended incorrectly.

- The alignment of the test samples within the physical test rig and the manner in which this is accommodated for in Finite Element simulation.
- The behaviour of the assigned material mapping relationship and the effect on the material markers.
- The variations observed in the results and accuracy following changes to the thresholding and geometry production process.
- Variations observed and the effect on the simulated accuracy due changes in the density calculation and phantom calibration procedure.

The following chapter considers the detailed assessment of the input parameters listed above, providing a measure of the importance of each parameter, and the effect the changes have on the accuracy of the simulation as a whole:

7.1 The Effect of Misalignment in Testing

Research has demonstrated that the elastic modulus of samples can vary significantly depending on the orientation from which the sample was taken. A reduction in elastic modulus of 10% has been demonstrated in material samples taken from the same bone at 10 degrees apart, whilst increasing this misalignment to around 20 degrees has shown a reduction of as much as 30 – 40 % [60, 208].

The torsional testing undertaken in this thesis provides a failure methodology that is theoretically less sensitive to misalignment than the buckling failure exhibited in compressive failure modes. Samples tested under torsion were aligned as close to the axis of rotation as possible. Potted constraints were used to constrain the samples. This allowed for three-axis alignment, ensuring the cortex could be

aligned with the principal axis of rotation. However, the geometry of the distal end of some of the porcine samples resulted in the centroid of the cortex being displaced from the centre of rotation.

To verify the alignment of the samples throughout testing, post-test CT scanning was undertaken. This theoretically matched the alignment of the physically-tested and simulated samples, ensuring that the reduction in elastic modulus would not be incurred, and that the 'as tested' alignment of the samples continued through both *real* and *in silico* testing. It was considered that this methodology offered suitable spatial accuracy, and offered a simpler methodology than that shown in literature, wherein extensive surface scanning is employed and the surface map correlated with the Finite Element model [70]. Simulation was undertaken to test the sensitivity of the results to changes in the alignment of the samples, the spatial registration, and how load was applied to the simulated bone samples.

7.1.1 Methodology - Torsion

Throughout simulation, the model was aligned with a reference surface created through post-test scanning. The same alignment process was followed in the sensitivity assessment, using a single gauged sample (sample SM1) to test the effect of intentionally misaligning the model.

The first step was to determine the original alignment of the sample that had been used for the strain gauge correlation in Chapter 6. The centroid was then determined by observing the cortex at discrete intervals along the samples length in a similar manner to the analytical calculation assessment performed in Chapter 4. For each interval, the interior and exterior position of the cortex was noted for both extremities on the central x and y axes. This allowed the area-weighted central position of the 2D centroid to be determined for each of the transverse slices Eq. 7.1, 7.2. The centroid position for each slice was then noted, and linear regression exercises undertaken in the x and y orientations, providing the 'axes of best fit'. The angle of these axes from the origin was then noted, providing the original 'aligned' orientation. The mid-point of the angled line was then determined. Rotation of the simulated sample was undertaken from this point.

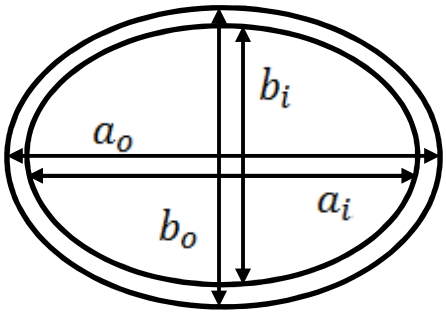

$$Centroid(x) = \left(\frac{a_o - \left(\frac{a_o - a_i}{2}\right)}{2}\right) \quad 7.1$$

$$Centroid(y) = \left(\frac{b_o - \left(\frac{b_o - b_i}{2}\right)}{2}\right) \quad 7.2$$

Where:

Centroid is measured from inner edge at $a_i = 0$ and $b_i = 0$

$a_o$is the outer diameter at its widest point

$a_i$is the inner diameter at its widest point

b_o is the outer diameter at its widest point

b_i is the inner diameter at its widest point

This process is shown in Figure 7.1.,which shows a number of the discrete slices, and the central line produced from the combined information. The sketch is an arbitrary cylindrical cortex, which does not represent the true geometry of the simulated samples. The effect of alignment changes was measured following rotation in the anterior-posterior orientation and in the medial-lateral orientation. Alignment changes were performed upon both the Finite Element model and the background images from which the model was derived. This ensured that the material-mapping algorithm yielded the same results for Young's modulus throughout testing, as the re-meshing procedure required following each alignment change must refer back to the original CT data to obtain the density information required for material mapping. From the original aligned position, the sample was rotated 1, 2, 4, 6, 10 and 15 degrees in the anterior-posterior (A-P) direction, and then in the same number of intervals and degrees in the medial-lateral (M-L) orientation. Simulations were finally undertaken in a combination of A-P and M-L alignment, with intervals at 1+1, 2+2, 4+4, 6+6, 10+10 and 15+15 degrees.

(a) 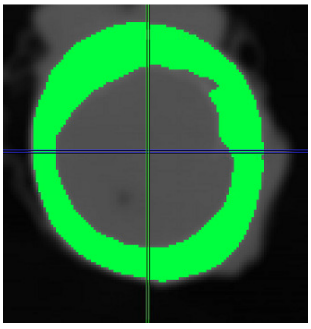 (b) 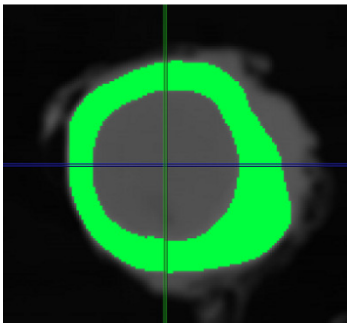 (c) 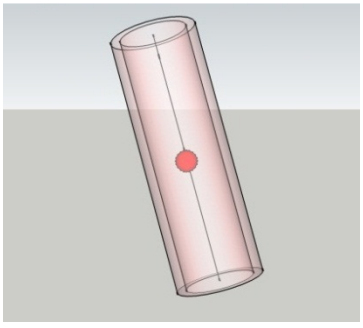

Figure 7.1. images (a) and (b) showing sections of cortex at discrete intervals along the sample length. The combined centers were used to derive a line through the center of the cortex (c). The midpoint of this line forms the center of rotation, as highlighted by the red sphere.

Force was applied at the A-P and M-L extremities on the cropped proximal face through the inclusion of opposing couples. The level of torque applied was maintained throughout orientation changes, with an arbitrarily assigned torque of 40 Nm. The sample length simulated was maintained throughout

testing, via the inclusion of surface markers, which ensured that the distance between constrained and forced positions was kept consistent, despite the changing orientation of the sample.

A single discrete result (1st principal strain) was extracted from the simulation for a single node (with the same node selected) for each alignment iteration. This was selected as principal strain is a key result in simulation and has previously been utilised in fracture testing studies [45].

7.1.2 Results

The results observed for the changing alignment are tabulated in Appendix A1.16 and provided graphically in Figure 7.2. As can be seen, the overall effect of changing the sample orientation is relatively consistent, generally showing a reduction in indicated strain, for increasing misalignment. Change in the anterior-posterior axis is shown to have the largest effect on the observed result, with initial small level change increasing the strain result. Following initial reduction in the observed values, alignment in the medial-lateral direction shows relatively little change throughout the remaining iterations.

The single largest change in an observed value is observed in the 4-degree anterior-posterior alignment, representing a significant 19.4% change in the strain reading for the single node selected. The percentage that the iteration result differed from the original 'aligned' result was also calculated, and showed that the anterior-posterior alignment has the greatest effect on the overall results. Despite the large difference in values, the average percentage result change per degree of rotational change (total percentage error divided by number of degrees of misalignment) is 1.84% for the A-P alignment, and notably lower at 0.77% for changes in the M-L alignment.

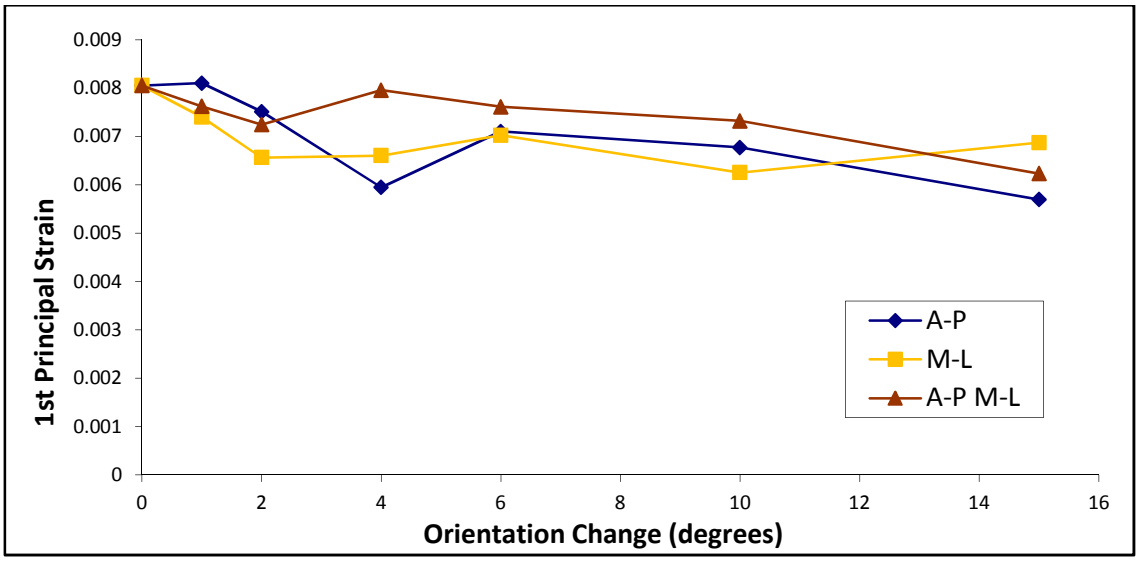

Figure 7.2. The change in 1st principal strain for sample SM1 when changing the orientation of the simulated sample in the Anterior-Posterior, Medial-Lateral and combined Anterior-Posterior-Medial-Lateral orientations.

7.1.3 Discussion

The result analysis shows a reduction in the result for 1st principal strain with increasing change in alignment from the original position. The value and polarity of the change is shown to fluctuate at higher values of misalignment. The lack of consistency in the observed change of the results can be seen in Figure 7.3, which demonstrates the continued fluctuation in observed error from the original value, particularly around 4 to 6 degrees. Continual change in the anterior-posterior and combined anterior-posterior medial-lateral arrangement is shown to provide reduction in strain following rotation of over 10 degrees; however, the percentage change in the result per degree of changed alignment remains small.

The combined A-P M-L results were obtained through independent testing as opposed to combining the individual results of the A-P and M-L simulation. As such, the strain result at 4 degrees of alignment is of interest. Here the change in A-P M-L is shown to be significantly positive, as opposed to significantly negative as was demonstrated by the A-P only arrangement.

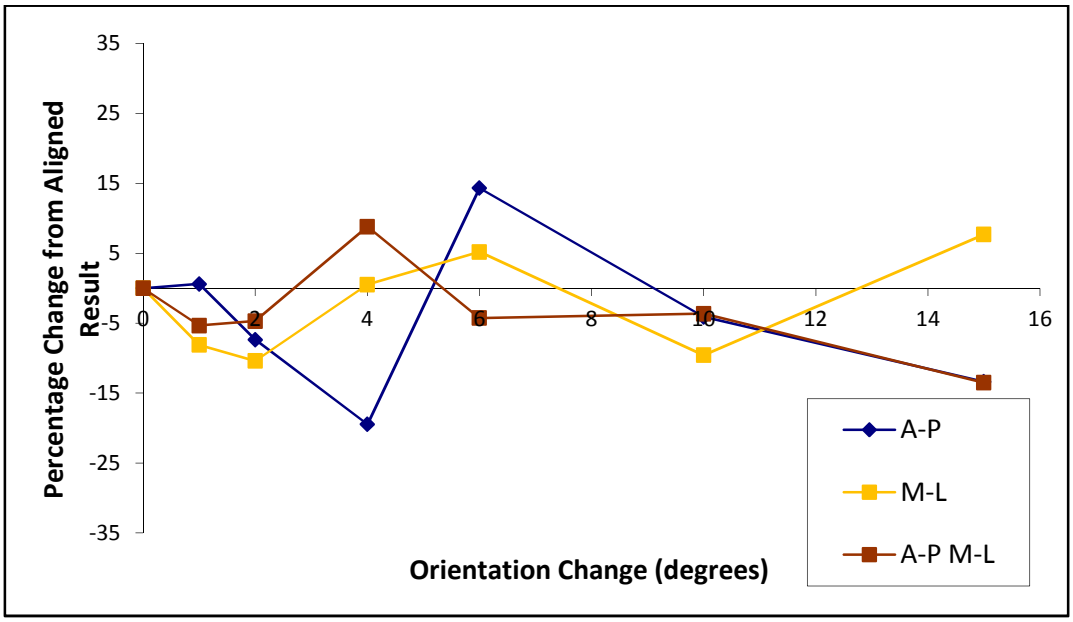

Figure 7.3. The percentage change in the 1st principal strain result for the same node, with respect to the result observed for the previous alignment step.

It was considered that taking a single strain value from a single node for the comparisons might have induced this anomaly, through a rogue high result at a node within a single element or at a point of singularity within the model. Consequently further simulation was undertaken to determine if the effect could be mitigated through an averaging process, similar to that used in stress correlation (Chapter 6). Five techniques were selected to review the result in the A-P alignment. For each

technique, elements were selected within a predefined region of interest surrounding the area of maximum strain indicated by the simulation. The five differing assessments were then used to assess the maximum and averaged results within that region. The different assessments were selected to assess the following:

- Absolute Maximum Principal Strain – The highest single node result within the region of interest.
- 99.99 Percentile Principal Strain – The 99.99 percentile, selected to omit rogue nodal result as a result of singularities.
- (i) Average Maximum Principal Strain (highest 15 individual values in ROI) – Averaged result, similar to that used in Chapter 6.
- (ii) Average Maximum Principal Strain (highest 5^{th} to 20^{th} individual values in ROI) – Average result, omitting the top four results to eliminate potential singularities.
- (iii) Average Maximum Principal Strain (highest 10 individual values in ROI) – Averaged result, similar to that used in Chapter 6.

Figure 7.4. shows the results of this study, and confirms that the general reduction of the 1^{st} principal strain with changing orientation continues for each assessment technique. The anomalous nature of the 4-degree orientation remains unchanged despite re-testing in the Finite Element solver. It is considered that this anomalous result may be a product of the re-meshing process that is required in the software following each alignment change. Re-meshing was attempted numerous times; however, the result remained, suggesting a software glitch/incident as a result of the manner in which the automated meshing procedure adapts to the change in the orientation of the background images.

Linear regression was performed on the results of the A-P alignment, and demonstrates similarity for each assessment method of the 1^{st} principal strain result (table 7.1). R^2 values show a relatively weak fit with the inclusion of the seemingly anomalous 4-degree iteration ($R^2 = 0.518$ to $R^2 = 0.617$) with correspondingly low confidence ($P = 0.68$ to $P = 0.36$). The exclusion of this result from the regression calculations retains the gradient observed previously and considerably increases the fit of the data ($R^2 = 0.815$ to $R^2 = 0.961$) ($P = 0.001$ to $P = 0.014$). In both iterations the highest R^2 and P scores are determined from the observation of the absolute maximum principal strain value, demonstrating that this type of individual result is appropriate for the description of changing boundary conditions.

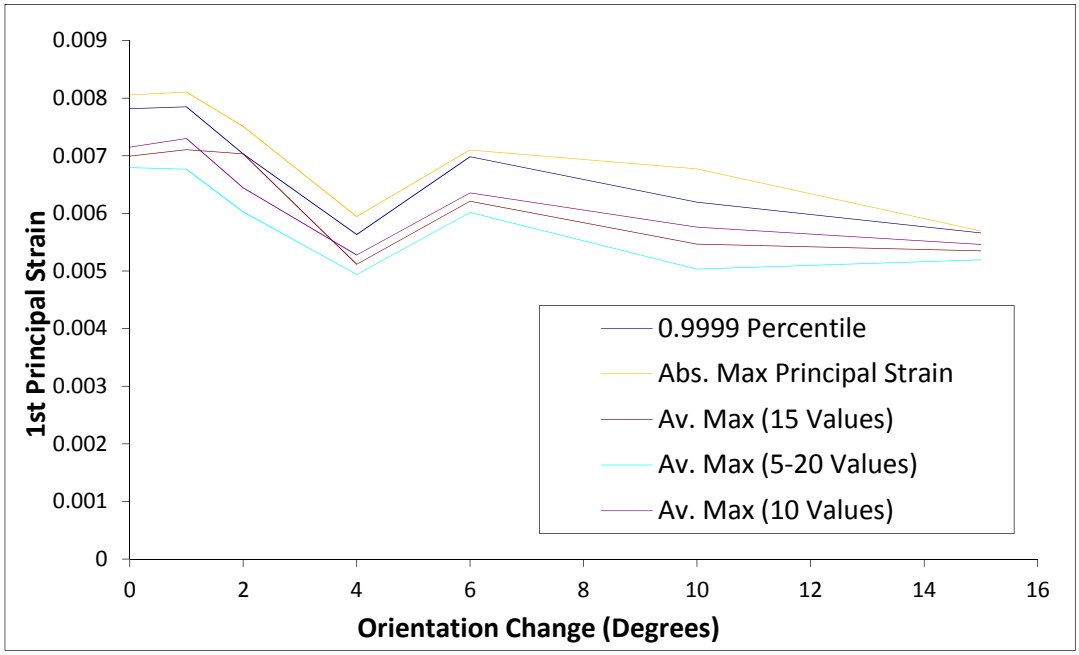

Figure 7.4. Changing 1st principal strain with respect to the alignment of the sample in the A-P orientation. Results are plotted for varying methods of observation of the maximum principal strain, demonstrating the anomalous nature of the 4-degree result.

Table 7.1 correlation of changes to alignment in A-P orientation in torsion. (*) Denotes removal of anomalous 4 degree result.

	Gradient	R^2	P Value	Gradient*	R^2*	P Value*
Abs Max Principal Strain	-0.000138	0.617	0.36	-0.000151	0.961	0.001
Av Max Principal Strain (i)	-0.000130	0.569	0.55	-0.000143	0.927	0.002
Av Max Principal Strain (iii)	-0.000105	0.520	0.68	-0.000116	0.879	0.006
Av Max Principal Strain (ii)	-0.000120	0.554	0.68	-0.000132	0.931	0.014
99.99 Percentile	-0.000105	0.518	0.50	-0.000115	0.815	0.002

The results demonstrate that there is an effect on the observed result for 1st principal strain with change of orientation angle, but with the exception of anomalous entries, the change is generally small (around 2.5% of the 'aligned' result per degree of orientation change). The correlation demonstrated by the sensitivity assessment shows that the maximum principal strain in simulation is linked to the alignment of the sample ($P < 0.001$). The variation in results, particularly as shown at low rotation in the M-L orientation, highlights the importance of determining the correct alignment of the sample within simulation and subsequently in post-test scanning.

It should be noted that the effect of a one-degree change at the centroid is a translation of approximately 1.1 mm in the A-P or M-L direction at the extremities. The accuracy of the alignment is a product of the sensitivity of the scanning equipment used during the scanning processes, and dependent on the exported voxel size (approximately 0.3 mm as discussed in Chapter 3). It was

considered that the theoretical alignment accuracy would therefore be able to accommodate for a 1.1 mm change in location at either extremity, and thus the alignment error of any given sample would be reduced to less than 1 degree in any given orientation.

7.1.4 Misalignment in Compression

Following the testing of alignment in torsion, alignment during compressive tests was considered. The importance of the correct alignment within compressive testing has been highlighted in literature [20]. This study focused more upon the alignment of the validatory measures, such as the position of strain gauges, than upon the alignment of the sample within the test equipment.

Generally in CT-FE studies the application of force involves applying of a point load to a surface, and the consequent deselecting of this region when reviewing the results, such that any high values for stress or strain at the point of application are ignored. This is a perfectly valid manner in which to not only apply the load, but also constrain the opposing end of the sample, and is commonly used [20, 45, 100]. The manner in which the bones were potted for compression in this study creates complications in determining which parts of the bone are active, and which are isolated. Whilst this could be considered a limitation, it replicates the effect of real loading *in vivo,* in which the precise constraining of the bone is also difficult to determine.

In the laboratory, force is applied on the potted bone samples at the end of the cemented constraint. Consequently, it would be reasonable to assume that the load was applied directly and centrally at the end of the potted region. In actuality, potting in this manner may allow for the transmission of forces from the femoral head, which may induce bending moments within the mid-shaft, or higher compressive loading on the medial aspect of the cortex, beneath the femoral neck.

In Chapter 6, modelling of the compressive force was simulated through the inclusion of segregated point loads upon the cropped upper proximal surface of the cortex. Whilst valid, the inclusion of a small number of single point loads induced unwanted local effects, and consequently spreading this force across the entire upper surface was considered. This process is valid for the majority of mechanical, regular structures; however, Figure 7.5 shows the limitation of this for biomechanical simulation, namely that the distribution of nodes within the mesh is asymmetrical.

Figure 7.5. Nodal plot of the upper face of a cropped sample of cortex. The medial aspect (uppermost) and posterior aspect (left) show thicker walls, providing complication during the application of distributed loading.

This is due to both the automated meshing algorithm increasing the node count at regions of interest, and the asymmetrical geometry of the cropped cortex surface. As a result, dividing the axial load equally across these nodes resulted in higher forces upon the anterior-medial aspect. In actuality this uneven load may be a better representation of the *in vivo* condition, as this increased depth of cortex is naturally produced as a response to the increased level of loading in this region during normal ambulation.

The complete potting of the femoral head was undertaken to isolate the mid-shaft of the bone. This assumes that compressive force is applied evenly to the diaphysis at the level of the cementing medium and that no off-axis loading occurs. In actuality, the bone is not physically cropped at this point in laboratory testing, and the continuation of the bone material within the potting medium may provide complication in the determination of applied force. The sensitivity assessment of simulation to misalignment in compression focused upon the manner in which force is applied to the static model rather than the alignment of the model itself (as was shown in the torsional alignment study).

7.1.5 Methodology

The effect of change in alignment was measured using the methodology shown for the strain gauge correlation (Chapter 6). The results compared were the maximum and minimum principal stress, as observed at each strain gauge location. The derivation of the stress result follows that shown in the general comparison of simulation and laboratory results. The following effects were considered for changing the application of force in compressive simulation:

- Effect of moving from ‘point’ to ‘distributed’ loading
- Effect of ‘off axis’ loading in Y direction
- Effect of ‘off axis’ loading in x direction
- ‘Over’ and ‘under’ loading of the sample in compression
    - All combinations of the above

Similar to the effect of incorrectly assigning nodal force in simulation, the constraining of the bone in physical testing may induce unwanted bending moment within the shaft. Consequently further simulation was undertaken to consider adding a proportion of the distributed vertical load in the x and Y directions. Sampling the strain gauge results in discrete intervals may have resulted in relaxation of the sample and consequently cause under-loading. This would have meant that applying a given load within the simulated model would have over-predicted the response. This effect may also be noted as a result of incorrect assessment of the sample length, as determined by the exposed (un-potted section). Therefore, in addition to simulating the effect of adding load in the x and y axes and the distribution of force to the cropped diaphysis, the final simulated effect was over and under-loading, i.e. applying more, or less force to the simulation than was applied within the laboratory

7.1.6 Results

Comparisons were undertaken for a single compressive loading interval (0.5 kN axial), with respect to a single set of gauge readings at each rosette, providing six principal stresses for each sensitivity test iteration. Once the most appropriate sensitivity iteration had been determined using the 0.5 kN load, the other load points were included, increasing the number of principal stress data points in the comparison. As meshing was unchanged throughout testing, the elements selected at each gauge location were kept consistent throughout all testing iterations. The details of the changing arrangement of input forces and the ratio of predicted to observed results at each of the three gauge locations tested is tabulated in Appendix A1.17

(a)

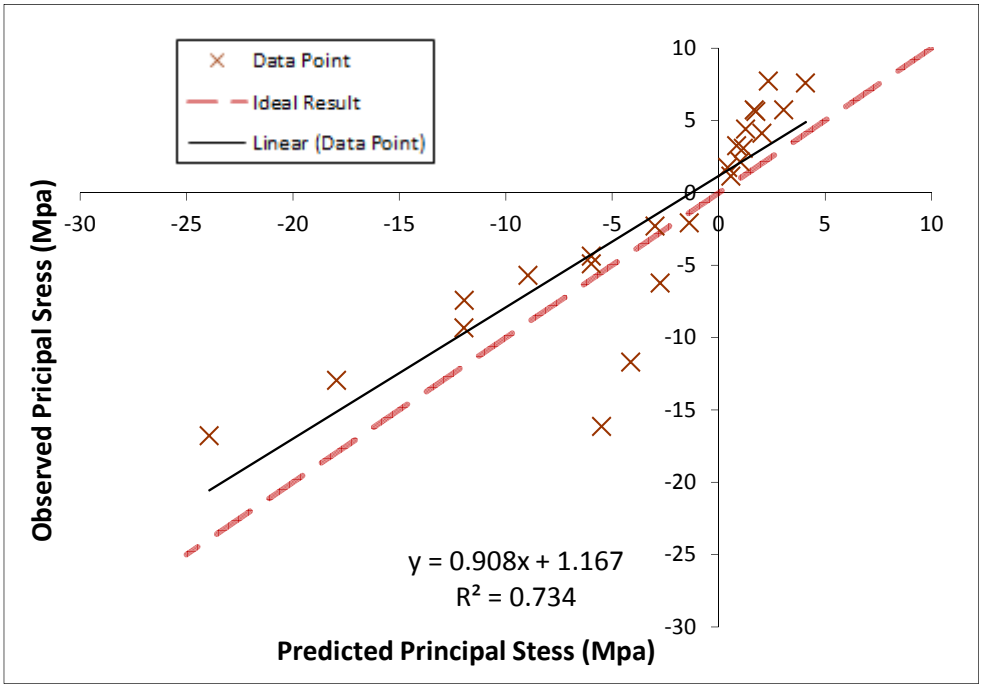

Figure 7.6. (a,b,c) The three best force input arrangements with respect to comparison of principle stress with the values measured in the laboratory. As can be seen, there remains significant variation in the three plots. Plot (a-c) demonstrates iterations 6,7 and 13 respectively.

(b)

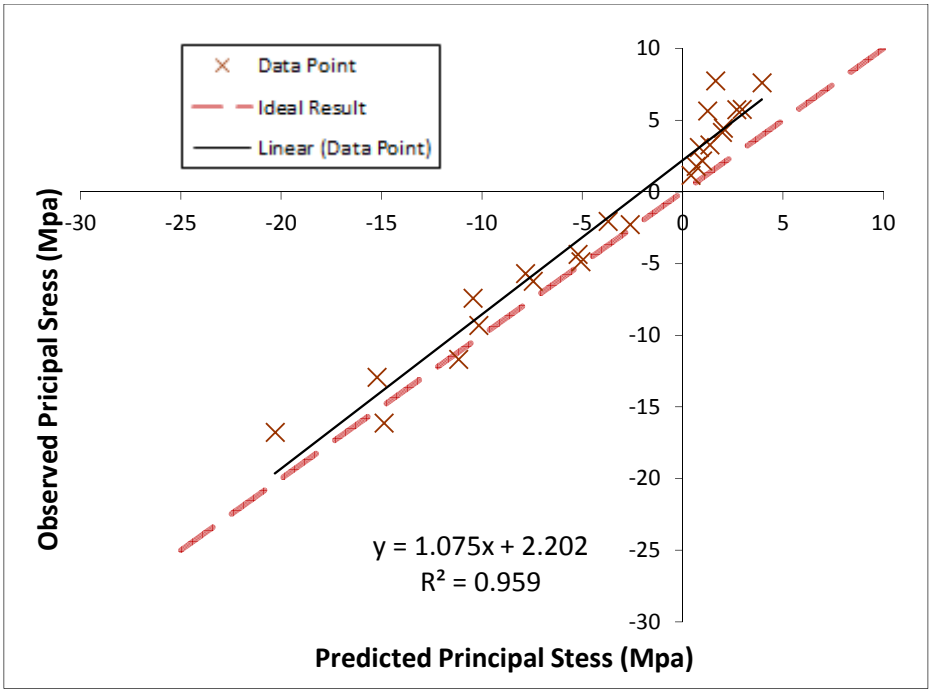

(c)

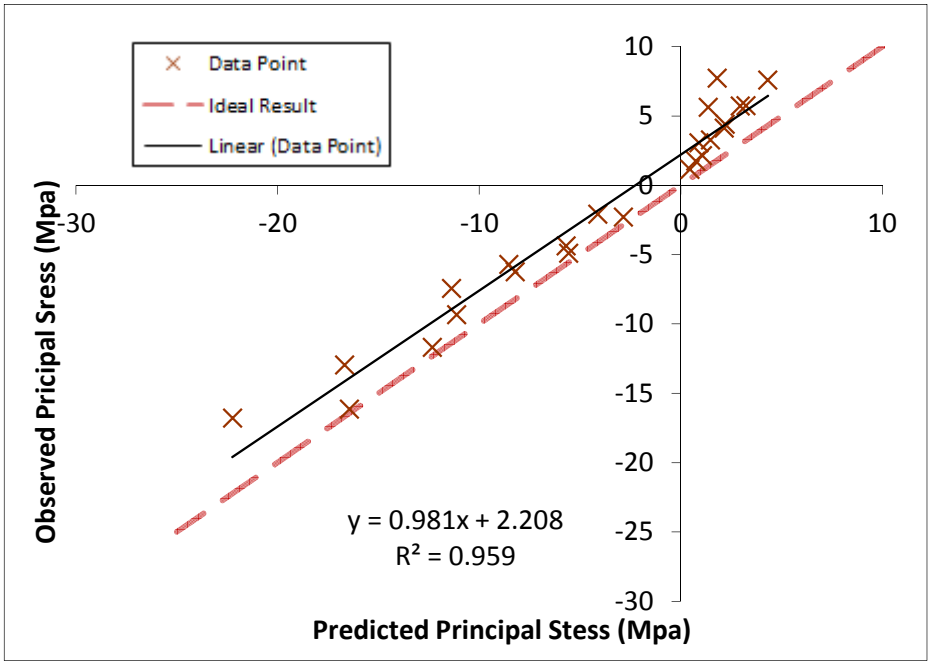

Linear regression of the initial load step was undertaken for all thirteen iterations, on a *predicted vs observed* basis. This determined the agreement of the sensitivity iteration to the ideal result of $x = y$, and the R^2 value denoting the fit of the plotted data to this ideal line.

Following this comparison, the three iterations that provided the closest correlation with the ideal result were extrapolated to consider the results of the arrangement with respect to the other loading intervals used in compressive loading (0.5 to 2kN). The iterations providing the closest match to the ideal result were iterations six, seven and thirteen as shown in Figure 7.6. Despite offering the three best correlations, the plots demonstrate significant variation. Iteration six shows a complete set of results for one of the gauges that doesn't match the general correlation, suggesting alignment was not correct in this iteration. The plots for iterations seven and thirteen improve upon this, and R^2 values are consequently significantly increased.

7.1.7 Misalignment Discussion

Correlating the principal stress results for these alignment iterations demonstrated that the alignment and loading procedure is critical in the determination of accurate results. For the single test above, the best agreement was noted for alignment iteration thirteen. This corresponded to a proportion of the load being applied in both the x (35 % of normal load) and y (5 % of normal load) directions as well as 100 % of the applied axial load applied vertically. The results of this distributed loading test ultimately obtain a similar accuracy to those initially used for comparison in Chapter 6. In Chapter 6, point loads at the center of the cortex demonstrated RMSE (abs) of 2.57 MPa (15.8 %) and R^2 = 0.938, with distributed loading and added lateral load the highest values achieved were RMSE (abs)

of 2.73 MPa (16.3 %) and $R^2 = 0.959$. The test ultimately demonstrates that the application of load within simulation requires extensive consideration. Whilst there are negative effects of point loading when compared to distributed loads, applying distributed loading to an automatically meshed surface requires significant manipulation to match the loading condition of the laboratory.

Alignment represents a potential source of error in testing methodology that has been published without accurate spatial registration [137, 140, 165]. The methodology utilised in this study involved the post-test scanning of each cemented subject, outside of the main test equipment. This offers a good level of accuracy with respect to the sample in the primary constraints, but has the potential to induce error with respect to the actual alignment during testing. For example, the position of the outer constraint with respect to the axis of rotation is assumed to be in line, with no accommodation provided for out-of-plane arrangement.

It was considered that these limitations would be accommodated through the 'jaw' arrangement of the crossheads; however, mapping of the reference positions *during* testing could be considered for future studies to increase overall accuracy. This would accurately determine the 'as tested' alignment, improving upon the pre-test alignment testing as shown in literature [37, 70] and the post-test alignment used in this thesis.

7.2 Changes to the Material Mapping Protocol

The material mapping methodology defined in Chapter 3 confirmed the applicability of Morgan et al.'s relationship for mapping porcine bone on the basis of a correctly mapped elasticity for a given apparent density. Cortical bone was selected as the material type to confirm the applicability of the relationship. More detailed consideration of the effect of the material relationship upon the ultimate results was not considered at that stage. Following increased accuracy in the determination of surface results (Chapter 6); the effects of material mapping can be considered in more detail.

The procedure of material mapping has been investigated in detail in human CT-FE studies, with relationships predominantly derived from small samples, rather than whole bone testing. The relationships derived have then been extrapolated to whole bone modelling, and used to obtain accurate results [37, 82, 102]. CT-FE research has been undertaken in human femoral samples, using various material mapping relationships [27, 59, 80]. Calculation of the most appropriate material mapping relationships for a single human bone model has also been undertaken [82]. This research, which undertook assessment of compressive load in a human femur, demonstrated the significantly increased accuracy available at local level following the selection of Morgan et al.'s relationship, as defined below [72].

$$E = 6.850\rho_{app}^{1.49} \qquad 8.1$$

The applicability and accuracy of material mapping relationships with respect to animal substitution has not been extensively considered in literature. In fact, studies have detailed the dissimilarity between human and animal tissue, Rice et al. stated:

"The data on the mechanical properties of cancellous bone tissue cannot be combined to form interspecies mechanical property relationships" [196]

The mapping of Young's modulus has a significant effect on the results, and it is therefore vital to consider not only if a mapping strategy is applicable, but also if the accuracy of results can be improved by changing the relationship used. Consequently an assessment was undertaken that assessed the accuracy of a number of relationships that met the initial density-elasticity criterion for the mapping of cortical bone.

7.2.1 Methodology

In this section, the selected material relationship from Morgan et al. was assessed in comparison with alternative mapping relationships from Carter and Hayes, Snyder et al. and Keller et al. [65, 71-73, 76] to assess the effect of the material relationship on stress results at a local level. The E-BMD relationship for each relationship was demonstrated in Figure 3.15. Each of the relationships selected was derived from material testing of both cortical and trabecular bone and each has a power-based relationship, with a corresponding rising rate in gradient as the apparent BMD of the source image increases. An additional relationship was originally proposed for testing, provided by Lotz et al. [71]. This relationship was physically derived for cortical bone only, and differs from the others in that it is linear. The relationship was ultimately omitted from testing, as negative Young's moduli are exported in the trabecular bone regions masked within each model.

In order to retain consistency during comparative runs, the geometry mapping, thresholding level and alignment of the tested sample were maintained throughout this study. The meshing protocol is based upon the meshing settings and voxel distribution of the source image (which were not to be changed) and consequently the elemental distribution between iterations was identical, with only the mapped material property changing within each element. This ensured complete consistency in modelling and the comparison of each iteration. Similarly, the boundary conditions such as constraining of the isolated regions and the application of force were maintained. Torsion was considered as the most appropriate methodology for loading, offering a reduced response to misalignment, and also providing consistently linear gauge results during physical testing.

Simulation was undertaken *in silico* using an increasing loading regimen at 5 and 10 Nm intervals to a maximum value of 40 Nm, to match the laboratory validation undertaken in Chapter 6. Values were

observed for maximum and minimum principal stresses at each of the gauge locations, whilst the principal strains within the cortex were also noted for each mapping protocol.

7.2.2 Results

After each of the models was exported into the Finite Element solver, the occurrence and material value of each material marker in the completed mesh was recorded. As the material marker corresponds with a specific density, which is retained throughout testing (due to the same sample being used), the occurrence of the material markers is consistent across each of the mapping relationships. The change observed between markers is consequently only the material property assigned to each, as is demonstrated in Figure 7.7. This graph shows the increasing material property value with respect to increasing material number (and consequently the increasing apparent density) and also demonstrates the occurrence of each marker.

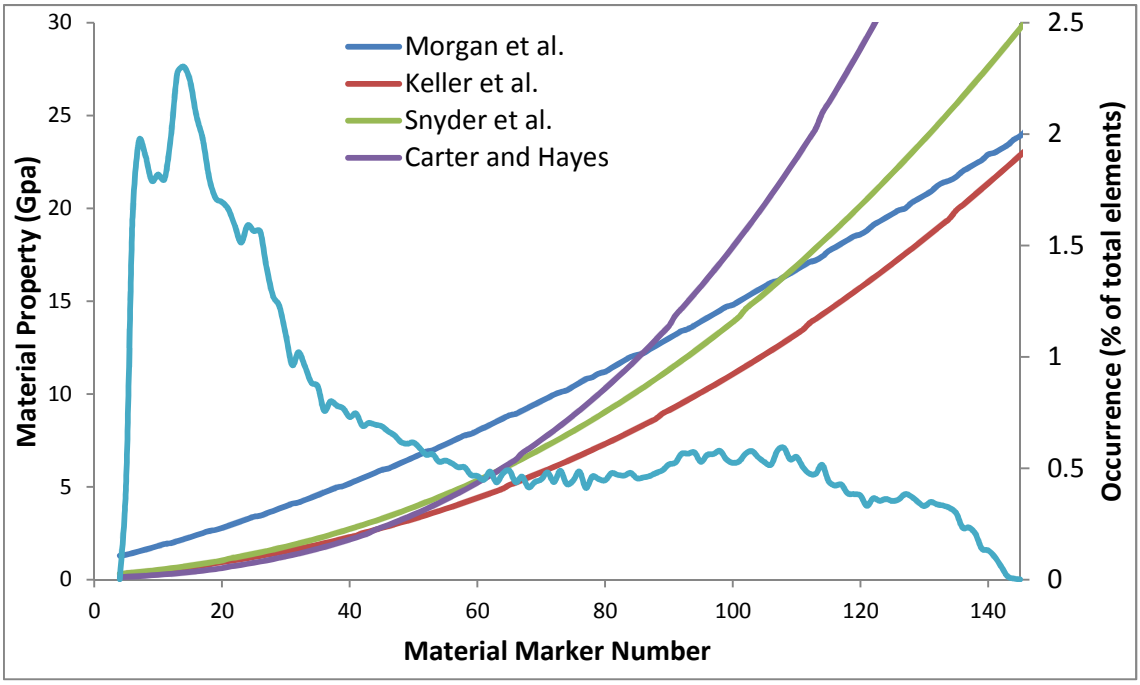

Figure 7.7. The occurrence rate of the material markers within the tested mesh (plotted as a percentage of the total number of elements). Additionally plotted is the Young's modulus of each material marker for each of the tested relationships.

Results were compared on a *predicted vs observed* basis (Figure 7.8). Results are recorded for maximum and minimum principal stress at the site of the strain gauge locations with re-calculation undertaken at each loading interval. This provides a direct comparison of the result recorded in the laboratory with that predicted in simulation. The linearity of the trendline and the R^2 value of the

combined data define the applicability of each of the mapping protocols. In addition the root mean squared error (RMSE) and the maximum error in absolute and percentage terms were noted for each relationship.

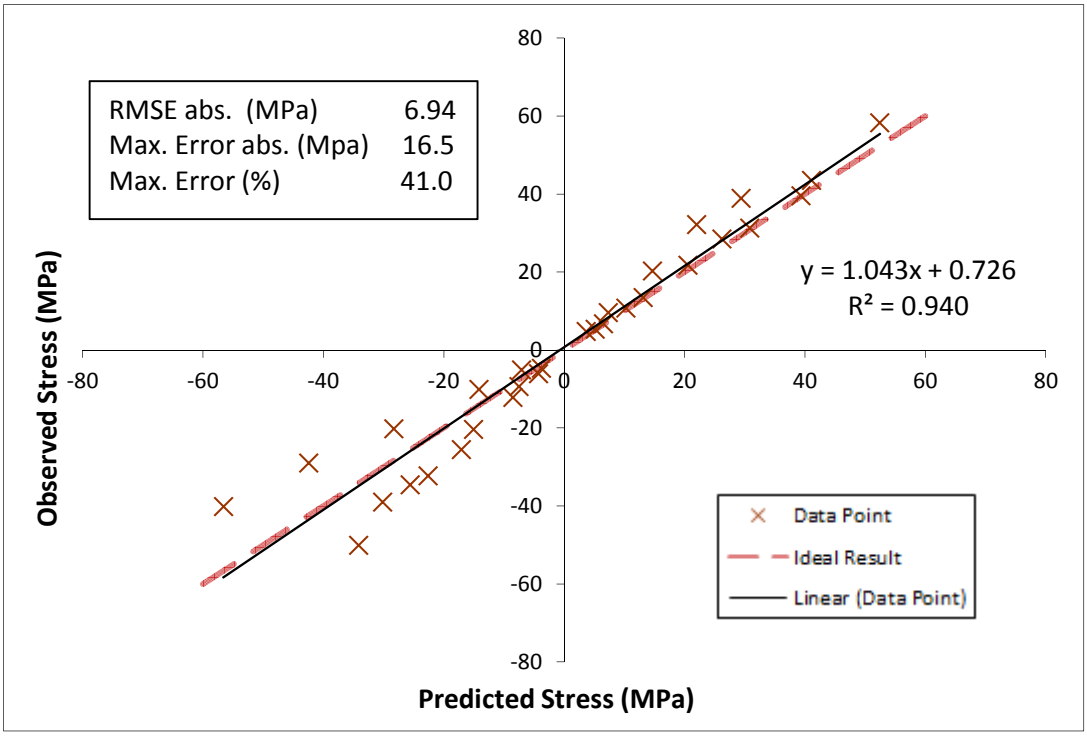

(a)

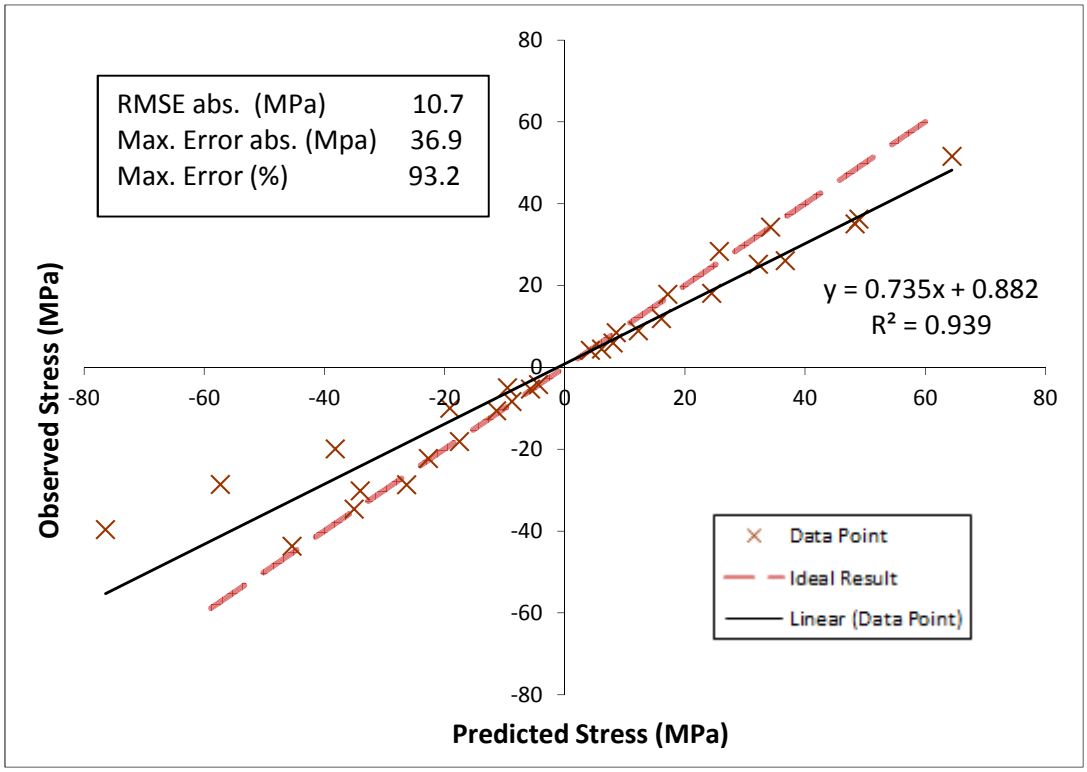

(b)

(c)

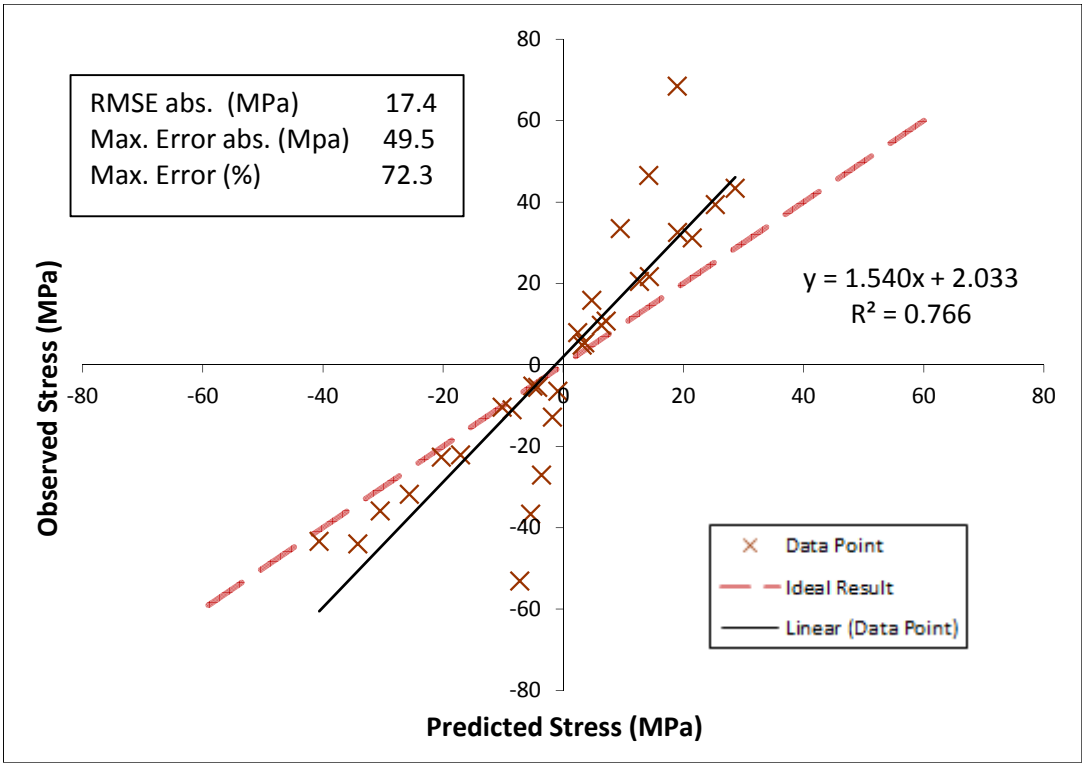

(d)

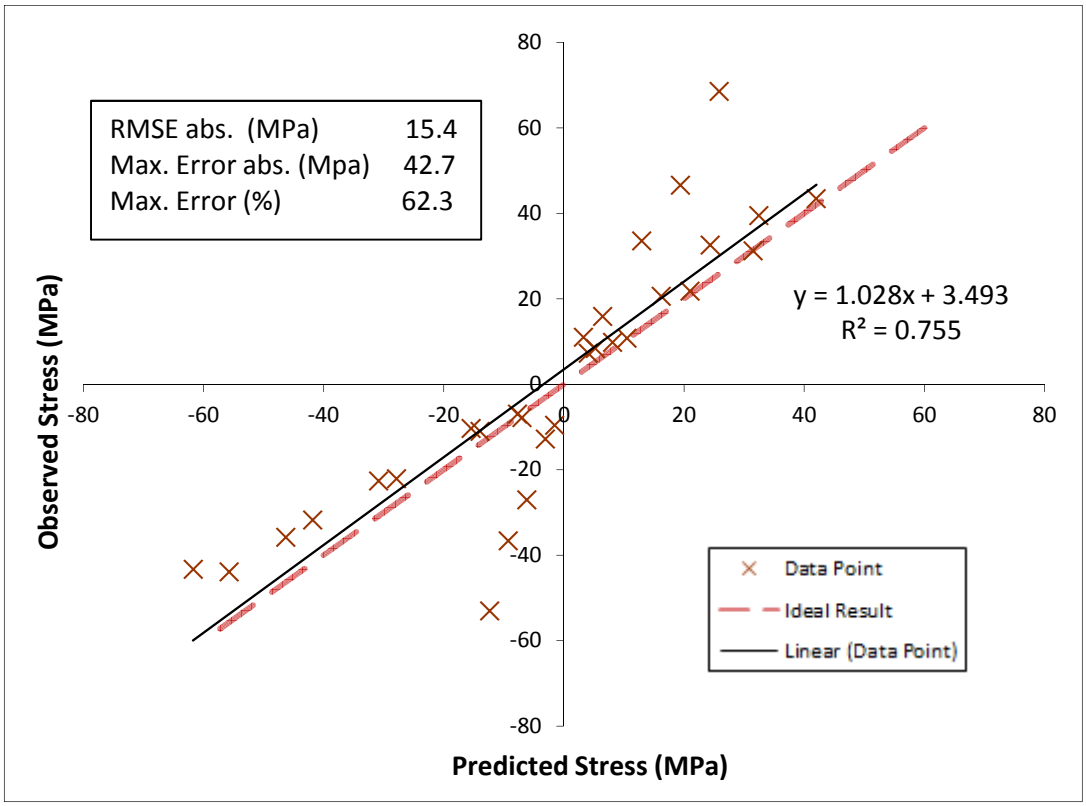

Figure 7.9 (a-d), the predicted vs observed results for the four tested material relationships. The relationships are shown in the following order: (a) Morgan et al., (b) Keller et al, (c) Snyder et al., and (d) Carter et al.

7.2.3 Discussion

As can be seen from Figure 7.8, there is significant variation in the accuracy observed for a single mask due to the relationship used for material mapping. The confirm those proposed by Taddei et al. [209] in that the material relationship can have a significant effect on the observed results, despite the consistency retained in all other aspects of simulation. The variation shown in this study is greater than the variation demonstrated by Taddei et al.; however, this is potentially explained by the larger range of densities observed in porcine bone, as shown in the material markers (Figure 7.7). As with the published research for human samples, Morgan et al. provides the best agreement with the results recorded within the laboratory, with the closest agreement to $x = y$ and the best R^2 value [72]. Peak error is also lowest using this technique, at a maximum of a 41% over prediction for a single value. The absolute results in this material mapping study differ from those shown for Morgan et al.'s relationship in Chapter 6, due to changes in the thresholding level selected for this test, which were approximately 9% higher than those used in that chapter.

The relationship proposed by Keller et al. [65] provides a comparatively close estimation; however, individual peak error of a single result is increased, with a single over prediction of 93% noted. An interesting dichotomy is noted in the results plots for Snyder et al. and Carter et al., which is brought about entirely as a result of the under prediction of the stress/strain field at gauge location three. This gauge was located on the posterior surface of the bone, at a region that had been defined as having a high stress gradient through laboratory testing and simulation. The manner in which the dichotomy is observed is similar to that observed during alignment tests, suggesting that this iteration was misaligned. This was; however, not the case, as all samples within this study were tested with identical boundary conditions. It is therefore suggested that the dichotomy is observed purely as a result of mapping protocol. The two equations that provide this dichotomous effect are those with the highest power, suggesting that the higher rising rate and consequent over prediction of material value may be a contributor to the inaccuracy in the comparison.

The results of this study highlight that relationships derived for human samples are appropriate for porcine studies, contradicting the hypothesis of Rice et al. However, Morgan et al.'s relationship dates from 2003, significantly later than the statement made by Rice et al. (1988), and following a significant level of development in the CT-FE process.

7.3 Thresholding Changes during Geometry Masking

Thresholding is the process discussed in Chapter 3 that is used for the selection of simulated geometry throughout this thesis. Thresholding adjustment links to the greyscale values of the voxels within a source image. Thresholding and the more clinically-used term of 'windowing' are therefore processes in which areas of greyscale and therefore apparent density are omitted or included within a given

selection. In simulation, this selection is then meshed to create the Finite Element model. The result of this is that mapping using a thresholding technique to define geometry also affects the average apparent density and therefore the average assigned Young's modulus within the model. As such, thresholding for geometry cannot be considered to be a geometrical input parameter in isolation. The manner in which the threshold level is applied to various constitutions of bone (specifically cortical bone) has been considered in literature [210]. Lim Fat's study, which used greyscale 'contours' (circumferential lines in a given image slice that occur at the boundary between greyscale values – for example the contour separates values above or below a given greyscale figure) to map regions of interest, was unable to determine differences in small changes to the thresholding levels. The methodology used in that study measured the area of cortical bone that was selected in 2D slices for a varying range of thresholded greyscale values. The effect of changing this range is the selection or de-selection of softer, less dense materials. Whilst the values in that study are useful for defining 'true' high density cortical bone, they are limited in Finite Element modelling, within which the bone structure requires the inclusion of less dense tissues to define the geometry accurately, and to transmit forces correctly through the less dense regions of a given bone sample.

During the majority of simulation, the thresholding levels were set to ensure that the simulated bone sample had the same external dimension as the physically-measured sample. This geometrical thresholding was checked via physical measurement with Vernier calipers and cross referenced with the source CT image at key locations to ensure that the physical size of the sample was accurately maintained. The effect of incorrect thresholding can be hidden in tests in which the mid-shaft is isolated due to the increased width of the higher densities observed in this region, whereas the inclusion of the epiphyses rapidly lose geometrical accuracy when thresholding values are over manipulated. Figure 7.9 shows this effect graphically with two sample masks, the first of which retains the appropriate geometry as physically measured from a single sample, using a thresholding setting of a minimum of 177, whilst the second shows the effect of thresholding to the value prescribed by Lim Fat et al. for cortical bone through the selection of a minimum value of 703 [210]. As can be seen, large areas of lower density material are omitted from the second model, which impinges on the geometrical accuracy of the simulated bone sample. It should be noted that the precise greyscale value for a model is determined as a response to the scanning parameters, ergo a value of GS = 703 in one scan may differ from the same greyscale value in a different scan (especially in terms of mapped density). This may be a limitation of Lim Fat's work, and calibration should be considered to standardise these values. The greyscale changes are therefore considered for effect only in this section of the thesis, although it should be noted that calibration is likely to exhibit a maximum change of a few per cent, and thus the effect is of importance, and a valid comparison.

The effect of thresholding changes was assessed in this study to correlate geometrical and material changes with the behaviour of the modelled sample. The changes to the average material values as a result of the thresholding changes were observed concurrently with the changing mask volume.

(a) 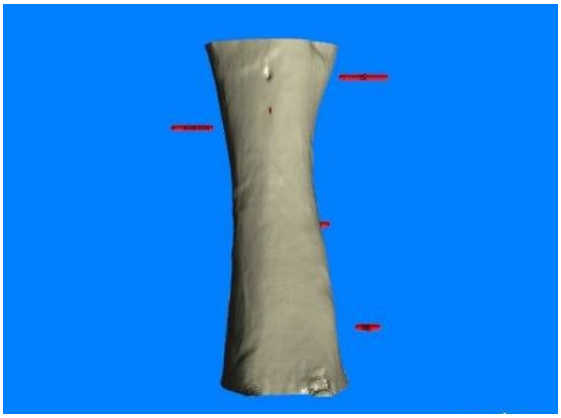 (b) 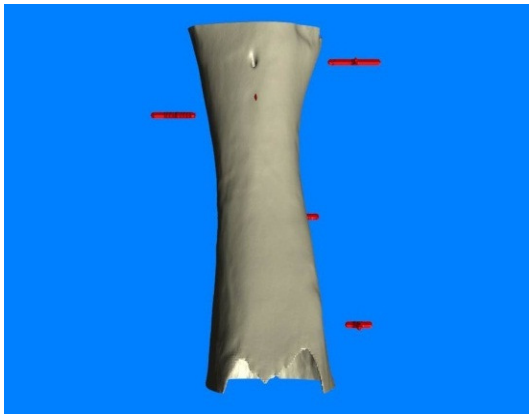

Figure 7.9 (a&b) Two sample masks as tested in the thresholding assessment. (a) shows a sample thresholded to match physical measurements of the actual sample, and (b) a mask thresholded to the levels defined by Lim Fat for the determination of true cortical bone [210].

7.3.1 Methodology

The thresholding process is undertaken by selecting a range of greyscale values. All voxels falling within this range are selected, and thus the mask is created. The intervals tested in simulation, along with the corresponding mask volume, minimum greyscale value, apparent density and applied mechanical properties are shown in Appendix A1.21. A single material mapping relationship was used throughout testing (Morgan et al.).

Only the lower bound of the threshold interval was changed. The upper threshold limit was maintained at a constant maximum throughout testing. This ensures that the upper limit is over and above the maximum values within the source image. This occurs within the internal geometry of the cortical wall, which was retained throughout testing such that no voids were masked within the internal geometry of the sample, at the most dense points.

The upper limit selected, 255 (GS = 2166) corresponds to an assumed BMD of 2.44 g/cm³ and Young's modulus of 26.48 GPa, which exceeds the maximum expected values for porcine bone. This upper limit had no effect on the highest exported material value within the mask, which was in the order of 24.4 GPa as no voxels matched the density required to meet the upper boundary. Each iteration was subjected to a static torsional load of 40 Nm, applied to the upper surface of the cropped mesh, whilst the lower surface was fully constrained in all directions.

Figure 7.10 shows two of the effects of altering the thresholding range. As can be seen, increasing the minimum bound of the range correspondingly increased the minimum assigned Young's modulus. As the source image has a finite and limited maximum greyscale value, the continuing refinement of the lower bound reduced the volume of the exported mask. The final values selected for thresholding were those proposed for pure cortex by Lim Fat et al., and are significantly higher than would be

ordinarily selected for thresholding of a whole-bone test sample. The loss of material definition at this range is unacceptable, as shown in Figure 7.9

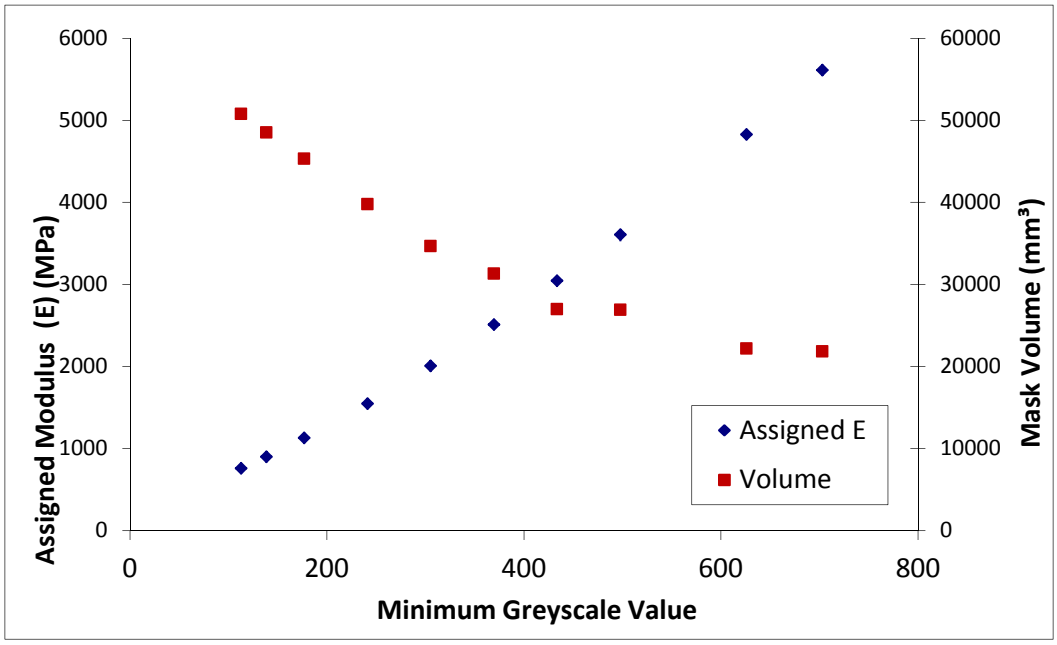

Figure 7.10 The effect of thresholding on the lowest value of Young's modulus mapped within the model, and the effect on the overall mask volume.

7.3.2 Results

As the effect of thresholding changes had the potential to impact upon the selected geometry of the sample, it was considered that the location of strain-gauged results could not be accurately considered for comparison, and thus stress calculations at a specific gauge location were not appropriate. Principal strain was therefore selected as the value from which to observe the effect of thresholding changes.

The effect of changing threshold values in modelling shows a varying and non-linear relationship with respect to the observed results for principal strain. There is initially a reduction in the observed result as the results tend towards a constant minimum value, similar to the expected result behaviour within a convergence study. The converging and diverging shape of the results is demonstrated in Figure 7.11. This effect is observed as the volume and occurrence of softer tissues (as shown in Figure 7.8) are increasingly omitted from the modelled mesh. The result of this removal of the softest tissues is that the results tend to the strain result provided by the stiffer supporting tissue that remains within in the model. For a few further iterations (in the range of 1200 – 2500 MPa minimum assigned Young's modulus) the initial converging result remains relatively static, with an increasing threshold interval having no significant impact on the observed strain results.

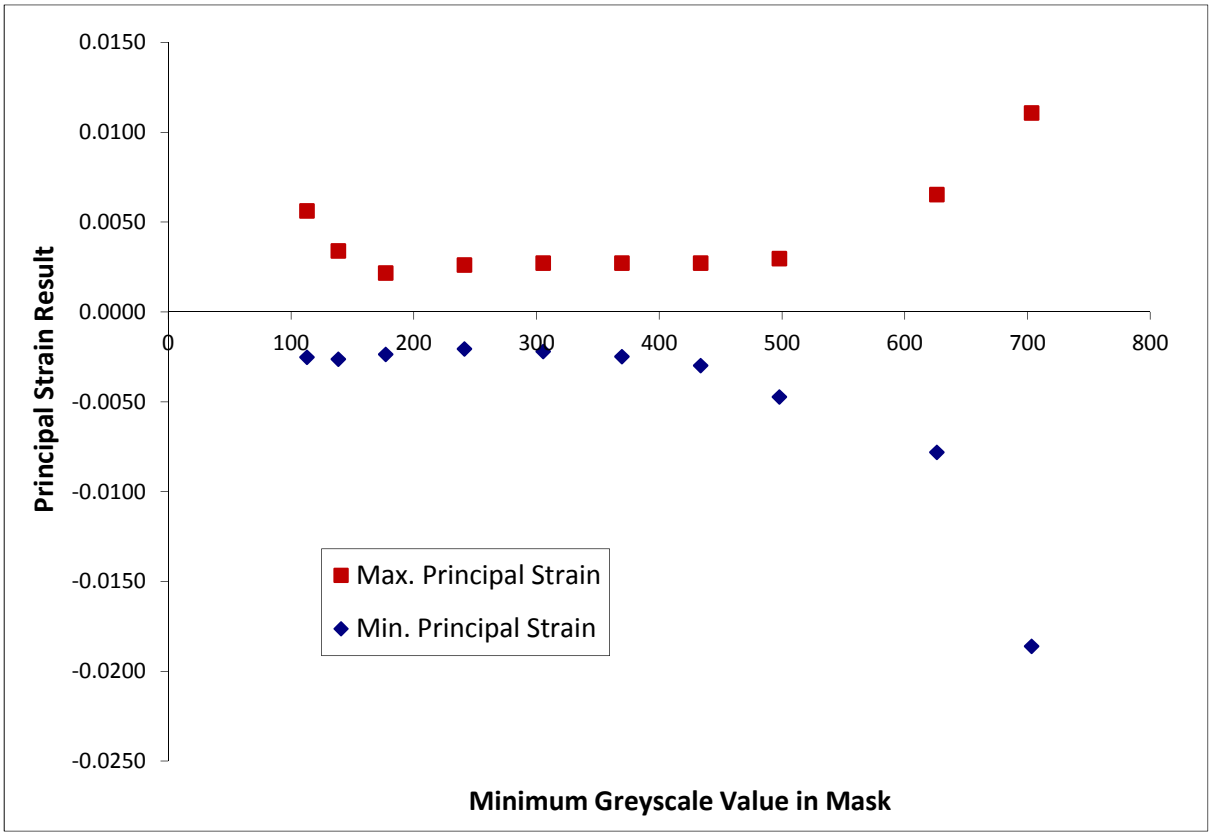

Figure 7.11. The effect of thresholding on the maximum and minimum principal strains recorded in a single sample subjected to a 40 Nm torsional load.

Where the overall result differs from that of a 'converged' solution plot is in the manner in which the result proceeds following the attainment of a minimum value. As all of the softer tissues are omitted from the model, the minimum assigned Young's modulus within the mask continues to rise. The continually reducing volume (as shown graphically in Figure 7.10) reaches a point at which the integrity of the modelled structure starts to be compromised. This continual thinning of the structure ultimately leads to a critical lack of rigidity. At which point (and despite the increasing average assigned Young's modulus), the application of the same force used in previous iterations results in higher observed strains within the system. As the results display increasing strain levels, a 'U' shape is observed in the results plot for principal strains with changing threshold values.

7.3.3 Discussion

The observation of a 'U' shaped result is significant when selecting the values from which to accurately model the behaviour of bone, and particularly in the modelling of an isolated cortex, as was used in torsional simulation. Thresholding is generally undertaken to automatically segment the

appropriate geometry of a sample. The result shown here demonstrates that the level of thresholding cannot be approached arbitrarily, as the range will directly affect the maximum values for strain within the model, which could have significant effect on the observed accuracy when undertaking strain correlation or fracture prediction. The result also shows that values suggested in literature are not appropriate as bounds for the thresholding of Finite Element models of isolated cortical bone. Values taken from literature for cortical bone demonstrated maximum strain values that were approximately 302% of those at the previously 'converged' minimum assigned Young's modulus of 1500 MPa.

Geometrical accuracy must be retained to ensure accurate simulation and appropriate replication of a given system. Consequently a proportion of less dense bone material will always be included in whole-bone models. Correspondingly, such models may fall within the early portion of Figure 7.12, at which point the results may not have fully 'converged' to the static section shown in the middle section. As such, small changes either side of the thresholding value used to define these models may have an effect on the predicted results in the simulation.

Ultimately, the geometry of a sample must be given precedence in the thresholding process. Within the cortex, less dense materials are generally noted at the edges of the defined geometry due to partial volume effects in CT scanning. Care should be taken to ensure if this geometry is required. If it is not required it should be omitted, as higher levels of strain will be noted in these regions, and these may have an unwanted effect on assessment of strain correlation, fracture prediction etc.

The thresholding tests as a whole demonstrate that in tests requiring the prediction of maximum strain, the *location* of the result must also be noted to observe the local material characteristics. This will allow for a true determination of yield (in failure prediction) for the local material type, ensuring that the failure criterion is assigned to fully calcified bone sections or softer tissues, as appropriate.

7.4 Scanner 'Drift' and Associated Changes in Young's modulus

A calibration phantom was included during all of the CT scans within this thesis. The phantom provides a continuous reference material and allows the direct comparison of the densities observed from one scan session to another. The ScanIP software used for model production included a simple methodology to output the greyscale values within a calibration phantom. The standard methodology describes a line through a section of an image, from which the greyscale values are plotted (Figure 7.12(a&b)). The software demonstrated the greyscale values only, on a very simple basis, with no further detail and, importantly, no means to export these numbers for further analysis. It was considered that the methodology provided within the software was therefore not sufficiently accurate to determine the scanner drift. In particular, the output offered by the software was not refined enough to observe the small changes in greyscale value noted within the phantom images between

consecutive scans. The inability to accurately portray these differences negated the inclusion of the calibration phantom and consequently this process required investigation and improvement.

7.4.1 Methodology

The material mapping relationships used in this study rely upon the accuracy of the greyscale values within the CT data, and thus a method was created to ensure that the data observed in the CT scans remained consistent. In order to do this, the calibration phantoms included in each of the CT scans were used to create additional, independent Finite Element models created from the voxels within the scanned phantom material.

A 5 mm diameter cylindrical mask was produced from the entire length of the central section of each of the phantom chambers. This improved the data available from the ScanIP software (Figure 7.12(c)), now demonstrating the occurrence rate of each greyscale within the mask (with respect to number of pixels) for a single chamber (chamber D); however, the data remained limited, and was not exportable.

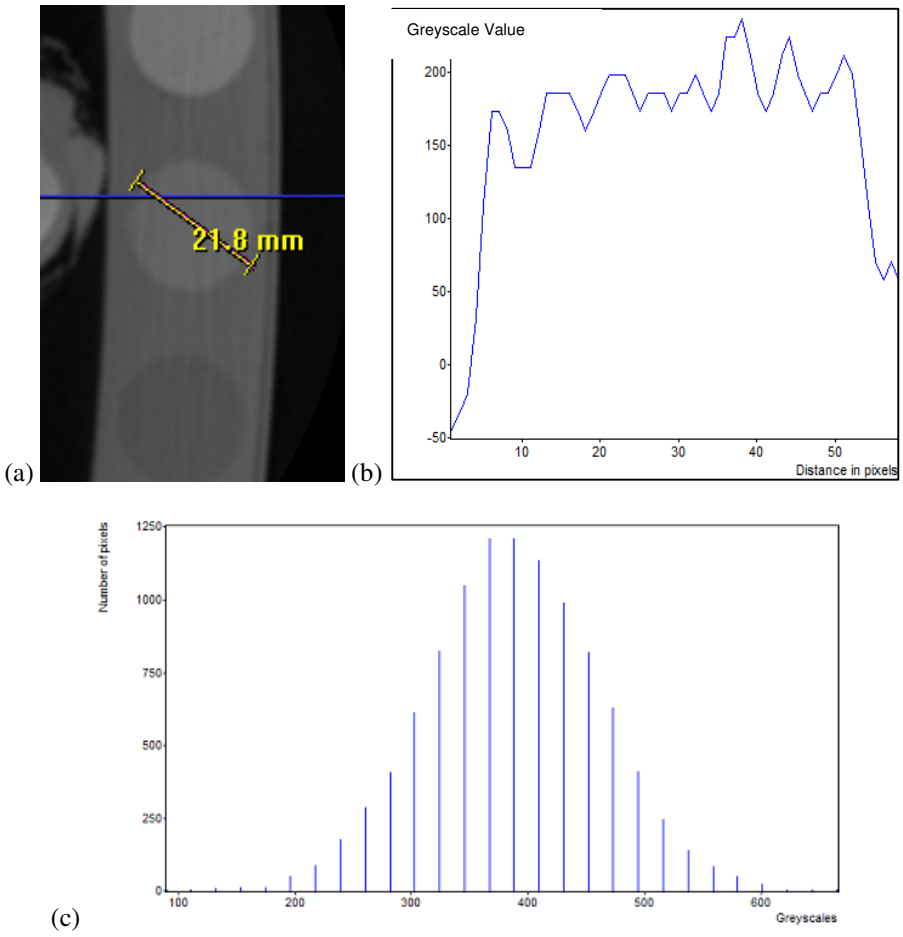

Figure 7.12. (a-c) Screen captures from ScanIp software (a&b) show the standard 2D methodology for assessing the occurrence of greyscale values along a single image slice. The final image shows the improved detail available when masking the volume of the phantom

Each of the 5mm cylindrical masks were then exported following the general testing methodology used for bone simulation and assigned Young's modulus on the basis of the density-elasticity relationship provided by Morgan et al. [72]. This greyscale-density relationship was initially based upon the average greyscale value observed in the ScanIP greyscale histogram (Figure 7.12(b)).

The masked cylinders were then imported into the Finite Element solver, which was used to list the occurrence and attributes of the material markers assigned within the elements of the phantom mesh. The distribution of Young's modulus used to calculate the average material property for the masked section of the phantom was then plotted. Combining the average property with Morgan et al.'s relationship, the corresponding average apparent BMD could be calculated for the phantom. From this apparent BMD, the average greyscale value could then be produced by reverse methods.

This methodology provided an increase in the amount of data available from the phantom, and gave a significantly more accurate assessment of the average greyscale value through the use of a three-dimensional volume-weighted average of the exported mesh as shown for chamber D of two scans in Figure 7.13.

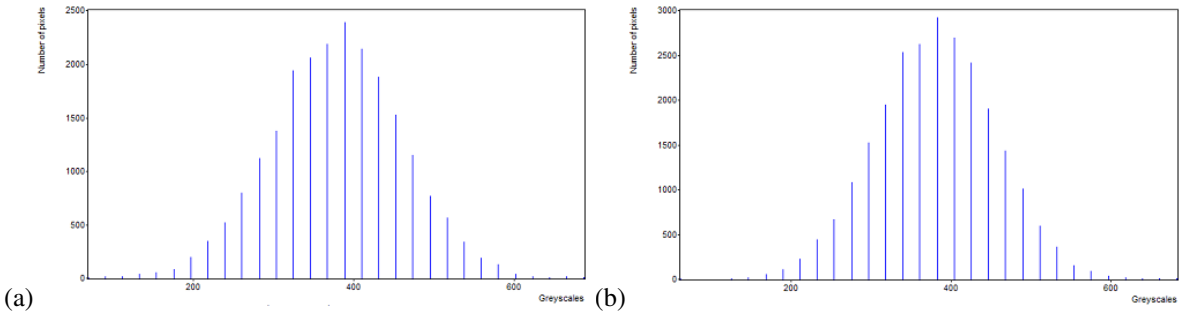

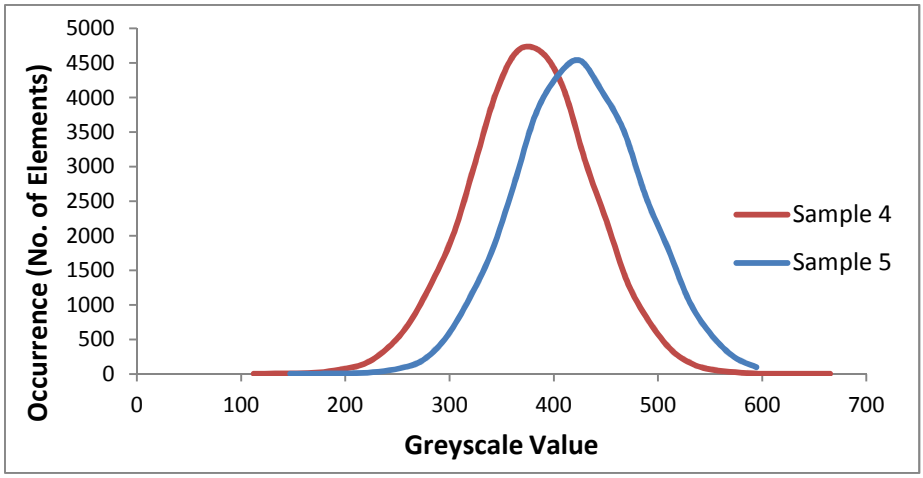

Figure 7.13. (a-c) Screen captures from ScanIp software (a&b) show the improved (but still insufficient) methodology when masking the phantoms, as can be seen the two occurrences appear near identical. Replotting the occurrences following exportation shows how the true occurrence rate differs.

7.4.2 Results

Figure 7.13. shows the results of the revised methodology. The ScanIP data provided for two phantom scans (from samples 4 and 5) are plotted. As can be seen the number of pixels selected in each mask varies, but it is not possible to quantify the all-important difference in average greyscale attenuation of the two masks. Exporting the mask data of these two phantoms to determine the distribution on a more accurate basis produces the plots shown in Figure 7.13(c). The comparative plot shows how the distribution of greyscales within the two masks differs significantly. This comparative graph demonstrates the effectiveness of the revised methodology, with a final area weighted value of 377.26 for sample 4 and 424.31 for sample 5, as opposed to the previously assumed value of *approximately* 390 for *both* phantoms, taken from the initial ScanIP plots. It is consequently imperative that a calibration phantom is included within the CT scanning protocol, and also that the phantom calibration is undertaken correctly to accurately map the Young's modulus to a final exported model.
Each of the phantoms scanned within the simulation of this thesis was assessed using this improved calibration methodology, prior to the creation of the Finite Element models. Figure 7.14 shows the variation in average greyscale value of 11 phantom scans. Importantly, each of these phantoms appeared near identical when compared using the standard ScanIP methodology. In addition to the average greyscale value, the material property attributed to the greyscale value is also shown. This shows the variation in property that would be exported, for 11 materials that should be exported with identical values. Chamber 'B' was selected for comparison of each of the phantoms; it should be noted that the calculated material property was determined using Morgan et al.'s relationship [72], other relationships would provide a different absolute material value for a given greyscale output.

7.4.3 Discussion

Figure 7.14 shows the variation in Young's modulus that would be observed when using the standard software to undertake phantom calibration. In actuality, following the methodology in this chapter, this potential material change was accounted for in Finite Element simulation, ensuring consistency between exported models and removing the effect of scanner drift from the independent scans.

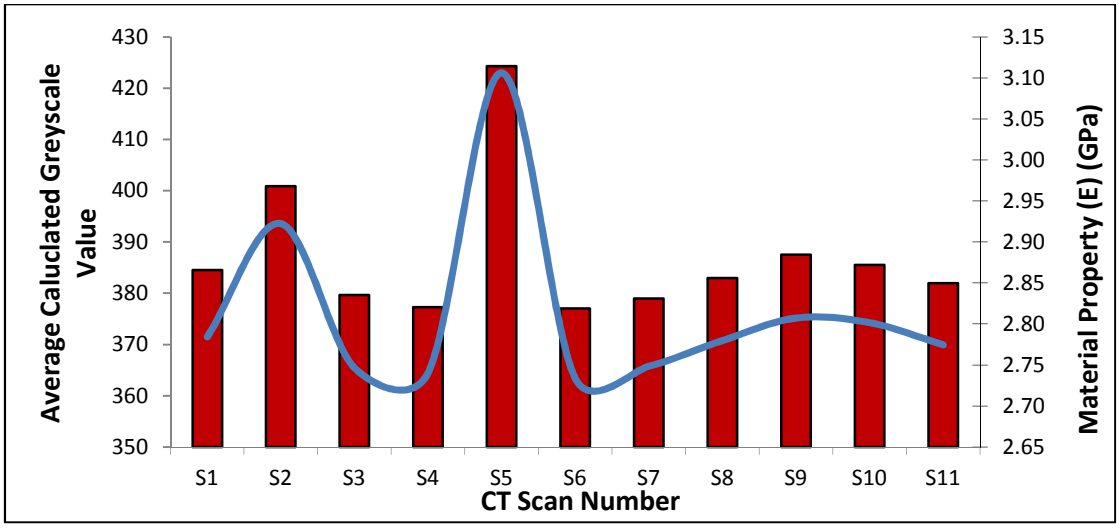

Figure 7.14. Average greyscale value for phantom chamber B for 11 CT scans (bar chart) calculated using the revised methodology. The exported material property in GPa is detailed (line graph).

The inaccurate representation of the greyscale values within the calibration phantom shown in the plot demonstrates a variation of approximately 0.4 GPa. This is significant, but only relevant for values around GS = 400. This can be extrapolated to assess the possible material error that would have been included within an entire exported bone model. At the extents of the minima and maxima for scanner drift as shown in the graph, the range of maximum exported value for elastic modulus at the maximum apparent BMD in a source image is as high as 3.34 GPa. This is a significant percentage of the maximum exported value (13.6% of 25.54 GPa) representing a potential source of error which is currently unaccounted for within the software package.

The increased accuracy of this methodology provides a technique that can genuinely accommodate and quantify scanner drift between independent scans. Importantly, the comparison technique increases the accuracy of the greyscale-density and thus density-elasticity calculations used to provide the critical material distribution in each of the individual models used in simulation. Discussion with Simpleware suggested that the calibration methodology was not regularly considered by researchers, and that a large proportion of the work that they saw had the geometrical data scanned without the inclusion of a calibration phantom. The omission of a calibration phantom has the potential to instigate significant variance between scans, and thus this should be considered a major limitation in studies that choose to exclude this reference.

The information was fed back to the software developers following the derivation of the improved technique shown here. It is expected that the greyscale calculation procedure will be amended by the developers to include the processes shown here, and Simpleware expect to include a revised procedure in their forthcoming software update.

7.5 Chapter Discussion

Changes to the inputs in simulation have been discussed in this chapter, and demonstrate how the alignment, thresholding, material mapping protocol and the accuracy of the scanning and calibration procedure have a significant and important contribution to the ultimate output and accuracy of simulation, as follows:

Alignment:

- The importance of accurate alignment was highlighted through the observation of significant changes in the results for small modifications in the alignment of each sample and changes to the applied load.
- Mapping of the reference positions *during* testing should be considered for future testing to increase overall accuracy. This would accurately determine the 'as tested' alignment, of the sample

Thresholding:

- Testing highlighted the manner in which thresholding affects the stiffness response, and therefore the results in simulation. This demonstrates the importance of correctly defining the greyscale boundaries to accurately segment the structure for simulation.

Phantom Calibration:

- Testing has highlighted inaccuracies in the standard software protocol for determining greyscale values. A methodology to overcome this inaccuracy has been devised, and demonstrated to function with significantly increased accuracy.
- Undertaking phantom calibration and determining material parameters correctly has been shown to be key in the production of accurate simulation results.
- The findings have been shared with the software developers, and a similar greyscale assessment technique is expected to be included in forthcoming software updates.

Material Mapping:

- Testing of a differing material mapping relationships confirmed that the relationship proposed by Morgan et al. is the most accurate for porcine simulation. This confirms the findings for human simulation in literature.
- The testing confirmed that relationships derived for human samples are not only appropriate for animal samples, but also may provide accurate results, directly

contradicting the statement made by Rice et al. in which it was claimed interspecial relationships could not be created.

- The material mapping study in this chapter was limited to a comparison of the accuracy obtainable in simulation when using existing mapping relationships provided in CT-FE literature. Consequently a new material mapping relationship for animal bone should be considered to see if accuracy can be improved further. Typically such relationships are determined by small scale rather than whole bone material testing.

8 Refinement and Application of the Simulation Procedure

In order to meet the ultimate objective of CT-FE, and thus utilise patient-specific simulation to aid in clinical diagnosis on a case by case basis, the process must be sufficiently and robustly validated. In Chapter 6, the simulated (predicted) results of this thesis were compared with those observed (measured) within the laboratory. This validation was undertaken successfully, demonstrating comparable accuracy to the simulation and techniques demonstrated in literature. In this optimisation and application chapter, further simulation to incorporate the modelling recommendations from Chapter 7.

Whilst extensive validation is a fundamental requirement of Finite Element simulation, care should be taken to ensure that modelling protocols are capable of performing in a *predictive* rather than purely *reactive* manner. It was considered prudent that the simulation process determined in this thesis should be applied to generate and predict results rather than to purely correlate simulation with test results measured within the laboratory. Therefore, following the optimisation process, the application of the validated simulation procedure was considered in the following ways:

- Derivation of a new density-elasticity relationship to use for porcine material mapping:
    - The model was interrogated to determine if the material mapping protocols proposed for human samples were the most accurate for animal substitution.
    - Further simulation was undertaken to see if the whole-bone modelling resolution was sufficient to allow for the production of a new material relationship for porcine bone.

Creation of a new relationship for porcine material mapping could potentially increase the simulation accuracy when modelling porcine bone. The process would also demonstrate the refinement and accuracy of the simulation procedure as a whole.

- Prediction of the fracture and/or yield load of porcine femur samples:
    - Simulation of fracture tests was undertaken to determine if the modelling procedure was capable of predicting the ultimate failure load or the load required to induce plastic yield in both torsional and compressive failure modes.

The prediction of the fracture load of a sample using just the initial CT and alignment data would demonstrate that the process was capable of providing meaningful output, could be used for fracture prediction in the future, and thus was appropriate for extension into further applications.

8.1 Refining the Simulation Procedure

The error investigation in Chapter 7 concluded with four key parameter changes that had an effect on the manner in which a sample was modeled and hence altered the accuracy of the results. In this chapter, the two parameters that could be *logically* manipulated (improved phantom calibration and re-thresholding using finer control) were considered, in order to optimise the simulation process and refine the accuracy to as great a degree as possible. Following this, the *predicted vs. observed* results for the entire testing process (all sub-maximal torsional and compressive tests combined) were re-plotted, demonstrating the effect of optimising the input changes on the accuracy of the simulation procedure as a whole.

To adopt the changes, the simulation was effectively restarted. The original, unaltered CT dataset used to create the original porcine geometry was freshly imported into the ScanIP software, using the revised phantom calibration procedure that had been proposed in Chapter 7. Following this, the thresholding and geometry masking process was undertaken, ensuring the correct external dimensions were retained whilst the mapped material results were as close to the 'converged' section of Figure 7.11 as possible. The changes made to the thresholding ranges used in Chapter 6 varied depending on the observed CT attenuation, the apparent density and the geometry of each sample. The largest change of the greyscale value used for masking in the thresholding process was in the order of 20% of the new minimum greyscale value (minimum GS = 177 amended to GS = 221 whilst retaining the required geometry).

8.1.1 Results

Plotting the 'original' (from Chapter 6) and 'amended' (following optimisation) data sets together (Figure 8.1) gives a comparison of the position of each of the individual data points from simulation, and a graphical depiction of the improvement as a whole. As can be seen, the gradient, intercept and R^2 values following the amendment process are significantly closer to the ideal result than was initially observed in Chapter 6. The revised thresholding process results in a slight increase in the average mapped material property within the simulated models. As a result, higher absolute values for principal stress were predicted. Correspondingly, the material parameter observed at the location of the strain gauge is also increased, and as this is used for strain transformation and stress calculation, the measured stress result from the laboratory testing is also increased over those results used for correlation in Chapter 6.

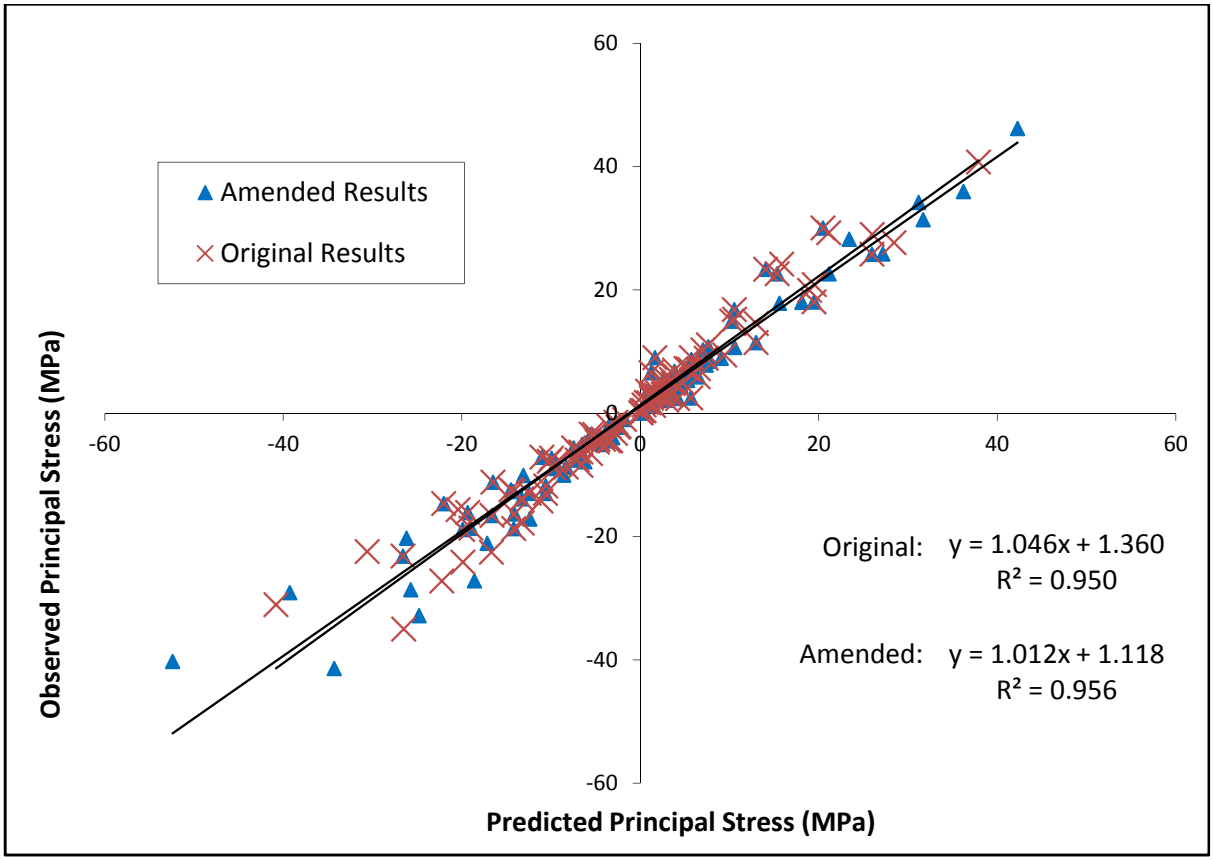

Figure 8.1. Comparison of the *predicted vs. observed* results of the original modeling procedure with the amended modelling procedure following the adoption of the thresholding and phantom calibration changes.

Error was recalculated for the amended procedure using the original protocol. The results of the error calculation are shown in table 8.1, showing the maximum absolute and percentage errors, in addition to the RMSE of both the amended and original simulation protocol.

Table. 8.1. Comparing the error results of both the original and amended simulation procedures for the entire testing process (torsion and compression at all loads).

	'Original' Results	Amended Results
Agreement (R^2 Value)	0.950	0.956
RMSE (MPa)	3.40	3.43
RMSE (%)	8.4%	7.4%
Max. error (MPa)	9.77	12.18
Max. error (% of observed result)	129%	127%

8.1.2 Discussion

A reduction in simulation error was observed following the adoption of the improvements suggested in Chapter 7. The error improvement is small, as would be expected with a refinement process rather than a fundamental alteration to the modelling procedure. The increase in average material property and thus the structure stiffness as a result of re-thresholding and correctly defining the phantom calibration process leads to an increase in the maximum observed values for principal stress from both the laboratory and simulation. Consequently the error and RMSE in absolute terms are slightly higher in the amended model. Reviewing this error on the basis of the percentage of the physically recorded values demonstrates that the overall error is actually reduced.

Despite returning only small improvements in accuracy, the refinement and optimisation of the modelling procedure is an important step in the *application* of the simulation. The refinement and optimisation process was adopted prior to the simulation undertaken in sections 8.2 and 8.3. This ensured that the simulation procedure was applied with the highest level of accuracy that was rationally achievable.

8.2 Defining a New Mapping Relationship for Porcine Bone

During the input parameter and sensitivity assessment of Chapter 7, the effect of changing the density-elasticity (E-BMD) relationship for material mapping on the simulation accuracy was measured. The most accurate mapping relationship was that proposed by Morgan et al. [72]. This confirmed the result proposed by studies that assessed the most appropriate material relationship for human samples, and demonstrated that Morgan et al.'s relationship was capable of interspecial mapping [46, 70]. Despite this confirmation, the relationship proposed by Morgan et al. was originally determined through the physical testing of human and not porcine samples. The relationship had been selected on the basis of examining existing relationships from literature and thus could be potentially be considered as the *best match* rather than the *optimum* relationship for porcine bone.

Further simulation was undertaken in this section to determine if a new density-elasticity relationship could be derived from the whole-bone simulation and physical testing results (from strain gauged testing). This new relationship could then be used to more accurately describe the behaviour of the porcine samples in simulation, and thus further increase the overall accuracy observed in the porcine validation process.

8.2.1 Methodology

The general format of most density-elasticity relationships is shown in Eq. 8.1. A number of other formats have been demonstrated, including linear relationships such as that proposed by Lotz et al. [22]; however, most follow the format shown below. The relationships are comprised of two main

parts, with the BMD figure operated by multiplying factor (a) and a power number(b). As mentioned in previous chapters, the correct selection of BMD is also important (as denoted by the star in the equation). Morgan et al. uses *apparent* BMD (ρ_{app}).

$$E = a \times \rho_*^b \qquad 8.1$$

The relationship proposed by Morgan et al. ($a = 6.85,\ b = 1.49$) has the second lowest power number of all relationships compared in Helgason et al.'s review paper, second only to the non-linear relationship proposed by Lotz et al. [19, 211]. As this relationship demonstrated the highest accuracy in Chapter 7, it was deemed as the most appropriate starting point prediction of a new material relationship.

Using Morgan et al.'s relationship as a starting point, simulation iterations were undertaken in which the values for (a) and (b) were manipulated. Initially, eight E-BMD predicted relationships (E-BMD P.R., Figure 8.2) were simulated to test the effect of the changing parameters within the material relationship. From this, stress correlation was undertaken using the methodology detailed in chapter 6, and the results in terms of gradient, intercept and R^2 value of each relationship were determined to examine where the ideal relationship lay and to compare the new accuracy with that found using Morgan et al.'s relationship. Linear interpolation was then used to produce the *ideal* relationship.

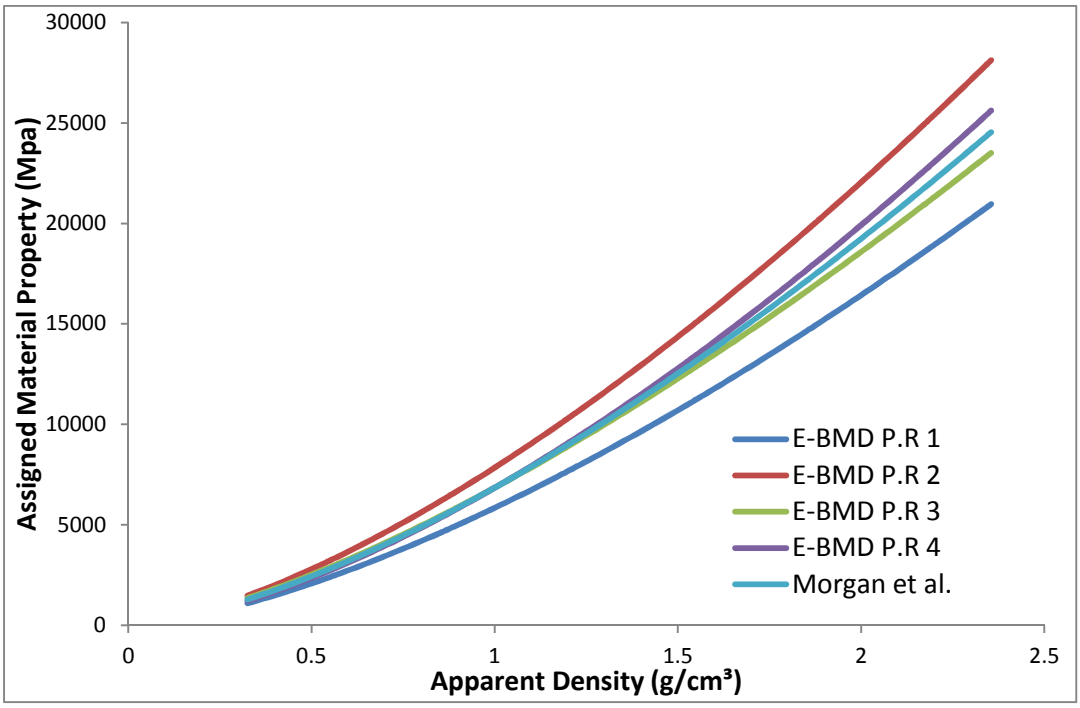

Figure 8.2. The changing assigned material property with respect to apparent BMD for each of the four initial E-BMD predicted relationships.

The material property output with respect to changing BMD for four of the initial E-BMD predicted relationships is shown in Figure 8.2. The remaining iterations are detailed in Appendix A1.22. A single femur sample was selected for simulation to isolate any changes in the geometry or apparent density. The additional parameters used in testing such as the phantom calibration, the alignment of the sample and the threshold level used for geometry masking were maintained throughout testing.
It should be noted that optimisation amendments (as detailed in 8.1) were made prior to testing. As such, an improvement in the results obtained for the single sample when using Morgan et al's realtionship is noted over those values detailed in Chapter 7 (Original: Gradient = 1.0431, Intercept = 0.726, R^2 = 0.940, Amended: Gradient = 0.998, Intercept = 0.311, R^2 = 0.965).

8.2.2 Results

The initial simulation iterations demonstrated that changes to the multiplying factor (a) had an immediate effect on the observed results, with both positive and negative amendments to (a) reducing the agreement of the data points to the linear result, indicated by a reducing R^2 value. Conversely, amendments to the power factor (b) demonstrated slight improvements in the observed accuracy, notably amending the gradient and intercept of the line described by the results data points. The full list of iterations and the gradient, intercept and statistical error are detailed in Appendix A1.23, as is a typical comparison plot produced during comparison of the revised relationship with Morgan et al.'s original (Appendix A1.24). The final relationship was determined using linear interpolation between the two iterations that fell either side of the ideal simulation result ($x = y$, intercept = 0,0, error minimised). The comparison plot of the final proposed relationship is shown below in Figure 8.3; statistical results and relationship information are detailed in table 8.2.
The proposed equation provides material values that are slightly increased over those in the original relationship. As a result, higher absolute stress readings are noted (in a similar manner to the re-thresholding process shown in 8.1). The maximum absolute error decreases (14.91 vs. 15.22 MPa), and a decrease of 0.075 MPa is noted at the intercept error. The percentage error with respect to the maximum-recorded value also reduces slightly (29.64% vs. 30.29%). Absolute root mean square error remains similar between the two relationships on a percentage basis reducing from 10.75 % to 10.71%.

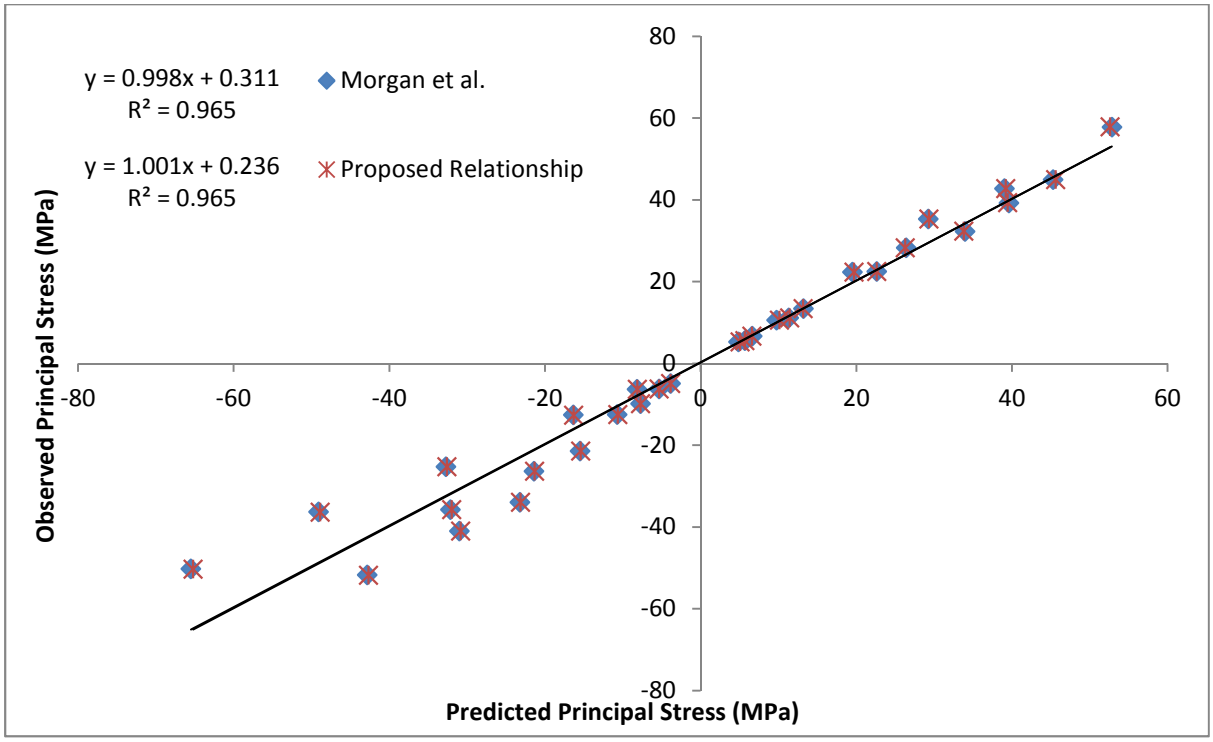

Figure 8.3. Comparison of the predicted and observed stress results for the proposed relationship and the original relationship provided by Morgan et al.

Table 8.2 Statistical and equation information of both the original (Morgan et al.) and proposed E-BMD material relationships tested in simulation.

	a	b	Gradient	Intercept	R^2	RMSE %	Max Error %
Proposed Relationship	6.85	1.4921	1.001	0.236	0.965	10.71	29.64
Morgan et al.	6.85	1.4900	0.998	0.311	0.965	10.75	30.29

8.2.3 Discussion

Studies in the literature have suggested that porcine and human density-elasticity relationships cannot be used interchangeably, despite the regular substitution of porcine bone for physical sample testing [145-148, 196]. Studies have also demonstrated significant variations in material values when physically testing samples for human and porcine samples from the same anatomical test site [147, 181]. For completeness, and to definitively corroborate or contradict Rice et al.'s statement, simulation was undertaken to define an improved material relationship to map porcine bone. Iterative simulation was undertaken to amend the existing relationship that most closely matched the ideal result (proposed by Morgan et al.), and to consider the effects on the observed accuracy.

The initial accuracy of the original relationship provided by Morgan et al. was improved considerably due to the optimisation process undertaken in section 8.1. This meant that further changes to the material mapping relationship only had the scope for small improvements to the simulation accuracy.

Re-plotting the predicted vs. observed comparison for each iteration demonstrated that the occurrence and position of the data points was consistent between each new proposed relationship and the original. Consequently the statistical error remains relatively constant, rising in absolute terms and falling in percentage terms in response to the absolute material values defined by the mapping relationship. This demonstrates that fundamentally the manipulation of the material relationship does not completely eradicate the error between predicted and observed results. It is considered that this error was retained within the plots as it is a fundamental response to the physical testing and validation process. The error is more likely to be related to alternative factors, such as the alignment of the sample and gauges, the accurate determination of load and strain values, and the replication of the boundary conditions in simulation.

In order to define a new material relationship from the final outputted data of whole-bone testing and simulation, it must be assumed that the errors included within the physical and *in silico* testing processes are close to negligible (or alternatively quantifiable). Testing a single sample with identical boundary conditions and meshing parameters helped to maintain consistency between individual iterations in simulation. However, the level of refinement required to improve the material relationship is very fine. It is considered that the refinement required is smaller than the potential error noted within the testing process as a whole. As such the improvements noted in the accuracy of the simulations may be accommodating for error within the testing and simulation processes, as opposed to actually improving upon the existing material mapping relationship.

Further testing using small scale material samples may ultimately provide improvement for the mapping of porcine Young's modulus; however it is considered that the resolution of the results in whole bone modelling is not sufficient to determine an improved material relationship.

Fundamentally the accuracy obtained during the validation and optimisation of the simulation procedure as whole using Morgan et al.'s relationship was high to the extent of being difficult to improve upon. It can therefore be considered that this human relationship is not only suitable for extension porcine simulation, but also capable of providing highly accurate simulation results.

8.3 Predicting Fracture Load

Chapters 6 and 7 detailed the ability of the simulation procedure to model the sub-maximal response to loading of the porcine femoral samples in both torsional and compressive loading. High levels of accuracy were achieved in this process; however the results of these studies are limited to correlating the stress and strain results at isolated locations across and beneath the surface of the bone samples. The ultimate application of biomechanical simulation of bone is in the prediction fracture risk.

Consequently the simulation procedure must be capable of predicting the external load required to induce fracture within a given sample for a prescribed loading situation. The determination of the risk of fracture, and the methodology used to assess the risk of fracture has been detailed in the literature [36, 45, 212, 213]; however, distinct limitations are noted in each of these assessment techniques.

As detailed in Chapter 2, the selection of failure criteria is a key step in determining the external load required to induce fracture.

A systematic review of the techniques proposed in the literature was undertaken to determine the most commonly proposed and most appropriate failure criteria in bone simulation. A variety of techniques have been implemented, including the use of both a limiting maximum stress value [213] and a limiting maximum strain value [22, 45, 51]. These techniques are generally implemented on an element by element basis, with a single limiting value, and the operator considering that failure has been reached when the individual element meets the prescribed limit. Whilst the implementation of stress based criteria has been shown to be applicable [213], papers that compare the accuracy of differing techniques generally demonstrate an improved accuracy in fracture prediction when using strain-based failure criterion [36, 45]. Throughout literature the use of linear elastic material models is prevalent, and the combination of this mapping technique with strain based failure has been demonstrated to be both rapid to implement [45] and accurate [22].Strain correlation, as detailed in Chapter 6, allows for area rather than volume averaging (as used in stress correlation), providing greater prediction of elemental behaviour at the bone surface, which is the region at which maximum strain is induced, and thus the region of interest for fracture studies.

Linear material models have been implemented throughout CT-FE simulation, and elastic fracture was noted for all samples in physical testing; however analysis of the physical testing results shows aspects of non-linearity and yield in the load/deflection response of some of the samples at high load. This is not uncommon, having been demonstrated previously in literature considering physical testing of bone samples [22]. In that study, simulation based upon linear material characteristics provided accurate correlation with both the onset of yield, and the total failure of the tested samples, despite poor strain gauge correlation and the use of only two samples for simulation and physical fracture testing.

Eleven porcine samples (samples re-numbered 1-11 for simplicity) were physically tested to fracture in torsion, with the fracture tests then recreated *in silico.* A strain rather than stress based failure criterion was used for failure correlation. This mitigated the partial volume effects, ensuring that the failure behaviour at the surface was captured correctly. The use of communally reared porcine samples offered an opportunity to test the patient-specific aspect of fracture prediction and simulation, as the samples have similar geometry and construction and have been reared under the same conditions.

Although strain based failure (as preferred in literature) was selected, the physical implementation of the failure criterion is open to further interpretation. Yosibash et al. considered and accurately

demonstrated failure on an area-averaged basis rather than at 'pointwise' (discrete) nodes or elements [36]. This approach theoretically minimises the effect of the stress and strain gradients created by the automated material mapping and meshing processes, ensuring that a single element returning higher than average results doesn't detrimentally effect the fracture prediction. The area that was selected for area-averaging changed from sample to sample as result of changing geometry and the location of maximum strain within the simulated sample, and thus this selection must be considered carefully. This technique is commonly used, although other techniques such as requiring conjoined elements to exceed the limiting value for stress or strain are also demonstrated in literature [212].

8.3.1 Methodology

The determination of fracture and yield load within the laboratory followed the protocol in the physical testing chapter. The samples were fully potted in the standard constraint sections (Figure 8.4). The sample was constrained at the distal end and rotated at the proximal end. The samples were removed from their saline cloths during testing, and this period was minimised to ensure no drying occurred. The orientation of the sample was noted to ensure that all samples were twisted in the same orientation. Continuously increasing load was applied to the femoral samples until failure was induced. Strain rate was 0.1 degrees per second, with fracture occurring in approximately 90 seconds and load/deflection data was continually sampled at 10.24 Hz. Strain gauging was not utilised during fracture testing.

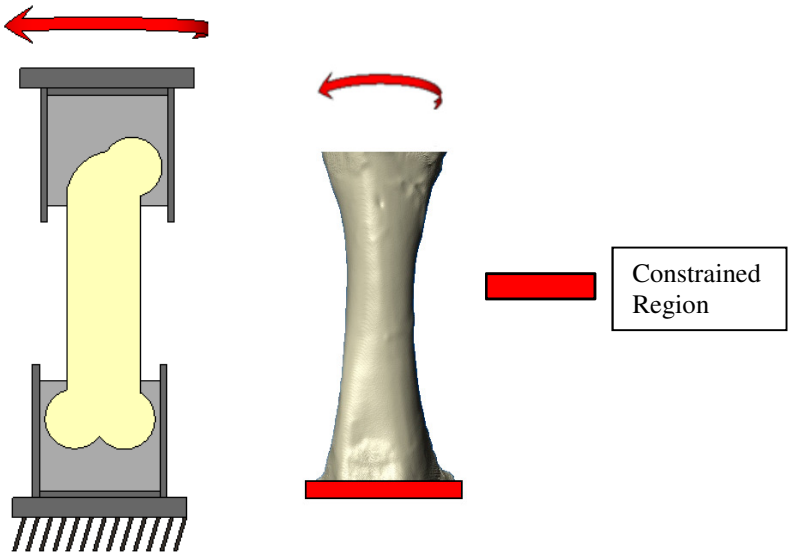

Figure 8.4. Sketch showing the physical testing and simulation arrangements. In both cases the distal extremity was constrained in all directions whilst the proximal was rotated from medial to lateral direction.

In simulation, the geometry and material mapping procedures for fracture prediction followed the general model creation procedure, with the material relationship provided by Morgan et al. [72]. The

input procedure included the revisions to the thresholding and phantom calibration procedure as detailed in section 8.1. The distal face of the cropped sample was constrained in all aspects, whilst force was induced upon the cropped proximal surface. The force applied to the simulation was initially matched to the total failure load of the sample. These were the loads detailed in Chapter 5, recorded at the point at which the samples displayed an instantaneous and total failure. As the simulation utilises linear modelling, it was also possible to quickly manipulate the inputted force, to consider the load value at the point of yield.

Failure in simulation was determined on a maximum principal strain basis, which has been proposed as the most accurate method in a review of failure assessment techniques [45]. Principal strain was assessed on the basis of a 'risk factor' for each element. This relates the predicted principal strain in simulation to the limiting values proposed in literature [88]. Bayrakter et al. proposed that the values selected for the strain limit vary depending upon the polarity and orientation of strain. The strain failure criterion under compressive loading was therefore higher than that observed under tensile failure (0.0104 and 0.0073 respectively). To accommodate for the disparity between compression and tension, the risk factor calculation used in simulation calculated the predicted to limiting ratio on a compressive and tensile basis concurrently. Failure of the sample was therefore predicted when either ratio exceeded one, a technique proposed in literature (although no finite calculation of failure load was performed in that paper) [45]. This methodology allowed for the calculation of risk factor on both an element-by-element basis, and an area-averaged basis, and consequently both were considered.

Principal strain was initially calculated for the entire model, with further consideration then applied to the region of interest of each model (the region of maximum principal strain). The location of this region of interest was referenced with the physical samples, allowing a comparison of the fracture location and point of failure initiation.

Visual examination of the samples during post-fracture scanning demonstrated no significant deviation from a linear result, with no visible plastic deformation. However, further inspection of the load/deflection curve exhibited the onset of yield in the majority of samples by way of an increased strain response under consistent loading, often significantly before the total fracture of the sample. The prediction and measurement of both *yield load* and *fracture load* have been considered in literature [22, 51, 91]. Yosibash et al. utilised failure selection based upon a 5% yield strain and considered that the display of increased strain above this figure indicated the onset of instability and failure of sample as a whole (Figure 8.5). This 5% yield strain methodology was therefore utilised to determine the onset of yield in the samples and used for correlation of the laboratory yield point with that predicted through simulation.

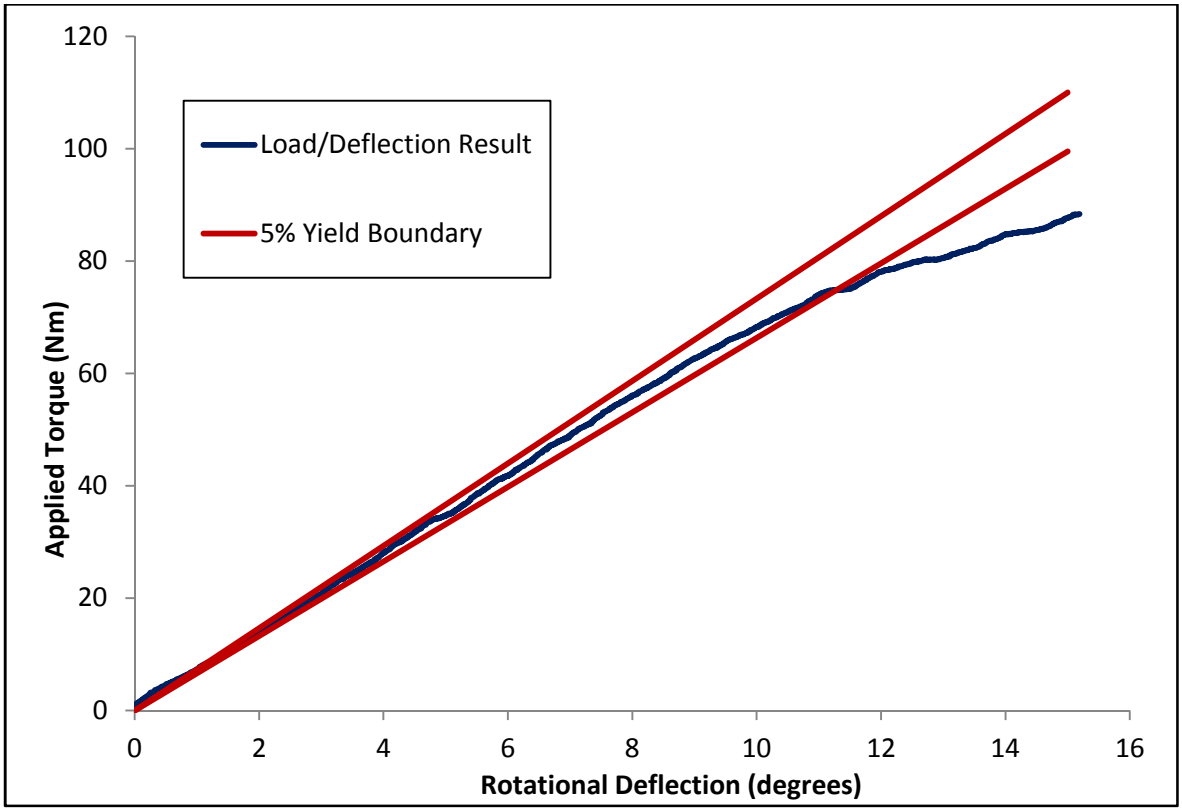

Figure 8.5. Plot demonstrating the torque/deflection curve for a single sample tested to fracture under torsion. The 5 % yield criterion is graphically demonstrated (red lines).

Results

8.3.2 Physical Results

The results of the physical fracture testing were detailed in Chapter 6. For this study, the results were re-assessed to determine the loss of linearity and the onset of yield in those samples exhibiting yielding. In tests that displayed yielding, the linear portion of the load/deflection response (which formed the majority of the data by proportion) was separated from the yielding section. Linear regression was undertaken, confirming the linearity of this initial region (R^2 was greater than 0.99 in all cases). A 5% yield strain was then calculated following the methodology proposed by Yosibash et al. [36, 51], which was overlaid upon the results. The point of yield was then determined as the point at which the load deflection curve crossed the 5% yield strain line (Figure 8.5). The calculated yield point was combined with the value for ultimate failure load from the force deflection curve, providing two reference failure loads for each physically tested sample (Figure 8.6). Simulation was then employed to attempt to correlate the predicted yield load and predicted total failure load with these two data points.

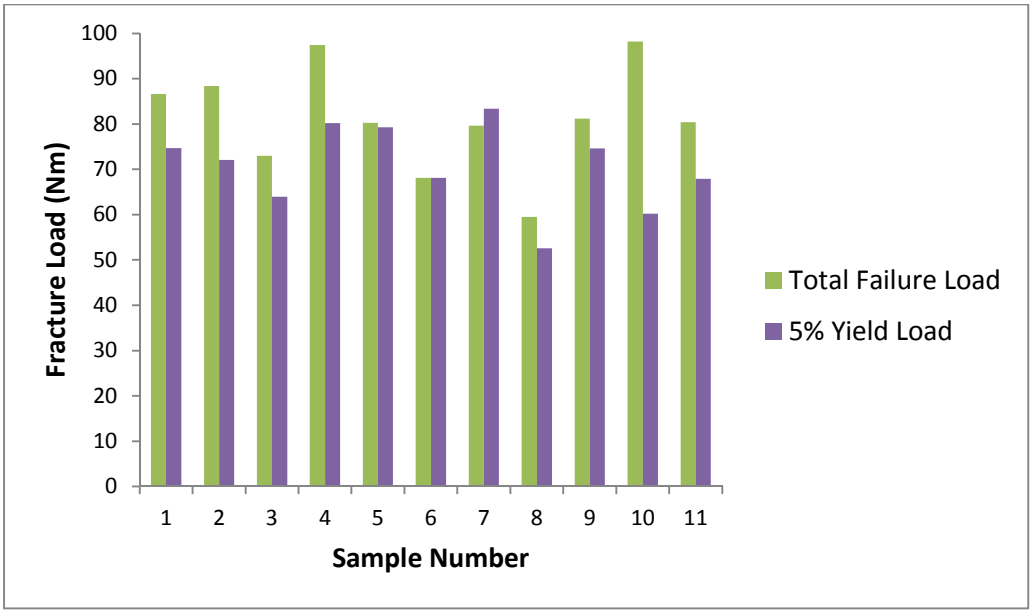

Figure 8.6. Plot demonstrating the measured total failure load and 5% yield load for each of the eleven samples tested in the laboratory.

As can be seen in Figure 8.6, 3 out of the 11 samples displayed continued linearity until the point of total failure, with the yield load matching, or close to matching, the total failure load. This examination of the load/deflection shows that the failure characteristics of each sample varies, consequently showing no correlation between the load at yield and the load at total failure (Pearson product-moment correlation coefficient, R = 0.432, statistical significance, P = 0.185).

The average total failure load was noted at 81.49 Nm whilst the average 5% yield load was 70.63 Nm. Despite single source selection, variations in the geometry were noted, and consequently variation in the total failure load was observed (values ranged from 59 to 98 Nm). The average assigned material property and the sample volume were extracted from the simulation data. These were combined to give an estimation of the arbitrary stiffness (assuming that the geometry is similar and the volume is thus directly linked with the sample diameter). Arbitrary stiffness and total failure load were shown to correlate (R = 0.796, P = 0.003). Isolating the material parameter estimated the reliance of the total failure load on the physical size of the sample. Total failure load was shown (Figure 8.7) to have a strong correlation with overall sample volume (R = 0.847, P = 0.001). The 5% yield load failed to demonstrate meaningful correlation with either sample volume (R = 0.043, P = 0.9) or with arbitrary stiffness (R = 0.227, P = 0.501). Plots for each of these are detailed in Appendix A1.25.

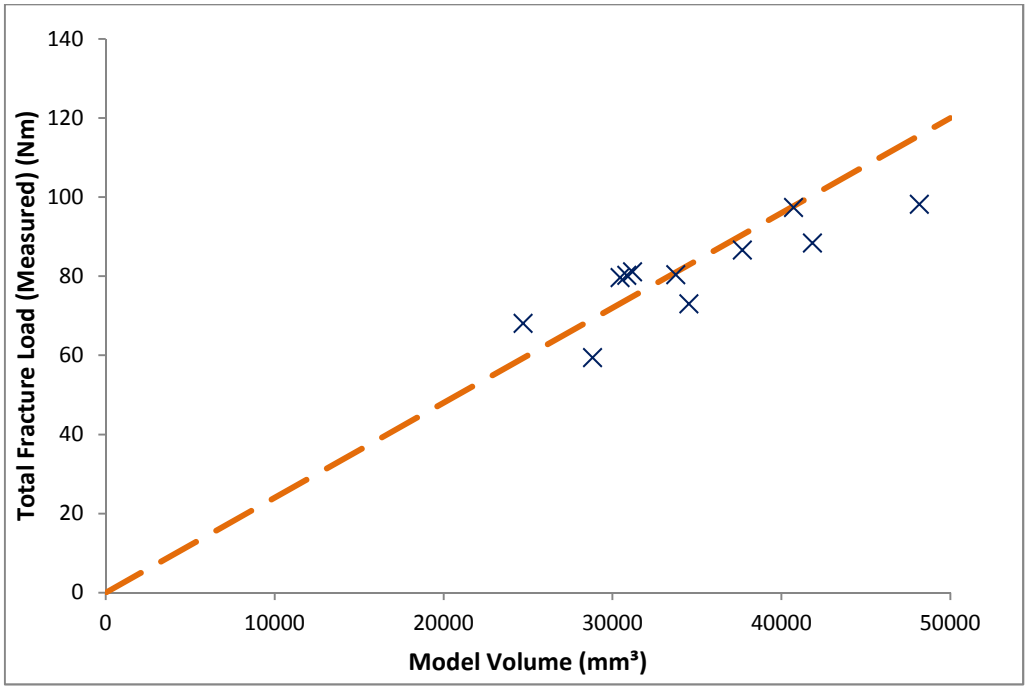

Figure 8.7. Correlation of the simulated volume of the eleven porcine samples with the total failure load of each of the samples, as measured within the laboratory.

8.3.2 Computational Results

Throughout testing, the simulation procedure demonstrated regions of maximum principal strain within an indentation in the posterior surface of the central cortex. Consequently, a region +/- 10 mm in the vertical plane from the boundaries of this indentation was extracted for each model. Within this region, the highest individual recording of strain was then noted. Statistical assessment of this region determined the proportion of elements within the region that were approaching (or had exceeded) the limiting strain value. The input load was then scaled to calculate the point at which a single element within the region of interest exceeded the risk factor in either tension or compression. This load was then proposed as the single element failure load. The 99.99 percentile load was calculated on a similar basis, at the point at which 0.01 % of elements had exceeded the limiting strain value.

8.3.3 Comparison of Simulation and Physical Testing

The ideal result in comparison would be that the predicted failure load from simulation matched the load measured during physical testing. Figure 8.8 shows the measured total failure load and the measured yield load (at which the 5% yield criteria is exceeded) and compares these measured failure loads to the predicted failure loads from simulation.

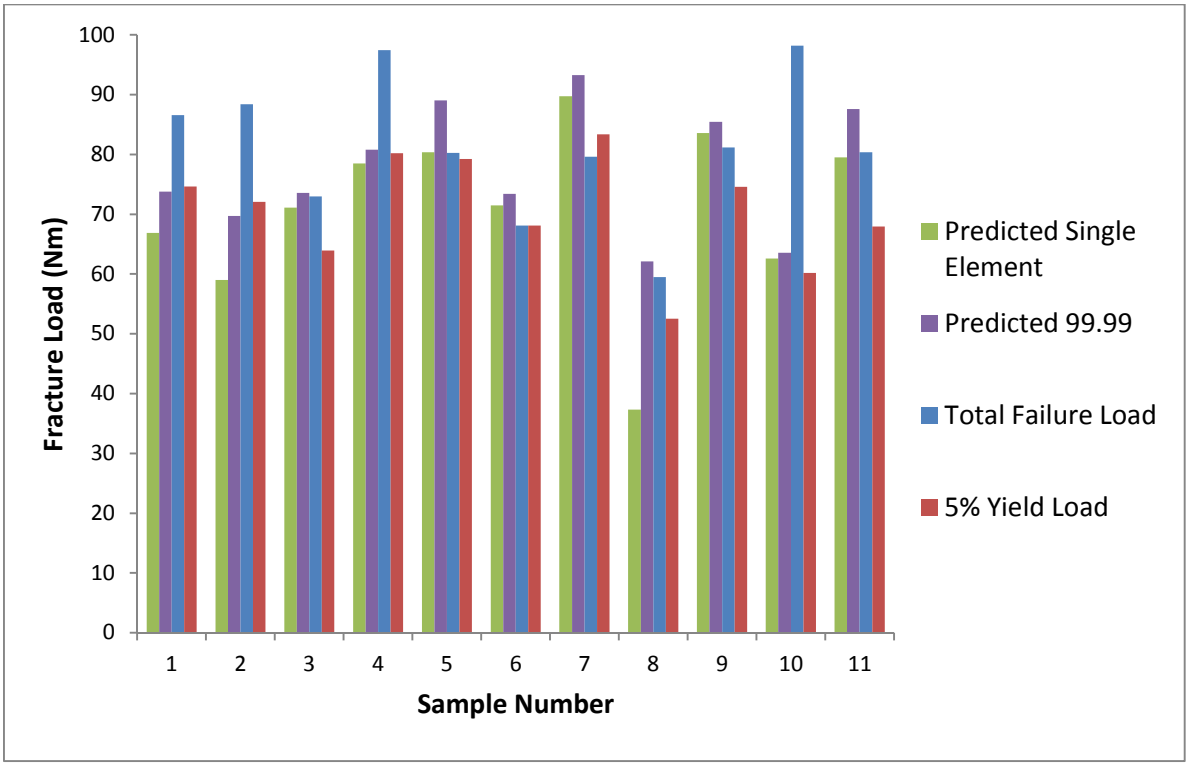

Figure 8.8. The total failure load and 5% yield load measured in the laboratory for each of the eleven samples and comparing these with the predicted failure load on a single element and 99.99 percentile basis.

As can be seen in Figure 8.8, the level of agreement is generally low between predicted and measured results for total failure load. By contrast, the correlation of predicted failure with 5% yield load is significantly improved. The best correlation is found between the single element result and the 5% yield load ($r = 0.806$, $P = 0.03$). This is re-plotted in Figure 8.9. The correlation between 99.99 % load and the 5% yield load is also strong ($r = 0.795$, $P = 0.03$) (plotted in Figure 8.8)

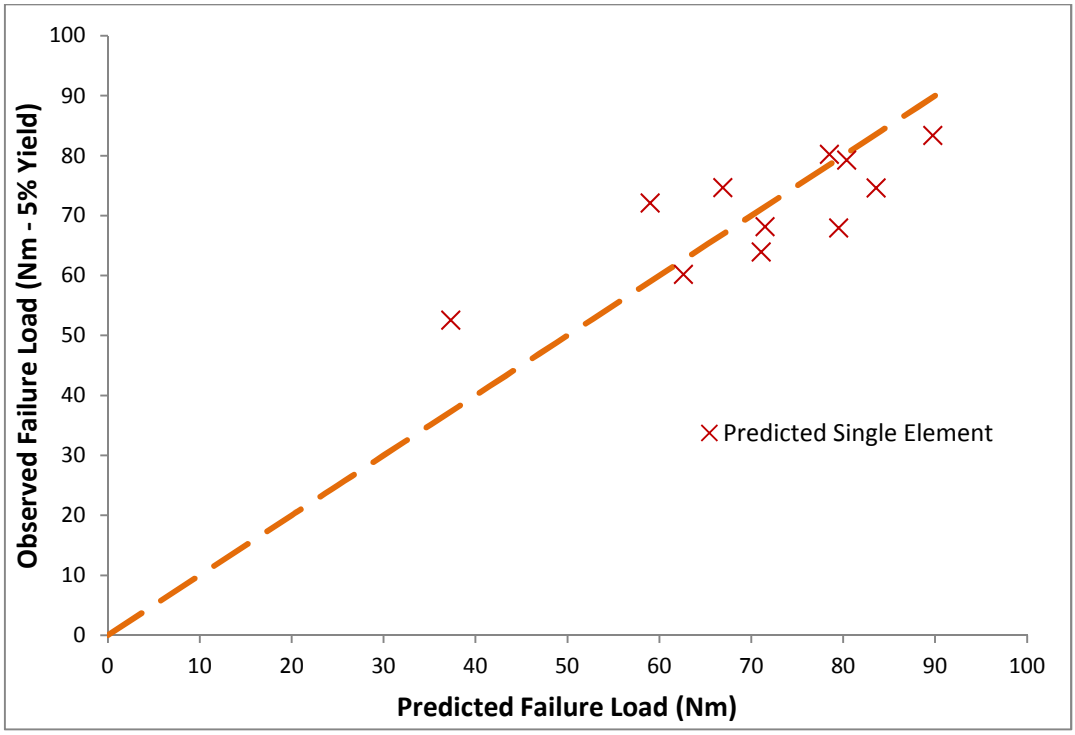

Figure 8.9. Plot demonstrating a comparison of the predicted failure load (single element) and observed failure load (5% yield). The ideal result line is included (orange dashed line).

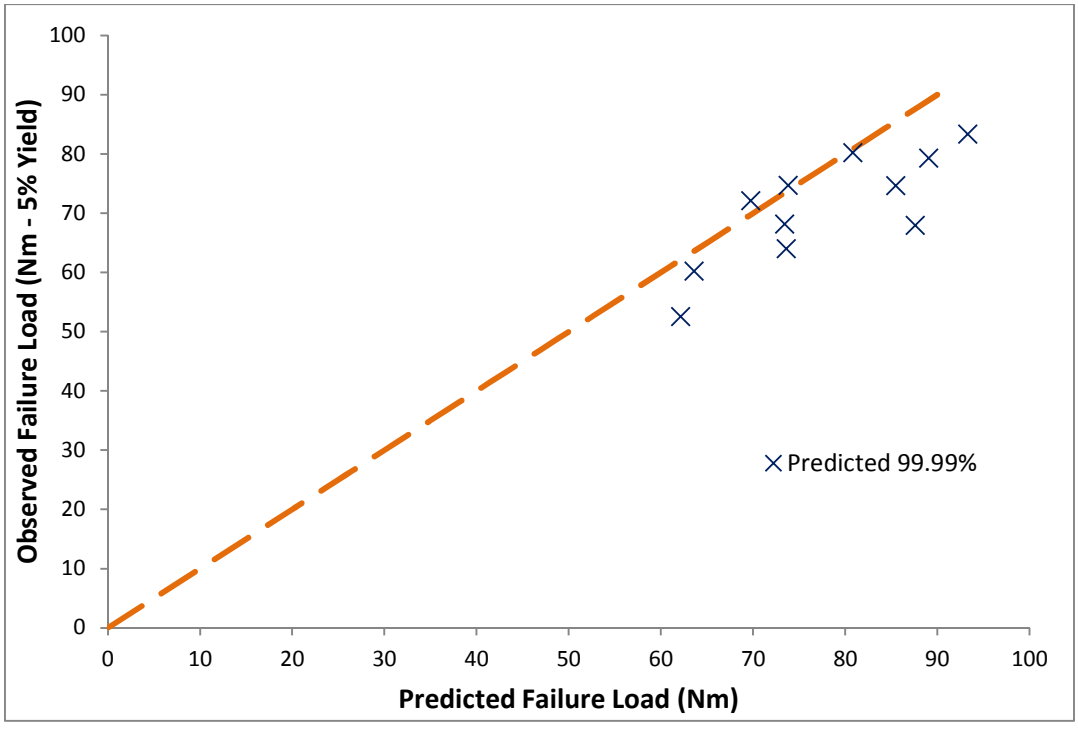

Figure 8.10. Plot demonstrating a comparison of the predicted failure load (99.99%) and observed failure load (5% yield). The ideal result line is included (orange dashed line).

Re-plotting these two correlations on the basis of predicted vs. observed result gives a direct visual comparison of all eleven results for each prediction methodology (Figures 8.9 and 8.10). The plots demonstrated that, whilst the ideal result of $x = y$ is not fully met in either comparison; a largely linear relationship and a good grouping to the ideal results line are observed. A gradient similar to the ideal result of unity is provided by the trendline of the 99.99% results ($y = 0.8142x$ Figure 8.8) and reasonable agreement to this trend is observed ($R^2 = 0.768$). The gradient of the single predicted trendline is notably lower ($y = 0.5155x$, Figure 8.9) and reduced agreement to this trend is observed ($R^2 = 0.650$). Error for the predicted vs. observed data was calculated for both the single element and 99.99% predictions, and is tabulated below (Table 8.3).

Selecting the best relationship from the table above (single element prediction) and replotting including the 95% confidence intervals provides the plot shown in Figure 8.11. This shows the 95% confidence of the sample mean, and the 95% confidence interval applicable when predicting the failure load of a new sample. The calculated intervals denote that any new sample can be predicted within -39.1% / +41.9% with 95% confidence

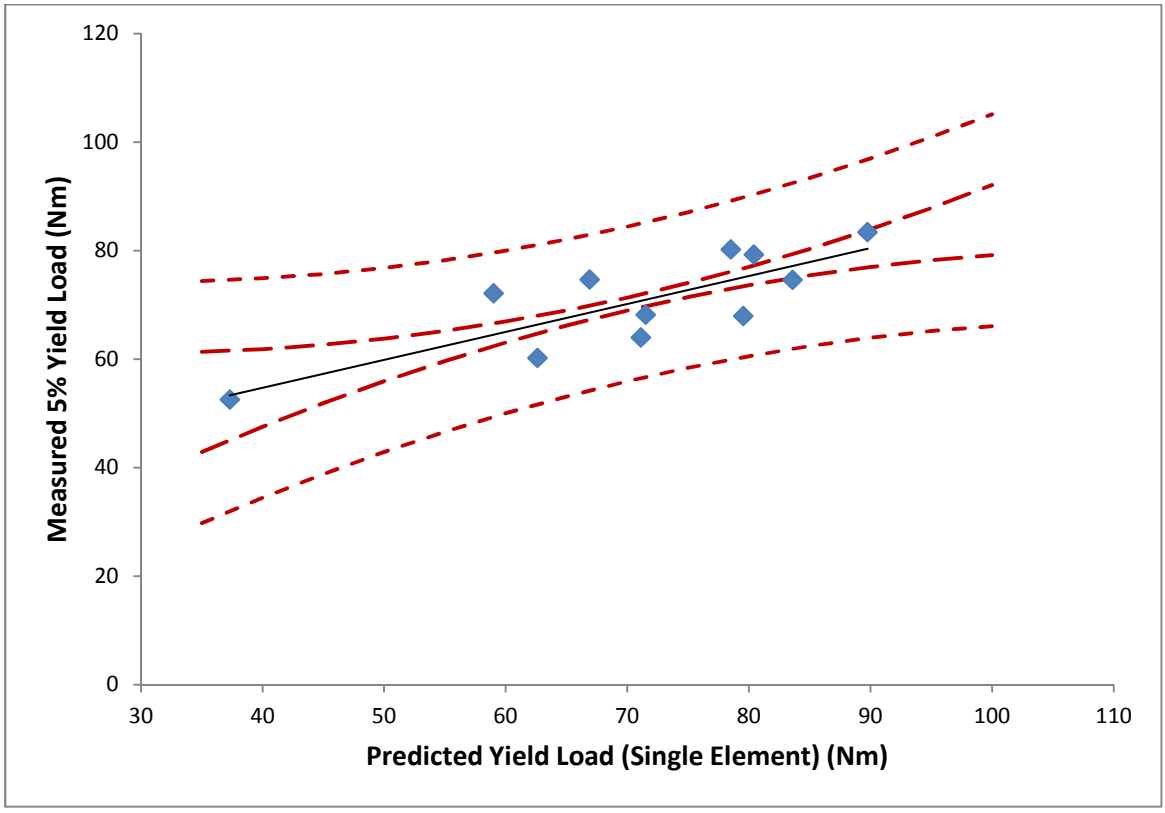

Figure 8.11 Predicted yield load (single element) versus measured yield load. Dashed lines represent the 95% confidence interval for the sample, (larger dashes) and for a new value (shorter dashes).

Table 8.3 Statistical information of both the single element and 99.99% predictions of 5% yield load as measured in the laboratory.

	Predicted (99.99%)	Predicted (Single Element)
Max Absolute Error (Nm)	19.67	11.59
Max Error (%)	28.95	13.90
RMSE (absolute)	9.19	8.49
RMSE (%)	11.03	10.18
Pearson's r	0.795	0.806
P Score	0.003	0.003

8.3.4 Fracture location

Correlation of the position of maximum principal strain and the initial fracture location was undertaken visually. The location was continually found to be within the indentation to the posterior surface during simulation (as demonstrated in Figure 8.12(b), which corresponds directly with the fracture line observed in testing (example shown in in Figure 8.12(a), and also the location at which aspects of the cortex were displaced in a number of test samples that displayed comminuted fractures. The approximate geometry and position of this feature was common to all of the porcine femurs in testing, and the fracture line for each test was repeatedly observed through this section in post fracture examinations.

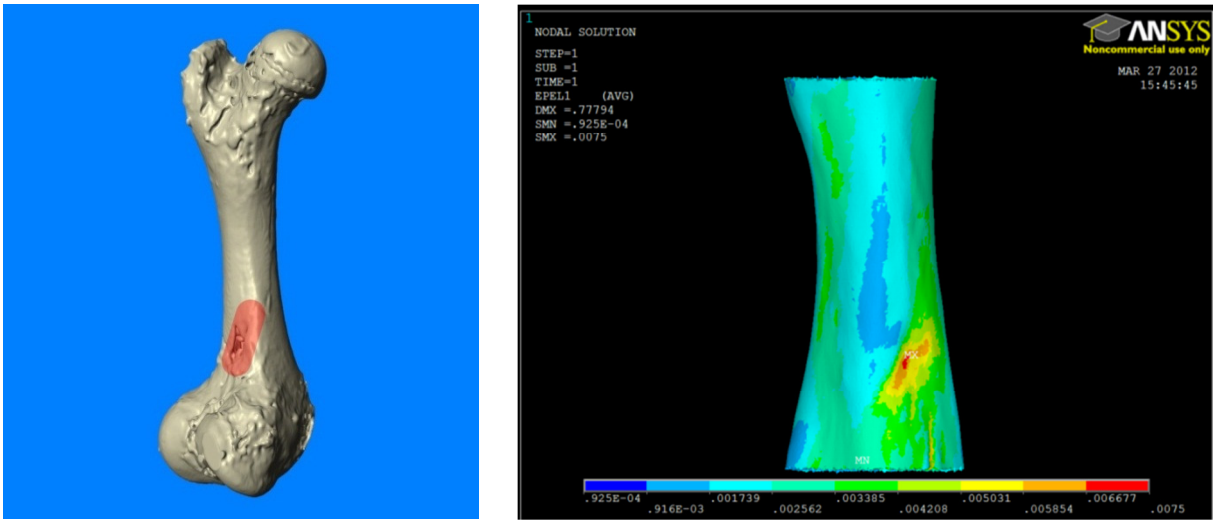

(a) (b)

Figure 8.12. Screen capture from the post-test scanning process detail the region of interest on a reconstructed model (a). Finite Element prediction of the same femur demonstrates the region of interest with respect to maximum principle strain (b).

8.3.5 Discussion

Despite the increasing use and development of CT-FE simulation, the application of the simulation procedure in the prediction of fracture load has had relatively little exposure in the literature. In fact, the experimentation and simulation in literature commonly details comparison between different fracture assessment techniques rather than predicting the absolute load required to instigate fracture in a given sample [36, 45]. As a result, the accuracy observed in this study has a reduced basis for comparison with results from studies published in the literature.

The predictions in this study were provided by determining a risk factor on the basis of a predicted principal strain compared to a prescribed limiting strain value. This has been demonstrated to be the most appropriate methodology for analysing risk in literature [45]. Despite this recommendation, the precise determination of fracture load was omitted from that study, and a review of the results plots in the paper exhibited the onset of failure in the predictive simulation at as little as 20% of the final fracture load, suggesting that the accuracy of that study would ultimately be questionable.

The measured onset of yield has been proposed as the most appropriate point at which to simulate the failure of a sample [36]. This technique increases the justification for the use of linear elastic models when predicting fracture. This is preferable to introducing more complex materials that describe the more unpredictable post yield behaviour [91]. The prediction of the point of yield may be more appropriate for the simulation of *in vivo* fracture, predicting the load at which the material failure and combined effect of microdamage (typically occurring in sub maximal loading through general ambulation and loading of bone structure) impacts upon the integrity of the structure as a whole.

The accuracy and correlation of the results observed in this facture study has been shown to be high both for predicting single element failure ($r = 0.806$, $P = 0.003$) and on the basis of correlating the 99.99% element result with the onset of yield ($r = 0.795$, $P = 0.003$).

Comparing the accuracy of this study with examples from literature (in which the prediction technique was based upon a limiting stress value rather than strain) [212] highlights the high levels of accuracy achieved in this study (Table 8.4). Keyak et al. detailed the 'standard error of the estimate' (synonymous with root mean squared error) as 1.56 kN (single axis axial loading was employed rather than torsional load). This error is not published on a percentage basis within the paper; however analysis of the results plots show maximum results in the order of 8 kN which would lead to RMSE on a percentage basis of approximately 19.5%, significantly higher than the accuracy achieved in this study. The correlation observed in Keyak et al.'s single stance study ($r = 0.867$, $P < 0.001$) benefited from test samples that failed at loads significantly above and below the mean failure load.

Table 8.4 Comparison of the statistical accuracy obtained in this study with that proposed in literature.

	Accuracy Reported by Keyak et al.	Accuracy Reported by Lotz et al.	Accuracy Observed in this Study (single element)
Pearson's (r)	0.867	-	0.806
P Score	P < 0.001	-	P = 0.003
RMSE (%)	19.5%	-	8.4%
Max. error (% of observed result)	-	4 and 22 %	13.9 %
Prediction precision (minimum/maximum)	-40% / +60%		-39.1% / +41.9% (-30.8% /+35.4%)*

Interestingly, Keyak et al. also correlated predicted vs. observed facture load on the basis of a non-linear relationship. In that paper the maximum failure load was approximately 400 % of the minimum failure load (2kN minimum, 8kN maximum). This not only gave the opportunity to test the range of the predictive capabilities of the simulation, but also provided better correlation of the results over a wide range of values. The range of values in this thesis was significantly smaller, with all samples failing close to the mean value (maximum result 159 % of minimum load to failure). The reduced range is likely to be the result of the manner in which the samples were selected, with common diet, ambulation during rearing and slaughter weight leading to more similar samples and failure loads. Only one porcine sample fell outside of the main group when predicting using single element selection. This had a distinctly lower predicted failure, contributing to the deviation from the ideal gradient of the trendline for the results.

Plotting the confidence intervals for the single element prediction (Figure 8.9) demonstrated the 95% confidence of the sample mean, and the 95% confidence interval applicable when predicting the failure load of a new sample. The intervals are significantly reduced over those shown by Keyak et al. (table 8.4). Removing the single result that fell outside of the main group lowers this interval further (as denoted by the starred item in the table) to (-30.8% /+35.4%).

Comparison with other papers in the literature highlights the importance and potential of animal substitution in fracture testing. Lotz et al. fractured just two human samples when correlating both the point of yield and the total failure load. Accuracy of that study was shown to be high (22 and 4 % accuracy for yield prediction, 8 and 5 % accuracy for total failure load) however no correlation was possible with such a small sample.

The manner in which the predicted failure loads are exported from the Finite Element solver must also be considered with caution. Both Keyak et al. and Yosibash et al. used relatively coarse meshes for fracture prediction, despite the modernity of the latter study. The 99.99 % and single element failure criteria used within this study refer to a significantly more refined "failed area" than was predicted in either of those studies. Schileo et al., for example, quoted a failed area of between 58 and 265 mm^2 during simulation, using differing fracture prediction techniques. The smallest failed area indicated the most appropriate prediction methodology in that paper. The limiting strain criterion used during this study and in the simulation performed by Schileo et al. is such that failure of any number of elements at the bone surface *should* indicate failure of the structure as a whole. As such the failed area for a true prediction of the failure load should be the equivalent of a single element at the sample surface. It is therefore not acceptable to detail a widely ranging 'failed area' for a given load, and this Figure should be refined as much as possible.

It is considered that the refined failed area at the predicted failure load demonstrated in this study, represents a significant improvement in the accuracy of the fracture prediction procedure.

8.4 Predicting Compressive Fracture Load

As described in Chapter 5, the manner in which the compressed porcine samples failed was notably different to the proximal femur fractures for human samples in the literature. It was considered that this was either a result of the geometrical differences and the propensity of the porcine bones to a given failure type, or of the constraint design used in testing. With torsion as the primary focus in testing and simulation, a reduced number of compressive samples were available for assessment of the compressive failure mode.

Simulation was undertaken to compare the principal strain on the proximal half of the medial face (in which failure was noted in the porcine samples) and on the proximal femoral neck (as predominantly noted for human fracture). The reduced number of samples tested removes the opportunity to test the general observation of effects across samples, however anecdotally the following was found:

- Significantly high levels of principal strain are noted on the proximal medial face as demonstrated in laboratory testing.
- High levels of tensile strain are noted in a specific notch that joins the femoral neck to the greater trochanter in the porcine samples.
- The risk factor with respect to strain based failure is higher on the proximal medial surface than on surface of the femoral neck (away from the notch at the base of the greater trochanter).

These effects are best described graphically (Figure 8.13). As can be seen, regions of high compressive strain are noted along the medial surface, particularly towards the base of the femoral head. The high tensile strain noted in the notch in the femoral neck is also displayed.

The key difference between the geometry of the proximal femur is noted in (Figure 8.14). The darker region at the base of the notch (b) is a region of low density, and consequently mapped with low material property (c) and susceptible to increased incidence of strain.

(a) 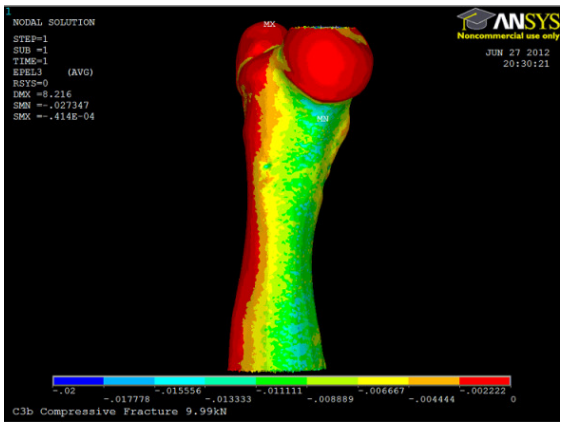

(b) 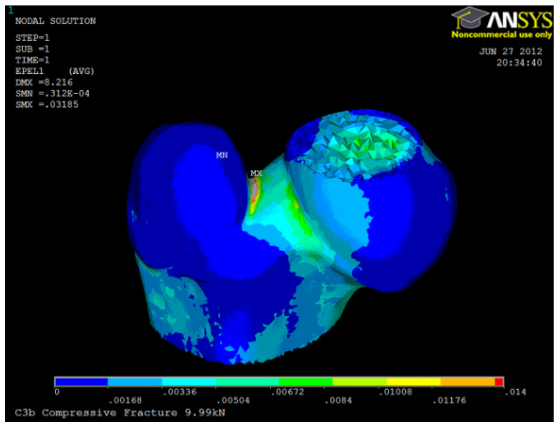

Figure 8.13 Finite Element screen shots of the simulation procedure detailing the compressive (a) and tensile (b) strains determined through compressive simulation.

Further simulation was undertaken omitting the results of the notch at the base of the greater trochanter, providing an estimation of the principal strain in the wider femoral neck region. This was then compared with the average principal strain on the proximal medial face, giving a comparison of the relative fracture risk of each region. Despite the increased strain limit used for to indicate compressive failure, the fracture risk was arbitrarily demonstrated (only two samples simulated) to be in the region of 30 - 40 % higher than the risk observed on the proximal femoral neck. The region of highest compressive principal strain in the Finite Element model was shown to be directly beneath the femoral head, as shown in Figure 8.13.

Ultimately the results observed with respect to compressive fracture mode are inconclusive. The levels of strain away from the notched region suggest the observed propensity to mid shaft fracture in porcine samples (as shown in physical testing) is not an erroneous result. Further mechanical testing with matched simulation is required to draw conclusions from the data. The effects of finer resolution CT scanning and re-meshing the notched area could also be considered to reduce the incidence of singularities, and ensure that the correct Young's modulus is mapped in this region.

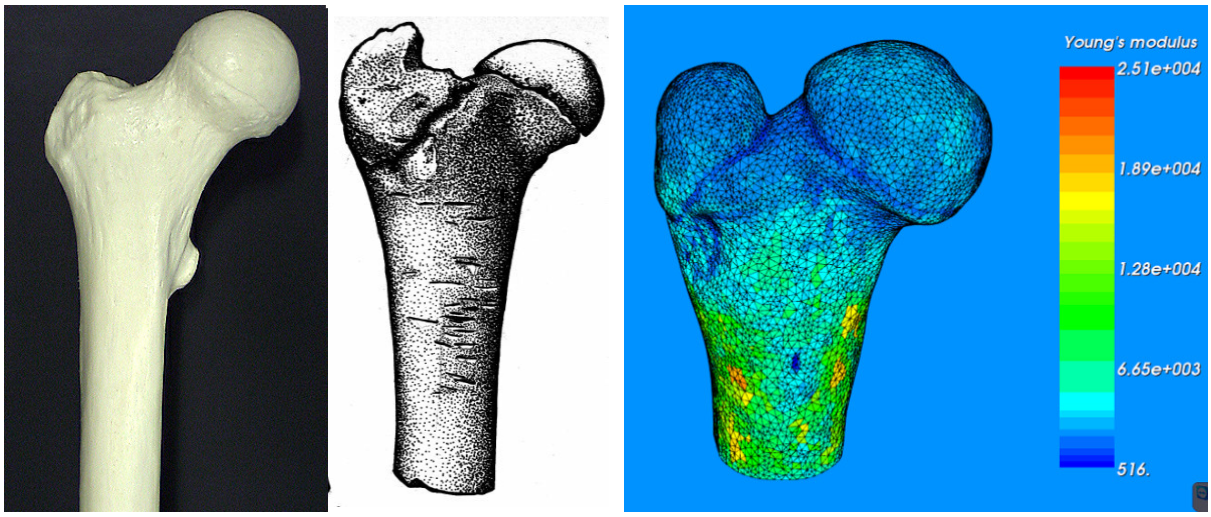

(a) (b) (c)

Figure 8.14. Comparison of the geometry of human (a) and porcine (b) proximal femur. The notch at the base of the greater trochanter can clearly be observed, and is the region of lowest material property in the sample (c).

8.5 Chapter Discussion

Following the extensive validation and the observation of high levels of accuracy in previous chapters, further simulation was undertaken to optimise and apply the porcine simulation technique.

- Small changes in the in the geometry production and phantom calibration processes were adopted. This optimisation demonstrated an improvement in the accuracy of the simulation process as a whole.
- The derivation of a new material relationship was undertaken with only marginally improved accuracy over the use of relationships from literature that were initially derived for human samples. Ultimately it was considered that the resolution of whole bone modelling was not sufficiently accurate to derive new material relationships. Consequently it was proposed that Morgan et al.'s relationship was the most appropriate for simulation at this stage.
- The prediction of fracture load was implemented with high levels of accuracy. Simulation of fracture tests determined strong correlations between the predicted and observed yield loads in 11 samples. It is considered that the accurate prediction of failure load is a fundamental step in simulation, demonstrating that the procedure is valid for extension, and the future assessment of additional failure modes and samples types.
- Statistical analysis demonstrated that the simulation was capable of predicting the yield load of any new porcine sample to within -30.8% / +35.4% with 95% confidence.

- Physical compressive fracture of porcine samples displayed evidence of propensity to failure in the mid-shaft rather than femoral neck. Using simulation to confirm this effect is so far inconclusive. Future research could consider the physical boundary conditions including the application of force, and/or consider the modelling and meshing protocol in the highlighted ‘notched’ region.

9 Discussion, Critical Reflection and Future Plans

Computed Tomography based Finite Element simulation is a developing research technique, offering the opportunity to test and simulate a wide variety of biomechanical situations with ever increasing complexity and accuracy. Using medical data increases the geometrical accuracy of the simulation, providing true patient specific representation. It is proposed that the development of these patient-specific simulation techniques will ultimately be employed clinically to aid in the determination of fracture risk on a case by case basis. As with all Finite Element simulation, appropriate and extensive physical validation is required. This can only be achieved through physical testing of the scanned and simulated subject bone, ensuring that the patient-specific nature of the process is retained.

The 'gold standard' in the validation of human bone simulation is unarguably the physical testing of *human* bone samples. Whilst validation using human samples has been undertaken for some injuries and medical conditions (notably proximal femoral injuries in older adults), other loading regimens and fracture types have yet to be considered in significant detail [20, 51, 213].The high occurrence of studies pertaining to older adults is no doubt due to the increased fracture risk in this cohort. Arguably studies may also be more likely to simulate in this age group due to the increased accessibility of bone samples for physical testing as a result of death from natural causes. Supporting this argument is the distinct lack of studies considering very worthwhile causes such as non-accidental injury in children.

Animal sample substitution in both physical testing and CT-FE simulation was employed in this thesis. Using animal bone offers the opportunity to test using samples that are more readily available than the human counterpart. This allows for fracture testing of larger numbers of samples, and for the researcher to obtain samples of varying age and at differing stages of development.

In order for the CT-FE simulation technique as a whole to be applied in the wide-ranging clinical environment, the validation mechanisms commonly demonstrated in literature (such as single axis loading of the proximal femur) must be expanded to consider an increased number of loading regimens, more complex paths to fracture and alternative bone types. Spiral fractures, for example, are a well-documented indicator of abuse in non-ambulatory children and yet very limited work has been published considering the application of torsion in CT-FE studies.

In this study, patient-specific Finite Element simulation based upon data from Computed Tomography scans was used to simulate the torsional and compressive fracture of adult porcine long bones. To investigate if the all-important geometry and material property mapping functioned correctly within the simulation and during expansion to animal simulation, extensive physical validation was undertaken.

Physical testing within the laboratory performed favourably. Analysis of the measured strain results in strain gauged testing, and of the load/deflection curves in fracture testing demonstrated that the selection of linear material models in the Finite Element simulation was appropriate. The simulation

procedure also performed well, demonstrating that the CT-FE process as a whole is capable of performing across different species and that the process is capable of simulating alternative loading regimens, such as torsion. Linear regression and mean error calculation demonstrated accurate correlation between predicted (simulated) and observed (measured in the laboratory) with comparable accuracy to those observed for human samples in notable and well cited technical papers [46]. The research also demonstrated that the material mapping relationships proposed for human samples could be used with a high degree of accuracy, directly contradicting Rice et al.'s proposal that interspecial relationships could not be determined [196]. The ultimate applicability of the validated simulation process was confirmed through prediction of the failure load of a number of porcine femoral samples that had been physically tested to fracture in torsion. Correlation of the predicted and measured yield load of the samples was demonstrated with notably increased accuracy over studies published in literature for the compressive testing of human samples [22, 213].

Whilst the accuracy of the thesis can be compared directly with published research (and is shown to compare favourably), the *success* of the project as a whole is best considered by revisiting the project aims. The original aims (detailed in section 9.2) were selected to investigate the gaps highlighted in the existing research and to provide a fully validated platform for the testing and simulation of bone.

The thesis aims, outputs and limitations are discussed in section 9.1; the flow of each project sub part is best described graphically, as shown in Figure 9.1.

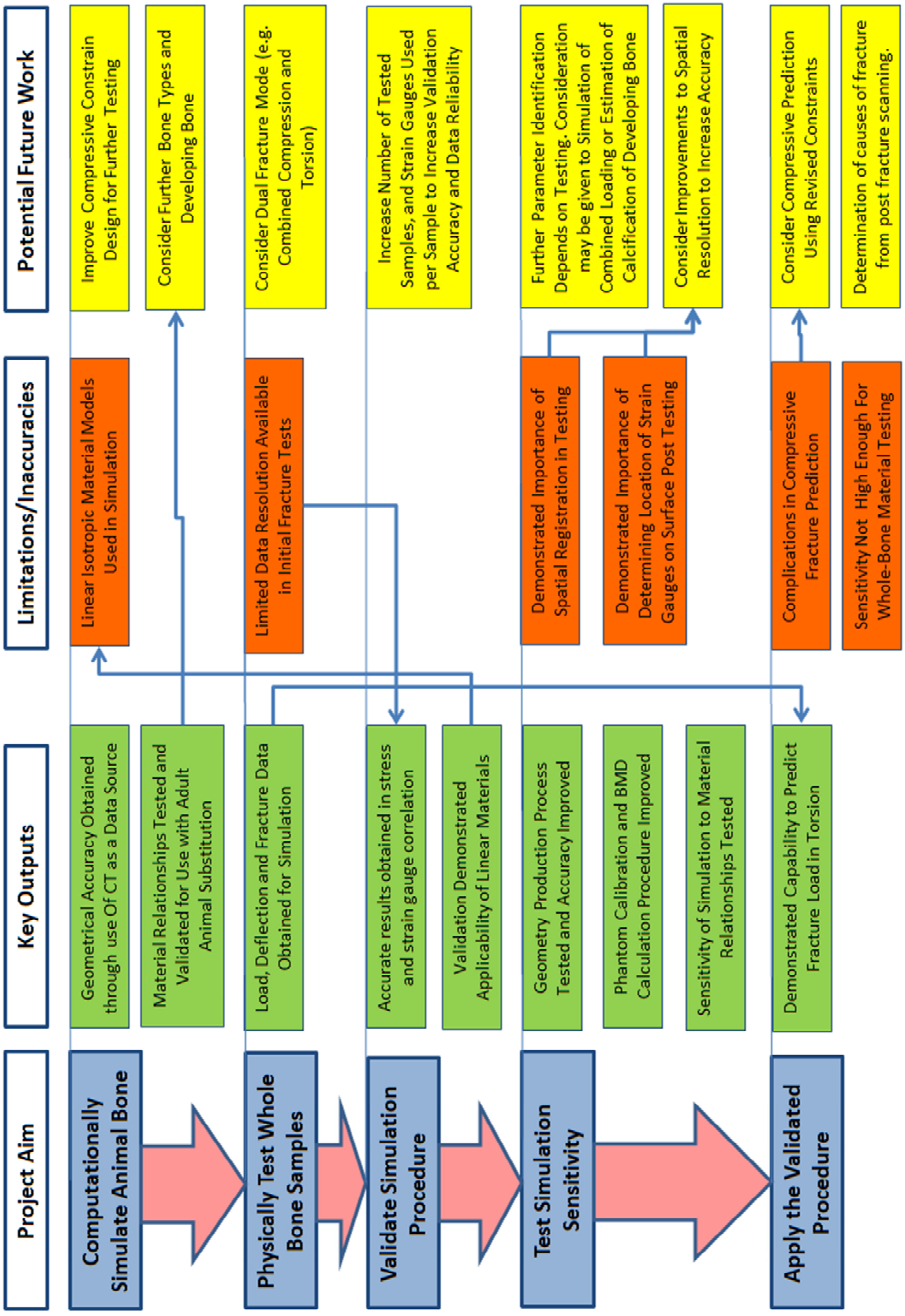

Figure 9.1. A flow chart demonstrating the thesis aims and the major outputs and limitations.

9.1 Achievement of the Project Aims

As a new piece of work, no previous studies provided background data or contributed initial information to the studies in this thesis. The project aims were therefore sequential in nature. Each of these aims provided a step in the modelling procedure that required completion before the commencement of the next.

1. ***Computationally Simulate Animal Bone: Investigate the capability and accuracy of the general Computed Tomography Finite Element process in the substitution and simulation of animal bone.***

Should this investigation prove successful, it will serve to demonstrate the applicability of animal substitution in CT-FE studies. The use of animal substitution provides the potential for increased sample size fracture studies and demonstrates the general ability of the CT-FE process in expansion towards alternative bone types.

Achievement of Project Aim:

The basic segmentation and simulation of the porcine bone samples proved to be successful. The software used provided a robust and rapid mechanism for segmenting data, allowing fine control of model parameters such as the meshing of the simulated structure. Samples were scanned using CT to provide geometrically accurate and patient specific geometry. CT was selected to provide fine definition of bone structure, and to allow for the semi-automated calculation of Young's modulus on the basis of greyscale attenuation and therefore apparent density.
At this stage of simulation, the material definition was undertaken using material relationships that had originally been derived from physical testing of human samples from literature. Small scale sample testing and material checking within the Finite Element model demonstrated that the applied relationships were appropriate for porcine simulation on the basis of predicting an appropriate Young's modulus for a given apparent density. The materials assigned to the mesh used for CT-FE simulation are linear and isotropic; however the overall array of materials ultimately provides an inhomogeneous structure.

Limitations and Inaccuracies:

Linear material models are necessary in order to use the automated material mapping algorithms for bone properties on the basis of apparent density, Literature had previously demonstrated that these linear material models performed capably for whole bone human samples, but despite the similarity

and regular substitution of porcine samples, these linear models had yet to be demonstrated as accurate in animal substitution.

2. ***Physically Test Whole Bone Samples: Consider the behaviour of samples in alternative loading regimens (such as torsion) and identify the manner in which the samples fail physically.***

The investigation of failure modes other than simple compression has shown limited investigation in literature. The detailed investigation of torsion is important, being a common failure mode for long bone fracture.

Achievement of Project Aim:

Physical fracture testing was undertaken successfully, demonstrating predominantly linear behaviour until a definable yield point, for the majority of the bone samples tested within the laboratory. Both compressive and torsional testing was undertaken, with the focus primarily on torsional fracture. In addition to physical sample testing, analytical calculations based upon geometry derived from the CT data were used to provide a logic check on the values predicted through Finite Element simulation.

Limitations and Inaccuracies:

A small percentage of fracture tests demonstrated behaviour that did not fit the general trend and displayed excessive plasticity. Closer inspection revealed that a number of compressive tests had failed as a result of errors during the potting process. The anomalous results were consequently discarded which significantly reduced the number of samples tested to compressive failure.
Post fracture scanning was used to determine the original alignment and position of the samples during testing. This is a potential source of error, making a number of assumptions regarding the initial alignment of the sample within the outer test constraints.

3. ***Validate the Simulation Procedure: Demonstrate the accuracy achieved during the animal CT-FE modelling process through appropriate laboratory validation.***

The ultimate capability of Finite Element modelling can only be demonstrated through appropriate validation. Extensive validation will be undertaken to demonstrate the capabilities of the modelling procedure at both a whole-bone and local level.

Achievement of Project Aim:

Extensive physical validation was undertaken through the implementation of strain gauged sub-maximal testing. This provided a much higher resolution of data, and allowed for greater correlation of the laboratory results with those proposed through Finite Element analysis. The results demonstrated a good degree of accuracy in the Finite Element models, comparable with highly cited papers in literature and demonstrating an improvement over many published studies. Both stress and strain correlation were undertaken, with strain correlation providing better agreement at the sample surface. Stress correlation is more commonly undertaken in CT-FE studies due to its relation to mapped Young's modulus.

Achievement of comparable accuracy to that in published literature demonstrated that the CT-FE process for porcine bone was suitably validated, supporting the continuation and expansion of the project as a whole.

Limitations and Inaccuracies:

Despite the general agreement that was demonstrated and the high level of accuracy achieved, relatively large error was noted in some isolated results. These tended to fall at specific gauge locations during stress correlation, which suggests that the most likely source of inaccuracy was related to spatial registration or material assignment.

The importance of the effects of small changes in the applied boundary conditions was assessed later during parameter identification. Key amongst those was consideration for the alignment of the sample during testing and simulation. The observed effects demonstrated the importance of the alignment procedure, showing how a change of only 1mm in any given axes can have significant impact on the observed results. It was considered that the alignment protocol used was capable of achieving this level of accuracy, however the alignment and spatial registration of the tested samples remained a potential source of error.

4. ***Test the Simulation Sensitivity: Consider the effect of various input parameters, and the sensitivity of the modelled solution to small changes in the modelling procedure.***

There is a large array of input parameters in complex CT-FE simulation. Modification of a single parameter can have a significant effect on the observed results. It is therefore important to assess the observed changes and the sensitivity of the modelling process to changes in the input and validation procedure.

Achievement of Project Aim:

A large array of input parameters was considered to demonstrate the effect of each on the ultimate Finite Element result and the correlation with the laboratory testing. This parameter identification

process highlighted the importance of each individual aspect, notably detailing a requirement for tight control of spatial registration and alignment during physical testing. The process also highlighted the importance of accurate segmentation during the initial modelling phase, to ensure both geometrical accuracy and the correct determination of Young's modulus.

Limitations and Inaccuracies:

Re-scanning through CT was used for spatial registration of the tested arrangement, but is not without limitations. Both published literature and the parameter identification tests within this study demonstrated the importance of determining the correct alignment and the CT re-scanning process makes notable assumptions. Firstly it is assumed that the primary test constraints remain consistently aligned and that each sample fits in the same way. The design of the two part constraints permits this and the alignment was checked during testing; however the possibility of error to the extent of approximately 0.5 mm in any given axis cannot be discounted.

Secondly, the re-scan process is undertaken *post* testing and considers that the orientation and the shape of the sample has not changed as a result of the application of force. This was partially confirmed through the observation of linear and repeatable results. Additionally comparison of the shape of the rescanned mask with the original counterpart was undertaken.

Finally, the effect of the metallic artefacts (strain gauges constrain edges etc.) within scanning should also be considered. Literature has demonstrated that the accuracy of a helical CT scan at a distance of more than 2 mm from a significant artefact is not impeded, however this cannot be achieved for the determination of the gauge locations, at which point it is the artefact itself that must be noted. Visual inspection demonstrates that the positioning of the gauges was not impeded; however a potential source of error remains.

5. ***Apply the Validated Procedure: Consider the ultimate applicability of the animal CT-FE process through the prediction of the fracture load of a given sample.***

The main focus of the study as a whole is the validation and observed accuracy when applying the CT-FE process in new directions (animal substitution and torsional fracture). However, the ultimate application of the process is in the prediction of fracture risk and the fracture load for a given subject. The final aim of the project is to demonstrate that the process is capable of predicting the fracture load of a given sample with a reasonable level of accuracy.

Achievement of Project Aim:

The validated procedure was applied in two ways; firstly through deriving a new material relationship from whole-bone testing results and secondly, prediction of the laboratory fracture load of scanned samples.

Production of a new material relationship for porcine bone was ultimately unsuccessful. Despite significant investigation, testing proved that it was difficult to improve upon the material relationship proposed by Morgan et al. Additionally, the level of improvement required was so fine that the resolution of the modelling was not sufficient and the inherent simulation and testing errors could not be ignored. Whilst the predicted vs. observed line defined by the improved relationship was closer to the ideal $x = y$ result, the simulation inaccuracies that determine the fit to that line (and consequently the R^2 result) could not be significantly improved upon.

Prediction of fracture load was more successful, particularly in torsional testing, but again provided complications when testing in compression. Torsional fracture prediction demonstrated root mean squared error and 95 % confidence intervals that improved upon that published in literature, particularly when correlating the 5 % yield load with the predicted Finite Element failure on a strain limit basis.

Physical compressive loading in this study was performed in a more complex manner than that typically shown within literature. The methodology used here was arguably more consistent with the expected loading *in vivo* wherein it is difficult to determine the precise activation forces upon a bone sample. Necessarily, it was therefore difficult to correlate the activation forces in the Finite Element model, which provided difficulties in fracture correlation.

Limitations and Inaccuracies:

As detailed above, the key limitations were the failure to determine a new material relationship and the failure to predict compressive failure load. The former demonstrated that whole bone testing may not be the most appropriate methodology for determining material mapping parameters.

Failure to accurately predict compressive failure load should be reconsidered in the future. It was considered that the issue arose due to over potting of the constraints in the compressive test regimen. The level of potting was difficult to determine during testing and consequently the distribution of load was not necessarily purely upon the femoral head (as simulated) but to some extent distributed across the femoral neck. Revisions to the potting procedure may improve upon this issue, however ultimately revised inner constraints may be required. Whilst the results of compressive prediction were inconclusive, the simulations indicated the correct general behaviour of the samples (highest compressive strain beneath femoral head, at the point of fracture). This indicates the potential of the simulation procedure, suggesting that with appropriate revisions the process may ultimately perform successfully.

9.2 Future Work and Expansion

The following section considers the short, medium and long term aims of future work. The short term aims typically consider accuracy improvements and slight changes to the testing and simulation process.

Short term expansion and accuracy improvements:

1. **Improve the spatial registration in physical testing**

It may be prudent to introduce improved mapping of key reference positions and the sample itself in future testing. Ideally this would occur *during* physical testing, which would provide improved detail regarding the actual tested arrnagement. This would be best performed non-invasively, and thus continually active laser scanning or infrared detection of reference positions could be considered. The inclusion of live positioning significantly increases test complexity, but would potentially provide robust orientational data for simulation.

2. **Reconsider the constraint design and force application in compressive testing**

Whilst sub-maximal compressive testing performed favourably, complications were noted during fracture prediction in compression. Potting to a reduced depth may reduce this issue, and could be considered in future testing. Alternatively the proximal constraint could be completely revised, which may additionally allow directional control and off axis loading.

3. **Increase data capture in strain gauged testing.**

Despite a high level of resolution offered in testing, the inclusion of further gauges on each sample and live strain gauge data would offer increased mapping of the behaviour at the sample surface. Inclusion of gauges upon the femoral neck in compressive testing would increase the information available in this key area. In addition, for fully potted samples, it may be useful to include a gauge within the potting medium. This gauge would be used as a reference to confirm the isolation of the section of bone to which it was mounted. Other options may also be explored, for example digital image correlation, in which a speckle is scattered over a subject, and the relative motion of the speckles with respect to each other is used to calculate the strain response of the subject across the surface.

Short/medium term investigation expansion: As a result of the work in this project, a number of additional aims that could be addressed in the short and medium term have been identified:

1. **Investigate the simulation of young and developing bone.**

The project demonstrated that animal bone could be simulated accurately. Further testing could be considered using samples that are less easily obtained in human testing such as developing bone. Whilst physical testing of developing bone samples has been undertaken, the ability of the CT-FE process to model this has yet to be significantly investigated.

2. **Consider multiple strain path loading.**

The ASP rig that was selected for physical testing offers the opportunity for multi-path loading. This provides the opportunity to combine compressive loading with torsional loading, better simulating a trip or fall, where a patient may twist a weight-bearing limb. This is potentially more difficult to simulate, however live strain gauged testing could be implemented initially to inform boundary conditions of the simulation procedure.

3. **Determine fracture conditions from post fracture scans.**

With fracture prediction, it was possible to predict the failure load of a sample under certain defined conditions. As CT offers rapid segmentation and modelling, it may be possible (particularly when modelling limbs) to use the uninjured opposing limb as a basis for simulation. With changing boundary conditions and activation forces in further simulation this could be used to determine the original fracture conditions that provided the fracture morphology observed in the injured limb.

4. **Consider paired testing.**

An additional benefit of animal substitution is the opportunity to test *pairs* of limbs. Aim 3 (above) proposes the unfractured limb acts as a data source for the 'clean' model. As such it relies upon both limbs sharing geometry and Young's modulus. Paired testing of both limbs would offer the opportunity to test this theory and compare the predicted (Finite Element) and physical (laboratory) fracture load of two theoretically identical samples.

Long term aim: The long-term aim of most studies using the CT-FE process is the complex goal of the simulation of complete biomechanical structures and the production of the 'virtual human'. The proposed long term aim of this thesis stops short of full body simulation, combining and expanding upon the medium and short term aims listed above.

CT-FE simulation to aid in the diagnosis of non-accidental injury in children.

The spiral fractures of long bones, as assessed in this study, are listed as an indicator of potential abuse and non-accidental injury in children. Combining the medium term aims with the accuracy

obtained in torsional validation and fracture prediction offers the potential to simulate the *causes* of an observed injury through simulation. This data could be used by the clinician to provide estimation of the activation force required, or the boundary conditions at the time of the incident, and therefore aid in the difficult task of diagnosis of non-accidental injury.

This is a goal that has far reaching social implications and could help in the protection of the most vulnerable of patients, helping injured and 'at risk' children who may not be old enough to describe the occurrence of their injuries.

10 Conclusions

In this thesis, Finite Element simulation based upon computed tomography data was used to simulate the behaviour of porcine femoral samples. Physical testing of whole-bone samples was undertaken, primarily in torsion but also in compressive loading. Parameter identification and optimisation were undertaken to determine the best possible accuracy of the simulation procedure. Following this, fracture prediction was undertaken.

The simulation of porcine sample is essentially novel in CT-FE studies. Whilst porcine bone has been used extensively for substitution in physical studies, little work has been done to expand and test the CT-FE simulation process in the examination of porcine bone behaviour. Additionally, testing in torsion has had very little exposure. Studies to date have focussed primarily upon fracture of the proximal femur through single axis loading. Torsional loading provided the opportunity to test the CT-FE methodology in the prediction of failure of the mid-shaft.

Methodology:

- Porcine samples were scanned using helical CT. The data was segmented and used to create the basis of the Finite Element models.
- The same samples were tested both sub-maximally and to destruction in the laboratory.
- Simulation was performed upon the models to match the physical loading in the laboratory and determine the simulation accuracy.
- Parameter identification, material property analysis and optimisation were undertaken to refine the simulation procedure.
- The procedure was then applied to predict the failure load of the specimens that had been fractured in the laboratory.

Findings:

- Chapter 3 (model creation) showed that the CT-FE process originally derived or simulating human bone is applicable for interspecial simulation.
- Material testing (also in Chapter 3 and revisited in Chapter 8) demonstrated that the material mapping relationships derived for human bone were appropriate for the simulation of porcine samples.
- The sub-maximal laboratory testing and subsequent simulation (Chapters 4 to 6) detailed the validation procedure. The accuracy of the simulation and physical testing was

determined in this procedure, notably improving upon the values published in literature strain correlation, and slightly improving upon literature during stress correlation.

- The effect of changes to the inputs during CT-FE simulation procedure was in Chapter 7. This highlighted the importance of spatial registration, and provided a means with which to further increase simulation accuracy. A new methodology was created for phantom calibration.
- The amendments from Chapter 7 were adopted for optimisation in Chapter 8. Stress correlation results and accuracy were further improved over the values from Chapter 6.
- The application of the procedure was demonstrated in the final chapter. Fracture prediction using a maximum principal strain criterion combined with the 5% yield load from physical testing was used to determine the failure load of the samples. Accuracy in prediction was notably improved over the accuracy detailed in literature.

The use of fully validated and highly accurate simulation is the long term future of healthcare. To reach this goal, testing and validation must be undertaken in every possible field. In the context of bone behaviour, research must consider extensive physical validation through fracture studies. The inaccessibility of human samples and the increased risk factor at age has led to a significant proportion of CT-FE research considering only proximal femur injury in older adults.

The results of this thesis demonstrate that porcine substitution is applicable and accurate in CT-FE simulation and fracture prediction. The results also show that the process is capable of simulating alternate fractures, such as spiral fractures. Through animal substitution, significantly larger and more complex fracture studies may be performed and validated, reducing the number of human samples required.

It is hoped that the research and the accuracy demonstrated while simulating porcine bone in this thesis will increase the rate at which studies can be validated, with testing expanded to more sensitive bone types such as young and developing bone in the near future. With further research the increased validation rate can help to meet the ultimate goal of CT-FE being implemented in a clinical environment to help most vulnerable of patients.

References

1. Pierce, M.C., A. Valdevit, L. Anderson, N. Inoue, and D.L. Hauser, *Biomechanical Evaluation of Dual-Energy X-Ray Absorptiometry for Predicting Fracture Loads of the Infant Femur for Injury Investigation: An In Vitro Porcine Model.* Journal of Orthopaedic Trauma, 2000. **14**(8): p. 571-576.
2. Strømsøe, K., A. Høiseth, A. Alho, and W.L. Kok, *Bending strength of the femur in relation to non-invasive bone mineral assessment.* Journal of Biomechanics, 1995. **28**(7): p. 857-861.
3. Lang, T.F., J.H. Keyak, M.W. Heitz, P. Augat, Y. Lu, A. Mathur, and H.K. Genant, *Volumetric quantitative computed tomography of the proximal femur: Precision and relation to bone strength.* Bone, 1997. **21**(1): p. 101-108.
4. Ammann, P. and R. Rizzoli, *Bone strength and its determinants.* Osteoporosis International, 2003. **14**(0): p. 13-18.
5. Koo, M.W.M., K.H. Yang, P. Begeman, M. Hammami, and W.W.K. Koo, *Prediction of Bone Strength in Growing Animals Using Noninvasive Bone Mass Measurements.* Calcified Tissue International, 2001. **68**(4): p. 230-234.
6. Clasey, J.L., C. Bouchard, C.D. Teates, J.E. Riblett, M.O. Thorner, M.L. Hartman, and A. Weltman, *The use of anthropometric and dual-energy X-ray absorptiometry (DXA) measures to estimate total abdominal and abdominal visceral fat in men and women.* Obesity research, 1999. **7**(3): p. 256-64.
7. Southard, R.N., J.D. Morris, J.D. Mahan, J.R. Hayes, M.A. Torch, A. Sommer, and W.B. Zipf, *Bone mass in healthy children: measurement with quantitative DXA.* Radiology, 1991. **179**(3): p. 735-738.
8. Bolotin, H., *DXA in vivo BMD methodology: An erroneous and misleading research and clinical gauge of bone mineral status, bone fragility, and bone remodelling.* Bone, 2007. **41**(1): p. 138-154.
9. Keyak, J.H., M.G. Fourkas, J.M. Meagher, and H.B. Skinner, *Validation of an automated method of three-dimensional finite element modelling of bone.* Journal of Biomedical Engineering, 1993. **15**(6): p. 505-509.
10. Young, P., Tabor, G., Collins, T., Richterova, J. et al., , *Automating the Generation of 3D Finite Element Models Based on Medical Imaging Data.* SAE Technical Paper, 2006. **2006-01-2371**.
11. Hounsfield, G.N., *Computerized transverse axial scanning (tomography): Part 1. Description of system.* British Journal of Radiology, 1973. **46**(552): p. 1016-1022.
12. MacWilliams, B., *Russian claims first in magnetic imaging.* Nature, 2003. **426**(6965): p. 375-375.
13. Ramsey, N.F., *Early History of Magnetic Resonance.* Physics in Perspective (PIP), 1999. **1**(2): p. 123-135.
14. Rabi, I.I., *On the Process of Space Quantization.* Physical Review, 1936. **49**(4): p. 324-328.
15. Yazar, F., N. Imre, B. Battal, S. Bilgic, and C. Tayfun, *Is there any relation between distal parameters of the femur and its height and width?* Surgical and Radiologic Anatomy, 2012. **34**(2): p. 125-132.
16. Murshed, K.A., A.E. Çiçekcibaşi, A. Karabacakoğlu, M. Şeker, and T. Ziylan, *Distal femur morphometry: a gender and bilateral comparative study using magnetic resonance imaging.* Surgical and Radiologic Anatomy, 2005. **27**(2): p. 108-112.
17. Laib, A., O. Barou, L. Vico, M. Lafage-Proust, C. Alexandre, and P. Rügsegger, *3D micro-computed tomography of trabecular and cortical bone architecture with application to a rat model of*

immobilisation osteoporosis. Medical and Biological Engineering and Computing, 2000. **38**(3): p. 326-332.

18. Crawford, R.P., C.E. Cann, and T.M. Keaveny, *Finite element models predict in vitro vertebral body compressive strength better than quantitative computed tomography.* Bone, 2003. **33**(4): p. 744-750.
19. Helgason, B., E. Perilli, E. Schileo, F. Taddei, S. Brynjólfsson, and M. Viceconti, *Mathematical relationships between bone density and mechanical properties: A literature review.* Clinical Biomechanics, 2008. **23**(2): p. 135-146.
20. Cristofolini, L., M. Juszczyk, S. Martelli, F. Taddei, and M. Viceconti, *In vitro replication of spontaneous fractures of the proximal human femur.* Journal of Biomechanics, 2007. **40**(13): p. 2837-2845.
21. Gomez-Benito, M.J., J.M. Garcia-Aznar, and M. Doblare, *Finite Element Prediction of Proximal Femoral Fracture Patterns Under Different Loads.* Journal of Biomechanical Engineering, 2005. **127**(1): p. 9-14.
22. Lotz, J.C., E.J. Cheal, and W.C. Hayes, *Fracture prediction for the proximal femur using finite element models: Part I--Linear analysis.* Journal of Biomechanical Engineering, 1991. **113**(4): p. 353-60.
23. Datta, A., M. Bikson, and F. Fregni, *Transcranial direct current stimulation in patients with skull defects and skull plates: High-resolution computational FEM study of factors altering cortical current flow.* NeuroImage, 2010. **52**(4): p. 1268-1278.
24. Johnson, E.A.C. and P.G. Young, *On the use of a patient-specific rapid-prototyped model to simulate the response of the human head to impact and comparison with analytical and finite element models.* Journal of Biomechanics, 2005. **38**(1): p. 39-45.
25. Said, R., C. Jenssen, P. Young, G. Tabor, and S. Coward. *Image-Based Meshing of Patient-Specific Data: Converting Medical Scans Into Highly Accurate Computational Models*. in *Bioinformatics and Biomedical Engineering, 2008. ICBBE 2008. The 2nd International Conference on*. 2008.
26. Wu, L., *Clinical significance of musculoskeletal finite element model of the second and the fifth foot ray with metatarsal cavities and calcaneal sinus.* 2007.
27. Bessho, M., I. Ohnishi, J. Matsuyama, T. Matsumoto, K. Imai, and K. Nakamura, *Prediction of strength and strain of the proximal femur by a CT-based finite element method.* Journal of Biomechanics, 2007. **40**(8): p. 1745-1753.
28. Cattaneo, C., E. Marinelli, A. Di Giancamillo, M. Di Giancamillo, O. Travetti, L. Vigano', P. Poppa, D. Porta, A. Gentilomo, and M. Grandi, *Sensitivity of autopsy and radiological examination in detecting bone fractures in an animal model: Implications for the assessment of fatal child physical abuse.* Forensic Science International, 2006. **164**(2–3): p. 131-137.
29. Augat, P. and S. Schorlemmer, *The role of cortical bone and its microstructure in bone strength.* Age and Ageing, 2006. **35**(suppl 2): p. ii27-ii31.
30. Keyak, J.H., J.M. Meagher, H.B. Skinner, and J.C.D. Mote, *Automated three-dimensional finite element modelling of bone: a new method.* Journal of Biomedical Engineering, 1990. **12**(5): p. 389-397.
31. Valliappan, S., N.L. Svensson, and R.D. Wood, *Three dimensional stress analysis of the human femur.* Computers in Biology and Medicine, 1977. **7**(4): p. 253-264.

32. Rybicki, E.F., F.A. Simonen, and E.B. Weis Jr, *On the mathematical analysis of stress in the human femur.* Journal of Biomechanics, 1972. **5**(2): p. 203-215.
33. Steele, D.G.B., Claud A. , *The anatomy and biology of the human skeleton.* Texas A&M University Press (College Station) 1988.
34. Marks, L.W. and T.N. Gardner, *The use of strain energy as a convergence criterion in the finite element modelling of bone and the effect of model geometry on stress convergence.* Journal of Biomedical Engineering, 1993. **15**(6): p. 474-476.
35. Lengsfeld, M., J. Schmitt, P. Alter, J. Kaminsky, and R. Leppek, *Comparison of geometry-based and CT voxel-based finite element modelling and experimental validation.* Medical Engineering & Physics, 1998. **20**(7): p. 515-522.
36. Yosibash, Z., D. Tal, and N. Trabelsi, *Predicting the yield of the proximal femur using high-order finite-element analysis with inhomogeneous orthotropic material properties.* Philosophical Transactions of the Royal Society A: Mathematical, Physical and Engineering Sciences, 2010. **368**(1920): p. 2707-2723.
37. Schileo, E., E. Dall'Ara, F. Taddei, A. Malandrino, T. Schotkamp, M. Baleani, and M. Viceconti, *An accurate estimation of bone density improves the accuracy of subject-specific finite element models.* Journal of Biomechanics, 2008. **41**(11): p. 2483-2491.
38. Christen, D., D.J. Webster, and R. Müller, *Multiscale modelling and nonlinear finite element analysis as clinical tools for the assessment of fracture risk.* Philosophical Transactions of the Royal Society A: Mathematical, Physical and Engineering Sciences, 2010. **368**(1920): p. 2653-2668.
39. Ciarelli, T.E., D.P. Fyhrie, M.B. Schaffler, and S.A. Goldstein, *Variations in Three-Dimensional Cancellous Bone Architecture of the Proximal Femur in Female Hip Fractures and in Controls.* Journal of Bone and Mineral Research, 2000. **15**(1): p. 32-40.
40. Lengsfeld, M., J. Schmitt, P. Alter, J. Kaminsky, and R. Leppek, *Comparison of geometry-based and CT voxel-based finite element modelling and experimental validation.* Medical Engineering & Physics, 1998. **20**(7): p. 515-522.
41. Simpleware, *Simpleware Ltd. Exeter, EX4 3PL.* 2012.
42. Materialise, *Materialise, Leuven, Belgium 3000.* 2012.
43. Rodrigues, F.P., J. Li, N. Silikas, R.Y. Ballester, and D.C. Watts, *Sequential software processing of micro-XCT dental-images for 3D-FE analysis.* Dental Materials, 2009. **25**(6): p. e47-e55.
44. Viceconti, M., L. Bellingeri, L. Cristofolini, and A. Toni, *A comparative study on different methods of automatic mesh generation of human femurs.* Medical Engineering & Physics, 1998. **20**(1): p. 1-10.
45. Schileo, E., F. Taddei, L. Cristofolini, and M. Viceconti, *Subject-specific finite element models implementing a maximum principal strain criterion are able to estimate failure risk and fracture location on human femurs tested in vitro.* Journal of Biomechanics, 2008. **41**(2): p. 356-367.
46. Taddei, F., L. Cristofolini, S. Martelli, H.S. Gill, and M. Viceconti, *Subject-specific finite element models of long bones: An in vitro evaluation of the overall accuracy.* Journal of Biomechanics, 2006. **39**(13): p. 2457-2467.

47. Viceconti, M., M. Davinelli, F. Taddei, and A. Cappello, *Automatic generation of accurate subject-specific bone finite element models to be used in clinical studies.* Journal of Biomechanics, 2004. **37**(10): p. 1597-1605.
48. Shah, C., *Mesh Discretization Error and Criteria for Accuracy of Finite Element Solutions.* Proceedings of International ANSYS Conference, 2002. **2002**.
49. Hayase, T., J.A.C. Humphrey, and R. Greif, *A consistently formulated QUICK scheme for fast and stable convergence using finite-volume iterative calculation procedures.* Journal of Computational Physics, 1992. **98**(1): p. 108-118.
50. Keyak, J.H. and H.B. Skinner, *Three-dimensional finite element modelling of bone: effects of element size.* Journal of Biomedical Engineering, 1992. **14**(6): p. 483-489.
51. Yosibash, Z., N. Trabelsi, and C. Milgrom, *Reliable simulations of the human proximal femur by high-order finite element analysis validated by experimental observations.* Journal of Biomechanics, 2007. **40**(16): p. 3688-3699.
52. Barker, D.S., D.J. Netherway, J. Krishnan, and T.C. Hearn, *Validation of a finite element model of the human metacarpal.* Medical Engineering & Physics, 2005. **27**(2): p. 103-113.
53. Taddei, F., A. Pancanti, and M. Viceconti, *An improved method for the automatic mapping of computed tomography numbers onto finite element models.* Medical Engineering & Physics, 2004. **26**(1): p. 61-69.
54. Viceconti, M., C. Zannoni, D. Testi, and A. Cappello, *CT data sets surface extraction for biomechanical modeling of long bones.* Computer Methods and Programs in Biomedicine, 1999. **59**(3): p. 159-166.
55. Pfafrod, G.O., Y.Z. Saulgozis, I.V. Knet-s, and K.A. Yanson, *Experimental determination of the shear modulus of compact bone tissue.* Mechanics of Composite Materials, 1972. **8**(4): p. 601-608.
56. Evans, F.G. and M. Lebow, *Regional differences in some of the physical properties of the human femur.* Journal of applied physiology, 1951. **3**(9): p. 563-72.
57. Evans, F.G., *The mechanical properties of bone.* Artif Limbs, 1969. **13**(1): p. 37-48.
58. Woo, S., S. Kuei, D. Amiel, M. Gomez, W. Hayes, F. White, and W. Akeson, *The effect of prolonged physical training on the properties of long bone: a study of Wolff's Law.* J Bone Joint Surg Am, 1981. **63**(5): p. 780-787.
59. Boyle, C. and I.Y. Kim, *Three-dimensional micro-level computational study of Wolff's law via trabecular bone remodeling in the human proximal femur using design space topology optimization.* Journal of Biomechanics, 2011. **44**(5): p. 935-942.
60. Öhman, C., M. Baleani, E. Perilli, E. Dall'Ara, S. Tassani, F. Baruffaldi, and M. Viceconti, *Mechanical testing of cancellous bone from the femoral head: Experimental errors due to off-axis measurements.* Journal of Biomechanics, 2007. **40**(11): p. 2426-2433.
61. Rho, J.-Y., L. Kuhn-Spearing, and P. Zioupos, *Mechanical properties and the hierarchical structure of bone.* Medical Engineering & Physics, 1998. **20**(2): p. 92-102.
62. Reilly, D.T. and A.H. Burstein, *The elastic and ultimate properties of compact bone tissue.* Journal of Biomechanics, 1975. **8**(6): p. 393-405.

63. Halawa, M., A.J.C. Lee, R.S.M. Ling, and S.S. Vangala, *The shear strength of trabecular bone from the femur, and some factors affecting the shear strength of the cement-bone interface.* Archives of Orthopaedic and Trauma Surgery, 1978. **92**(1): p. 19-30.
64. Evans, F.G., H.E. Pedersen, and H.R. Lissner, *The role of tensile stress in the mechanism of femoral fractures.* J Bone Joint Surg Am, 1951. **33-A**(2): p. 485-501.
65. Keller, T.S., Z. Mao, and D.M. Spengler, *Young's modulus, bending strength, and tissue physical properties of human compact bone.* Journal of orthopaedic research : official publication of the Orthopaedic Research Society, 1990. **8**(4): p. 592-603.
66. Ciarelli, M.J., S.A. Goldstein, J.L. Kuhn, D.D. Cody, and M.B. Brown, *Evaluation of orthogonal mechanical properties and density of human trabecular bone from the major metaphyseal regions with materials testing and computed tomography.* Journal of Orthopaedic Research, 1991. **9**(5): p. 674-682.
67. Rho, J.Y., M.C. Hobatho, and R.B. Ashman, *Relations of mechanical properties to density and CT numbers in human bone.* Medical Engineering & Physics, 1995. **17**(5): p. 347-355.
68. McBroom, R.J., W.C. Hayes, W.T. Edwards, R.P. Goldberg, and A.A. White, *Prediction of vertebral body compressive fracture using quantitative computed tomography.* Journal of Bone and Joint Surgery Incorporated, 1985. **67**(8).
69. Kaneko, T.S., J.S. Bell, M.R. Pejcic, J. Tehranzadeh, and J.H. Keyak, *Mechanical properties, density and quantitative CT scan data of trabecular bone with and without metastases.* Journal of Biomechanics, 2004. **37**(4): p. 523-530.
70. Schileo, E., F. Taddei, A. Malandrino, L. Cristofolini, and M. Viceconti, *Subject-specific finite element models can accurately predict strain levels in long bones.* Journal of Biomechanics, 2007. **40**(13): p. 2982-2989.
71. Lotz, J.C., T.N. Gerhart, and W.C. Hayes, *Mechanical Properties of Trabecular Bone from the Proximal Femur: A Quantitative CT Study.* Journal of Computer Assisted Tomography, 1990. **14**(1): p. 107-114.
72. Morgan, E.F., H.H. Bayraktar, and T.M. Keaveny, *Trabecular bone modulus–density relationships depend on anatomic site.* Journal of Biomechanics, 2003. **36**(7): p. 897-904.
73. Snyder, S.M. and E. Schneider, *Estimation of mechanical properties of cortical bone by computed tomography.* Journal of Orthopaedic Research, 1991. **9**(3): p. 422-431.
74. Helgason, B., E. Perilli, E. Schileo, F. Taddei, S. Brynjólfsson, and M. Viceconti, *Mathematical relationships between bone density and mechanical properties: A literature review.* Clinical biomechanics (Bristol, Avon), 2008. **23**(2): p. 135-146.
75. Keller, T.S., *Predicting the compressive mechanical behavior of bone.* Journal of Biomechanics, 1994. **27**(9): p. 1159-1168.
76. Carter, D. and W. Hayes, *Bone compressive strength: the influence of density and strain rate.* Science, 1976. **194**(4270): p. 1174-1176.
77. Les, C.M., J.H. Keyak, S.M. Stover, and K.T. Taylor, *Development and validation of a series of three-dimensional finite element models of the equine metacarpus.* Journal of Biomechanics, 1997. **30**(7): p. 737-742.

78. Zannoni, C., R. Mantovani, and M. Viceconti, *Material properties assignment to finite element models of bone structures: a new method.* Medical Engineering & Physics, 1999. **20**(10): p. 735-740.
79. Gupta, S., F.C.T. van der Helm, J.C. Sterk, F. van Keulen, and B.L. Kaptein, *Development and experimental validation of a three-dimensional finite element model of the human scapula.* Proceedings of the Institution of Mechanical Engineers, Part H: Journal of Engineering in Medicine, 2004. **218**(2): p. 127-142.
80. Helgason, B., F. Taddei, H. Pálsson, E. Schileo, L. Cristofolini, M. Viceconti, and S. Brynjólfsson, *A modified method for assigning material properties to FE models of bones.* Medical Engineering & Physics, 2008. **30**(4): p. 444-453.
81. Grecu D, P.I., Negru M, Tarniţă DN, Ionovici N, Diţă R., *Numerical simulations of the 3D virtual model of the human hip joint, using finite element method.* Rom J Morphol Embryol, 2010. **51**(1): p. 151-5.
82. Taddei, F., E. Schileo, B. Helgason, L. Cristofolini, and M. Viceconti, *The material mapping strategy influences the accuracy of CT-based finite element models of bones: An evaluation against experimental measurements.* Medical Engineering & Physics, 2007. **29**(9): p. 973-979.
83. Taylor, W.R., E. Roland, H. Ploeg, D. Hertig, R. Klabunde, M.D. Warner, M.C. Hobatho, L. Rakotomanana, and S.E. Clift, *Determination of orthotropic bone elastic constants using FEA and modal analysis.* Journal of Biomechanics, 2002. **35**(6): p. 767-773.
84. Zioupos, P. and J.D. Currey, *Changes in the Stiffness, Strength, and Toughness of Human Cortical Bone With Age.* Bone, 1998. **22**(1): p. 57-66.
85. Parkkari, J., P. Kannus, M. Palvanen, A. Natri, J. Vainio, H. Aho, I. Vuori, and M. Järvinen, *Majority of Hip Fractures Occur as a Result of a Fall and Impact on the Greater Trochanter of the Femur: A Prospective Controlled Hip Fracture Study with 206 Consecutive Patients.* Calcified Tissue International, 1999. **65**(3): p. 183-187.
86. Taylor, M.E., K.E. Tanner, M.A.R. Freeman, and A.L. Yettram, *Stress and strain distribution within the intact femur: compression or bending?* Medical Engineering & Physics, 1996. **18**(2): p. 122-131.
87. Kopperdahl, D.L. and T.M. Keaveny, *Yield strain behavior of trabecular bone.* Journal of Biomechanics, 1998. **31**(7): p. 601-608.
88. Bayraktar, H.H., E.F. Morgan, G.L. Niebur, G.E. Morris, E.K. Wong, and T.M. Keaveny, *Comparison of the elastic and yield properties of human femoral trabecular and cortical bone tissue.* Journal of Biomechanics, 2004. **37**(1): p. 27-35.
89. Niebur, G.L., M.J. Feldstein, J.C. Yuen, T.J. Chen, and T.M. Keaveny, *High-resolution finite element models with tissue strength asymmetry accurately predict failure of trabecular bone.* Journal of Biomechanics, 2000. **33**(12): p. 1575-1583.
90. Li, W., J. Kornak, T. Harris, J. Keyak, C. Li, Y. Lu, X. Cheng, and T. Lang, *Identify fracture-critical regions inside the proximal femur using statistical parametric mapping.* Bone, 2009. **44**(4): p. 596-602.
91. Hambli, R., A. Bettamer, and S. Allaoui, *Finite element prediction of proximal femur fracture pattern based on orthotropic behaviour law coupled to quasi-brittle damage.* Medical Engineering & Physics, 2012. **34**(2): p. 202-210.

92. Jungmann, R., M.E. Szabo, G. Schitter, R.Y.-S. Tang, D. Vashishth, P.K. Hansma, and P.J. Thurner, *Local strain and damage mapping in single trabeculae during three-point bending tests.* Journal of the Mechanical Behavior of Biomedical Materials, 2011. **4**(4): p. 523-534.
93. Carter, D.R., W.E. Caler, D.M. Spengler, and V.H. Frankel, *Fatigue Behavior of Adult Cortical Bone: The Influence of Mean Strain and Strain Range.* Acta Orthopaedica, 1981. **52**(5): p. 481-490.
94. Carter, D.R. and W.E. Caler, *A cumulative damage model for bone fracture.* Journal of Orthopaedic Research, 1985. **3**(1): p. 84-90.
95. Gilbert RS, J.H., *Stress Fractures in Military Recruits - A review of twelve years experience.* Military Media, 1966. **131**: p. 716-721.
96. Giladi, M., C. Milgrom, A. Simkin, M. Stein, H. Kashtan, J. Margulies, N. Rand, R. Chisin, R. Steinberg, Z. Aharonson, and a. et, *Stress fractures and tibial bone width. A risk factor.* J Bone Joint Surg Br, 1987. **69-B**(2): p. 326-329.
97. Miller, G.J. and W.W. Purkey Jr, *The geometric properties of paired human tibiae.* Journal of Biomechanics, 1980. **13**(1): p. 1-8.
98. Lee, T., B. Pereira, Y.-S. Chung, H. Oh, J. Choi, D. Lim, and J. Shin, *Novel Approach of Predicting Fracture Load in the Human Proximal Femur Using Non-Invasive QCT Imaging Technique.* Annals of Biomedical Engineering, 2009. **37**(5): p. 966-975.
99. Taddei, F., M. Viceconti, M. Manfrini, and A. Toni, *Mechanical strength of a femoral reconstruction in paediatric oncology: A finite element study.* Proceedings of the Institution of Mechanical Engineers, Part H: Journal of Engineering in Medicine, 2003. **217**(2): p. 111-119.
100. Cristofolini, L. and M. Viceconti, *Mechanical validation of whole bone composite tibia models.* Journal of Biomechanics, 2000. **33**(3): p. 279-288.
101. Ferretti, J.L., R.F. Capozza, and J.R. Zanchetta, *Mechanical validation of a tomographic (pQCT) index for noninvasive estimation of rat femur bending strength.* Bone, 1996. **18**(2): p. 97-102.
102. Viceconti, M., F. Taddei, S. Van Sint Jan, A. Leardini, L. Cristofolini, S. Stea, F. Baruffaldi, and M. Baleani, *Multiscale modelling of the skeleton for the prediction of the risk of fracture.* Clinical Biomechanics, 2008. **23**(7): p. 845-852.
103. Henning, C.E., M.A. Lynch, and K.R. Glick, *An in vivo strain gage study of elongation of the anterior cruciate ligament.* The American Journal of Sports Medicine, 1985. **13**(1): p. 22-26.
104. Lanyon, L.E., W.G.J. Hampson, A.E. Goodship, and J.S. Shah, *Bone Deformation Recorded in vivo from Strain Gauges Attached to the Human Tibial Shaft.* Acta Orthopaedica, 1975. **46**(2): p. 256-268.
105. Trabelsi, N., Z. Yosibash, and C. Milgrom, *Validation of subject-specific automated p-FE analysis of the proximal femur.* Journal of Biomechanics, 2009. **42**(3): p. 234-241.
106. Shahar, R., P. Zaslansky, M. Barak, A.A. Friesem, J.D. Currey, and S. Weiner, *Anisotropic Poisson's ratio and compression modulus of cortical bone determined by speckle interferometry.* Journal of Biomechanics, 2007. **40**(2): p. 252-264.
107. De Lim, F.Z., T. Long Bin, Q. Chenggen, and T. Tong Yan. *Whole-field board strain and displacement characterization during drop impact using a single camera DIC technique*. in *Electronics Packaging Technology Conference, 2009. EPTC '09. 11th*. 2009.

108. *A novel speckle pattern—Adaptive digital image correlation approach with robust strain calculation.* Optics and Lasers in Engineering, 2011.
109. *Improved Newton–Raphson digital image correlation method for full-field displacement and strain calculation.* Applied Optics, 2010. **49**(33): p. 6472.
110. Szabó, M.E., Zekonyte, J., Katsamenis, O.L., Taylor, M and Thurner, P.J. , *Similar damage initiation but different failure behavior in trabecular and cortical bone tissue.* . Journal of the Mechanical Behavior of Biomedical Materials 2011. **4**(8): p. 1787-1796.
111. Zhang, D., D.D. Arola, and J.A. Rouland, *Evaluating The Elastic Modulus Of Bone Using Electronic Speckle Pattern Interferometry.* Experimental Techniques, 2001. **25**(5): p. 32-34.
112. Dalstra, M., R. Huiskes, and L.v. Erning, *Development and Validation of a Three-Dimensional Finite Element Model of the Pelvic Bone.* Journal of Biomechanical Engineering, 1995. **117**(3): p. 272-278.
113. Burstein, A., D. Reilly, and M. Martens, *Aging of bone tissue: mechanical properties.* J Bone Joint Surg Am, 1976. **58**(1): p. 82-86.
114. Evans, F.G., *Mechanical properties and histology of cortical bone from younger and older men.* Anat Rec, 1976. **185**(1): p. 1-11.
115. Neu, C.M., F. Rauch, F. Manz, and E. Schœnau, *Modeling of Cross-sectional Bone Size, Mass and Geometry at the Proximal Radius: A Study of Normal Bone Development Using Peripheral Quantitative Computed Tomography.* Osteoporosis International, 2001. **12**(7): p. 538-547.
116. Boyle, C. and I.Y. Kim, *Comparison of different hip prosthesis shapes considering micro-level bone remodeling and stress-shielding criteria using three-dimensional design space topology optimization.* Journal of Biomechanics, 2011. **44**(9): p. 1722-1728.
117. Viceconti, M., R. Muccini, M. Bernakiewicz, M. Baleani, and L. Cristofolini, *Large-sliding contact elements accurately predict levels of bone–implant micromotion relevant to osseointegration.* Journal of Biomechanics, 2000. **33**(12): p. 1611-1618.
118. Viceconti, M., L. Monti, R. Muccini, M. Bernakiewicz, and A. Toni, *Even a thin layer of soft tissue may compromise the primary stability of cementless hip stems.* Clinical Biomechanics, 2001. **16**(9): p. 765-775.
119. Chamay, A. and P. Tschantz, *Mechanical influences in bone remodeling. Experimental research on Wolff's law.* Journal of Biomechanics, 1972. **5**(2): p. 173-180.
120. Carter, D., *Mechanical loading histories and cortical bone remodeling.* Calcified Tissue International, 1984. **36**(0): p. S19-S24.
121. Wolff, J., *The law of bone remodelling.* Book (ISBN 038716281X) 1986 p. xii, 126 p. .
122. Huiskes, R., *If bone is the answer, then what is the question?* Journal of Anatomy, 2000. **197**(2): p. 145-156.
123. Roux, W., *Beitrage zur Morphologie der funktionnellen Anspassung.* Arch. Anat. Physiol., 1885. **9**: p. 120-158.
124. Duncan, R.L. and C.H. Turner, *Mechanotransduction and the functional response of bone to mechanical strain.* Calcified Tissue International, 1995. **57**(5): p. 344-358.
125. Rubin, C. and L. Lanyon, *Regulation of bone mass by mechanical strain magnitude.* Calcified Tissue International, 1985. **37**(4): p. 411-417.

126. Turner, C.H., M.P. Akhter, D.M. Raab, D.B. Kimmel, and R.R. Recker, *A noninvasive, in vivo model for studying strain adaptive bone modeling.* Bone, 1991. **12**(2): p. 73-79.
127. Lanyon, L., *Functional strain as a determinant for bone remodeling.* Calcified Tissue International, 1984. **36**(0): p. S56-S61.
128. Mayhew, P.M., C.D. Thomas, J.G. Clement, N. Loveridge, T.J. Beck, W. Bonfield, C.J. Burgoyne, and J. Reeve, *Relation between age, femoral neck cortical stability, and hip fracture risk.* The Lancet, 2005. **366**(9480): p. 129-135.
129. van der Linden, J.C., D.H. Birkenhäger-Frenkel, J.A.N. Verhaar, and H. Weinans, *Trabecular bone's mechanical properties are affected by its non-uniform mineral distribution.* Journal of Biomechanics, 2001. **34**(12): p. 1573-1580.
130. Park, H.S., C. Ahn, D.T. Fung, Y. Ren, and L.Q. Zhang, *A knee-specific finite element analysis of the human anterior cruciate ligament impingement against the femoral intercondylar notch.* Journal of Biomechanics, 2010. **43**(10): p. 2039-42.
131. Duda, G.N., M. Heller, J. Albinger, O. Schulz, E. Schneider, and L. Claes, *Influence of muscle forces on femoral strain distribution.* Journal of Biomechanics, 1998. **31**(9): p. 841-846.
132. Lawford, P.V., A.V. Narracott, K. McCormack, J. Bisbal, C. Martin, B. Brook, M. Zachariou, P. Kohl, K. Fletcher, and V. Diaz-Zuccarini, *Virtual physiological human: training challenges.* Philosophical Transactions of the Royal Society A: Mathematical, Physical and Engineering Sciences, 2010. **368**(1921): p. 2841-2851.
133. Crenshaw, T.D., E.R. Peo, Jr., A.J. Lewis, B.D. Moser, and D. Olson, *Influence of Age, Sex and Calcium and Phosphorus Levels on the Mechanical Properties of Various Bones in Swine.* J. Anim Sci., 1981. **52**(6): p. 1319-1329.
134. Nazarian, A., M. Bauernschmitt, C. Eberle, D. Meier, R. Müller, and B.D. Snyder, *Design and validation of a testing system to assess torsional cancellous bone failure in conjunction with time-lapsed micro-computed tomographic imaging.* Journal of Biomechanics, 2008. **41**(16): p. 3496-3501.
135. Shefelbine, S.J., U. Simon, L. Claes, A. Gold, Y. Gabet, I. Bab, R. Müller, and P. Augat, *Prediction of fracture callus mechanical properties using micro-CT images and voxel-based finite element analysis.* Bone, 2005. **36**(3): p. 480-488.
136. Burstein, A.H. and V.H. Frankel, *A standard test for laboratory animal bone.* Journal of Biomechanics, 1971. **4**(2): p. 155-156, IN7, 157-158.
137. Lind, P.M., L. Lind, S. Larsson, and J. Örberg, *Torsional testing and peripheral quantitative computed tomography in rat humerus.* Bone, 2001. **29**(3): p. 265-270.
138. Sammarco, G.J., A.H. Burstein, W.L. Davis, and V.H. Frankel, *The biomechanics of torsional fractures: The effect of loading on ultimate properties.* Journal of Biomechanics, 1971. **4**(2): p. 113-117.
139. Taylor, D., P. O'Reilly, L. Vallet, and T.C. Lee, *The fatigue strength of compact bone in torsion.* Journal of Biomechanics, 2003. **36**(8): p. 1103-1109.
140. Saunders, M.M., R.B. Burger, B. Kalantari, A.D. Nichols, and C. Witman, *Development of a cost-effective torsional unit for rodent long bone assessment.* Medical Engineering & Physics, 2010. **32**(7): p. 802-807.

141. Carter, D.R., E.E. Shimaoka, W.H. Harris, E.I. Gates, W.E. Caler, and J.C. McCarthy, *Changes in long-bone structural properties during the first 8 weeks of plate implantation.* Journal of Orthopaedic Research, 1984. **2**(1): p. 80-89.

142. Crenshaw, T.D., E.R. Peo, Jr., A.J. Lewis, and B.D. Moser, *Bone Strength as a Trait for Assessing Mineralization in Swine: a Critical Review of Techniques Involved.* J. Anim Sci., 1981. **53**(3): p. 827-835.

143. Les, C.M., J.H. Keyak, S.M. Stover, K.T. Taylor, and A.J. Kaneps, *Estimation of material properties in the equine metacarpus with use of quantitative computed tomography.* Journal of Orthopaedic Research, 1994. **12**(6): p. 822-833.

144. Keyak, J.H., I.Y. Lee, and H.B. Skinner, *Correlations between orthogonal mechanical properties and density of trabecular bone: Use of different densitometric measures.* Journal of Biomedical Materials Research, 1994. **28**(11): p. 1329-1336.

145. Seil, R., S. Rupp, P.W. Krauss, A. Benz, and D.M. Kohn, *Comparison of Initial Fixation Strength Between Biodegradable and Metallic Interference Screws and a Press-Fit Fixation Technique in a Porcine Model.* The American Journal of Sports Medicine, 1998. **26**(6): p. 815-819.

146. Southern EP, O.T., Panjabi MM, Duranceau JS., *Cervical spine injury patterns in three modes of high-speed trauma: a biomechanical porcine model.* J Spinal Disord., 1990. **3**: p. 316-28.

147. Bonney, H., B.J. Colston, and A.M. Goodman, *Regional variation in the mechanical properties of cortical bone from the porcine femur.* Medical Engineering & Physics, 2011. **33**(4): p. 513-520.

148. Baumer, T.G., B.J. Powell, T.W. Fenton, and R.C. Haut, *Age Dependent Mechanical Properties of the Infant Porcine Parietal Bone and a Correlation to the Human.* Journal of Biomechanical Engineering, 2009. **131**(11): p. 111006.

149. Mosekilde, L., J. Kragstrup, and A. Richards, *Compressive strength, ash weight, and volume of vertebral trabecular bone in experimental fluorosis in pigs.* Calcified Tissue International, 1987. **40**(6): p. 318-322.

150. Boot, A.M., M.A.J. de Ridder, H.A.P. Pols, E.P. Krenning, and S.M.P.F. de Muinck Keizer-Schrama, *Bone Mineral Density in Children and Adolescents: Relation to Puberty, Calcium Intake, and Physical Activity.* Journal of Clinical Endocrinology & Metabolism, 1997. **82**(1): p. 57-62.

151. GRIMSTON, S.K., N.D. WILLOWS, and D.A. HANLEY, *Mechanical loading regime and its relationship to bone mineral density in children.* Medicine & Science in Sports & Exercise, 1993. **25**(11): p. 1203-1210.

152. Leonard, M. and B. Zemel, *Assessment of bone mineralization in children and adolescents.* Clinical Reviews in Bone and Mineral Metabolism, 2004. **2**(1): p. 3-18.

153. Neu, C.M., F. Manz, F. Rauch, A. Merkel, and E. Schoenau, *Bone densities and bone size at the distal radius in healthy children and adolescents: a study using peripheral quantitative computed tomography.* Bone, 2001. **28**(2): p. 227-232.

154. Neu, C.P., R.D. McGovern, and J.J. Crisco, *Kinematic Accuracy of Three Surface Registration Methods in a Three-Dimensional Wrist Bone Study.* Journal of Biomechanical Engineering, 2000. **122**(5): p. 528-533.

155. Moyer-Mileur, L.J., J.L. Quick, and M.A. Murray, *Peripheral Quantitative Computed Tomography of the Tibia: Pediatric Reference Values.* Journal of Clinical Densitometry, 2008. **11**(2): p. 283-294.

156. Rauch, F., C. Neu, F. Manz, and E. Schoenau, *The Development of Metaphyseal Cortex—Implications for Distal Radius Fractures During Growth.* Journal of Bone and Mineral Research, 2001. **16**(8): p. 1547-1555.

157. Schoenau, E., C.M. Neu, F. Rauch, and F. Manz, *The Development of Bone Strength at the Proximal Radius during Childhood and Adolescence.* Journal of Clinical Endocrinology & Metabolism, 2001. **86**(2): p. 613-618.

158. Schoenau, E., C.M. Neu, E. Mokov, G. Wassmer, and F. Manz, *Influence of Puberty on Muscle Area and Cortical Bone Area of the Forearm in Boys and Girls.* Journal of Clinical Endocrinology & Metabolism, 2000. **85**(3): p. 1095-1098.

159. Carty, H. and A. Pierce, *Non-accidental injury: a retrospective analysis of a large cohort.* European Radiology, 2002. **12**(12): p. 2919-2925.

160. Bertocci, G.E., M.C. Pierce, E. Deemer, F. Aguel, J.E. Janosky, and E. Vogeley, *Influence of fall height and impact surface on biomechanics of feet-first free falls in children.* Injury, 2004. **35**(4): p. 417-424.

161. Thompson, A.K., G. Bertocci, and M.C. Pierce, *Assessment of Head Injury Risk Associated With Feet-First Free Falls in 12-Month-Old Children Using an Anthropomorphic Test Device.* The Journal of Trauma and Acute Care Surgery, 2009. **66**(4): p. 1019-1029 10.1097/TA.0b013e31817dac8b.

162. Wang, X., R.A. Bank, J.M. Tekoppele, and C.M. Agrawal, *The role of collagen in determining bone mechanical properties.* Journal of Orthopaedic Research, 2001. **19**(6): p. 1021-1026.

163. Kozloff, K.M., A. Carden, C. Bergwitz, A. Forlino, T.E. Uveges, M.D. Morris, J.C. Marini, and S.A. Goldstein, *Brittle IV Mouse Model for Osteogenesis Imperfecta IV Demonstrates Postpubertal Adaptations to Improve Whole Bone Strength.* Journal of Bone and Mineral Research, 2004. **19**(4): p. 614-622.

164. Bernakiewicz, M. and M. Viceconti, *The role of parameter identification in finite element contact analyses with reference to orthopaedic biomechanics applications.* Journal of Biomechanics, 2002. **35**(1): p. 61-67.

165. Edgerton, B.C., K.-N. An, and B.F. Morrey, *Torsional strength reduction due to cortical defects in bone.* Journal of Orthopaedic Research, 1990. **8**(6): p. 851-855.

166. Ho, K., J. Gilbody, T. Jameson, and A. Miles, *The effect of 4 mm bicortical drill hole defect on bone strength in a pig femur model.* Archives of Orthopaedic and Trauma Surgery, 2010. **130**(6): p. 797-802.

167. Taddei, F., R. Stagni, A. Cappello, M. Manfrini, U. Albisinni, and M. Viceconti, *Kinematic study of a reconstructed hip in paediatric oncology.* Medical and Biological Engineering and Computing, 2005. **43**(1): p. 102-106.

168. Morega, A.M., A. Dobre, M. Morega, and D. Mocanu, *Computational Modeling of Arterial Blood Flow*

International Conference on Advancements of Medicine and Health Care through Technology, S. Vlad, R.V. Ciupa, and A.I. Nicu, Editors. 2009, Springer Berlin Heidelberg. p. 373-378.

169. Sreeranganathan, A., A.M. Gokhale, and P. Young, *Realistic micromechanical modeling of discontinuously reinforced composites.* Computational Materials Science, 2010. **49**(2): p. 407-413.
170. Rayfield, E.J., A.C. Milner, V.B. Xuan, and P.G. Young, *Functional Morphology Of Spinsaur 'Crocodile-Mimic' Dinosaurs.* Journal of Vertebrate Paleontology, 2007. **27**(4): p. 892-901.
171. Healthcare, G., A division of General Electric Company, 2012.
172. Bordelon, R.L., *Orthotics, shoes, and braces.* Orthopedic Clinics of North America, 1989. **Oct;20(4)**: p. 751-7.
173. Perić, M., R. Kessler, and G. Scheuerer, *Comparison of finite-volume numerical methods with staggered and colocated grids.* Computers & Fluids, 1988. **16**(4): p. 389-403.
174. Ramon, C., *Comparison of some finite element methods for solving the diffusion-convection-reaction equation.* Computer Methods in Applied Mechanics and Engineering, 1998. **156**(1-4): p. 185-210.
175. Burnett, D.S., *Finite Element Analysis: from concepts to applications.* Addison-Wesley Pub. Co., 1987: p. 844.
176. Zienkiewicz, O.C. and J.Z. Zhu, *A simple error estimator and adaptive procedure for practical engineerng analysis.* International Journal for Numerical Methods in Engineering, 1987. **24**(2): p. 337-357.
177. Pointer, J., *Understanding Accuracy and Discretization Error in an FEA Model.* Ansys User's Conference, 2004.
178. Rossi, M.A., G. Stebbins, C. Murphy, D. Greene, S. Brinker, D. Sarcu, A. Tenharmsel, T. Stoub, M.A. Stein, T.J. Hoeppner, R.W. Byrne, M.E. Moseley, R.A. Bammer, S. Bild, J. Dennis, N. Arnett, A. Balabanov, D. Bergen, A.M. Kanner, and M.C. Smith, *Predicting white matter targets for direct neurostimulation therapy.* Epilepsy Research, 2010. **91**(2–3): p. 176-186.
179. Linde, F., I. Hvid, and F. Madsen, *The effect of specimen geometry on the mechanical behaviour of trabecular bone specimens.* Journal of Biomechanics, 1992. **25**(4): p. 359-368.
180. Taylor, D., P. O'Reilly, L. Vallet, and T.C. Lee, *The fatigue strength of compact bone in torsion.* Journal of Biomechanics, 2003. **36**(8): p. 1103-1109.
181. Currey, J.D., *Mechanical properties of bone tissues with greatly differing functions.* Journal of Biomechanics, 1979. **12**(4): p. 313-319.
182. *An improved method for the automatic mapping of computed tomography numbers onto finite element models.* Medical Engineering and Physics, 2004. **26**: p. 61-69.
183. Rho, J.Y., M.C. Hobatho, and R.B. Ashman, *Relations of mechanical properties to density and CT numbers in human bone.* Medical Engineering & Physics, 1995. **17**(5): p. 347-355.
184. Ford, C.M. and T.M. Keaveny, *The dependence of shear failure properties of trabecular bone on apparent density and trabecular orientation.* Journal of Biomechanics, 1996. **29**(10): p. 1309-1317.
185. Carter, D.R. and W.C. Hayes, *The compressive behavior of bone as a two-phase porous structure.* The Journal of bone and joint surgery. American volume, 1977. **59**(7): p. 954-962.
186. Wirtz, D.C., N. Schiffers, T. Pandorf, K. Radermacher, D. Weichert, and R. Forst, *Critical evaluation of known bone material properties to realize anisotropic FE-simulation of the proximal femur.* Journal of Biomechanics, 2000. **33**(10): p. 1325-1330.

187. Willinger, R., H.-S. Kang, and B. Diaw, *Three-Dimensional Human Head Finite-Element Model Validation Against Two Experimental Impacts.* Annals of Biomedical Engineering, 1999. **27**(3): p. 403-410.

188. Evans, F.G., *Factors affecting the mechanical properties of bone.* Bull N Y Acad Med, 1973. **49**(9): p. 751-64.

189. Arangio, G.A., D. Xiao, and E.P. Salathe, *Biomechanical study of stress in the fifth metatarsal.* 1997.

190. Bunch, T.S.G.a.R.P., *A mechanical model of metatarsal stress fracture during distance running.* 1989.

191. Stokes A, H.W.C., Stott J R, *Forces acting on the metatarsals during normal walking.* Journal of Anatomy, 1979. **J Anat. 1979 October; 129(Pt 3): 579–590.**

192. Lopez-Pedrosa, M., B.P. Wynne, and W.M. Rainforth, *An analysis of microband orientation in a commercial purity aluminium alloy subjected to forward and reverse torsion using Electron Backscatter Diffraction (EBSD).* Journal of Microscopy, 2006. **222**(2): p. 97-104.

193. Poths, R., B. Wynne, W. Rainforth, J. Beynon, G. Angella, and S. Semiatin, *Effect of strain reversal on the dynamic spheroidization of Ti-6Al-4V during hot deformation.* Metallurgical and Materials Transactions A, 2004. **35**(9): p. 2993-3001.

194. Taddei, F., A. Pancanti, and M. Viceconti, *An improved method for the automatic mapping of computed tomography numbers onto finite element models.* Medical Engineering & Physics, 2004. **26**(1): p. 61-69.

195. LIBRARY, S.I.U.S.P., *Human femur bone.*

196. Rice, J.C., S.C. Cowin, and J.A. Bowman, *On the dependence of the elasticity and strength of cancellous bone on apparent density.* Journal of Biomechanics, 1988. **21**(2): p. 155-168.

197. Linde, F., P. Nørgaard, I. Hvid, A. Odgaard, and K. Søballe, *Mechanical properties of trabecular bone. Dependency on strain rate.* Journal of Biomechanics, 1991. **24**(9): p. 803-809.

198. Thompson, M.S., H. Schell, J. Lienau, and G.N. Duda, *Digital image correlation: A technique for determining local mechanical conditions within early bone callus.* Medical Engineering & Physics, 2007. **29**(7): p. 820-823.

199. Yang, G.Y., V.J. Bailey, G. Lin, W.C. Tang, and J.H. Keyak. *Design of microfabricated strain gauge array to monitor bone deformation in vitro and in vivo*. in *Bioinformatics and Bioengineering, 2004. BIBE 2004. Proceedings. Fourth IEEE Symposium on*. 2004.

200. Lang, S.B., *Ultrasonic Method for Measuring Elastic Coefficients of Bone and Results on Fresh and Dried Bovine Bones.* Biomedical Engineering, IEEE Transactions on, 1970. **BME-17**(2): p. 101-105.

201. Park, J.B., *Biomaterials science and engineering.* Book (ISBN 0306416891), 1984: p. xv, 459 p.

202. Rho, J.Y., R.B. Ashman, and C.H. Turner, *Young's modulus of trabecular and cortical bone material: Ultrasonic and microtensile measurements.* Journal of Biomechanics, 1993. **26**(2): p. 111-119.

203. Ouyang, J., G.T. Yang, W.Z. Wu, Q.A. Zhu, and S.Z. Zhong, *Biomechanical characteristics of human trabecular bone.* Clinical Biomechanics, 1997. **12**(7–8): p. 522-524.

204. Reilly, G.C. and J.D. Currey, *The effects of damage and microcracking on the impact strength of bone.* Journal of Biomechanics, 2000. **33**(3): p. 337-343.

205. Reilly, G.C., *Observations of microdamage around osteocyte lacunae in bone.* Journal of Biomechanics, 2000. **33**(9): p. 1131-1134.

206. Ota, T., I. Yamamoto, and R. Morita, *Fracture simulation of the femoral bone using the finite-element method: How a fracture initiates and proceeds.* Journal of Bone and Mineral Metabolism, 1999. **17**(2): p. 108-112.

207. Peleg, E., M. Beek, L. Joskowicz, M. Liebergall, R. Mosheiff, and C. Whyne, *Patient specific quantitative analysis of fracture fixation in the proximal femur implementing principal strain ratios. Method and experimental validation.* Journal of Biomechanics, 2010. **43**(14): p. 2684-2688.

208. Turner, C.H. and S.C. Cowin, *Errors induced by off-axis measurement of the elastic properties of bone.* Journal of biomechanical engineering, 1988. **110**(3): p. 213-215.

209. Taddei, F., E. Schileo, B. Helgason, L. Cristofolini, and M. Viceconti, *The material mapping strategy influences the accuracy of CT-based finite element models of bones: An evaluation against experimental measurements.* Medical Engineering & Physics, 2007. **29**(9): p. 973-979.

210. Lim Fat, D., J. Kennedy, R. Galvin, F. O'Brien, F. Mc Grath, and H. Mullett, *The Hounsfield value for cortical bone geometry in the proximal humerus—an in vitro study.* Skeletal Radiology, 2012. **41**(5): p. 557-568.

211. Lotz, J.C., E.J. Cheal, and W.C. Hayes, *Fracture prediction for the proximal femur using finite element models: Part II--Nonlinear analysis.* Journal of Biomechanical Engineering, 1991. **113**(4): p. 361-5.

212. Keyak, J.H., T.S. Kaneko, J. Tehranzadeh, and H.B. Skinner, *Predicting Proximal Femoral Strength Using Structural Engineering Models.* Clinical Orthopaedics and Related Research, 2005. **437**: p. 219-228 10.1097/01.blo.0000164400.37905.22.

213. Keyak, J.H., S.A. Rossi, K.A. Jones, and H.B. Skinner, *Prediction of femoral fracture load using automated finite element modeling.* Journal of Biomechanics, 1997. **31**(2): p. 125-133.

11 Appendix A1

Appendix A1 contains data plots and images from the main bulk of the thesis. Most are referenced from within the text. Those that are not are organized to correspond with the appropriate chapter.

From Chapter 3:

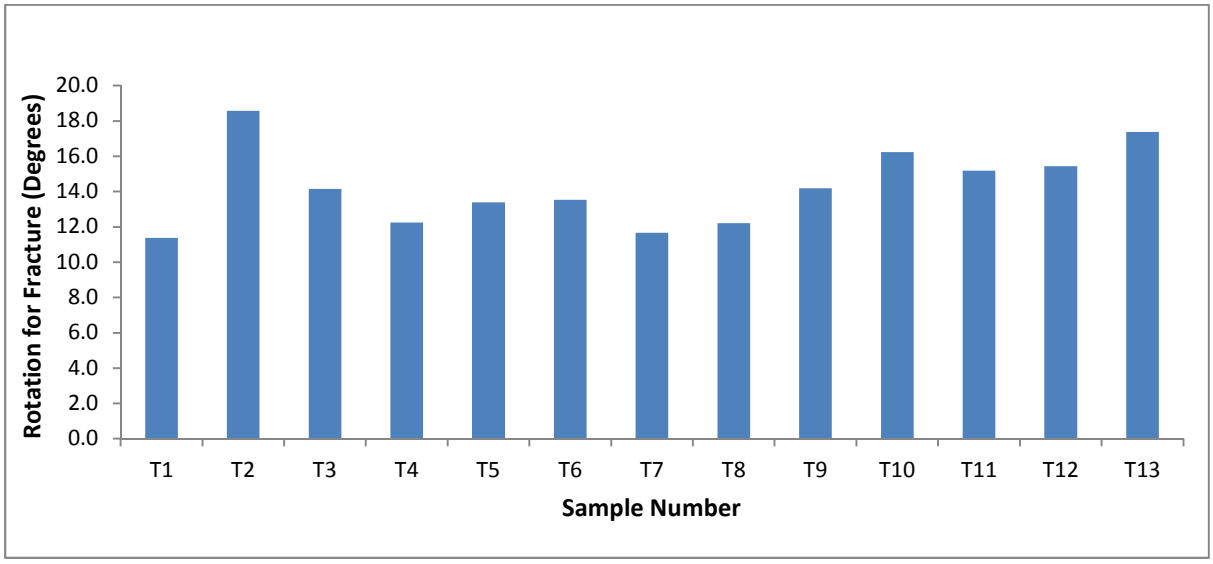

Figure A1.1 The maximum rotation of each 13 samples tested to fracture within the laboratory (from Chapter 3).

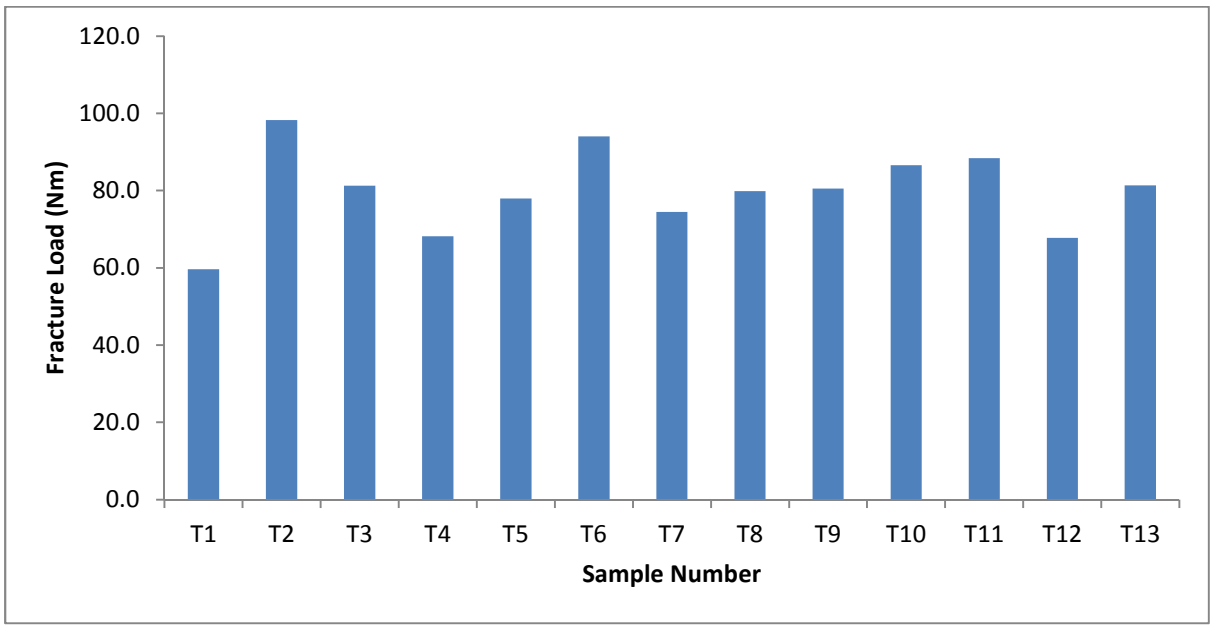

Figure A1.2 The maximum permitted torque (Nm) of each 13 samples tested to fracture within the laboratory (from Chapter 3).

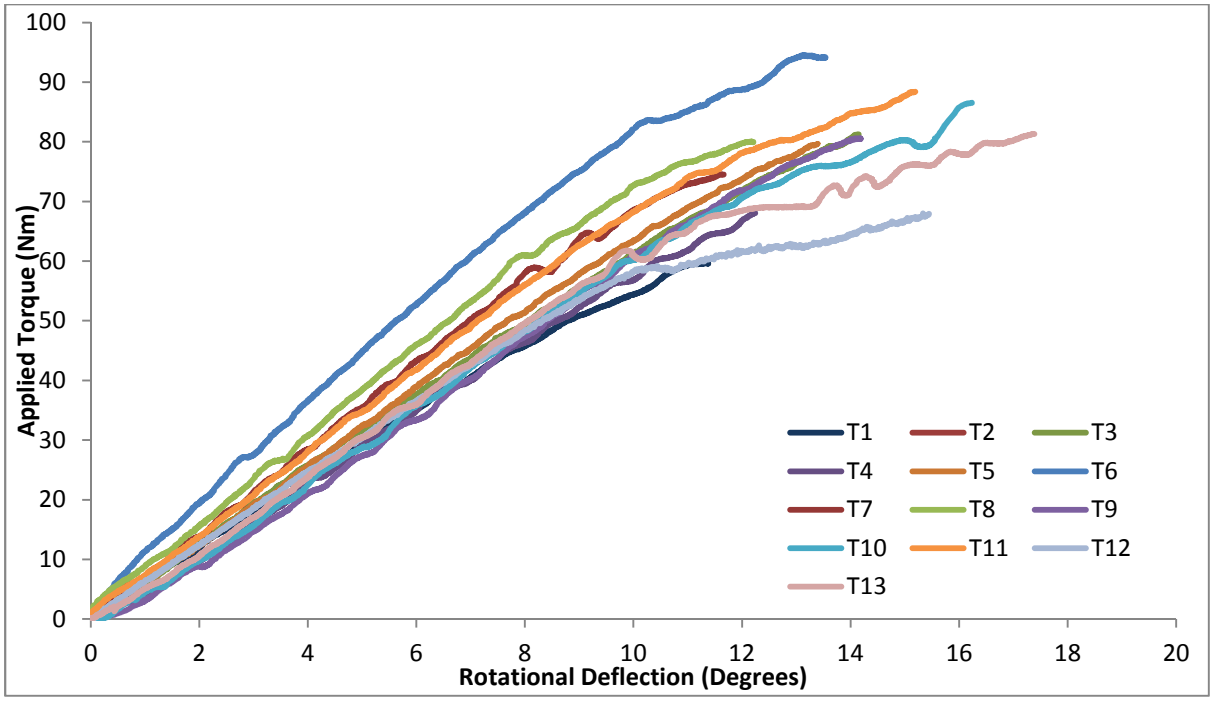

Figure A1.3 The load/deflection plots for the eleven remaining samples tested to fracture within the laboratory (from Chapter 3).

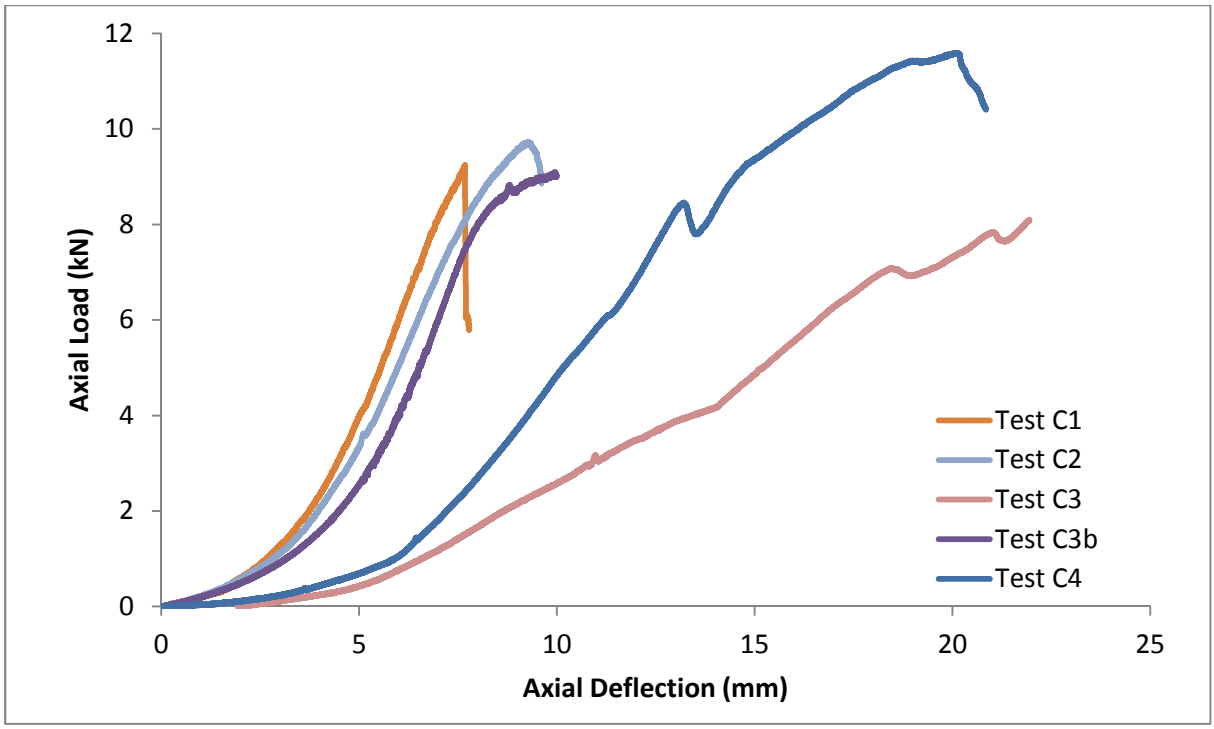

Figure A1.4 The load/deflection plots for the five samples tested to fracture in compression. The failed tests of C4 and C3 can clearly be seen. (from Chapter 3).

Test Number	Maximum Rotation (Degrees)	Max Torque (Nm)	R^2 Value (linear strain behaviour)	P significance (linear strain behaviour)
T1	11.4	59.7	0.997	< 0.001
T2	18.6	98.2	0.998	< 0.001
T3	14.1	81.3	0.997	< 0.001
T4	12.2	68.1	0.999	< 0.001
T5	13.4	77.9	0.990	< 0.001
T6	13.5	94.1	0.986	< 0.001
T7	11.7	74.5	0.997	< 0.001
T8	13.2	79.9	0.994	< 0.001
T9	14.2	80.6	0.973	< 0.001
T10	16.9	86.6	0.991	< 0.001
T11	15.2	88.4	0.990	< 0.001
T12	15.4	73.0	0.967	< 0.001
T13	18.4	81.3	0.977	< 0.001

Table. A1.5. Table details the results and statistical significance of fracture testing in torsion (from Chapter 3).

From Chapter 6:

Test Number	Zeroed	T2 5	T2 10	T3 20	T4 30	T5 40
Gauge Number	Reading (Microstrain)	Reading (Microstrain)	Reading (Microstrain)	Reading (Microstrain)	Reading (Microstrain)	Reading (Microstrain)
Torque (Nm)	0	5	10	20	30	40
Gauge 1	0	176	352	734	1161	1406
Gauge 2	0	20	45	70	115	145
Gauge 3	0	-3	-6	-29	-52	-65
Gauge 4	0	-185	-425	-849	-1221	-1681
Gauge 5	0	-67	-131	-260	-373	-526
Gauge 6	0	34	68	143	203	307
Gauge 7	0	-216	-410	-860	-1151	-1652
Gauge 8	0	19	35	95	179	313
Gauge 9	0	15	26	43	67	103

Table. A1.6. Table details the strain gauge results from sub-maximal testing of sample SM1 in torsion (from Chapter 6).

Test Number	Zeroed	T2 5	T2 10	T3 20	T4 30	T5 40
Gauge Number	Reading (Microstrain)	Reading (Microstrain)	Reading (Microstrain)	Reading (Microstrain)	Reading (Microstrain)	Reading (Microstrain)
Torque (Nm)	0	5	10	20	30	40
Gauge 1	0	14	30	8	24	6
Gauge 2	0	170	357	693	1001	1326
Gauge 3	0	38	73	195	265	316
Gauge 4	0	6	11	30	55	78
Gauge 5	0	133	305	580	835	1115
Gauge 6	0	-5	-11	-60	-135	-170
Gauge 7	0	-69	-138	-75	-86	-193
Gauge 8	0	86	163	315	482	630
Gauge 9	0	4	8	8	8	95

Table. A1.7. Table details the strain gauge results from sub-maximal testing of sample SM2 in torsion (from Chapter 6).

Test Number	Zeroed	C2 0.5	C3 1	C4 1.5	C5 2
Gauge Number	Reading (Microstrain)	Reading (Microstrain)	Reading (Microstrain)	Reading (Microstrain)	Reading (Microstrain)
Axial Load (kN)	0	0.5	1	1.5	2
Gauge 1	0	-3	-6	-21	-38
Gauge 2	0	-120	-230	-301	-393
Gauge 3	0	74	134	189	246
Gauge 4	0	-146	-313	-443	-589
Gauge 5	0	-305	-574	-795	-1021
Gauge 6	0	55	101	139	186
Gauge 7	0	6	-35	-66	-107
Gauge 8	0	-102	-325	-611	-848
Gauge 9	0	60	152	271	372

Table. A1.8. Table details the strain gauge results from sub-maximal testing of sample SM1 in compression (from Chapter 6).

Test Number	Zeroed	TC1	TC2	TC3
Gauge Number	Reading (Microstrain)	Reading (Microstrain)	Reading (Microstrain)	Reading (Microstrain)
Torque (Nm)	0	0	13.9	23.2
Axial Load (kN)	0	1.26	0.795	1.45
Gauge 1	0	44	118	345
Gauge 2	0	34	-660	-1555
Gauge 3	0	20	-72	-290
Gauge 4	0	265	-124	-330
Gauge 5	0	24	-362	-850
Gauge 6	0	-340	-140	-170
Gauge 7	0	130	22	-10
Gauge 8	0	-300	-1030	-1580
Gauge 9	0	-540	-814	-996

Table. A1.9. Table details the strain gauge results from sub-maximal testing of sample SM2 in compression (from Chapter 6).

Test Number	Zeroed	C2 0.5	C3 1	C4 1.5	C5 2
Gauge Number	Reading (Microstrain)	Reading (Microstrain)	Reading (Microstrain)	Reading (Microstrain)	Reading (Microstrain)
Axial Load (kN)	0	0.5	1	1.5	2
Gauge 1	0	29	30	57	97
Gauge 2	0	53	85	126	162
Gauge 3	0	59	80	86	80
Gauge 4	0	65	130	186	225
Gauge 5	0	-30	-103	-152	-185
Gauge 6	0	-107	-197	-305	-410
Gauge 7	0	55	209	230	280
Gauge 8	0	-135	-250	-340	-390
Gauge 9	0	-216	-420	-620	-785

Table. A1.10. Table details the strain gauge results from sub-maximal testing of sample SM3 in combined compression and torsion (from Chapter 6).

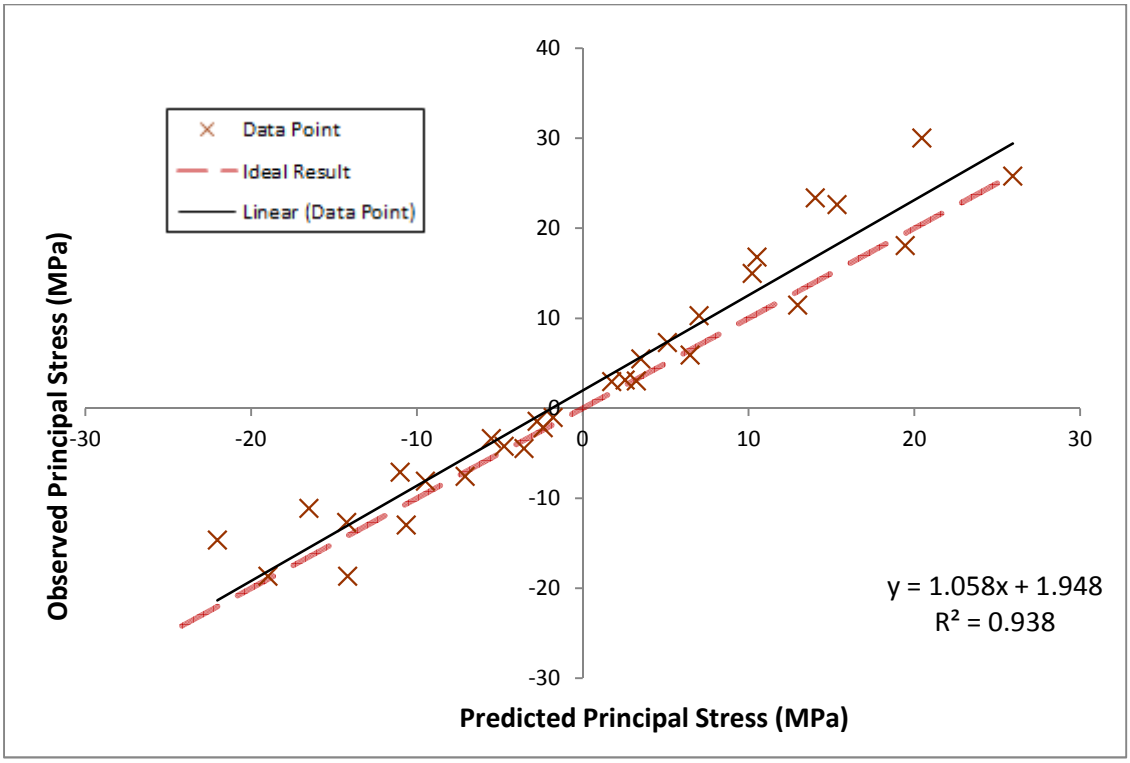

Figure A1.11 The predicted vs. observed principal stress plot for sample SM2 in torsion (from Chapter 6).

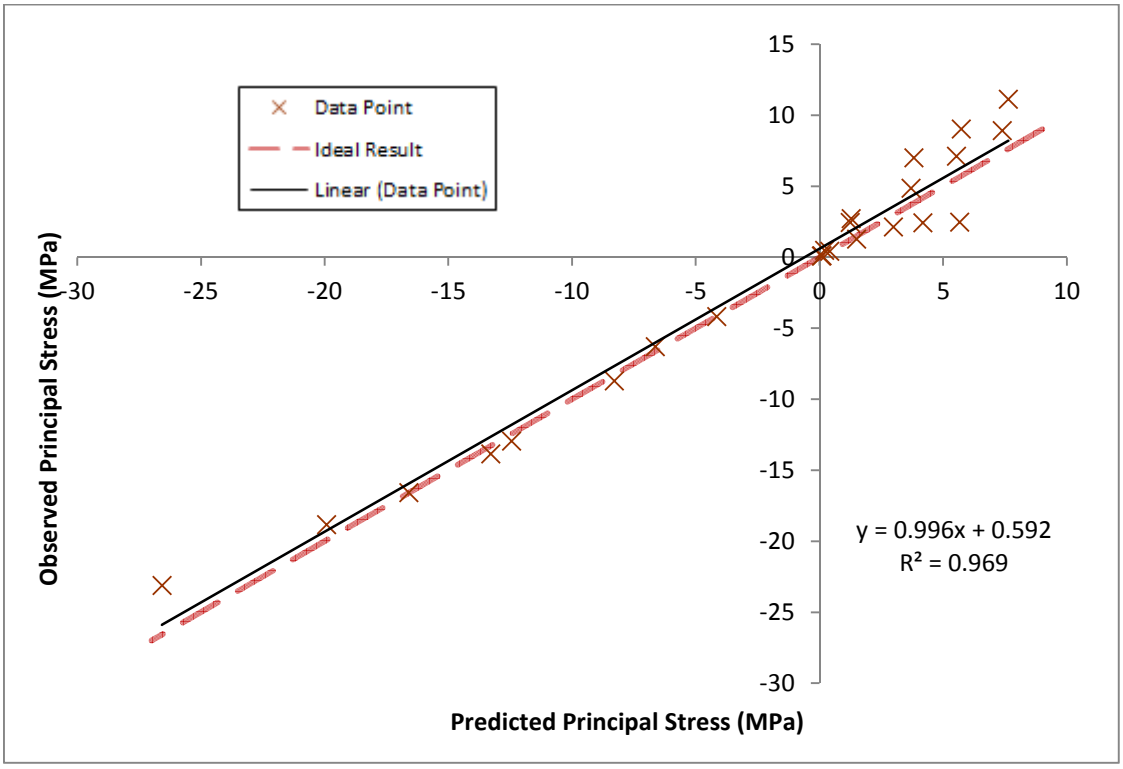

Figure A1.12 The predicted vs. observed principal stress plot for sample SM2 in compression (from Ch.6).

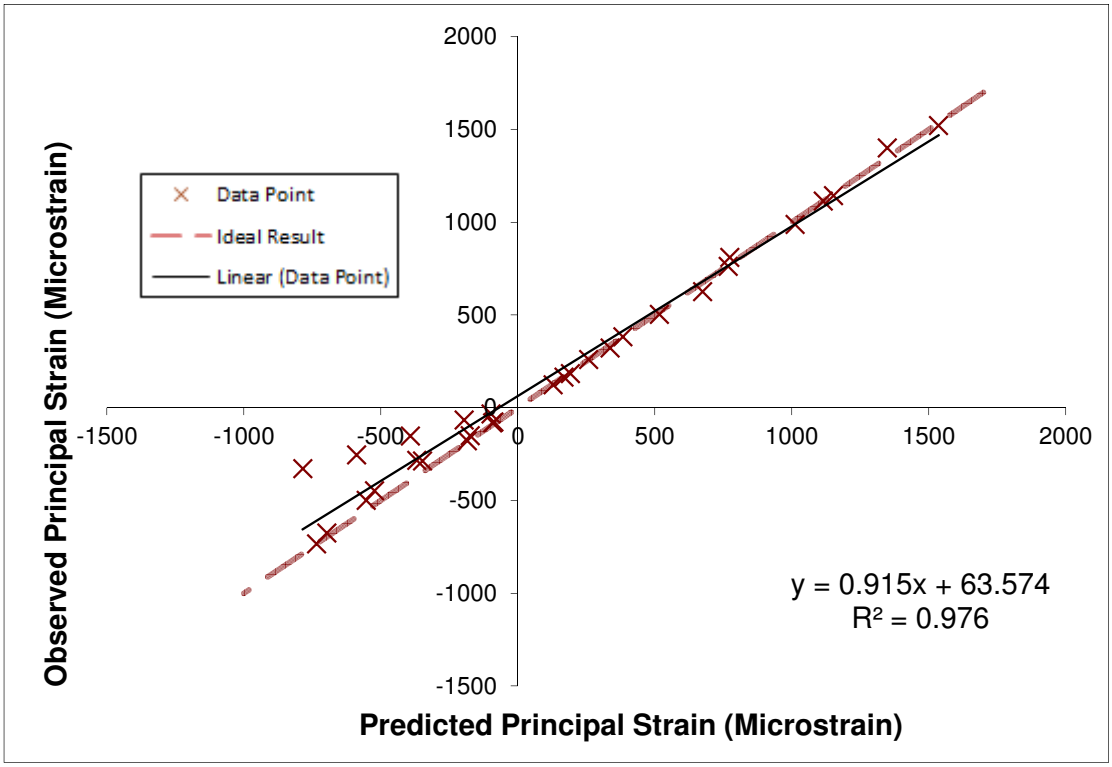

Figure A1.13 The predicted vs. observed principal strain plot for sample SM2 in torsion (from Ch.6)

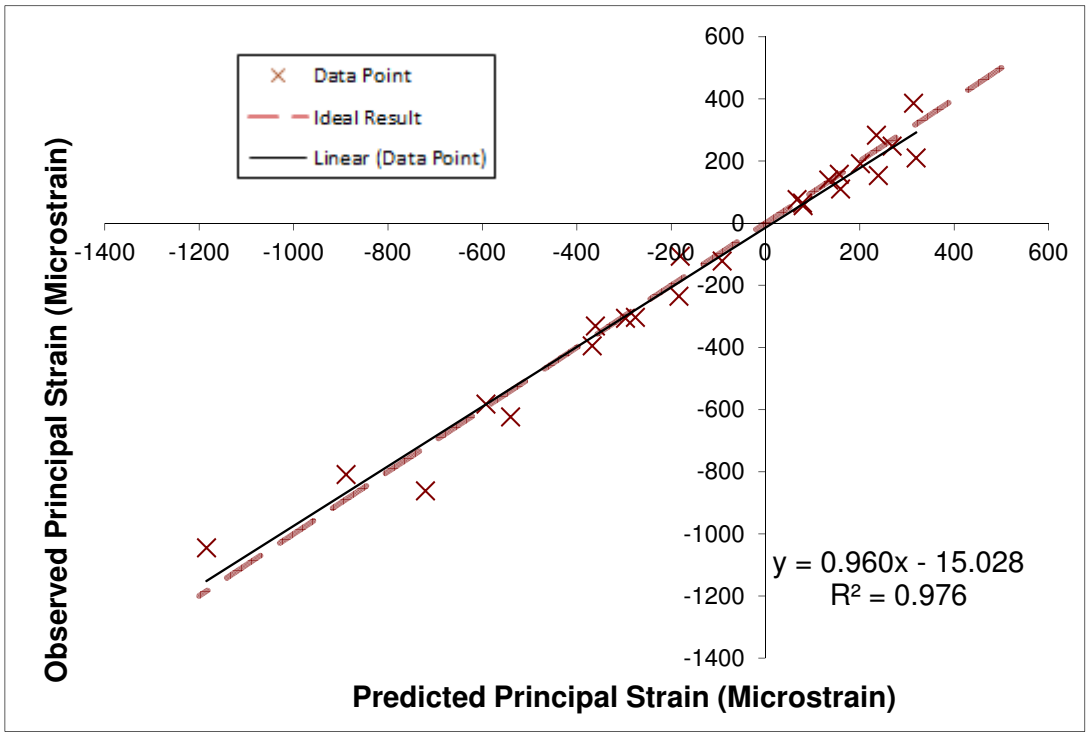

Figure A1.14 The predicted vs. observed principal strain plot for sample SM1 in compression (from Ch.6)

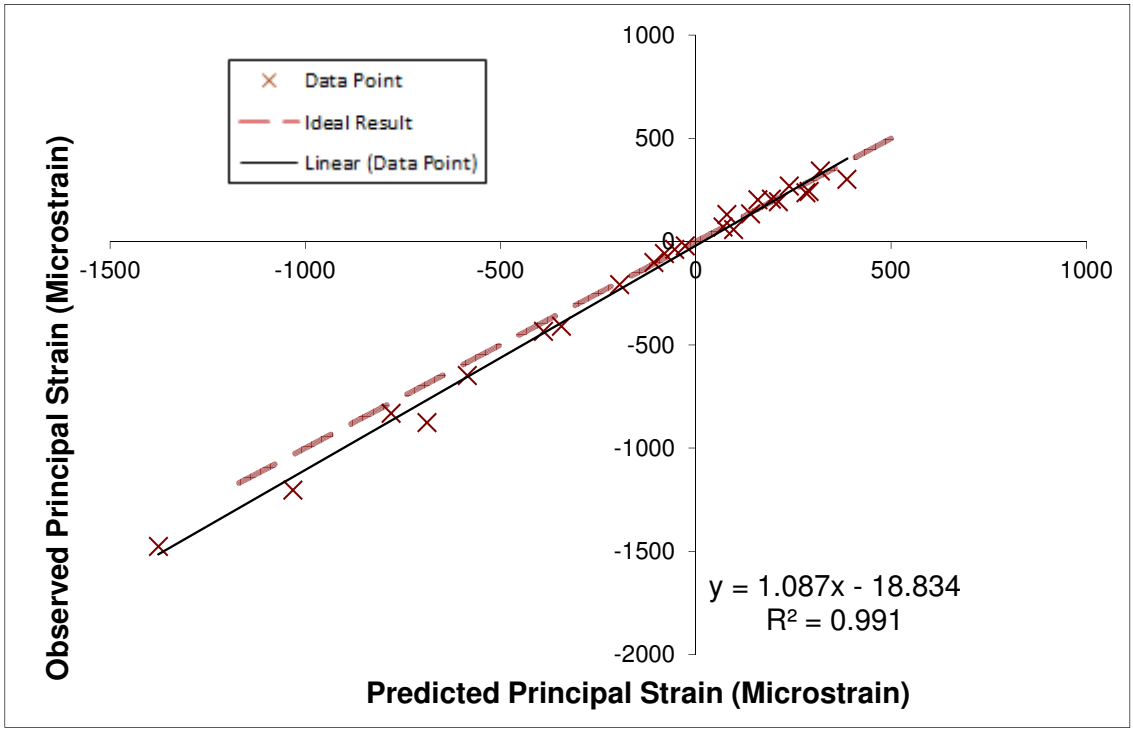

Figure A1.15 The predicted vs. observed principal strain plot for sample SM2 in compression (from Ch.6)

From Chapter 7:

AP				
Orientation	1st Principle Strain	Change from A	Change from A %	% Per Degree
0	0.008052	0.0000	0.0	0.00
-1	0.008103	0.0001	0.6	0.63
-2	0.007512	-0.0006	-7.3	3.67
-4	0.005946	-0.0016	-19.4	4.86
-6	0.007101	0.0012	14.3	2.39
-10	0.006771	-0.0003	-4.1	0.41
-15	0.005695	-0.0011	-13.4	0.89

Table. A1.16. Table details the 1st principal strain results from alignment testing in the anterior-posterior alignment. (Chapter 7).

ML				
Orientation	1st Principle Strain	Change from A	Change from A %	% Per Degree
0	0.008052	0.0000	0.0	0.00
1	0.007399	-0.0007	-8.1	8.11
2	0.006562	-0.0008	-10.4	-5.20
4	0.006604	0.0000	0.5	0.13
6	0.007023	0.0004	5.2	0.87
10	0.006252	-0.0008	-9.6	0.96
15	0.006872	0.0006	7.7	0.51

Table. A1.17. Table details the 1st principal strain results from alignment testing in the medial-lateral alignment. (Chapter 7).

MLAP				
Orientation	1st Principle Strain	Change from A	Change from A %	% Per Degree
0	0.008052	0.0000	0.0	0.00
1+1	0.007623	-0.0004	-5.3	-5.33
2+2	0.007245	-0.0004	-4.7	2.35
4+4	0.007955	0.0007	8.8	2.20
6+6	0.007612	-0.0003	-4.3	0.71
10+10	0.00732	-0.0003	-3.6	0.36
15+15	0.006232	-0.0011	-13.5	0.90

Table. A1.18. Table details the 1st principal strain results from alignment testing in the both the medial-lateral and anterior-posterior alignment. (Chapter 7).

Gauge/Test Number	Brief Description of Load Amendment	Stress Result (MPa)		Ratio (FE/SG)
G 1-9	Vertical SPREAD + 40% X	FE	SG	
G1	Max	0.42	1.69	0.25
G1	Min	-2.99	-1.48	2.02
G2	Max	1.02	2.34	0.44
G2	Min	-5.98	-5.04	1.19
G3	Max	0.59	1.05	0.56
G3	Min	-1.38	-2.18	0.63
20	Vertical SPREAD + 35% X +5% Y	FE	SG	
G1	Max	0.67	1.69	0.40
G1	Min	-2.61	-1.48	1.77
G2	Max	0.99	2.34	0.42
G2	Min	-5.08	-5.04	1.01
G3	Max	0.41	1.05	0.39
G3	Min	-3.72	-2.18	1.70
21	Vertical SPREAD + 30% X +5% Y	FE	SG	
G1	Max	0.71	1.69	0.42
G1	Min	-2.10	-1.48	1.42
G2	Max	1.04	2.34	0.44
G2	Min	-5.22	-5.04	1.04
G3	Max	0.41	1.05	0.39
G3	Min	-5.43	-2.18	2.49
22	Vertical SPREAD 450N + 35% X +5% Y	FE	SG	
G1	Max	0.62	1.69	0.37
G1	Min	-2.40	-1.48	1.62
G2	Max	0.91	2.34	0.39
G2	Min	-4.70	-5.04	0.93
G3	Max	0.38	1.05	0.36
G3	Min	-3.47	-2.18	1.59
23	Vertical SPREAD 450N + 35% 500 X +5% 500 Y	FE	SG	
G1	Max	0.66	1.69	0.39
G1	Min	-2.79	-1.48	1.89
G2	Max	0.90	2.34	0.39
G2	Min	-4.55	-5.04	0.90
G3	Max	0.40	1.05	0.38
G3	Min	-2.56	-2.18	1.18
24	Vertical SPREAD 450N + 35% 450 X +5% 500 Y	FE	SG	
G1	Max	0.67	1.69	0.40
G1	Min	-2.43	-1.48	1.64
G2	Max	0.91	2.34	0.39
G2	Min	-4.60	-5.04	0.91
G3	Max	0.38	1.05	0.36
G3	Min	-3.57	-2.18	1.64

25	Vertical SPREAD 390N + 35% X +5% Y	FE	SG	
G1	Max	0.54	1.69	0.32
G1	Min	-2.09	-1.48	1.41
G2	Max	0.79	2.34	0.34
G2	Min	-4.09	-5.04	0.81
G3	Max	0.33	1.05	0.31
G3	Min	-3.02	-2.18	1.38
26	Vertical SPREAD 535N + 35% X +5% Y	FE	SG	
G1	Max	0.74	1.69	0.43
G1	Min	-2.84	-1.48	1.92
G2	Max	1.08	2.34	0.46
G2	Min	-5.56	-5.04	1.10
G3	Max	0.45	1.05	0.43
G3	Min	-4.11	-2.18	1.88

Table. A1.19 Table details the predicted (Finite Element) and measured (strain gauge) principal stress results for a single load step for the application of force testing in the compressive alignment study. (Chapter 7).

Gauge/Test Number	**Brief Description of Load Amendment**	**Load (kN)**	**Stress Result (MPa)**	
G 1-9	Vertical SPREAD + 40% X	Load (kN)	FE	SG
G1	Max	0.5	0.42	1.76
		1	0.84	3.27
		1.5	1.26	4.42
		2	1.68	5.73
		0.5	-2.99	-2.29
		1	-5.97	-4.37
		1.5	-8.96	-5.71
		2	-11.94	-7.43
G2	Max	0.5	1.02	2.15
		1	2.04	4.13
		1.5	3.06	5.74
		2	4.08	7.60
G2	Min	0.5	-5.98	-4.90
		1	-11.96	-9.32
		1.5	-17.94	-12.95
		2	-23.93	-16.79
G3	Max	0.5	0.59	1.16
		1	1.17	3.08
		1.5	1.76	5.64
		2	2.34	7.73
G3	Min	0.5	-1.38	-2.08
		1	-2.75	-6.24
		1.5	-4.13	-11.69
		2	-5.50	-16.14
20	Vertical SPREAD + 35% X +5% Y		FE	SG
G1	Max	0.5	0.67	1.76
		1	1.35	3.27
		1.5	2.02	4.42

		2	2.69	5.73
G1	Min	0.5	-2.61	-2.29
		1	-5.22	-4.37
		1.5	-7.83	-5.71
		2	-10.44	-7.43
G2	Max	0.5	0.99	2.15
		1	1.98	4.13
		1.5	2.96	5.74
		2	3.95	7.60
G2	Min	0.5	-5.08	-4.90
		1	-10.15	-9.32
		1.5	-15.23	-12.95
		2	-20.30	-16.79
G3	Max	0.5	0.41	1.16
		1	0.82	3.08
		1.5	1.24	5.64
		2	1.65	7.73
G3	Min	0.5	-3.72	-2.08
		1	-7.44	-6.24
		1.5	-11.16	-11.69
		2	-14.88	-16.14
26	Vertical SPREAD 535N + 35% X +5% Y		FE	SG
G1	Max	0.5	0.74	1.76
		1	1.47	3.27
		1.5	2.21	4.42
		2	2.94	5.73
G1	Min	0.5	-2.84	-2.29
		1	-5.68	-4.37
		1.5	-8.53	-5.71
		2	-11.37	-7.43
G2	Max	0.5	1.08	2.15
		1	2.16	4.13
		1.5	3.24	5.74
		2	4.32	7.60
G2	Min	0.5	-5.56	-4.90
		1	-11.12	-9.32
		1.5	-16.68	-12.95
		2	-22.24	-16.79
G3	Max	0.5	0.45	1.16
		1	0.90	3.08
		1.5	1.35	5.64
		2	1.81	7.73
G3	Min	0.5	-4.11	-2.08
		1	-8.22	-6.24
		1.5	-12.33	-11.69
		2	-16.44	-16.14

Table. A1.20. Table details the predicted (Finite Element) and measured (strain gauge) principal stress results for each load step for the application of force testing in the compressive alignment study in the three most accurate iterations. (Chapter 7).

Interval	Minimum Thold	Volume mm³	GS	BMD (app)	Assigned E (MPa)	Max Principal Strain	Min Principal Strain
1	95	50810	113	0.252	761	0.0056	-0.0025
2	97	48520	139	0.278	900	0.0034	-0.0026
3	100	45320	177	0.320	1133	0.0022	-0.0024
4	110	34680	305	0.456	2010	0.0027	-0.0022
5	105	39790	241	0.388	1551	0.0026	-0.0021
6	141	21860	703	0.881	5616	0.0111	-0.0186
7	120	27000	434	0.594	3046	0.0027	-0.0030
8	115	31320	370	0.526	2514	0.0027	-0.0025
9	125	26940	498	0.662	3610	0.0030	-0.0047
10	135	22210	626	0.799	4828	0.0065	-0.0078

Table. A1.21. Table details the response to the changing threshold level for 10 iterations during thresholding assessment. (Chapter 7).

From Chapter 8:

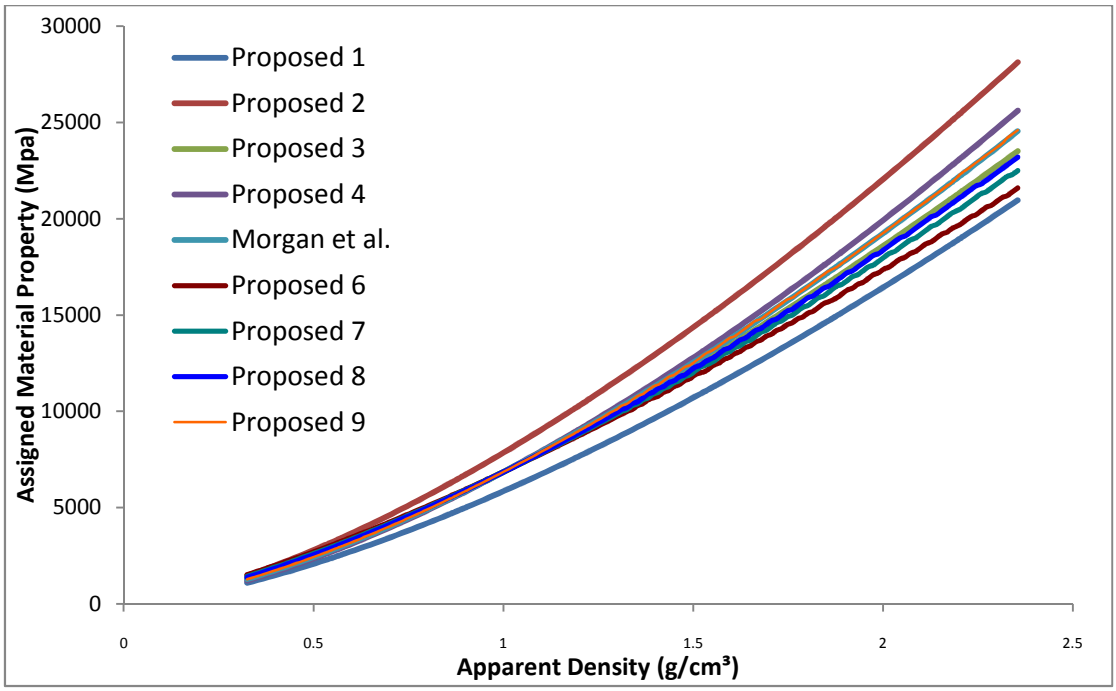

Figure A1.22. The eight additional material relationships used during the production of an improved material mapping relationship. (Chapter 8)

	Proposed Relationship		Results Output				
Relationship	Gradient	Power	Gradient	Intercept	R^2	RMSE %	Max Error %
Morgan et al.	6.85	1.490	0.998	0.310	0.965	10.7	30.3
Proposed 1	5.85	1.490	0.860	0.410	0.964	14.3	34.5
Proposed 2	7.85	1.490	1.189	0.144	0.943	15.7	60.2
Proposed 3	6.85	1.440	0.993	0.754	0.965	10.9	25.0
Proposed 4	6.85	1.540	1.045	0.321	0.945	13.6	39.6
Proposed 7	6.85	1.340	0.942	0.515	0.965	11.3	28.2
Proposed 6	6.85	1.290	0.962	0.512	0.965	10.9	26.6
Proposed 8	6.85	1.390	0.976	0.487	0.965	10.8	25.5
Proposed 9	6.85	1.420	1.000	0.333	0.965	10.6	30.3

Table. A1.23. The eight additional material relationships used during the production of an improved material mapping relationship. (Chapter 8)

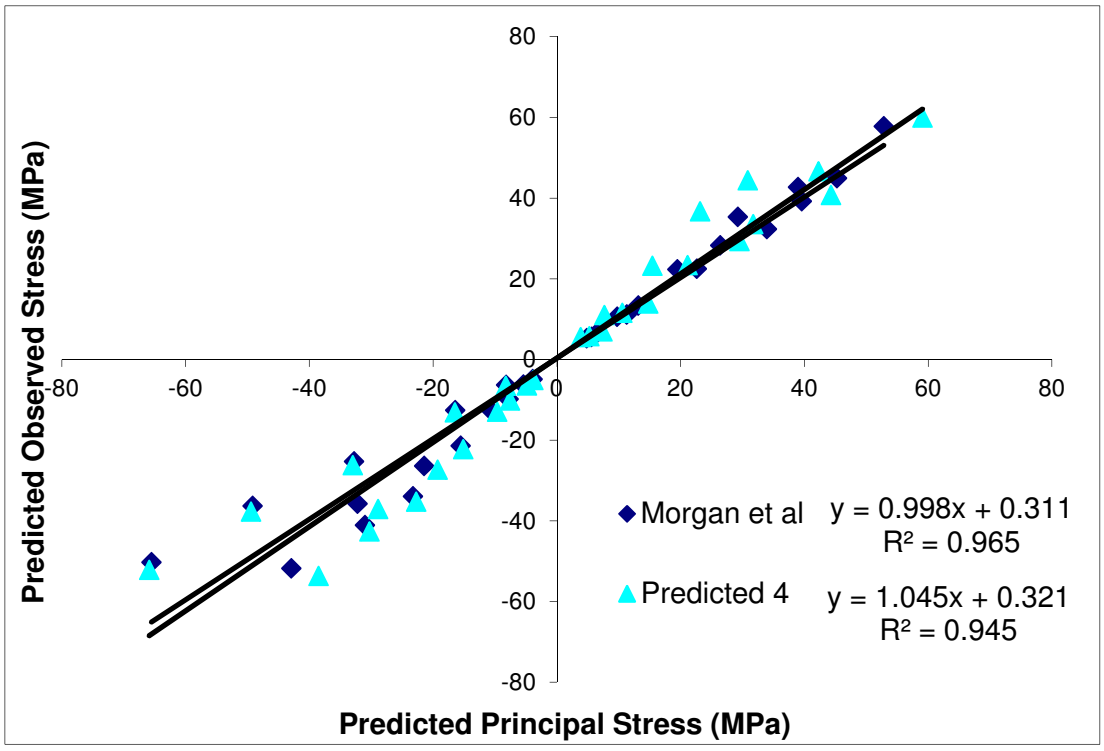

Figure A1.24. Correlation of the most accurate material relationship prior to linear interpolation (predicted 4) during the production of an improved material mapping relationship. (Chapter 8)

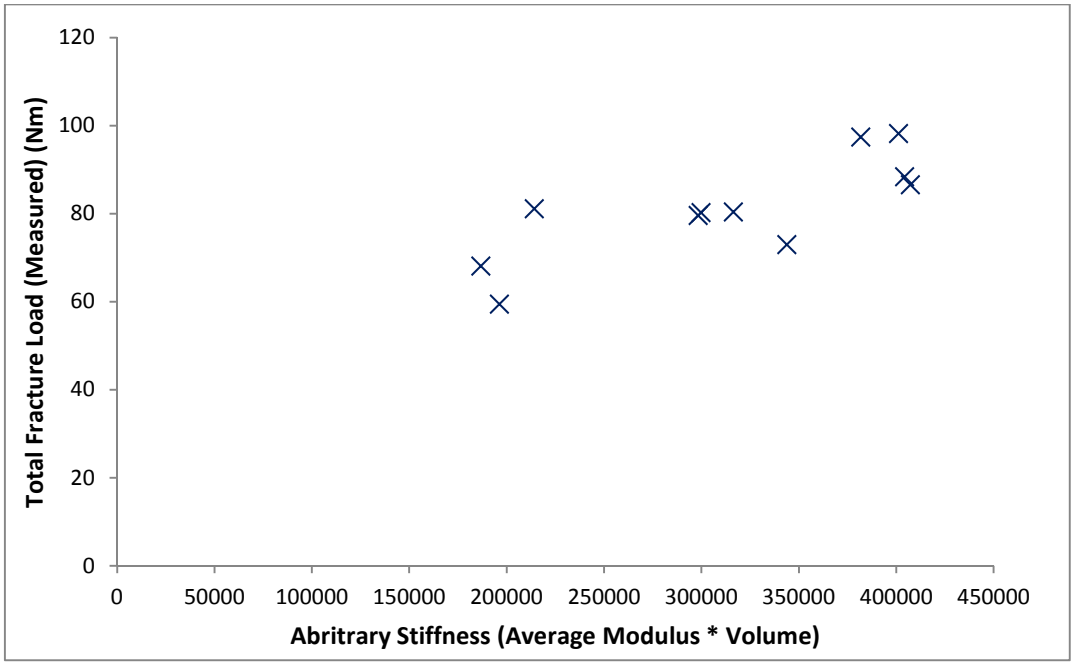

Figure A1.25. Correlation of the arbitrary stiffness (volume multiplied by average material property) and total fracture load of the 11 samples tested to fracture. (Chapter 8)

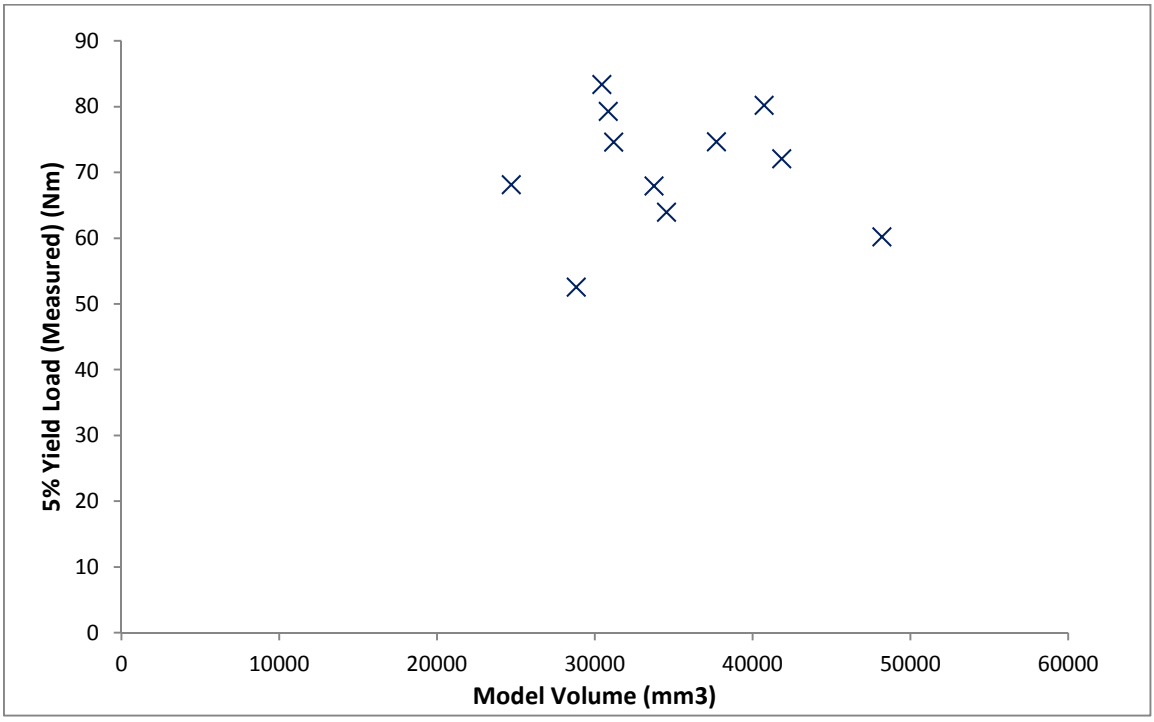

Figure A1.26 Correlation of the model volume and 5% yield load of the 11 samples tested to fracture. (Chapter 8)